SUPERNOVAE THEORY: STUDY OF ELECTRO-WEAK PROCESSES DURING GRAVITATIONAL COLLAPSE OF MASSIVE STARS

A. F. Fantina

Université Paris Sud XI - U.F.R. Scientifique d'Orsay
Institut de Physique Nucléaire d'Orsay
Università degli Studi di Milano - Facoltà di SS.MM.FF.NN.
Dipartimento di Fisica

THÈSE DE DOCTORAT

présentée pour obtenir le grade de docteur de l'Université Paris Sud XI par

Anthea Francesca FANTINA

Sujet :

SUPERNOVAE THEORY: STUDY OF ELECTRO-WEAK PROCESSES DURING GRAVITATIONAL COLLAPSE OF MASSIVE STARS

soutenue le 18 Octobre 2010 devant la Commission d'examen :

M.	**Marcello BALDO**	Rapporteur
M.	**Eric GOURGOULHON**	Examinateur
Mme	**Francesca GULMINELLI**	Rapporteur
M.	**Elias KHAN**	Directeur de Thèse
M.	**Pierre M. PIZZOCHERO**	Directeur de Thèse
Mme	**Tiina SUOMIJÄRVI**	Président
M.	**Patrick BLOTTIAU**	Invité
M.	**Jérôme MARGUERON**	Invité

"I ask you to look both ways. For the road to a knowledge of the stars leads through the atom; and important knowledge of the atom has been reached through the stars."

Sir Arthur Eddington (1882-1944), from "Stars and Atoms" (1928)

"... Got the stars, to guide my way..."

Guy Clark, from "Boats to build" (1992)

Contents

List of Figures

List of Tables

Abstract

The physics of supernova requires the understanding of both the complex hydrodynamical phenomena (such as transfer of energy, neutrino transport, shock) as well as the microphysics related to the dense and hot matter. In the framework of type II Supernovae theory, currently most of numerical simulations that simulate the supernova core collapse up to the formation and propagation of the shock wave fail to reproduce the observed explosion of the outer layers of massive stars. The reason for that could be due both to hydrodynamical phenomena such as rotation, convection, and general relativity, and to some microphysical processes involved in the picture and not yet completely understood. The aim of this work is to investigate some of these microphysical inputs, namely the electro-weak processes, that play a crucial role during the gravitational collapse and to analyse their effects by means of hydrodynamical simulations. Among nuclear processes which occur in core-collapse supernova, the most important electro-weak process taking place during the collapse is the electron capture; it occurs both on free protons and on protons bound in nuclei. This capture is essential to determine the evolution of the lepton fraction of the core during the neutronization phase. It affects the efficiency of the bounce and, as a consequence, the strength of the shock wave. Moreover, both the equation of state of supernova matter and electron capture rates in nuclei are modified by the effective mass of nucleons in nuclei, induced by many-body correlations in the dense medium, and its temperature dependence.

In the first part of the thesis, a nuclear model aimed at studying the nuclear effective mass is presented. We show how we have included in a energy density functional (EDF) approach a surface-peaked nucleon effective mass to mimic some effects beyond Hartree-Fock. We have added a term to the Skyrme functional, in order to reproduce the enhancement of the effective mass at the nuclear surface, increasing the level density around the Fermi surface. We apply this framework to analyse the mean field properties in ^{40}Ca and ^{208}Pb nuclei, and the pairing properties at zero and finite temperature in the nucleus ^{120}Sn. New calculations to evaluate the temperature dependence of the nucleon effective mass in the microscopic RPA framework are underway.

The second part of the thesis is devoted to the supernova models I have worked on. The results obtained within a one-zone approximation, such as the ones achieved in spherically symmetric one-dimensional Newtonian and General Relativistic codes are presented. Even if there are many facet of a supernova event that cannot be consistently captured by a spherically symmetric model, and observations of neutron star kicks, or inhomogeneous ejecta, invoke multi-dimensional effects, one dimensional simulations allow a first and detailed study of different specific inputs and can focus on the uncertainties in nuclear physics.
In particular, we show that, introducing a temperature dependent nuclear symmetry en-

ergy (via a temperature dependent nucleon effective mass) into the supernova simulations, in the case of a one-zone and a spherically symmetric one dimensional Newtonian code with neutrino transport, the deleptonization is systematically reduced, and the effect on the shock wave energetics is non-negligible.
Furthermore, the results obtained with a General Relativistic code, without neutrino transport but with the evolution equation for neutrinos already implemented in a multi-group fashion, are analysed. We study the impact of the equation of state and the electron capture on the collapse phase. A Newtonian version of the code has been implemented, thus comparisons are carried out. The obtained results are in global agreement with the literature.

The development of numerical codes done in this thesis in order to simulate the core-collapse is suitable to test microscopical properties of the matter and can provide a useful tool for future research projects.

Résumé en français

La physique des supernovae requiert la connaissance soit des phénomènes complexes hydrodynamiques dans la matière dense (comme le transport d'énergie et des neutrinos, le traitement du choc) soit de la microphysique liée à la physique des noyaux et de la matière nucléaire dans la matière dense et chaude. Dans le cadre de la théorie des supernovae de type II, la plus part des simulations numériques qui simulent l'effondrement du coeur de supernova jusqu'à la formation et la propagation de l'onde du choc n'arrive pas à reproduire l'explosion des couches extérieures des étoiles massives. La raison pour cela pourrait être due soit aux phénomènes hydrodynamiques comme la rotation, la convection, ou bien la relativité générale, soit aux processus microphysiques qui ne sont pas très bien connus dans ce domaine de densités, températures et asymétries. Le but de ce travail de thèse est d'étudier l'effet de certaines processus microphysiques, en particulier les processus électro-faibles, qui jouent un rôle fondamental pendant l'effondrement gravitationnel, et d'analyser leur impact avec une simulation hydrodynamique. Parmi les processus microphysiques qui interviennent lors d'un effondrement de supernova, le plus important processus électro-faible est la capture électronique sur les protons libres et sur les noyaux. La capture est essentielle pour déterminer l'évolution de la fraction leptonique dans le coeur pendant la phase de neutronisation. Elle a un impact sur l'efficacité du rebond et, par conséquent, sur l'énergie de l'onde du choc. De plus, l'équation d'état de la matière et les taux de capture électronique sur les noyaux sont modifiés par la masse effective des nucléons dans les noyaux, due aux correlations à multi-corps dans le milieu dense, et à sa dépendence de la température.

Après une introduction générale qui contient une revue de la phénoménologie des supernovae en appuyant sur la nécessité de la connaissance des données nucléaires pour les simulations numériques, dans la première partie de la thèse les aspects nucléaires abordés dans ce travail sont présentés. Le Chapitre 2 est constitué par une courte introduction sur les concepts importantes qui sont développés dans la Partie I et utilisés dans la Partie II de la thèse; en particulier: la théorie du champ moyen, de l'appariement en approximation BCS, la définition de masse effective en connexion avec la densité des niveaux et l'énergie de symétrie. Dans le Chapitre 3, un modèle nucléaire dont le but est d'améliorer la densité d'états autours du niveau de Fermi dans les noyaux est présenté. On a inclu dans l'approche de la fonctionnelle de la densité une masse effective piquée en surface qui simule certains effets au delà de Hartree-Fock. Cela a été possible en ajoutant un terme à la fonctionnelle de Skyrme qui puisse reproduire l'augmentation de la masse effective et de la densité d'états à la surface de Fermi, comme attendu par les données expérimentales. On a étudié l'impact de ce nouveau terme sur les propriétés de champ moyen dans les noyaux ^{40}Ca et ^{208}Pb, et sur les propriétés d'appariement à température nulle et à température finie dans le noyau ^{120}Sn.

On a aussi commencé des nouveaux calculs pour évaluer la dépendance en température de la masse effective dans l'approche microphysique de la RPA, dont les résultats préliminaires sont montrés dans l'Appendice D.
Cette partie nucléaire est complétée par une appendice (Appendice B), qui donne les détails des paramétrisations de Skyrme utilisées dans le texte, et par l'Appendice C qui analyse la dépendence de la température de la masse effective en connection avec le paramètre de densité des niveaux qui peut être extrait par les expériences de physique nucléaire.

La deuxième partie de la thèse est dediée aux modèles de supernova sur lequels j'ai travaillé. On présente les résultats obtenus avec un approche à une zone, et deux modèles monodimensionnels en symétrie sphérique: newtonien et en relativité générale. Bien que un modèle en symétrie sphérique n'est pas capable de saisir tous les aspects complexes du phénomène de supernova, et les observations des vitesses des étoiles à neutrons ou des inhomogéneitées des éjecta requièrent l'inclusion dans les simulations des effets multidimensionnels, un modèle monodimensionnel permet un premier étude détaillé de l'impact des différentes données microphysiques en focalisant l'analyse sur l'incertitude des données de physique nucléaire.
Après une introduction générale faite dans le Chapitre 4 qui décrit les principals ingrédients des différentes simulations numériques (comme le traitement du choc et le transport de neutrinos), les codes sur lequels j'ai travaillé sont illustrés en détail.
Le Chapitre 5 présente un modèle à une zone, où le coeur de supernova a été approximé par une sphère de densité homogène. Bien que ceci est un modèle simple, il est capable de reproduire de façon qualitative (et quantitative dans ses ordres de grandeur) la "trajectoire" d'effondrement (i.e. l'évolution des grandeurs thérmodynamiques le long de l'effondrement). Dans ce cadre, on a évalué l'impact de la dépendance en température de l'énergie de symétrie (via la dépendance en température de la masse effective) dans la dymanique du *collapse*, et on a montré que, en incluant cette dépendance en température, la deleptonisation dans le coeur est systématiquement réduite et l'effet sur l'énergie du choc est non-négligeable. Ces résultats nous ont conduit à effectuer des simulations plus réalistes, en employant un code monodimensionnel newtonien en symétrie sphérique, avec transport des neutrinos. La description de ce code, développé par P. Blottiau et Ph. Mellor au CEA,DAM,DIF, est l'object du Chapitre 6. On a inclu dans l'équation d'état dérivée par Bethe *et al.*(BBAL), aussi utilisée dans le code à une zone, la même paramétrisation de la masse effective, qui agit à la fois sur les Q-valeurs des taux de capture et sur l'équation d'état du système. Les résultats de ces simulations ont confirmés ceux qui avaient été obtenus avec le code *one-zone*, c'est à dire la reduction systématique de la deleptonisation dans le coeur si on inclue la dépendance en température de l'énergie de symétrie. De plus, on en a estimé l'impact sur la position de la formation de l'onde du choc, qui est déplacée vers l'extérieur d'une quantité non-négligeable. On a aussi travaillé pour inclure dans le code l'équation d'état plus récente de Lattimer et Swesty.
Enfin, le Chapitre 7 décrit un code, à l'origine développé par le groupe de Valence, écrit en rélativité générale et qui utilise un approche moderne pour le traitment du choc (la "capture du choc"). Bien que ce modèle ne contient pas le transport des neutrinos, l'équation de l'évolution de la fraction neutrinique est déjà écrite avec un schema multi-groupe qui permet une première analyse spectrale des neutrinos. On étudie l'effet de l'équation d'état dans la dynamique d'effondrement ainsi que l'impact de la capture électronique. Une versione newtonienne a été aussi implémentée et les résultats obtenus sont en accord avec la

littérature.
Cette partie est complétée par plusieurs appendices. Dans l'Appendice A, les différentes unités de mesure employées dans les codes sont listées. Les Appendices E et F sont dédiées à deux équations d'état: la prémière est celle d'un gas de neutrons, protons et électrons; la deuxième décrit l'équations d'état de Lattimer et Swesty et les modifications qu'on a apportés pour corriger une erreur dans la définition de l'énergie de liaison des particules alpha et pour étendre l'équation d'état à des densités plus basses. Enfin, l'Appendice G détaille les processus des neutrinos implémentés dans les simulations.

Le développement des codes numériques pour simuler l'effondrement gravitationnel de supernova effectué dans ce travail de thèse est apte pour tester les propriétés de la matière et peux constituer un outil pour des projets de recherche futurs.

Riassunto in italiano

La fisica delle supernovae richiede la comprensione sia dei complessi fenomeni idrodinamici (come il trasporto di energia e di neutrini, la fisica delle onde d'urto) sia dei processi microfisici nella materia densa. Nell'ambito della teoria delle supernovae di tipo II, attualmente la maggior parte delle simulazioni numeriche che simulano il collasso del *core* fino alla formazione e alla propagazione dell'onda d'urto fallisce nel riprodurre l'esplosione degli strati esterni delle stelle massive. La motivazione di ciò è da ricercarsi sia nell'effetto di fenomeni idrodinamici come la rotazione, la convezione e la relatività generale, sia di alcuni processi microfisici coinvolti e non ancora completamente compresi. Lo scopo di questo lavoro di tesi è di investigare alcuni di questi processi microfisici, in particolare i processi elettrodeboli, che svolgono un ruolo essenziale durante il collasso gravitazionale e di analizzare il loro effetto per mezzo di una simulazione idrodinamica. Tra i processi microfisici che intervengono durante il collasso di supernova, il più importante processo elettrodebole è la cattura elettronica sui protoni liberi e sui nuclei. Tale cattura è cruciale per determinare l'evoluzione della frazione leptonica nel nucleo durante la fase di neutronizzazione; ha un impatto sull'efficacia del *bounce* e, di conseguenza, sull'energia dell'onda d'urto. Inoltre, l'equazione di stato della materia e i tassi di cattura elettronica sui nuclei sono modificati dalla massa efficace dei nucleoni nei nuclei, dovuta alle correlazioni a molti corpi nella materia densa, e alla sua dipendenza dalla temperatura.

Dopo un'introduzione generale che contiene una panoramica della fenomenologia delle supernovae, con particolare riferimento all'importanza degli *inputs* di fisica nucleare nelle simulazioni numeriche, nella Parte I della tesi sono presentati gli aspetti nucleari sviluppati nel presente lavoro. Il Capitolo 2 è costituito da una breve introduzione sui principali concetti sviluppati nella Parte I e utilizzati nella Parte II della tesi; in particolare, vengono introdotte le teorie di campo medio e di *pairing* in approssimazione BCS, il concetto di massa efficace in relazione alla densità di stati attorno al livello di Fermi, e l'energia di simmetria. Nel Capitolo 3 viene descritto un modello nucleare il cui scopo è di migliorare la descrizione della densità di stati attorno al livello di Fermi nei nuclei. Nell'approccio del funzionale della densità, è stata introdotta una massa efficace piccata in superficie che simuli gli effetti dovuti all'accoppiamento particella-vibrazione e che vanno al di là del modello Hartree-Fock. A questo scopo, è stato aggiunto un nuovo termine al funzionale della densità di Skyrme, tale da produrre un aumento della massa efficace e della densità di stati in corrispondenza della superficie di Fermi, come atteso dagli esperimenti di fisica nucleare. L'impatto di questo nuovo termine sulle proprietà di campo medio è stato testato sui nuclei ^{40}Ca e ^{208}Pb, mentre l'analisi dell'effetto sul *pairing* è stata condotta per il nucleo ^{120}Sn. Abbiamo inoltre iniziato nuovi calcoli per valutare la dipendenza dalla temperatura della massa efficace nell'approccio microscopico

della RPA, il cui formalismo e i cui risultati preliminari sono presentati in Appendice D. Questa prima parte dedicata ai modelli nucleari è completata dall'Appendice B che riporta i dettagli delle parametrizzazioni di Skyrme usate o citate nel corpo della tesi, e dall'Appendice C dove viene analizzata la dipendenza dalla temperatura della massa efficace in connessione con il parametro di densità di livelli che può essere estratto negli esperimenti di fisica nucleare.

La seconda parte della tesi è dedicata ai modelli di supernova sui quali ho lavorato. Vengono presentati i risultati ottenuti attraverso un modello a una zona, newtoniano a simmetria sferica e un modello scritto in relatività generale a simmetria sferica. Ci sono molti aspetti della fenomenologia di supernova che non possono essere consistentemente inclusi in un modello a simmetria sferica, e le osservazioni delle velocità delle stelle di neutroni, delle inomogeneità degli *ejecta* richiedono che effetti multidimensionali siano inclusi nelle simulazioni numeriche. Tuttavia, le simulazioni monodimensionali permettono un primo studio dettagliato dell'impatto di differenti input microfisici focalizzando l'analisi sulle incertezze presenti nei modelli di fisica nucleare.
Successivamente a un'introduzione generale effettuata nel Capitolo 4, dove vengono descritti i principali ingredienti delle differenti simulazioni numeriche (come la trattazione dell'onda d'urto o il trasporto di neutrini), vengono illustrati i codici sui quali ho lavorato. Il Capitolo 5 presenta un modello *one-zone*, in cui il *core* di supernova viene approssimato da una sfera di densità omogenea. Nonostante sia un toy-model pedagogico, tale modello ha dato prova di efficacità nel riprodurre la fase di deleptonizzazione durante il collasso gravitazionale. È pertanto un modello in grado di descrivere qualitativamente e quantitativamente nei corretti ordini di grandezza la traiettoria di collasso, ovvero l'evoluzione delle grandezze termodinamiche durante il collasso. In questo approccio, è stato valutato l'impatto della dipendenza dalla temperatura dell'energia di simmetria (via la dipendenza dalla temperatura della massa efficace) nella dinamica di collasso. L'inclusione della suddetta dipendenza dalla temperatura porta a una sistematica riduzione della deleptonizzazione nel *core* di supernova e gli effetti sull'energia dell'onda d'urto sono stimati essere non trascurabili. I risultati si questa simulazione ci hanno motivato a condurre simulazioni più realistiche con un codice idrodinamico newtoniano a simmetria sferica, originariamente sviluppato da P. Blottiau e Ph. Mellor al CEA,DAM,DIF. La descrizione di questo codice è l'oggetto del Capitolo 6. La dipendenza dalla temperatura dell'energia di simmetria, che agisce sia sul Q-valore delle reazioni di cattura sia sull'equazione di stato del sistema, è stata implementata in tale codice nell'equazione di stato derivata da Bethe *et al.*(BBAL), utilizzata anche nel precedente modello a una zona. I risultati delle simulazioni condotte con il codice newtoniano confermano quelli ottenuti con il codice *one-zone*, i.e. una sistematica riduzione della deleptonizzazione nel *core*. Inoltre, è possibile in questo caso valutare l'effetto della dipendenza dalla temperatura dell'energia di simmetria sulla posizione della formazione dell'onda d'urto, che si forma più esteriormente di una quantità non trascurabile. Abbiamo anche lavorato all'inclusione nel codice dell'equazione di stato più recente di Lattimer e Swesty.
Infine, il Capitolo 7 descrive un codice monodimensionale, originariamente sviluppato dal gruppo di Valencia, scritto in relatività generale e che utilizza la moderna tecnica di *shock capturing* per la trattazione dello shock. Nonostante questo codice non sia avanzato come quello newtoniano per quanto riguarda la trattazione dei neutrini (infatti, nessun modello di trasporto è presente), l'equazione dell'evoluzione della frazione dei neutrini

è già implementata in uno schema multi-gruppo, il che consente di effettuare una prima analisi spettrale dei neutrini, essenziale per il confronto con le osservazioni. L'impatto dell'equazione di stato del sistema così come della cattura elettronica durante il collasso è analizzato. È stata inoltre implementata una versione newtoniana e i risultati ottenuti sono in accordo globale con la letteratura.
Questa parte astrofisica è completata da numerose appendici. Nell'Appendice A, vengono fornite le conversioni di unità di misura utilizzate nei codici. Le Appendici E e F sono dedicate a due equazioni di stato: la prima è quella di un gas di neutroni, protoni ed elettroni; la seconda descrive l'equazione di stato di Lattimer e Swesty e come è stata modificata al fine di correggere un noto errore nell'energia di legame delle particelle alpha e al fine di estendere l'applicabilità della routine a densità più basse. Infine, l'Appendice G riporta i processi dei neutrini implementati nei codici.

Lo sviluppo di codici numerici per simulare il collasso del *core* di supernova effettuato in questo lavoro di tesi è rilevante per testare le proprietà della materia e può costituire un utile strumento per progetti di ricerca futuri.

Abbreviations:

ADM : "Arnowitt-Deser-Misner".
It refers to the $\{3+1\}$ formalism based on the $\{3+1\}$ splitting of the spacetime [10].

AIC : "Accretion-Induced Collapse".
It refers to a kind of supernovae, which undergoes collapse after reaching the Chandrasekhar mass by accretion. The AIC supernovae have been also proposed as explanation for gamma-ray bursts.

BBAL : "Bethe-Brown-Applegate-Lattimer".
It refers to the paper Ref. [34].

BH : "Black Hole".

CCSN : "Core-Collapse Supernova(e)".

EDF : "Energy Density Functional".

EoS : "Equation(s) of State".

FFN : "Fuller-Fowler-Newman".
It refers to the papers Refs. [127, 128, 129, 130].

GR : "General Relativity".

GRB : "Gamma-Ray Burst(s)".

GT : "Gamow-Teller".
It refers to the transition playing a central role in electron capture (GT^+) and beta decay (GT^-). Unlike Fermi transition, in a GT transition spin-flip occurs.

HF : "Hartree-Fock".

HRSC : "High-Resolution Shock Capturing".
It is a technique to treat discontinuities in hydrodynamical equations avoiding the use of the artificial viscosity.

IM : "Interstellar Medium".

IPM : "Independent-Particle-Model".
It is an approximation used in describing the many-body problem: particles are supposed to move independently from the other particles, feeling the mean field generated by them.

LMC (SMC) : "Large (Small) Magellanic Cloud".
It is a Milky Way's satellite galaxy, distant about 50 kpc. SN1987A was observed in the LMC.

LMP : "Langanke Martínez-Pinedo".
It refers to the weak interaction rates derived in the shell model framework by Langanke and Martínez-Pinedo (Refs. [184, 185]).

LS : "Lattimer-Swesty".
This acronym stands for the EoS derived by Lattimer and Swesty [192]. We will also use the notation: LSXXX, where XXX = 180, 220, 375, according to the value of the incompressibility modulus we want to refer to.

MF : "Mean Field".

MGFLD : "Multi(energy)-Group Flux-Limited Diffusion".
It refers to an approximation in solving the Boltzmann equation for neutrino transport. It computes the energy dependent transport in diffusion approximation by considering neutrino energies divided into a certain number of energy bin (typically 20). It is extensively treated in Bruenn [56].

MS : "Main Sequence".
In the Hertzsprung-Russel diagram (luminosity vs surface temperature), stars are positioned according to their radiative properties. According to their mass, chemical composition and age, stars follow different evolution paths in this diagram. The main sequence is a rough diagonal line (from down-right to top-left) in this diagram, and represents the phase in which a star converts hydrogen into helium [85, 295].

npe : "neutron-proton-electron".
It refers to the npe gas EoS (see e.g. the Shapiro and Teukolski textbook [295], or Appendix E).

NS : "Neutron Star(s)".

NSE (QSE) : "Nuclear (Quasi) Statistical Equilibrium".
In the NSE, the condition of complete equilibrium among nuclear species under exchange of neutrons and protons is assumed. The relative abundances of the species can thus be computed by means of the Saha equation.
In the QSE, the processes occur "as if" they were in instantaneous equilibrium; for this to be true the process must be slow compared to the time needed for the system to come to equilibrium.

ODE : "Ordinary Differential Equation(s)"

PDE : "Partial Differential Equation(s)"

PNS : "Proto-Neutron Star(s)".

PVC : "Particle-vibration coupling".

RGPS : "Radial Gauge Polar Slicing".
It is a choice of slicing (i.e. of the hypersurfaces Σ_t) and of coordinates in spherical symmetry [141]. It is used in the Relativistic code by Romero *et al.* [285] described in Chapter 7.

RMF : "Relativistic Mean Field".

RPA : "Random Phase Approximation".
It is a well known many-body approximation that treats the long-range correlations on top of an HF state [282].

SASI : "Standing Accretion Shock Instability".
It is a generic hydrodynamical instability of the accretion shock to non-radial deformation [116, 40].

SM : "Shell Model".

SMMC : "Shell Model Monte Carlo".

SN : "Supernova(e)".

sp : "single-particle".

WW95 : "Woosley and Weaver 1995".
It refers to presupernova models computed in [348].

ZAMS : "Zero Age Main Sequence".
It refers to the stellar evolution stage when the star burns hydrogen to helium, i.e. when the star lies, in the Hertzsprung-Russell diagram, on the main sequence.

Chapter 1

Introduction

1.1 Supernovae

Supernovae are one of nature's most powerful phenomena. They release in one second about 10^{53} erg, which is comparable with the integrated light radiated by their host galaxies. 99% of the energy is emitted in neutrinos, 1% goes to the kinetic energy of the ejecta partially converted into electromagnetic radiation, and a very tiny fraction is radiated as gravitational waves.

The name *supernova* was first introduced by Baade and Zwicky [11] to designate a "remarkable type of giant novae", a rare and very energetic phenomenon, characterized by a sudden burst in luminosity followed by a slow decay, and they suggested that "a super-nova process represents the transition to an ordinary star into a neutron star". Since then, scientists have tried to understand in detail how they work, and despite enormous progresses have been made, both from theoretical, computational and observational point of view, the whole picture is yet to be completely understood.
There exist different kinds of supernovae, and even if all of them represent the explosive end point of stellar evolution and play a central role in enriching the interstellar medium with heavy elements, different physical mechanisms power them. Core-collapse supernovae (CCSN) represent the end point of stellar evolution of massive stars, typically with mass more than $\sim 8\ M_{\odot}$ and they have never been observed in elliptical galaxies. These kind of stars go through all burning stages, starting from hydrogen up to iron, and at the end of their lives, they have an *onion-skin* structure, with a core mainly composed by iron-peak nuclei, and a sequence of layers formed by lighter and lighter elements going from the center to the surface of the star. Their cores undergo gravitational collapse, leaving a compact remnant (neutron star or black hole).
There is another class of supernovae (type Ia, as it will be explained below), powered by a different physical mechanism: thermonuclear explosion, occurring for stars in the mass range $\sim 4 - 8\ M_{\odot}$ [1], which end their lives as carbon-oxygen white dwarf, often in binary systems. When, by accretion from the companion star, their core reaches the Chandrasekhar limit[2], compression and heating lead to an explosive combustion of the white dwarf which destroys the star leaving no compact remnant behind.

[1] In astrophysics, the mass of the Sun is often used as a unit of measure, being $1\ M_{\odot} = 1.98 \times 10^{33}$ g.

Other than thermonuclear explosion, more massive O/Ne/Mg white dwarfs in binary systems can accrete mass from the companion star and can collapse to a neutron star. These stars undergo an accretion-induced collapse (AIC), similar to a CCSN, but with observational features more similar to type Ia events.

Historically, supernovae (SN) were classified according to observational features [11]: Minkowski [245] published the first paper on their spectra, in which he introduced two main classes: *Type I* and *Type II*, the first ones showing a lack of hydrogen lines while the spectra of the second type displaying strong hydrogen lines. As more spectra have become available, sub-classes were introduced; in the following, it will be presented a schematic summary of SN classification (see e.g. Refs. [345, 148] and Refs. therein).

- **Type I**: this kind of SN exhibits no hydrogen lines, while they show ^{56}Fe and ^{56}Co lines. Their light curves (i.e. luminosity as a function of time) display a sudden increase of luminosity, which lasts one or two weeks, a quite narrow peak and an exponential decrease which lasts some months. Type I SN are divided into:

  Ia : their spectra show strong absorption lines attributed to Si II. They occur in all types of galaxies but seem to favour the elliptic ones, suggesting that they have old stars as progenitors, and they can be 10 times more luminous than other SN types. Since the conditions of their formation and, as a consequence, their spectra, are quite similar, type Ia SN can be used as "standard candle" to determine distances. It is a common thought that they result from thermonuclear explosion of low-mass white dwarfs, leaving no compact remnant. This could explain the absence of H lines, since H would have been already converted into He or expelled via interstellar winds. During the explosive combustion, $\sim 0.6\, M_\odot$ of ^{56}Ni is produced, whose radioactive decay in ^{56}Co ($\tau = 8.8$ days) and ^{56}Fe ($\tau = 111.3$ days) generates the tail of their light curves.

  Ib/Ic : their spectra display no evident Balmer lines[3], weak or absent Si II lines, but strong He I (Ib) or Ca II and O I (Ic) absorption lines and, like type IIdw SN, they emit in radio. Like type II SN, they occur mainly in spiral galaxies, in regions where the density of young and massive stars is high, suggesting that their progenitors are quite massive and, as a consequence, have relatively short lifetime. They are thought to be the result of the evolution of very massive stars (like Wolf-Rayet stars) which have lost their hydrogen envelope via strong winds or transfer to a binary companion via Roche overflow. About 25% of all CCSN are type Ib/Ic. Recently, a new class of Type Ic was identified and often called SN **Id** or **Ic hypernovae**. They share the common spectral features of type Ic SN, but with high Doppler broadening due to high expansion velocities.

- **Type II**: classical type II SN have strong Balmer lines, indicating an expanding atmosphere. Besides Balmer lines, their light curves exhibit strong Ca, Na I and Fe lines, and a tail associated to the radioactive decay of Ni into Co. There is a large

[2]The Chandrasekhar limit represents the maximum possible mass of a white dwarf, usually abbreviated as M_{ch}. It comes out as a solution of the *Lane-Emden* equation for the structure of a degenerate white dwarf in the ultra-relativistic case [80, 295].

[3]Balmer lines designate a set of spectral lines of hydrogen, located in the visible or near-ultraviolet part of the spectrum.

variety of type II SN, characterized by a wide range of explosion energies (from 0.6 to 5.5 foes[4]) and ejected masses (from 14 to 56 $M_\odot$), and by a production of Ni which varies from 0.0016 to 0.26 $M_\odot$. The explosion energy seems to be correlated with the ejected mass and the amount of produced nickel (i.e. more energetic they are, higher is the amount of mass they eject and the nickel they produce). Among type II SN one can recognize:

II-P ("plateau"): they are the most frequent ones, characterized by a long plateau at high luminosity in their light curves, associated to the optically thick phase, where hydrogen recombinates. The plateau shape is due to the fact that after the explosion (highest luminosity), the photosphere is expanding fast enough to compensate the decrease of surface temperature, so that luminosity remains constant[5].

II-L ("linear"): their spectra exhibit a short plateau, followed by the linear tail characteristic of Ni to Co decay.

II-dw ("dense wind"): their spectra show no absorption in the Balmer lines and are dominated by strong Hα emission. This kind of SN is thought to interact strongly with the interstellar medium expelled by the SN progenitor as stellar wind before the explosion, producing radio emission. Generally, type IIdw are characterized by high luminosity (due to the collision of SN envelope with the wind), eject less mass than a classical type II SN and their $8 - 10\ M_\odot$ progenitors undergo high mass loss during the red giant phase. They represent $\sim 30\%$ of all CCSN and $\sim 40\%$ of all type II SN.

- **AIC**: the spectra of SN resulting from accretion-induced collapse is not clear, but it could be similar to the type Ia one. However, the AIC supernovae avoid the thermonuclear explosion (characteristic of a type Ia) and reach the Chandrasekhar limit by accretion at a density which assures collapse. AIC SN have been proposed as explanation for gamma-ray bursts, type Ia SN and the ejecta have been claimed to be possible source of r-process [124].

1.1.1 Observations and Supernova rates

Supernova events are quite rare in our Galaxy; moreover, since it is not possible to determine *a priori* when and where a supernova will occur, the only way to observe it is to perform a continuous and extensive survey of a large number of galaxies. Once a SN is observed, its name is constructed from the year of discovery followed by a capital letter (from A to Z), or two small letters if the letter Z is reached in labelling.
Since 185 A.D., when a SN now visible in X-ray (its remnant is thought to be RCW 86) was seen, Chinese astronomers recorded "guest stars", which suddenly appeared in the sky, lasted for some time, and then faded away. From 1000 A.D., 6 galactic SN in our Galaxy and one in Large Magellanic Cloud (LMC, one of Milky Way's nearby galaxies) were registered [321]:

[4] 1 foe = 10^{51} erg, which is the typical order of magnitude of a SN explosion. This unit was first introduced by H. Bethe and G. Brown as acronym of "(ten to the) *fifty-one erg*".

[5] Luminosity scales according to the relation: $L = 4\pi R^2 \sigma T_e^4$, where σ is the Stefan-Boltzmann constant, R is the stellar radius and T_e is the surface temperature.

- 1006: type Ia SN, often called Lupus SN. It is the most brilliant SN appeared. It was recorded by Chinese, Middle East and European astronomers. Its remnant is now visible in radio wavelengths, but no neutron star has been associated to it.

- 1054: type II SN, it was observed in China but not everywhere in Europe. Its remnant, the *Crab Nebula*, is visible in Taurus constellation. A *pulsar* (i.e. a rotating neutron star), which is located at its center, emits both electromagnetic radiation in all frequencies at regular intervals of about 33 ms, and electrons which, interacting with the interstellar medium, emit visible and polarized light.

- 1181(?): named 3C 58, maybe a type II one, observed in Cassiopeia.

- 1572: probably type Ia SN. It was observed by Tycho Brahe in Cassiopeia constellation. It emits in X-ray and radio, but no pulsar has been detected.

- 1604: type Ia SN, it is the Kepler SN. Accurately described by the astronomers at that time, its remnant has been measured in X-ray band.

Another SN exploded in our Galaxy between 1650 and 1680, but it wasn't recognized as a SN; known as Cas A (Cas stands for Cassiopeia), maybe a type Ib SN, it is a strong radio emitting source.
Extragalatic SN were recently observed, up to about a hundred per year. Among them, SN1987A, the most well-observed SN to date, recorded the 24th February 1987 in LMC, at about 50 kpc[6]from our Galaxy. Its light curve is quite different from a classical type II SN one, characterized by a steady rise during three months, followed by a fast decline in luminosity lasting ~ 20 days, and a typical linear tail expected from Ni to Co decay (in SN1987A, $\sim 0.08\ M_\odot$ of ^{56}Ni was produced [347]). This peculiarity in the spectrum was attributed to its progenitor features, *Sanduleak* Sk 202-69, a blue supergiant, warmer and more compact than a red giant, maybe because of its low metallicity [347]. Its mass is believed to have been around $18 - 20\ M_\odot$ and its radius of about 3×10^{12} cm. SN1978A was first detected through neutrino signal (by the laboratories Kamiokande II in Japan and IMB in Ohio detectors), then in UV, visible, IR, X and γ rays; from the neutrino signal (20 neutrinos were detected in a period of 10 seconds) it was possible to estimate that the energy released by the SN was about 3×10^{53} ergs [33].

The supernovae rate in galaxies is very important to determine their evolution, structure and kinematics and the composition of the interstellar medium. Estimates of CCSN rates can be made by galactic and extragalactic observations (radio distribution, Hα luminosity, pulsar observation, etc.), star formation rates and initial mass function[7]. Table 1.1 summarizes the rate estimates in the Local Group (i.e. Milky Way plus neighbouring galaxies), referring to CCSN rates and shows that one can expect to observe maximum one SN each $\sim$ 50 years in our Galaxy and one SN each $\sim$ 20 years in the whole Local Group. Type Ia SN are about 10 times less prevalent than CCSN.

[6] 1 kpc = 10^3 pc, where 1 pc = 3×10^{18} cm.

[7] The initial mass function (IMF) is an empirical function which specifies the mass distribution of a population of stars, i.e. the number of stars as a function of the initial mass they were formed with. It is frequently assumed to be a power law: $\mathrm{d}N/\mathrm{d}M \propto M^{-\alpha}$, where α is a dimensionless coefficient (see e.g. Refs. [290, 73]).

Galaxy	Distance $[\mathrm{kpc}]$	CCSN rate $[100\ \mathrm{yr}^{-1}]$
Milky Way	0 - ∼15	0.5 - 2.5
LMC	∼ 50	∼ 0.2 - 0.5
SMC	∼ 60	∼ 0.05 - 0.1
M31	∼ 770	∼ 0.2 - 0.8
M33	∼ 840	∼ 0.2 - 0.6

Table 1.1: CCSN rate estimates for the galaxies belonging to the Local group: Large and Small Magellanic Cloud (LMC/SMC), Andromeda (M31), Triangulum (M33) [72, 321, 310].

1.2 Core-collapse supernovae

Since this thesis deals mainly with CCSN physics, an overview on the current understanding of CCSN mechanism and models will be described.

1.2.1 Stellar evolution

Stars start their lives, after a first stage of contraction from interstellar medium mainly composed by light elements, entering the *main sequence* (MS), where their cores begin to ignite hydrogen into helium at a central temperature of $\sim 1.5 \times 10^7$ K. The following sequence of thermonuclear burning stage which determines the fate of a star is driven by its mass[8]. A star lasts on the MS until ∼ 10% of its total mass is converted to helium. At this point, called *Schönberg-Chandrasekhar limit*, helium core contracts under gravitational force; stars with mass in the range $\sim 0.1 - 0.5\ M_\odot$ are not able to reach the central temperature required to burn helium into carbon ($T \simeq 10^8$ K) and they cool down becoming white dwarfs.
More massive stars proceed in their nucleosynthesis, the gravitational energy released from the contraction of the core is counterbalanced by an expansion, which moves the star from the MS towards the red giant branch. Low mass stars, with masses $M \lesssim 3 - 4\ M_\odot$, undergo helium combustion into carbon in an explosive way (*helium flash*); once carbon is formed, core again contracts, causing an increase of temperature, as a consequence of which external layers heat up and expand, giving birth to a Planetary Nebula, while the central part cools down as a degenerate white dwarf [85, 73].
Intermediate mass stars, with masses between $4 - 8\ M_\odot$, undergo ignition of helium into carbon, and then into oxygen at a central temperature of $\sim 5 \times 10^8$ K. They develop electron-degenerate carbon-oxygen cores and expel their envelopes via stellar winds. If their final mass is above the Chandrasekhar limit, they undergo thermonuclear explosion, becoming a Type Ia SN. If they experience strong winds, they end up in a small mass remnant (carbon-oxygen white dwarf), at the center of a Planetary Nebula [85, 73].

[8]Stellar objects with masses $M \lesssim 0.07 - 0.1\ M_\odot$ do not even become a star; gravitational contraction is their only source of energy, and, in $10^9 - 10^{10}$ yr, they cool down, becoming a *brown dwarf* supported by degeneracy pressure.

More massive stars, $M \simeq 8 - 10\ M_\odot$, can ignite in their cores elements up to neon and magnesium, but their central temperature is too low to reach silicon burning. They can either lose their envelopes ending up in O/Ne/Mg white dwarfs maybe progenitors of a AIC SN, or undergo collapse of their low-mass O/Ne/Mg cores [73].
Stars with mass from ~ 10 to $\sim 100\ M_\odot$ complete the exothermic nuclear reaction chain up to silicon burning into iron at central temperatures of $\simeq 10^9$ K. As thermonuclear burning proceeds, the energy released in each nuclear reaction decreases, reaction rate increases and burning stages become faster and faster: if H to He conversion lasts 10^7 yr, Si into Fe combustion lasts some days. As a consequence of this burning sequence, at the end of their lives, these massive stars develop a onion-like structure, with a central core composed by iron-peak nuclei (silicon and iron group isotopes like ^{48}Ca, ^{50}Ti, ^{54}Cr, ^{58}Fe, ^{62}Ni, ^{66}Ni [34, 295]) and surrounded by layers formed by progressively lower atomic weight (silicon shell, oxygen shell, carbon shell, up to the helium and hydrogen envelope, unless the star has already lost the outermost layers via stellar winds) at progressively lower temperatures and densities.

1.2.2 Physics of Type II supernovae: from collapse to explosion

The exothermic chain of reactions in the core of massive stars ends with the formation of iron, which is the element with the highest binding energy; at this point fusion of heavier elements is no longer possible. As already mentioned, at this stage the star has an onion-like structure, with a central core composed by iron group nuclei, mainly sustained by electron degeneracy pressure. All model calculations of stellar evolution give a similar final state (*core convergence* [8]), characterized by a central density $\rho_c \sim 10^{10}\ \mathrm{g\ cm^{-3}}$, a temperature $T_c \sim 10^{10}$ K, entropy $s \sim 1\ \mathrm{k_B}$ and electron fraction (i.e. electron over baryon ratio) $Y_e \simeq 0.43 - 0.46$. Accordingly, the mass of the core reaches the Chandrasekhar mass [295]:

$$M_{ch} = 1.457\ (2Y_e)^2\ M_\odot\ , \tag{1.1}$$

whose value is around $1.4\ M_\odot$; this value decreases if one considers General Relativity and increases if rotation and thermal pressure components are taken into account [295]. The electron degeneracy pressure, which represents the main contribution to the total pressure,

$$P \propto Y_e^{4/3}\ \rho^\Gamma\ , \tag{1.2}$$

where Γ, the adiabatic index, is 4/3 for relativistic particles, cannot anymore stabilize the core which collapses under the action of the gravitational force, starting the so-called *core-collapse supernova*. This process can be divided into three phases:

1. *Infall epoch*, characterized by core contraction

2. *Bounce phase*, characterized by the formation of the shock wave

3. *Explosive phase*, characterized by the propagation of the shock wave and the expulsion of the outer layers of the stars, leaving a compact remnant at the center.

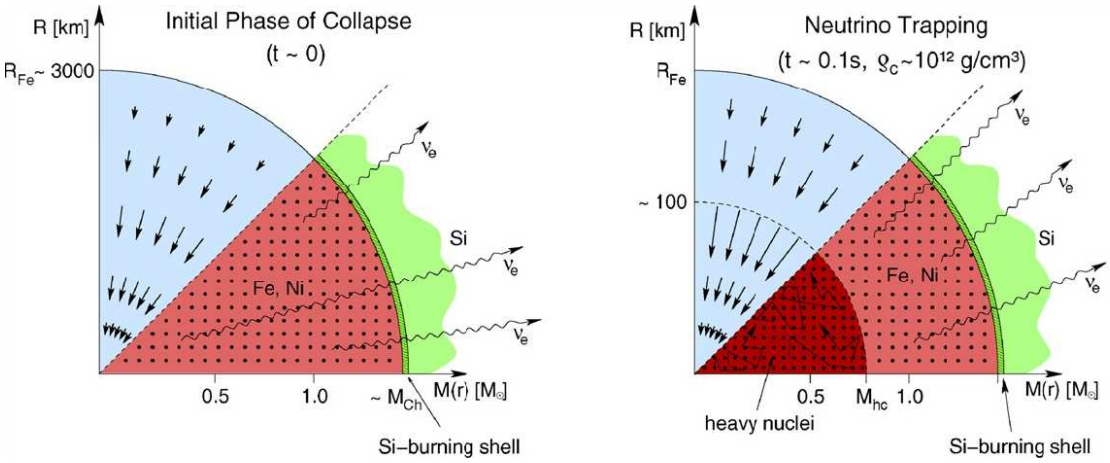

Figure 1.1: Schematic representation of the initial phases of the collapse of the core (here a cut of the core is shown, in spherical symmetry). In the upper half part of each plot the hydrodynamics is displayed, while in the bottom half part the nuclear physics is sketched. In the left panel, the initial phase of the collapse is plotted; the core is mainly composed by iron group nuclei and neutrinos are free to escape. In the right panel, neutrino trapping is shown: in the homologous subsonically collapsing core M_{hc}, neutrinos start interacting with matter (from [173]).

In the first phase, the dynamics is dominated by the entropy and electron fraction, quantities mainly determined by the weak processes. Electron capture on nuclei and free protons:

$$(A, Z) \quad + \quad e^- \rightarrow (A, Z-1) + \nu_e \tag{1.3}$$

$$p \quad + \quad e^- \rightarrow n + \nu_e \ , \tag{1.4}$$

which is allowed at the densities encountered during collapse, reduces Y_e and produces electron type neutrinos, which in the early stage of collapse are able to escape from the star, removing additional pressure and energy to the system, thus accelerating the collapse and neutronizing the matter. The collapse is also accelerated by photodissociation of iron group nuclei into α particles, e.g.

$$^{56}\mathrm{Fe} + \gamma \rightarrow 13\alpha + 4n \ , \tag{1.5}$$

an endothermic reaction whose energy requirement is ~ 124 MeV [295]. At higher temperatures, also α particles dissociate, according to the reaction [295]:

$$^{4}\mathrm{He} + \gamma \rightarrow 2p + 2n \ , \tag{1.6}$$

with a Q-value of 28.3 MeV.
When the core reaches densities around 10^{12} g cm^{-3}, neutrino opacities increase, letting the neutrino mean free path become smaller than the size of the core; as a consequence the diffusion timescale becomes greater than the dynamical timescale of the collapse: neutrinos are *trapped* and β-equilibrium is established, keeping the total lepton fraction $Y_l = Y_e + Y_\nu$ constant [295, 33] (see Fig. 1.1).

As the collapse proceeds, the density increases, and up to nuclear density ($\rho_0 \simeq 2.8 \times 10^{14}$ g cm^{-3}), the core density and velocity obey a self-similar solution for a $\Gamma = 4/3$

polytrope. The core is divided into a homologous inner core, which falls at subsonic infall velocity ($v \propto r$, self-similar), and a outer core, whose infall velocity is supersonic (and $v \propto 1/\sqrt{r}$); the *sonic point* being the border between the two regions. The sonic point is the point (or, in the spherical case, the surface) where the infall velocity equals the speed of sound in the medium. If one defines the Mach number as $M := v_{infall}/c_s$, where c_s is the speed of sound, the sonic point is defined as the region where $M = 1$. In a supernova this condition is verified at a radius of about $R \sim 20 - 30$ km [33]. The mass of the inner core, which is found to be $\sim 0.6 - 0.9\ M_\odot$, is approximately the Chandrasekhar mass corresponding to the reduced value of Y_e, and can be expressed as:

$$M_{ic} \simeq \frac{K}{K_{in}}^{3/2} M_{in} \ , \tag{1.7}$$

where K is the coefficient of the polytropic equation of state (EoS) $P = K\rho^\Gamma$, with $\Gamma \approx 4/3$, and the subscript "in" refers to the initial condition of the collapse [135, 349]. For degenerate ultra-relativistic electron gas, one has [295]:

$$K = \frac{\hbar c}{4}(3\pi)^{1/3}\left(\frac{Y_e}{m_u}\right)^{4/3} \ , \tag{1.8}$$

being c the speed of light and m_u the baryon mass unit; from Eq. (1.8) one can easily deduce that the mass of the inner core scales as Y_e^2. This analytical result was then confirmed by numerical collapse simulations.

When nuclear density is reached, about few hundreds of milliseconds after collapse, the repulsive component of the nuclear force between nucleons becomes important, and the EoS stiffens; the collapse halts, provoking the so-called *core bounce*. Pressure waves from the bouncing mass shell start propagating outwards, accumulate near the sonic point and steepen into a shock wave, which moves through the outer core with an initial kinetic energy of some foes, and if the shock wave reaches the outer layers of the star we observe the supernova explosion. Nevertheless, the exact mechanism triggering the explosion is still controversial and uncertain. Even if the initial energy of the shock wave could, in principle, be enough to produce a supernova explosion, about 8.8 MeV per nucleon (i.e. about 17 foe per solar mass crossed) are lost by the shock wave in dissociating nuclei into neutrons and α particles, while moving out of the core. Moreover, additional energy is lost, since neutrinos produced behind the shock in electron capture (mainly on free protons since the Q-value of the electron capture on nuclei is too high) leave quickly the star once the shock reaches the neutrinosphere, carrying away energy and causing the so called *neutrino burst* at shock break-out (see Fig. 1.2).

In the *prompt mechanism*, mainly occurring for low mass stars ($M \lesssim 11\ M_\odot$) with less iron-rich cores, the shock wave is strong enough to cross the outer core and eject the envelope [33].

For more massive stars, the weakened shock finally stalls and turns into an accretion shock at a radius of about 100 - 200 km [33]; the matter behind the shock continues falling inward, forming a *proto-neutron star* (PNS) which contracts and cools down via neutrino emission (that could be enhanced if convection is present) in a timescale of about hundreds of milliseconds. The PNS will evolve to a neutron star (NS) or eventually collapse into a black hole (BH), depending on the progenitor mass (below or above $\sim 25\ M_\odot$). The

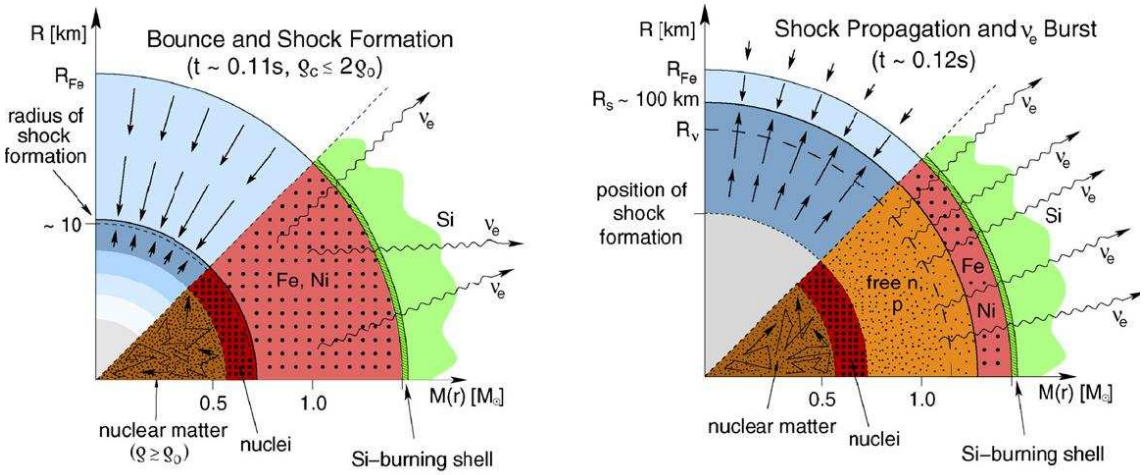

Figure 1.2: Schematic representation of the bounce formation and shock propagation (as in Fig. 1.1, a cut of the core is shown, in spherical symmetry). In the left panel, the shock formation is shown at the edge of the homologous core; in the center of the star nuclei dissolve in nuclear matter, while between the radius of shock formation and the edge of the iron core, matter is still formed by heavy nuclei in the iron group. In the right panel, shock propagation is displayed: the shock wave tries to propagate outwards, dissociating matter and loosing energy; shock stalls at $R_s \simeq 100$ km (from [173]).

further cooling of the interior then proceeds by neutrino pair production and diffusive lost of neutrinos of all flavours; ν_μ and μ_τ are created by thermal processes (see Fig. 1.3, left panel).
In the *delayed mechanism* the neutrinos emitted by the PNS play a crucial role: they carry most of the energy and if they deposit some of it in the *gain region* (the region between the nascent NS and the stalled shock) by the following reactions:

$$\nu_e \quad + \quad n \rightarrow e^- + p \tag{1.9}$$
$$\bar{\nu}_e \quad + \quad p \rightarrow e^+ + n \,, \tag{1.10}$$

they can "revive" the shock leading to a successful explosion. This neutrino heating, indeed, increases pressure behind the shock, expands the layers and creates a region of high temperature and low density (the so-called "hot bubble" [33]); the high pressure could drive the shock further out and let it reach the envelope of the star, provoking the explosion (see Fig. 1.3, left panel).

Even if the existence of a heating region is also confirmed by different numerical simulations (see e.g. [63]), in one-dimensional simulations no supernova explosion was obtained with a neutrino-driven mechanism, except for low mass O/Mg/Ne cores. Multi-dimensional effects must come into play. Already Bethe [33] pointed out that the "hot bubble" must be convectively unstable, and that convection enhances neutrino energy deposition. In this scenario where convection plays an important role, neutrino-driven explosion in multi-dimensional codes were obtained[9].

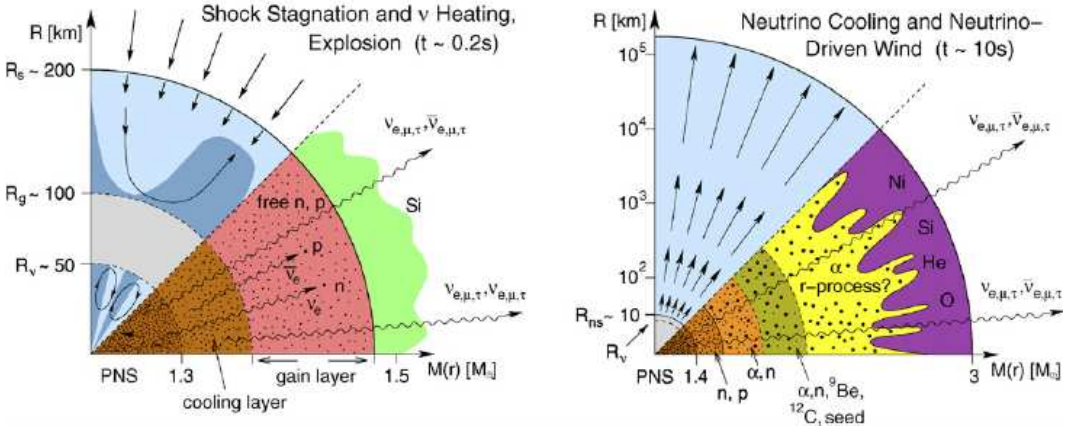

Figure 1.3: Schematic representation of the shock stagnation and neutrino heating and cooling (as in Fig. 1.1, a cut of the core is shown, in spherical symmetry). In the left panel, the cooling region is located between the neutrinosphere (R_ν) and the gain radius (R_g). Inside the neutrinosphere, where PNS is forming, convection and production of neutrinos of all flavours are expected. The region of neutrino heating is located between the gain radius (R_g) and the shock radius (R_s). In the right panel, the shock goes out of the star (explosion by neutrino mechanism). Early proton rich SN ejecta together with neutrino-driven wind are shown. If free neutrons are left, neutron rich nuclei can become seeds for r-process (from [173]).

Moreover, the presence of hydrodynamical instabilities like SASI (Standing Accretion Shock Instability), which are instabilities of the accretion shock to non-radial deformation, seem to be essential, both in analytical models ([40], [117] and Refs. therein) and in numerical simulations, to obtain the explosion of massive stars. In this scenario, the onset of the explosion was obtained in a 2D simulation for a $11.2\ M_\odot$ progenitor star [64]. However, the effect of SASI is not directly to cause the explosion of the star, but to support shock expansion and to increase the efficiency of the neutrino heating.
Another scenario invoked for the explosion was proposed by Burrows *et al.* [68]: the *acoustic mechanism*. In their 2D simulations, they observed that, because of anisotropic accretion and turbulence, the forming neutron star is excited to strong g-mode oscillations. The core g-modes act as to convert the gravitational binding energy to acoustic power, which is deposited in the mantle and could drive the explosion.
Finally, different mechanisms are to be investigated in multi-dimensional simulations to have a better understanding of the problem, such as different types of hydrodynamical instabilities (e.g. Rayleigh-Taylor instabilities which could induce vortices in the velocity field, magneto-rotational instabilities, etc.), effects of very rapid rotation and/or magnetic field (see e.g. Ref. [173] et Refs. therein for a review). At present, no unified consensus is agreed to explain the CCSN mechanism.

If the explosion occurs, the outer layers of the stars are ejected, enriching the Interstellar Medium (IM) with the elements produced during the different burning stages. It is indeed undoubted that a SN event is one of the main contributors to the formation of heavy elements in the Universe (for a review of nucleosynthesis, one can refer to

[9]More details and references on the current status of numerical simulations can be found also in Sec. 1.2.4.

Refs. [9, 345, 187, 173] and Refs. therein).
To study nucleosynthesis processes in supernova environment, the effects of the shock wave were studied in simulations by igniting a bomb in the star's interior or by initiate the explosion by a piston. Then it has become possible to study explosive nucleosynthesis by means of stellar trajectories given as output of SN simulations coupled with nuclear networks, or obtain directly the explosion by tuning some governing parameters. The nucleosynthesis process and final elemental abundances are determined by outflow parameters like expansion timescale, entropy and electron fraction of the matter. Already in the 1950s [65], it was recognized that two main processes are responsible for the formation of heavy elements: the slow (*s-process*) and rapid (*r-process*) neutron capture process. The first one requires lifetime for neutron-capture to be longer than the competing process, the β decay: $\tau_\beta < \tau_{n,s}$, so that the s-process can run through nuclei in the valley of stability. The second one requires that $\tau_{n,r} \ll \tau_\beta$, i.e. r-process runs in very neutron rich environment and through very neutron rich unstable nuclei, hardly known in experiments. Although sites for r-process are still not completely determined, it is thought to occur in presence of high neutrino and free neutron fluxes. Expanding neutron-rich matter can be found in the baryonic outflow driven outwards from the surface of the PNS by the heating of neutrinos radiated from the neutrinosphere (the so-called "neutrino-driven wind"). In this high entropy environment, nucleons recombine to α particles, which can assemble to ^{12}C. Carbon nuclei can then capture α and neutrons to form heavier nuclei up to iron. Under certain conditions, if free neutrons and neutron-rich nuclei are present, the latter can become seeds for r-processes (see Fig. 1.3, right panel).

1.2.3 SN-GRB connection

The standard CCSN scenario explained above ignores rotation. Nevertheless, observations of gamma-ray bursts (GRB) in conjunction with supernova events suggest that this assumption is not valid. GRB are intense relativistic (Lorentz factor $\Gamma = [1 - (u/c)^2]^{-1/2} \gtrsim 200$, where u is the velocity of the outflow) beamed (opening angle of $\sim 5^\circ$) flashes of γ-rays, lasting from fraction of seconds to hundreds seconds, isotropically distributed and coming from cosmological distances (for a review, see e.g. [238, 344]). The short-hard GRB ("short" since they last ~ 0.3 s, "hard" since their spectra are peaked at higher energies, ~ 360 keV) are associated to merger of compact binaries, while the long-soft ones ("long" since they last ~ 20 s, "soft" since their spectra are peaked at lower energies, ~ 220 keV) occur mainly in star-forming galaxies, which, together with their energetics (~ 10 foe), allows to connect GRB with highly energetic SN events. The first GRB-SN connection was established for SN1998bw, and while all long-soft GRB may be related to SN, not all SN emit GRB. Even if it is still unclear how a GRB works, or what distinguish a normal SN to a SN making GRB, it seems well established that only rapidly rotating and massive stars, mainly in region of low metallicity, can make GRB [344]. It is thought, indeed, that one of the possible engine for GRB is Type I collapsar (black hole formation after core-collapse with no explosion but accretion on the surface of the PNS), typically characterized by fast rotation[10]. The rotational axis gives a natural preferred direction for the propagation of the jet.

[10]Type II collapsar, instead, refers to SN events characterized by a weak explosion and a long-term fallback accretion.

1.2.4 Current status of Supernova simulations

Simulation of CCSN is a very challenging task. Analytical models can only give us a general idea and a rough estimation of the quantities playing a role in the picture, so our current understanding of the complex problem of SN requires numerical simulations. However, since a CCSN event involves hydrodynamics, General Relativity, and requires different nuclear physics inputs as well as a careful treatment of neutrino physics, could be influenced by rotation and magnetic field, and should take into account multi-dimensional effects, its numerical simulation is all but a trivial task. Moreover, it is very time consuming, and only powerful computers can perform this kind of calculations.

History of CCSN simulations is quite long (see Refs. [33, 173] and Refs. therein); the first numerical simulations were computed by Arnett (e.g. [5, 6, 7]), Colgate and Johnson [88], who assumed that the bounce would happen at a density of about 3×10^{13} g cm^{-3}, Colgate and White [89], who already introduced the idea that neutrinos could transfer their energy to the envelope provoking the explosion, and then refined by Wilson who showed that the prompt shock driven by neutrino-energy deposition fails because of the small neutrino cross sections [338] and discovered the delayed mechanism [340] as a possible explanation for the explosion. In the delayed scenario proposed by Wilson [38], the region behind the shock was divided into three zones: a central core (0-50 km), a cooling region (50-100 km), and a gain region (100-200 km) where the neutrinos can revive the shock by energy deposition. However, this did not yet produce a successful numerical explosion. Wilson and Mayle [342] pointed out that convective instabilities present in the PNS contribute to increase the energy transferred to the shock. In the 1990s, the two-dimensional models developed by Herant *et al.*[158] or Burrows *et al.*[66], show that convection helps the neutrino energy deposition in the gain region.

Different groups have then been working in order to introduce more realistic physics, from the one hand a precise treatment of neutrino physics in spherically symmetric models either in Newtonian gravity [274] or in General Relativity (GR) [202], from the other hand the development of multi-dimensional codes with different approximation schemes for neutrino transport. However, all state-of-art simulations of CCSN, performed in Newtonian gravity [274, 313], in Newtonian gravity with relativistic corrections in the Newtonian potential [63, 64, 62], in full GR [243, 202, 201, 200, 203], and with different EoS (e.g. [172, 303]), agree with the results obtained in the 1980s and 1990s (e.g. [343, 253, 307]) which showed that the prompt shock is not able to drive a supernova explosion, except in the case of small iron cores [58, 17] or very soft EoS [16].
In the case of delayed mechanism, spherically symmetric simulations with more and more accurate hydrodynamics and neutrino transport agree that no explosion can be obtained for progenitors more massive than $10\,M_\odot$, while, for O/Ne/Mg cores of $8-10\,M_\odot$ progenitors, neutrino heating was found to trigger explosion even in 1D simulations [235, 177]. In particular, improved algorithms were introduced in these simulations, both to compute hydrodynamics and neutrino transport. New algorithms either based on implicit, adaptive grid solvers for hydrodynamics with Boltzmann equation for neutrino transport [200], or explicit, conservative, third-order schemes with Riemann-solver for hydrodynamics coupled with an implicit solver for neutrino equation (variable Eddington factor) [275] were employed [11], and big efforts were put in order to implement a set of nuclear reactions

other than the ones treated in Bruenn [56].

In multi-dimensional simulations, neutrino-driven explosion mechanism was found to work in presence of convection (see e.g. Refs. [159, 66, 124, 125]), but when replacing an energy-dependent neutrino transport to a simple grey diffusion approximation, the picture of the success of the first 2D simulation with postshock convection changed to a failure in reproducing the explosion scenario.
First introduced by Foglizzo [116], and then by Blondin *et al.*[40] in the SN scenario, SASI was found to be present in several 2D simulations (see e.g. [64, 68, 291]), which show that, after about 600 ms, the gas accreted in the heating region generates non-radial deformations with dipolar and quadrupolar modes. This mechanism can reduce the velocity of matter accretion behind the shock, helps the shock wave to achieve bigger radii and improves the efficiency of the neutrino energy deposition. An explosion aided by SASI was obtained for a $11.2\ M_{\odot}$ [64] and a $15\ M_{\odot}$ [221] progenitor. The asymmetry of SN explosion (e.g. proven by asymmetric neutron star kicks) would favour the SASI scenario. Magnetic field [249] and rotation in axisymmetry or without symmetry assumption (see e.g. [250, 356]) were also included in some simulations.

In conclusion, despite enormous progresses have been made since the first simulations in the 1960s, several improvements could still be done, both from hydrodynamics and from nuclear physics inputs point of view.

1.3 Microphysics in CCSN

Nuclear physics in core-collapse supernova plays a crucial role: the EoS relates the internal energy and the pressure which are two important macroscopic quantities during collapse and at shock formation; electron capture drives the behaviour of the electron fraction determining the position of formation of the shock, neutrino interactions and transport govern the neutronization and cooling of the nascent PNS and neutrino energy deposition could even help in driving the explosion. However, the full picture of how nuclear physics works in this scenario is very complicated and not yet completely understood. A lot of uncertainties come from capture rates and neutrino opacities in the condition of matter composition, density and temperature encountered during collapse, and we have almost no knowledge about the equation of state at supranuclear density. Moreover, the wide range of density (roughly from 10^5 to 10^{15} g cm^{-3}), temperature (from ~ 0.1 to $\sim 15 - 80$ MeV, depending on the progenitor and the EoS employed) and asymmetry (electron over baryon ratio from ~ 0.05 to 0.5) spanned by the core during its collapse and early post-bounce phase ([308], and cf. also Chapters 5-7) makes difficult a unified description of the matter.
For all of these reasons a lot of work needs to be done in order to improve our knowledge both from theoretical and, wherever possible, experimental point of view to provide nuclear physics inputs for simulation as much realistic as possible.

[11] More details on the techniques about how to solve hydrodynamics and neutrino transport equation will be given in Part II of this thesis.

1.3.1 Description of dense and hot matter

The EoS in supernova environment at subnuclear densities was investigated for a long time and different models have been developed (a review can be found in [33]). In the following I will give only a brief overview on the subject.

The thermodynamics is determined by the density ρ, the temperature T and the electron fraction Y_e (strictly speaking, Y_e is the difference between the electron and positron fraction, but during collapse the positron abundance is very low under electron-degenerate conditions).
The structure of the matter is mainly determined by the competition of surface and Coulomb energy: at low density, $\rho < \rho_0/10$, matter is composed by nuclei and a nucleonic gas; above saturation density no more nuclei are present. However, the transition between the two states is not abrupt, but it passes through different geometrical configurations, the ones which minimize the energy of the system.
While during stellar evolution the composition is determined by a nuclear reactions network, where electromagnetic reactions play an important role in fusion processes to form heavier and heavier nuclei, in a supernova environment, for temperatures higher than few hundreds of keV, reactions mediated by strong and electromagnetic interactions are in equilibrium. This means that reactions of the form:

$$(Z,A) + p \;\rightleftarrows\; (Z+1, A+1) + \gamma \tag{1.11}$$
$$(Z,A) + n \;\rightleftarrows\; (Z, A+1) + \gamma\ , \tag{1.12}$$

as well as (α,γ), (α,n), (α,p), (p,n) reactions, are in equilibrium. The chemical equilibrium among different components (bound in nuclei or free) is given by the equilibrium among the chemical potentials:

$$\begin{aligned} \mu_n(Z,A) &= \mu_{n,free} \\ \mu_p(Z,A) &= \mu_{p,free}\ . \end{aligned} \tag{1.13}$$

In the nuclear statistical equilibrium (NSE), under particle and charge conservation conditions, there exist only two independent chemical potentials (usually the neutron and proton ones: μ_n and μ_p); the chemical potential for a nucleus with Z protons and $A-Z$ neutrons is given by [295]:

$$\mu(Z,A) = Z\ \mu_p + (A-Z)\ \mu_n\ , \tag{1.14}$$

and since at the onset of the collapse nuclei and nucleons are often supposed to obey to Boltzmann statistics, the Saha equation gives the relative abundance of the species present in the environment [295, 266]:

$$n_i := n(Z,A) = \frac{g(Z,A)A^{3/2}}{2^A}\left(\frac{2\pi\hbar^2}{m_u k_B T}\right)^{3/2(A-1)} n_p^Z n_n^{A-Z}\ e^{\frac{Q(Z,A)}{k_B T}}\ , \tag{1.15}$$

where n_i is the number abundance of the species i, $g(Z,A)$ is the nuclear partition function:

$$g(Z,A) = \sum_i (2J_i+1)e^{-E_i/k_B T}\ , \tag{1.16}$$

where the sum runs over all nuclear states with excitation energy E_i and total angular momentum J_i; Q is the Q-value of the reaction (i.e. the nuclear binding energy):

$$Q(Z,A) := [Zm_p + (A-Z)m_n - M(Z,A)]\ c^2\ , \tag{1.17}$$

being $M(Z,A)$ the mass of the nucleus. The Saha equation, Eq. (1.15), is valid for classical particles when the ratio between their chemical potential and their temperature (measured in units of energy) is much smaller than 1: $\mu/T \ll 1$; in the non relativistic free particle case, the chemical potential scales as $\mu \propto n^{2/3}$, so that:

$$\frac{\mu}{k_B T} \ll 1 \Longrightarrow \frac{\hbar^2 n^{2/3}}{m_A\ k_B T} \ll 1\ , \tag{1.18}$$

which, for typical temperatures of 1 MeV, the relation (1.18) gives the range of validity of Eq. (1.15):

$$n \ll 10^{-2}\ A^{2/3}\ \mathrm{fm}^{-3}\ . \tag{1.19}$$

Therefore, since at the beginning of the collapse $A \approx 60$ and $n_B \approx 10^{-7}\ \mathrm{fm}^{-3}$, employing the Saha equation is a good assumption.
We will adopt the following notation: n_i indicates the number density (typically in cm^{-3} or fm^{-3}), i.e.:

$$n_i := \frac{\rho_i}{m_u}\ , \tag{1.20}$$

ρ_i indicates the mass density (typically in g cm^{-3}). Y_i denotes the abundance of the species i:

$$Y_i := \frac{N_i}{N_b} = \frac{\rho_i}{\rho} = \frac{n_i}{n}\ , \tag{1.21}$$

being N_b the total number of baryons and N_i the number of particles belonging to the species i, and X_i will refer to the mass fraction of the species i:

$$X_i := A_i\ Y_i\ ; \tag{1.22}$$

so: $X_n \equiv Y_n$ and $X_p \equiv Y_p$. The mass and charge conservation are given by:

$$\sum_i X_i = 1\ (\text{baryon number conservation}) \tag{1.23}$$

$$\sum_i Y_i Z_i = Y_e\ (\text{charge conservation})\ . \tag{1.24}$$

In the SN environment, only weak processes are out of equilibrium, until neutrino trapping is reached.

In the density-temperature-Y_e plane significant for core-collapse supernova simulation, the composition of matter can be considered as a mixture of heavy nuclei, free nucleons, light nuclei, electrons and photons. Bethe *et al.* [34] (BBAL) pointed out that because of the low entropy ($s/k_B \approx 1$) and quite high lepton fraction ($Y_l \approx 0.3 - 0.5$) during collapse, nucleons tend to stay bound in nuclei, preventing the neutron drip; as a

consequence nuclei are present all along the collapse even after the neutron drip density $\rho_{drip} \simeq 4 \times 10^{11}$ g cm^{-3}[34, 295]. In a realistic calculation, the entire set of nuclei should be considered, but it is computationally very expensive. For this reason, the full ensemble of nuclei is usually replaced by an average heavy nucleus, the one which minimizes the energy. It has been found, indeed, that thermodynamical properties are not much affected by this approximation [67], but that is no longer valid in the treatment of electron capture, since the nucleus which is the most energetically favoured (the "mean nucleus") could be not the one for which the capture is more probable [232], as well as for the neutrino scattering through the dense core after the bounce [224, 70]. The mean nucleus approximation also induces, when nuclei dissolve in nuclear matter by increasing temperature, density or asymmetry, a sharp phase transition (see Appendix F).

The basis for one of the most used EoS in supernova simulation, the Lattimer and Swesty one [192], has been derived by Lamb *et al.* [180, 181] and Lattimer *et al.* [190], where statistical mechanics together with a semi-classical treatment based on a compressible liquid drop model for the gas and bubble phase was used to derive the EoS; matter is assumed to be composed by nuclei immersed in a lower density gas of nucleons and α particles; the transition between the two phases must assure the continuity of chemical potentials for neutrons and protons at the boundary. Electrons are supposed to be uniformly distributed. At high temperatures ($T \approx 15$ MeV), nuclei evaporate into a gas of nucleons, as described in [180, 181]. At above about one-half of nuclear saturation density, the nuclei change their structure and the condition for the minimum energy is achieved by different structures (from "*pasta*" to "*Swiss cheese*" phase), until, with increasing density, the space becomes completely filled by nuclear matter. Ravenhall *et al.* [276] discussed the shape of nuclei and bubbles. In fact, while at low density surface tension favours spherical nuclei, at higher density, the spherical shape turns into deformed structures, more favoured by Coulomb energy, like prolate ellipsoids parallel to each others, cylinders and flat plates (the so-called nuclear "*pasta*"-phase [92]), finally reaching a configuration in which empty bubbles are distributed in nuclear matter with uniform density ("*Swiss cheese*" phase) and then a phase in which no more clusters are present. A recent study on the properties of nuclear "*pasta*" has been made by Watanabe *et al.* [335], while its dynamical properties have been investigated, e.g. in Refs. [167, 175]. The transition from nuclei to "*Swiss cheese*" [90] as well as the one to nuclear matter [276] were found to be smooth. A different Skyrme interaction in deriving the EoS with respect to the one derived by Lamb *et al.* [181] and Ravenhall *et al.* [276] was employed by Bonche and Vautherin [45, 46], who solved the Hartree-Fock equation in a Wigner-Seitz cell assuming spherical nuclei immersed in a low-density nucleonic gas at low densities, and empty bubbles in nuclear matter at higher densities.
Above saturation density, obtaining an EoS is very challenging: there are no direct experimental data and heavy-ion collisions require, to be analysed, the use of transport models, where the simplified nucleon-nucleon interaction, the in medium NN cross sections, and other approximations induce large theoretical uncertainties. The temperatures reached in heavy-ion collisions at relativistic energies are very large (the RHIC at Brookhaven created matter that seems to be at a temperature of hundreds of MeV) and extrapolations to lower temperatures for supernova is also a matter of discussion. However, Danielewicz *et al.*[94] have obtained constraints for the pressure up to $3\rho_0$ in symmetric matter that exclude some EoS [178], such as, for instance, the one by Typel and Wolter [319]. From

a theoretical point of view, Bethe and Johnson [36] performed calculations assuming that nucleons are non-relativistic and interact by mean of the Reid nucleon-nucleon (NN) potential [278], and they considered the possibility for Λ, Σ and Δ hyperons to appear, with the consequence of a softening of the EoS (i.e. pressure is much reduced). Friedman and Pandariphande [123] carried out calculations in a variational method, adding to a more refined two-body interaction a three-body density dependent interaction, finding a softer EoS with respect to Lamb *et al.* [181] who used a Skyrme interaction. Then, Baron *et al.* [18, 19] introduced a schematic formula for the EoS above saturation, which does not have any theoretical basis, but it reproduces the qualitative behaviour of pressure and it was convenient for supernova simulation because of its analytical form:

$$P = \frac{K_0}{9}\frac{\rho_0}{\Gamma}\left[\left(\frac{\rho}{\rho_0}\right)^{\Gamma} - 1\right] , \tag{1.25}$$

where K_0 is the compression modulus; in more sophisticated calculations, K_0 and ρ_0 were taken density and asymmetry dependent.
At even higher densities, nucleons become relativistic; Dirac theory should be employed to derive the EoS. The relativistic interaction has been derived both in a mean field approximation (see, e.g., [293, 168]) and in Brueckner-Hartree-Fock approach (see e.g. [312, 213]) and the resulting EoS was found to be quite stiff.

In the last twenty years, two EoS has been used in supernova simulations: the one by Lattimer and Swesty (LS) [192] and the one by Shen *et al.* [297]. The LS EoS is derived by minimizing the free energy of the system, which is supposed to be composed by a mean nucleus treated in the Wigner-Seitz approximation[12], surrounded by a gas of neutrons, protons, and α particles. Electrons and positrons are treated as a non-interacting gas and photons as an ideal gas; they are included in the EoS but decoupled from the baryonic part, so that the minimization procedure can be computed separately. Effects of the neutron skin were ignored in the original analytical version of the EoS, while in the last tables made available it was included, as in the original work by Lattimer *et al.* [190]. Similarly, the improved EoS tables were built both for non-relativistic and relativistic NN potential models. Phase transition to non-spherical nuclei ("*pasta*"-phase) is done by modifying the Coulomb and surface energies of nuclei: a shape function which recovers the correct limit of having nuclei at low density and bubbles at high density and which reproduces the more sophisticated calculations by Ravenhall *et al.* [276] in the in-between region is introduced to model the transition (see Section 2.8 in Ref. [192]). Phase transition to bulk nuclear matter phase is treated by the inclusion of a Maxwell construction between the two phases.
However, it has been recognized [189] that the original routine version of this EoS has some problems, such as an error in the definition of the α particles binding energy and some convergence issues at low temperatures and proton fractions or near critical temperature/density. I refer to the Appendix F for a discussion on these problems and how we have studied and corrected some of them.

[12]The Wigner-Seitz approximation consists in assuming that the nucleus is at the center of a spherical charge-neutral cell, surrounded by a gas of neutrons, protons, and α particles. The Wigner-Seitz cell is decomposed into two regions where each of the phases is located. The nuclei form a lattice (usually a BBC, i.e. body-centered-cubic) in order to minimize the Coulomb lattice energy. The volume of the Wigner-Seitz cell is equal to the one of the unit cell in the BBC lattice.

The Shen *et al.* EoS is derived in the relativistic mean field (RMF) framework based on the Thomas-Fermi model. It does not take into account non-spherical shapes and, as a consequence, the phase transition is not smooth. At low density, the NN interaction is considered as negligible, so matter is modelled as an ideal gas of neutrons, protons and α particles. Ideal gas approximation is used for $\tilde{n}_n + \tilde{n}_p < 10^{-5}$ fm^{-3}, where $\tilde{n}_i := n_i/(1 - n_\alpha v_\alpha)$, being n_α the number density of α particles and $v_\alpha = 24$ fm^3 the effective volume occupied by an α particle [299]. At higher densities, a smooth connection with calculations obtained in the RMF theory is done. The EoS is derived performing Thomas-Fermi calculations. Matter is modelled as a mixture of free neutrons, protons, α particles and a mean nucleus representative of the ensemble of heavy nuclei, treated in the Wigner-Seitz approximation. Leptons are treated separately since, as in the case of the LS EoS, they are decoupled from the baryons in the minimization procedure.
The Shen EoS has been recently updated in Ref. [296].

A third EoS, the Hillebrandt and Wolff EoS (HW) [163] one, is also used by groups performing supernova simulations, and comparisons of the results have been made for example in Ref. [173]. It is derived in a temperature-dependent Skyrme Hartree-Fock framework and takes into account a distribution of nuclei in NSE in the density regime from 10^9 g cm^{-3}to 3×10^{12} g cm^{-3}(including 450 nuclei up to iron, plus about 20 nuclei in the Zr and Pb region) and a mean nucleus in Wigner-Seitz cell approximation for densities above 3×10^{12} g cm^{-3}.

In addition to these widely used EoS, recently, different studies in the density, temperature and asymmetry range of interest for CCSN have been carried out both at low density in order to include light clusters other than α particles, or, more generally, a distribution of nuclei, and at high density in order to investigate the effect of a possible phase transition to exotic and quark matter. In the paper by Blinnikov *et al.* [39], for example, a distribution of nuclei is taken into account via a Saha approach. When comparing to the Shen EoS [297], the presence of nuclei starts at lower density (Fig. 5 in [39]), and the abundance of α particles is lower around 10^{11} g cm^{-3}(Fig. 6 in [39]), as a result of the appearance of light nuclei (in addition to ^{4}He nuclei). While these differences do not affect very much the thermodynamical quantities (Fig. 8 in [39]), as expected [67], they might have a non-negligible impact on the electron capture rates. An EoS in which a distribution of nuclei instead of one mean nucleus is considered and treated in a statistical model is also presented by Hempel and Schaffner-Bielich [157]. The matter is modelled as an ensemble of nuclei and interacting nucleons treated in NSE, and using a RMF model. The authors find that the contribution of light clusters is very important and only poorly represented by α-particles alone. When comparing with the existing EoS (LS and Shen), apart from the composition, in general only small differences among the equations of state are found, proving once more that the mean nucleus approximation is not too bad for the determination of the thermodynamical quantities.

Gulminelli and Raduta have also recently derived an EoS in the statistical mixing approach [143, 272]. The concept of two phases (nucleons plus a gas of nuclei) is largely discussed and proven to bring inconsistencies in the description of phase transition. Instead of a Maxwell or Gibbs construction, the authors have derived the phase transition from the statistical mixing of the many components present in dense matter ($n, p, \alpha, \ldots$). The phase transition is shown to be very smooth and this new feature might largely reduce

numerical noises around the critical temperature (cf. Appendix F).

On the other hand, at high density, the presence of exotic particles have been investigated. Hyperons are expected to appear at high density and temperature ($T > 40$ MeV, or $\rho_b > 0.4$ fm^{-3} [170]), so they are believed to likely appear in the NS cores for massive SN; in Ref. [170], the effect of an EoS with hyperons and pions derived in the RMF approach has been included in a CCSN simulation for a 15 $M_\odot$, finding a small fraction (within 10^{-3}) up to bounce.
In Ref. [289], the consequences of a possible QCD phase transition during postbounce evolution of CCSN are analysed; quark matter is described in the MIT bag model framework[13]. The phase transition is shown to produce a second shock, which should be resolvable by terrestrial neutrino detectors in the case of a Galactic SN, and which can trigger a delayed SN explosion.

1.3.2 Weak processes

Weak interactions play a fundamental role in the life of the star, especially during the late evolution stages (a review on the subject can be found in Ref. [186]). In the pre-supernova stage, a competition between β decay and electron capture determines the core entropy and the electron fraction Y_e, which defines the mass of the core according to Eq. (1.1). Electron capture lets the number of electrons in the system decrease, hence reduces pressure. Neutrinos produced in such processes leave the star (before neutrino trapping), carrying energy and cooling the star; the cooling rate depends on the properties of the star, namely the density and above all the temperature.
Electron capture and β decay are dominated by Gamow-Teller (GT) transitions, in which spin-flip occurs, and Fermi transitions, if there is no spin exchange. The importance of GT transitions, which are allowed in stellar environment since the electrons have high enough energy to induce the reactions to the GT resonance, was recognized by Bethe *et al.* [34]. However, the treatment of such transitions is not a straightforward task in nuclear structure. On the other hand, β decay rates in stars are strongly reduced or blocked at high density since the degenerate gas of electrons blocks the phase space available for the electrons to be produced. However, because of finite temperature effects, excited states can be thermally populated, and their connection to the low-lying states in the daughter nucleus by the GT transitions can contribute to β decay rates. This was first recognized by Fuller, Fowler and Newman (FFN) [127, 128, 129, 130] who called these states "back-resonances" (see Fig. 1.4).

For about 15 years, the reference rates for electron and positron capture, beta decay and positron emission for nuclei encountered in astrophysical environment ($21 \leq A \leq 60$) were the ones tabulated by FFN in the 1980s [127, 128, 129, 130], which computed the rates in the independent-particle-model (IPM), using experimental informations, whenever available. New experimental data performed in the iron mass region (see e.g. Refs. [337, 108]) showed that GT transitions are quenched with respect to the calculations based on IPM and fragmented over many states in the daughter nucleus, because of the

[13]The MIT bag model [83] is a phenomenological model which considers the quarks in the nucleon as confined to a finite region of space, a "bag". To hold the confinement, a pressure $B > 0$, the *bag constant*, is imposed (see e.g. [295]).

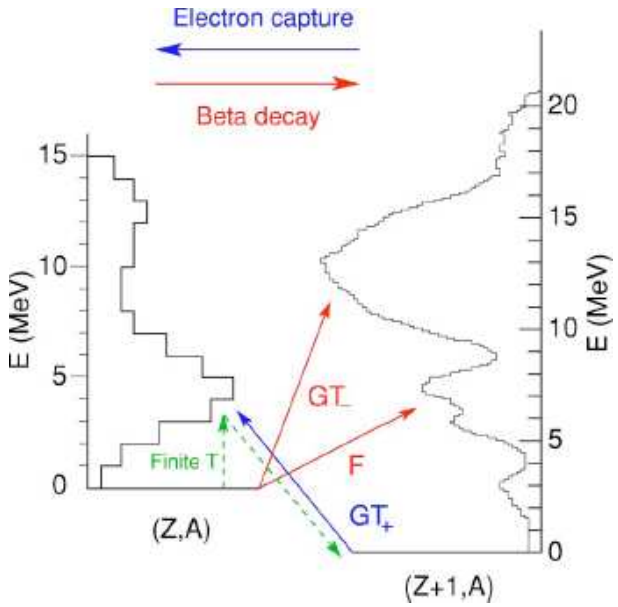

Figure 1.4: Scheme of electron capture and β decay processes. Fermi (F) and Gamow-Teller (GT) transitions are displayed. Backresonances (states in the decaying nucleus which have GT transitions to low-lying states in the daughter nucleus because of finite temperature effects) are also shown (from [186]).

effect of residual interaction which is neglected in an IPM approach.
Then, Caurier *et al.* [75] performed shell model calculations for iron group nuclei: their results reproduced quite well the data, showing that shell model was a good tool to calculate weak interaction rates. Shell model rates for stellar condition in the mass range $A = 45 - 65$ were computed for more than 100 nuclei by Langanke and Martínez-Pinedo [184, 231] and compared to the FFN rates; the shell model rates are nearly always smaller than the IPM ones, for the range of ρ, T studied, because of the reduction of GT strength and the misplacement of GT centroid[14]for some nuclei with pairing.
Using the improved rates, presupernova models were recomputed by Heger *et al.* [154], keeping as much as possible the same physics inputs as in Woosley and Weaver (WW95) [348], except for the weak-interaction rates (for electron capture, FFN rates were employed in WW95). The resulting changes were: (i) an increase of the central Y_e by 0.01-0.015 at the onset of the collapse, which in turn increases the Chandrasekhar mass by about 0.075 $M_\odot$ for a 20 $M_\odot$ progenitor; (ii) a lower core entropies for stars with $M \leq 20\ M_\odot$ and a slightly larger entropies for $M \geq 20\ M_\odot$; (iii) a smaller iron core (reduction by about 0.05 $M_\odot$ for stars with $M \leq 20\ M_\odot$). These presupernova models are then input for collapse simulations.

Processes mediated by weak interaction play a crucial role not only in presupernova evolution, but especially during the core-collapse phase. The main weak processes occurring during collapse and postbounce evolution are ([56, 186, 69, 232] and Refs. therein):

[14]The centroid of a distribution indicates its mean value; in this case the GT centroid is defined as the mean energy value of GT distribution.

$$(A,Z)+e^- \rightleftarrows (A,Z-1)+\nu_e \quad \text{electron capture on nuclei} \tag{1.26a}$$
$$p+e^- \rightleftarrows n+\nu_e \quad \text{electron capture on free protons} \tag{1.26b}$$
$$\nu+(A,Z) \rightleftarrows \nu+(A,Z) \quad \text{elastic scattering on nuclei} \tag{1.26c}$$
$$\nu+e^\pm \rightleftarrows \nu+e^\pm \quad \text{inelastic scattering off electrons} \tag{1.26d}$$
$$\nu+N \rightleftarrows \nu+N \quad \text{elastic scattering on nucleons} \tag{1.26e}$$
$$(A,Z)+e^+ \rightleftarrows (A,Z+1)+\bar{\nu}_e \quad \text{positron capture on nuclei} \tag{1.26f}$$
$$n+e^+ \rightleftarrows p+\bar{\nu}_e \quad \text{positron capture on free neutrons} \tag{1.26g}$$
$$\nu+(A,Z) \rightleftarrows \nu+(A,Z)^* \quad \text{inelastic scattering on nuclei} \tag{1.26h}$$
$$(A,Z)^* \rightleftarrows (A,Z)+\nu+\bar{\nu} \quad \text{nucleus decay} \tag{1.26i}$$
$$N+N \rightleftarrows N+N+\nu+\bar{\nu} \quad \text{nucleon nucleon bremsstrahlung} \tag{1.26j}$$
$$\nu_e+\bar{\nu}_e \rightleftarrows \nu_{\mu,\tau}+\bar{\nu}_{\mu,\tau} \quad \nu_e\bar{\nu}_e \text{ annihilation} \tag{1.26k}$$
$$e^-+e^+ \rightleftarrows \nu+\bar{\nu} \quad e^+e^- \text{ annihilation ,} \tag{1.26l}$$

where A denotes the mass number and Z the charge of a nucleus, N indicates a nucleon (neutron or proton) and ν ($\bar{\nu}$) is a neutrino (antineutrino). Electron capture on nuclei and free protons, Eqs. (1.26a) and (1.26b), governs the neutronization of the system and they are crucial to determine the final lepton fraction (and, as a consequence, the mass of the homologous core); while elastic scattering on nuclei, Eq. (1.26c), is mainly responsible for the trapping and determines the diffusion timescale of the outgoing neutrinos; the inelastic scattering off electrons, Eq. (1.26d), acts after neutrino trapping and contributes to the thermalization of neutrinos (cross sections for these processes are derived in Refs. [56, 69]). After bounce, the elastic scattering on nucleons, Eq. (1.26e), contributes at most to the opacity, since neutrinos scatter on nucleons dissociated by the shock wave; while electron and positron capture, Eqs. (1.26b) and (1.26g), regulate absorption and emission of electron flavour neutrinos. Muon and tau neutrinos are mainly produced through nucleon-nucleon bremsstrahlung, Eq. (1.26j), and $\nu_e\bar{\nu}_e$ annihilation, Eq. (1.26k); electron-positron annihilation, Eq. (1.26l), plays a secondary role. Reactions listed in Eqs. (1.26f), (1.26h) and (1.26i) have not yet been included in the simulations.

Electron capture rates

As the core density increases, the high electron Fermi energy allows electron capture reactions, which are the most significant neutronization processes and the major sources of neutrino production. Electron capture occurs both on protons bound in nuclei and on free protons:

$$(A,Z)+e^- \rightleftarrows (A,Z-1)+\nu_e \quad \text{electron capture on nuclei} \tag{1.27}$$
$$p+e^- \rightleftarrows n+\nu_e \quad \text{electron capture on free protons .} \tag{1.28}$$

While cross section for the latter reaction is well known (see e.g. [295]), since it can be treated in a similar way as free neutron decay, the correct treatment of electron capture on nuclei is a challenging task. Moreover, even if the electron capture rates on free protons are larger by an order of magnitude with respect to the capture rates on nuclei, nuclei are a

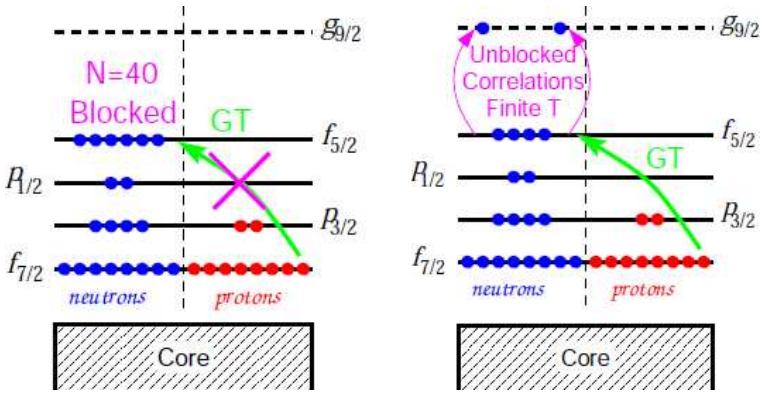

Figure 1.5: In the IPM, for nuclei with $Z < 40$ and $N > 40$, GT transitions are Pauli blocked (left panel). At finite temperature, thermal excitations can promote nucleons into $s-d-g$ shell re-allowing GT transitions (right panel) (from [182]).

much more abundant target than free protons, so it is difficult to determine *a priori* which of the two processes would dominate.
Early theories assumed that capture takes place only on free protons. Bethe *et al.* [34] revised this view, pointing out that the free proton fraction is very low during collapse and they concluded that the capture occurs mainly on nuclei with $A = 60 - 80$. They modelled the capture as an allowed GT transition of protons in the $f_{7/2}$ shell to neutrons in the $f_{5/2}$ shell. Subsequently, Fuller [126], who studied the electron capture in an IPM framework, argued that electron capture on nuclei vanishes for nuclei with $Z < 40$ and $N \geq 40$, since all possible neutron final states are already occupied and thus GT transitions are blocked by the Pauli principle (see Fig 1.5, left panel); so electron capture on free protons should dominate. Shortly after, Fuller, Fowler and Newman [127, 128, 129, 130] generated the first standard tabulated version of nuclear weak interaction rates (including electron capture rates) calculated in the IPM, for nuclei in $A = 21 - 60$ range, adding the contribution of Fermi transitions to the GT ones, and even experimental data whenever available. Cooperstein and Wambach [93] realized, performing calculations based on Random Phase Approximation (RPA), that finite temperature effects are important and "thermal unblocking" can occur: thermal excitations at $T \sim 1.5$ MeV can indeed promote protons into $g_{9/2}$ orbitals or remove neutrons from the $p-f$ shells, re-allowing GT transitions and letting capture on nuclei dominate the deleptonization process (see Fig 1.5, right panel).

Another unblocking effect, already present at lower temperatures ($T = 0.5$ MeV), is due to the configuration mixing between $s-d-g$ shell ($g_{9/2}$) with the $p-f$ shells ($f_{5/2}$, $p_{1/2}$), induced by the residual interaction. Diagonalization shell model (SM) calculations, which were successfully employed by Langanke and Martínez-Pinedo [185] in calculating electron capture rates for rather light nuclei (the so-called LMP rates), cannot be performed for heavier nuclei ($A \gtrsim 60$) including configuration mixing and finite temperature effects, because of the huge dimension of the model space involved. To overcome this problem, Langanke *et al.* [183] proposed a so-called *hybrid model*. The calculation of capture rates is performed in two steps: (i) the nucleus is described by a Slater determinant with temperature-dependent occupation factors, determined within a

Shell Model Monte Carlo (SMMC) approach; (ii) capture rates are then calculated from the GT strength distribution determined within the RPA framework. Using the hybrid model, electron capture rates for about 200 nuclei have been calculated, and tables have been compiled. The back door of such a model with respect to a full SM diagonalization is that RPA approach takes into account only 1-particle-1-hole correlations, missing high order correlations which are important to reproduce the details of the GT distribution; however it gives good results both for the centroid of the GT distribution and for the total GT strength. Nevertheless, electron capture rates are sensitive to the detailed GT^+ strength distribution when the electron chemical potential is of the same order of the Q-value of the reaction, i.e. for density and temperature at which the core composition is dominated by nuclei with $A \approx 55 - 65$. For these nuclei, large-scale shell model rates are available [184]. For heavier nuclei, $\mu_e > Q$, so electron capture rates are mainly sensitive to global properties of the GT^+ distribution (centroid and total strength). Thus, the hybrid model can be adopted, as it is shown in Fig. 2 of Ref. [187], where electron capture rates on nuclei for three different stellar conditions are displayed as a function of the Q-value of the reaction. The Q-dependence of the capture rates for a transition from a parent state at excitation energy E_i to a daughter state at excitation energy E_j is well approximated by [130]:

$$\lambda_{ec}(Q) = \ln 2 \, \frac{B}{K} \, \left(\frac{k_B T}{m_e c^2}\right)^5 \, \left[F_4(\eta) - 2\chi F_3(\eta) + \chi^2 F_2(\eta)\right] \, , \tag{1.29}$$

where $\chi = (Q + E_i - E_j)/(k_B T)$, $\eta = \mu_e + Q + E_i - E_j$, B represents a typical matrix element (GT plus forbidden), $K = 6164 \pm 6$ s and F_k are the relativistic Fermi integrals of order k:

$$F_k(\eta) = \int_0^\infty \mathrm{d}x \frac{x^k}{1 + e^{x-\eta}} \, . \tag{1.30}$$

We will argue in the following parts of the thesis that the role of the nuclear symmetry energy and in particular its temperature dependence acts in the difference $Q + E_i - E_j$ and thus influences the electron capture rates on nuclei making the reaction more difficult to happen.

Even if electron capture rates on a proton is larger than that on a nucleus, because of the smaller Q-value (for capture on free protons, we remind that $Q = (m_p - m_n)c^2$), as already noticed by Bethe *et al.* [34], the abundance of free protons is low during collapse, so the reaction rate on nuclei, which is related to the product of the abundance Y_i times the capture rate λ_{ec}, is higher than the reaction rate on free protons. Therefore, the capture on nuclei dominates the collapse phase (see Figs. 1-3 in Ref. [187]).

Electron capture on nuclei and on free protons differ also in neutrino energy spectra they generate, as shown in Ref. [187].

To compute electron capture rates on nuclei, a detailed knowledge of the abundances of nuclei present in the matter is necessary. In fact, if for thermodynamical quantities a mean nucleus description is enough, it is not always true that the mean nucleus is also the one for which capture is most probable. For this purpose, in Refs. [184, 165], a Saha-like NSE is used to get the nuclear abundances Y_i; then the reaction rates on heavy nuclei and on

protons are computed:

$$R_h = \sum_i Y_i \, \lambda_{ec,i} \tag{1.31}$$

$$R_p = Y_p \, \lambda_{ec,p} \, . \tag{1.32}$$

This more realistic implementation of electron capture rates on nuclei was included in SN simulations performed by the Oak Ridge and Garching collaboration [165, 222] and compared with the previous simulation employing IPM rates derived in [56]. The most important result is shown in Fig. 1 of Ref. [165]: in denser regions (i.e. deeper in the core) the new capture rates result in more capture, while in outer regions where nuclei with $A < 65$ dominate the new rates result in less electron capture. This causes a smaller final lepton fraction for the shell model rates, and as a consequence a displacement of the position of the shock formation inwards (16% difference in the mass of the inner core), altering the energetics of the shock wave propagation.

Very recently, Paar and collaborators [263] introduced a fully self-consistent microscopic framework for the evaluation of nuclear weak-interaction rates at finite temperature based on Skyrme functionals. In such a model, single-nucleon levels, wave functions, and thermal occupation factors for the initial nuclear state are determined in the finite-temperature Skyrme Hartree-Fock model. Then, transitions to excited states are computed in the finite-temperature charge-exchange RPA framework, as extensively explained in Ref. [263]. The calculations have been performed for different Skyrme functionals on selected iron group nuclei and for neutron-rich isotopes of Ge, but more systematic calculations are underway. For iron group nuclei, the results of the model have been compared to the SMMC rates, showing that: (i) at low electron energy the cross sections are systematically smaller than the ones obtained within the SMMC model (because of the sensitivity of the cross section to the detailed GT distribution); (ii) at higher electron energies (> 10 MeV), the cross sections predicted by the HF + RPA model are larger (at higher energies, the cross sections depend on the integral of the strength more than on the detailed GT distribution). The results for Ge isotopes have been compared to the hybrid model results, showing a very good agreement between the two models, especially at higher electron energies and temperatures.
It would be then interesting to have a complete set of nuclear capture rates for stellar conditions in order to introduce the HF + RPA rates in a supernova simulations.

1.4 Organization of the thesis

It has been shown that the macrophysics of stellar collapse and explosion observables are sensitive to the microphysics implemented in the models (see, e.g., Refs. [166, 173]). It is thus very important to know with the highest accuracy possible and the more consistent approach all the microscopic inputs required in a supernova simulation needed to reproduce as realistic as possible the supernova mechanism.
In this thesis we are interested both to investigate nuclear models which are deeply related to some key quantities such as the incompressibility modulus, the nuclear symmetry energy, the saturation density both in nuclei and nuclear matter, and to test the relevance of these nuclear inputs for the supernova outcome.

The thesis is organized as follows: after the above general introduction, this work is divided into two parts. Part I concerns nuclear models: the inclusion of a surface-peaked effective mass in the Energy Density Functional framework is discussed, while in Appendix D preliminary calculations on a more microscopic approach based on RPA to calculate the particle-vibration coupling is presented. Part II deals with the astrophysical models: after describing a first attempt to model supernova core-collapse by means of a one-zone code, whose results motivated us to perform one-dimensional calculations, two distinct astrophysical codes in one dimension will be depicted: a Newtonian code with neutrino transport, and a fully Relativistic hydrodynamical code, which we have modified both in the treatment of the electron capture in the first stage of the collapse, and in implementing a Newtonian version.

Part I

Nuclear models

Chapter 2

Introduction - The nuclear many-body problem

In this part of the thesis I will present briefly the important concepts and microphysics that will be developed in Part I and used in Part II. In particular, in Chapter 3 I will describe an improvement to the Energy Density Functional framework which includes a surface-peaked effective mass. In Appendix D, preliminary calculations and results of a more microscopic approach for the treatment of the particle-vibration coupling at finite temperature are presented.

The importance of the many-body problem in physics going from QCD to large scale cosmology derives from the fact that these systems are formed of interacting particles. For example, nucleons in a nucleus interact via nuclear forces, electrons in a metal interact via Coulomb forces, self-gravitating systems interact via gravitational force, etc. The many-body theory provides general methods to describe the properties of self-interacting particles and could be applied to finite systems like nuclei or infinite systems like supraconductors. In particular, the nuclear many-body problem we are interested in, although it has a long history, is still a source of many kinds of uncertainties and challenges for physicists. Models for nuclear structure have been developed since the 1930s, and a new interest is lead from the active development of radioactive ion facilities. Unlike other many-body systems, in the nuclear case the interaction among the constituents (neutrons and protons), the nucleon-nucleon (NN) interaction, is not completely known, even if one can extract experimental informations for example from nucleon-nucleon (NN) collisions in the energy range from 0 to 300 MeV in the laboratory frame in order to constrain some of its properties[1]. Among these properties are the short-range nature to explain the compactness of the nucleus and the saturation of the binding energy of finite nuclei, the long-range attractive nature to let finite nuclei to be bound systems, and the strongly repulsive character at short distance to prevent a nucleon to penetrate the hard-core generated by the other nucleons.

The different approaches employed to describe the nuclear system can be casted into three main groups:

(i) *macroscopic nuclear liquid-drop* models [252], which are the first semi-classical models based on a hydrodynamical picture of nuclei. The energy is parameterized in

[1] See for instance in the websites [357, 358] for a compilation of the available data on NN collision.

terms of global properties, among which the increasing trend of the binding energy with A up to iron nuclei, and the decreasing behaviour for larger nuclei, for which the Coulomb interaction is important enough to let the repulsive force dominate. The parameters of the models are fitted phenomenologically. Thus, these models describe well the general trend of nuclear binding energies but fail to reproduce shell effects.

(ii) *self-consistent mean field (SCMF) and shell model (SM)* theories, which work at microscopic level but employ effective interactions. In the SCMF methods, based on the Hartree-Fock approximation, one determines self-consistently and microscopically the nuclear mean field. In the SM approaches, one takes as mean field a phenomenological single particle (sp) model and then perform a configuration-mixing calculation; the residual interaction is usually fitted phenomenologically. The dimensions of SM calculations grow with system size, so in the nuclear many-body this kind of approaches cannot be used to study too heavy nuclei ($A < 100$).

(iii) *ab initio* methods, which start from a given nucleon-nucleon potential which reproduces NN scattering data. The models employing the given NN potential without the inclusion of (empirical) three-body force reproduce the main features of nuclear saturation, but fail in quantitatively getting the saturation point. These methods are quite involved and time consuming, so that usually they can be applied only for small systems; recently, advanced computational techniques allow *ab initio* methods to be performed for finite nuclei up to carbon (A=12).

An overview on the nuclear chart of the domain of applicability covered by the models (i)-(iii) is given in Fig. 2.1.

From now on, I will concentrate on non-relativistic mean field models. Reviews on the different approaches for treating the many-body problem can be found for example in Refs. [282, 24, 283] and in Refs. therein.

2.1 Mean field description

Mean field (MF) approaches are based on the Hartree-Fock (HF) approximation. The underlying idea is that the many-body system can be described as a system of A particles moving independently one from each other under the action of an average potential generated by the other $A - 1$ particles. An important concept associated to this picture is the idea of *quasiparticle*; many-body systems could generally be described as being formed by the excitations around the Fermi energy, called "quasiparticles". This kind of effect gives to the quasiparticles some properties, which can be experimentally observed, and which are different from the properties of constituent particles; for instance, they can have different masses or a finite lifetime.

The Hamiltonian of a many-body system, if only 2-body interactions are considered, can be written as:

$$H = \sum_{i=1}^{A} T_i + \frac{1}{2!} \sum_{i \neq j} V_{ij} \ , \tag{2.1}$$

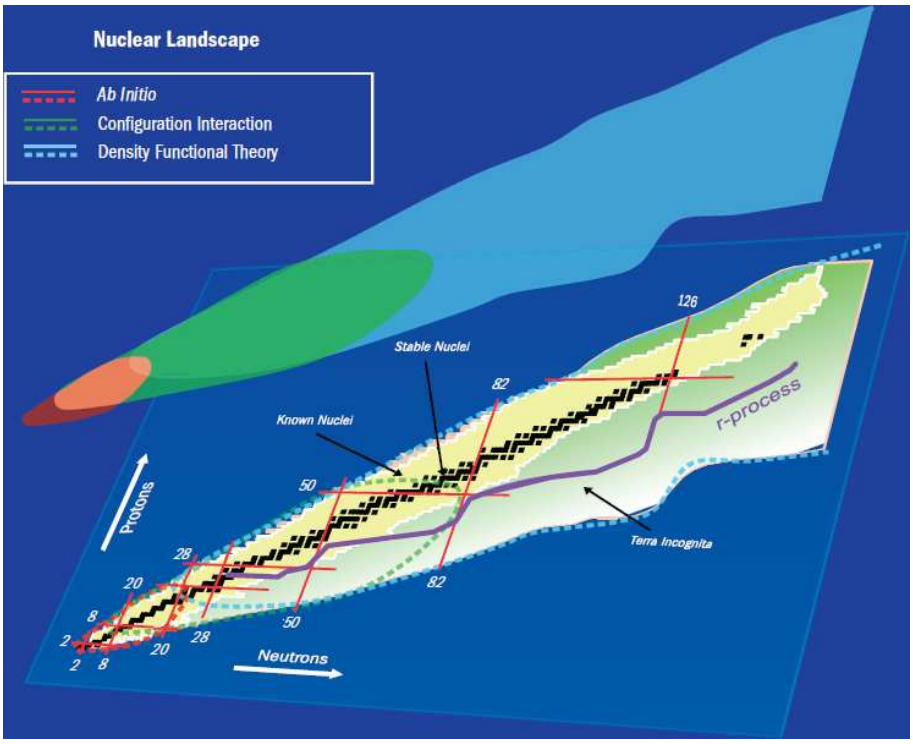

Figure 2.1: Theoretical and computational methods used to solve the many-body problem. The chart of nuclides in the (N,Z) plan is shown: black (yellow) squares represent stable (unstable) nuclei, the unknown nuclei are indicated in green (*terra incognita*), the red lines identify magic numbers, the purple line indicates the expected path of the r-processes. The shaded regions, projected onto the chart through thick dotted lines, show the domain of the theoretical approaches to the nuclear problem: for the lightest nuclei, *ab initio* calculations (in red, e.g. Green's function Monte Carlo, no-core shell model, coupled cluster method) is the matter of choice, for intermediate-mass nuclei configuration interaction techniques (in green, e.g. interacting shell model) can be used, for heavy nuclei, the density functional theory (in blue, based on SCMF theories) is applied (from [28]).

where T_i is the kinetic energy and V_{ij} refers to the NN interaction. The exact diagonalization of the full Hamiltonian is a task which cannot be solved. Therefore, one has to rely on some approximations.
One can think, for example, to split the Hamiltonian (2.1) as:

$$H = H_0 + H_1 \ , \tag{2.2}$$

where:

$$H_0 = \sum_{i=1}^{A} T_i + \sum_{i=1}^{A} U_i \tag{2.3}$$

$$H_1 = \frac{1}{2} \sum_{i \neq j} V_{ij} - \sum_{i=1}^{A} U_i \ , \tag{2.4}$$

where U_i is some auxiliary potential to localize the nucleons. An example of the auxiliary potential $\sum_{i=1}^{A} U_i$ is given by an attractive potential well such as the harmonic oscillator

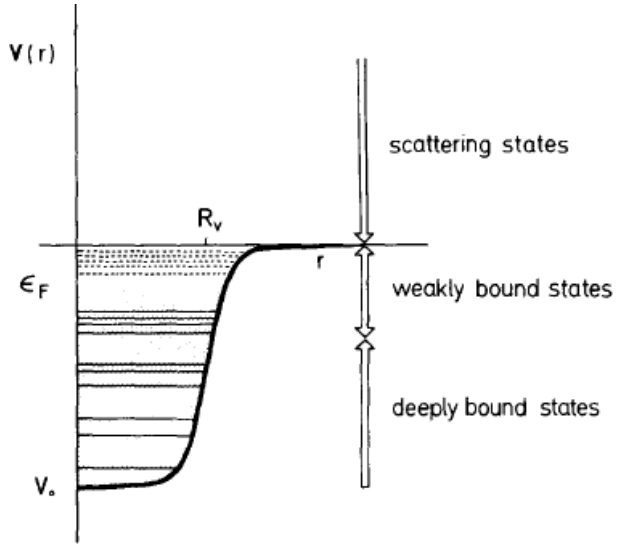

Figure 2.2: Sketch of a Woods-Saxon potential $U(r) = V_0\ [1 + exp[(r - R_v)/a_v]]^{-1}$, where, typically: $V_0 \simeq 50$ MeV, $R_v = 1.2\ A^{1/3}$ fm and $a_v = 0.65$ fm. The Fermi energy is ϵ_F (from [216]).

or the Woods-Saxon one, represented in Fig. 2.2.
H_0, the *shell model* Hamiltonian, and H_1, the *residual interaction*, are often approximated by phenomenological forms whose parameters are adjusted to agree with experiments.

2.1.1 Hartree-Fock Approximation

In a pure MF approach, the sp potential is computed under the assumption that the system can be described by a wave function which is approximated by a Slater determinant:

$$|\Phi(1,\ldots,A)\rangle = \prod_{i=1}^{A} |\Phi_i\rangle = \prod_{i=1}^{A} \hat{a}_i^\dagger |0\rangle \ , \tag{2.5}$$

where $\hat{a}^\dagger$ is the creator operator and $|0\rangle$ is the vacuum state.
By means of the variational method, minimizing the total energy of the nucleus, one thus obtains the single particle HF energies and the wave functions which have to satisfy the following set of HF equations:

$$(T_i + U_i)\ |\Phi_{\lambda,i}\rangle = \epsilon_{\lambda,i}\ |\Phi_{\lambda,i}\rangle \ , \qquad i = 1,\ldots A \ , \tag{2.6}$$

where λ accounts for the quantum numbers. In a MF scheme, $\sum_{i=1}^{A} U_i$ represents the average potential felt by a nucleon in a nucleus because of the presence of the other nucleons. In such a framework, each particle is described in terms of its single particle energy:

$$\epsilon_i = \frac{\hbar^2 k_i^2}{2m} + U_i \ , \tag{2.7}$$

where k_i is the momentum, m the bare mass and U_i is the sp potential. In the Hartree-Fock approximation, the sp potential, the *mean field*, is given by the sum of the interaction of a nucleon of momentum $\mathbf{k}$ with the remaining nucleons in terms of the effective interaction:

$$U_i = \sum_j \langle ij|V_{ij}|ij - ji\rangle \ , \tag{2.8}$$

where $|ij - ji\rangle = |ij\rangle_A$ and accounts for the antisymmetrization.

2.1.2 Skyrme interaction

To account for many-body effects that influence the MF, one has to rely on phenomenological parameterizations of the many-body interactions, like Skyrme (zero-range) or Gogny (finite-range) interactions, that describe such effects in an effective way. The standard form of these interactions usually have a simple functional form and do not include tensor component, which is spin and isospin dependent and whose existence in the NN potential is hinted by the quadrupole moment for the deuteron [282].
Since the results presented in Chapter 3 of this thesis are obtained in the Skyrme HF framework, I recall here the general form of the Skyrme force while I refer to the Appendix B for the explicit expressions of the functional terms and the parameters of some of the Skyrme forces which will be used in the following.

The Skyrme force is a phenomenological interaction, which contains a certain number of parameters which have to be fitted to reproduce experimental data at saturation density. Starting from the consideration that the range of nuclear force is quite short, the simplest hypothesis is that it is a zero-range force, whose radial dependence is just given by a δ-function. The finite range component can be represented by a dependence on the momentum. The first successful application of this force has been done by Vautherin and Brink [328], who performed calculations to get ground state properties of spherical nuclei.

The "standard" form of the Skyrme interaction [302] can be written as a sum of terms:

$$\begin{aligned} V^{Sky}(\mathbf{r}_1,\mathbf{r}_2) &= t_0\,(1+x_0\hat{P}_\sigma)\,\delta(\mathbf{r}_1-\mathbf{r}_2) \\ &+ \frac{1}{2}t_1\,(1+x_1\hat{P}_\sigma)\,\left[\delta(\mathbf{r}_1-\mathbf{r}_2)\hat{\mathbf{k}}^{\dagger 2}+\hat{\mathbf{k}}^2\delta(\mathbf{r}_1-\mathbf{r}_2)\right] \\ &\quad +t_2\,(1+x_2\hat{P}_\sigma)\,\hat{\mathbf{k}}^\dagger\cdot\delta(\mathbf{r}_1-\mathbf{r}_2)\hat{\mathbf{k}} \\ &+ \frac{1}{6}t_3\,(1+x_3\hat{P}_\sigma)\,\delta(\mathbf{r}_1-\mathbf{r}_2)\,\rho^\alpha\left(\frac{\mathbf{r}_1+\mathbf{r}_2}{2}\right) \\ &+ i\,W_0\,(\hat{\sigma}_1+\hat{\sigma}_2)\cdot\hat{\mathbf{k}}^\dagger\times\delta(\mathbf{r}_1-\mathbf{r}_2)\hat{\mathbf{k}}\,, \end{aligned} \tag{2.9}$$

where the first term is the central term (0-range), the second one is the non-local one, the third term is the density-dependent term which can be interpreted as representing the finite-range effects and the last one accounts for the spin-orbit. Moreover, t_i and x_i are parameters of the force, and $\hat{P}_\sigma$, the spin operator, and $\hat{\mathbf{k}}$, the momentum operator, are defined as:

$$\hat{P}_\sigma = \frac{1}{2}\,(1+\hat{\sigma}_1\cdot\hat{\sigma}_2) \tag{2.10}$$

$$\hat{\mathbf{k}} = \frac{1}{\hbar}\,\hat{\mathbf{p}} = -\frac{i}{2}\,(\nabla_1-\nabla_2)\ . \tag{2.11}$$

The energy functional is derived, in the independent particle approximation where the wave function of the system is written as a Slater determinant, from the expectation value of the force on the HF state $|HF\rangle = |\Phi(1,\ldots,A)\rangle$:

$$\mathcal{H} = \mathcal{H}^{Sky} = \langle HF|V^{Sky}|HF\rangle \ . \tag{2.12}$$

The Skyrme functional for nuclei

The total integrated energy H_0 of the system is related to the energy density $\mathcal{H}$ as:

$$H_0 = H = \int d\mathbf{r}\, \mathcal{H}(\mathbf{r}) \ , \tag{2.13}$$

where the energy density $\mathcal{H}(\mathbf{r})$ is a function of the nucleon density $\rho(\mathbf{r})$, the kinetic density $\tau(\mathbf{r})$ and the spin-orbit density $\mathbf{J}(\mathbf{r})$ (q runs over neutrons and protons):

$$\rho_q(\mathbf{r}) = \sum_{\lambda,\sigma} |\Phi_{\lambda,q}(\mathbf{r},\sigma)|^2 \, n_{\lambda,q} \tag{2.14}$$

$$\tau_q(\mathbf{r}) = \sum_{\lambda,\sigma} |\nabla\Phi_{\lambda,q}(\mathbf{r},\sigma)|^2 \, n_{\lambda,q} \tag{2.15}$$

$$\mathbf{J}_q(\mathbf{r}) = \sum_{\lambda,\sigma,\sigma'} \Phi^*_{\lambda,q}(\mathbf{r},\sigma')\nabla\Phi_{\lambda,q}(\mathbf{r},\sigma) \times \langle\sigma'|\hat{\sigma}|\sigma\rangle \, n_{\lambda,q} \ , \tag{2.16}$$

where σ is the spin quantum number and $n_{\lambda,q}$ is the occupation number of the state λ. The standard Skyrme energy density $\mathcal{H}(\mathbf{r})$ is expressed in terms of a kinetic term $\mathcal{K}(\mathbf{r})$ and an interaction term written as [24]:

$$\mathcal{H}(\mathbf{r}) = \mathcal{K}(\mathbf{r}) + \sum_{T=0,1} \mathcal{H}_T(\mathbf{r}) \ , \tag{2.17}$$

where:

$$\mathcal{K}(\mathbf{r}) = \frac{\hbar^2}{2m}\tau(\mathbf{r}) \tag{2.18}$$

$$\mathcal{H}_T(\mathbf{r}) = \mathcal{H}_T^{even}(\mathbf{r}) + \mathcal{H}_T^{odd}(\mathbf{r}) \ , \tag{2.19}$$

with:

$$\begin{aligned}\mathcal{H}_T^{even}(\mathbf{r}) &= C_T^{\rho}\rho_T^2(\mathbf{r}) + C_T^{\nabla^2\rho}\rho_T(\mathbf{r})\nabla^2\rho_T(\mathbf{r}) + C_T^{\tau}\rho_T(\mathbf{r})\tau_T(\mathbf{r}) \\ &+ C_T^{J}\mathbb{J}_T^2(\mathbf{r}) + C_T^{\nabla J}\rho_T(\mathbf{r})\nabla\cdot\mathbf{J}_T(\mathbf{r}) \qquad (2.20)\\ \mathcal{H}_T^{odd}(\mathbf{r}) &= C_T^{s}\mathbf{s}_T^2(\mathbf{r}) + C_T^{\nabla^2 s}\mathbf{s}_T(\mathbf{r})\nabla^2\mathbf{s}_T(\mathbf{r}) \\ &+ C_T^{sT}\mathbf{s}_T(\mathbf{r})\cdot\mathbf{T}_T(\mathbf{r}) + C_T^{\nabla s}(\nabla\cdot\mathbf{s}_T(\mathbf{r}))^2 \\ &+ C_T^{j}\mathbf{j}_T^2(\mathbf{r}) + C_T^{\nabla j}\mathbf{s}_T(\mathbf{r})\cdot\nabla\times\mathbf{j}_T(\mathbf{r}) \ , \qquad (2.21)\end{aligned}$$

where isoscalar ($T = 0$) densities stand for total densities (e.g. $\rho_0 = \rho_n + \rho_p$), and isovector ones ($T = 1$) account for asymmetry (e.g. $\rho_1 = \rho_n - \rho_p$). The kinetic density $\tau(\mathbf{r})$, the density $\rho_T(\mathbf{r})$, the spin-current $\mathbb{J}_T^2(\mathbf{r})$ and the current $\mathbf{J}(\mathbf{r})$ as well as the relation between the Skyrme parameters and the coefficients in Eqs. (2.20)-(2.21) are defined in

Eqs. (2.14)-(2.16) and in Ref. [24]. For the application in Chapter 3, we have kept only the time-even component since we will focus on even nuclei; time-odd fields contribute to the single-particle Hamiltonian only if time-reversal symmetry is broken[2].

The energy per particle, H/A, has its minimum (≈ -16 MeV) at saturation density[3] $\rho_{0,s} \approx 0.16$ fm^{-3}, and its curvature is given by the incompressibility modulus K_∞:

$$K_\infty = 9\rho_0^2 \left.\frac{\partial^2}{\partial\rho_0^2}\frac{H}{A}\right|_{\rho_{0,s}} , \tag{2.22}$$

which is related to breathing modes like the giant monopole resonance and it is well known from nuclear physics experiments. Today, the preferred value for K_∞ is 240 ± 10 MeV [267]. The bulk symmetry energy coefficient, which will be discussed later in connection to the nucleon effective mass, is related to the isospin curvature as (see [197] for a review, and Refs. therein):

$$s = \frac{1}{2}\left.\frac{\partial^2}{\partial\rho_1^2}\frac{H}{A}\right|_{\rho_{0,s}} , \tag{2.23}$$

which, at saturation density, assumes the value ≈ 30 MeV. The non-relativistic Skyrme HF approaches predict for $s(\rho_{0,s})$ values between 26 and 35 MeV, depending on the nuclear interaction, while RMF models give $s(\rho_{0,s})$ around 30-44 MeV. Using the empirical parabolic law:

$$H(\rho_0,\beta) = H(\rho_0,\beta=0) + s\,\beta^2 + O(\beta^4) , \tag{2.24}$$

being $\beta = \rho_1/\rho_0$, one can extract the bulk symmetry energy coefficient from the two extreme cases:

$$s(\rho_0) \approx H(\rho_0,\beta=1) - H(\rho_0,\beta=0) , \tag{2.25}$$

which means that the symmetry energy is an estimate of the energy needed to convert all protons in symmetric nuclear matter to neutrons at fixed ρ_0. Moreover, around $\rho_{0,s}$, the nuclear symmetry energy coefficient can be expanded to second-order in density as:

$$s(\rho_0) = s(\rho_{0,s}) + L\left(\frac{\rho_0-\rho_{0,s}}{3\rho_{0,s}}\right) + \frac{K_{sym}}{2}\left(\frac{\rho_0-\rho_{0,s}}{3\rho_{0,s}}\right)^2 , \tag{2.26}$$

where L and K_{sym} are the slope and curvature parameters of the nuclear symmetry energy at $\rho_{0,s}$, and characterize the density dependence of nuclear symmetry energy around normal nuclear matter density:

$$L = 3\rho_0 \left.\frac{\partial s}{\partial\rho_0}\right|_{\rho_{0,s}} \tag{2.27}$$

$$K_{sym} = 9\rho_0^2 \left.\frac{\partial^2 s}{\partial\rho_0^2}\right|_{\rho_{0,s}} . \tag{2.28}$$

[2]Time reversal is one of the properties of the bare NN force which guarantees that the equations of motion are invariant with respect to the direction of time [44, 282].

[3]In this thesis the saturation density is usually labelled just as ρ_0. The change of notation in this paragraph is justified not to be mistaken with ρ_0, the isoscalar density according to the notation in Ref. [24].

Despite the different models give values for $s(\rho_{0,s})$ which lie in a relatively narrow range, the predicted L and K_{sym} are very different. The slope parameter L has been found to be correlated linearly with the neutron-skin thickness of heavy nuclei; thus, informations on L can in principle be obtained from it. However, since this kind of measures suffers from large uncertainties, this technique has not been exploited so far. The value of L can also be extracted from studying isospin-sensitive observables in heavy-ion reactions, and it is estimated to be $L = 88 \pm 25$ MeV (see [197] and Refs. therein). Moreover, is has been shown that the slope parameter L is inversely correlated to the crust-core transition density in neutron stars (see e.g. [330]); therefore, its knowledge can provide valuable astrophysical informations on neutron stars structure. Conversely, the value of K_{sym} is poorly constrained by nuclear physics experiments. At nuclear matter saturation density and around $\beta = 0$, the isobaric incompressibility of asymmetric nuclear matter can also be expressed to the second-order in β:

$$K(\beta) = K_\infty + K_{asy}\,\beta^2\,, \tag{2.29}$$

where K_{asy} characterizes the density dependence of the nuclear symmetry energy and is related to L and K_{sym} by:

$$K_{asy} \approx K_{sym} - 6L\,, \tag{2.30}$$

if one neglects high-order terms in β [197]. Systematic studies of the giant monopole resonance had given a very wide range for K_{asy}, which could assume negative as well as positive values. Very recently, measurements of the isotopic dependence of the giant monopole resonance in the even-A Sn isotopes have led to a more stringent value, even if still uncertain, of $K_{asy} = -550 \pm 100$ MeV [198], which is consistent with that extracted from the analysis of isospin diffusion data. Thus, K_{sym} lies in the range $\sim -140 - 140$ MeV.
At finite temperature, the parabolic approximation (2.24) is still valid. Therefore, in principle, all the terms s, L, K_{sym} should be temperature dependent. In the following analysis and for the astrophysical applications considered in Part II of this thesis, we will focus only on the T-dependence of the bulk symmetry energy coefficient s.

From the variation of the total energy H with respect to the ground state density matrix we obtain the following set of self-consistent Kohn-Sham equations ($q = n, p$) [328]:

$$\left[-\nabla \cdot \frac{\hbar^2}{2m_q^*(\mathbf{r})}\nabla + U_q(\mathbf{r}) - i\,\mathbf{W}_q(\mathbf{r}) \cdot (\nabla \times \hat{\sigma})\right] \Phi_{\lambda,q}(\mathbf{r},\sigma) = \epsilon_{\lambda,q}\,\Phi_{\lambda,q}(\mathbf{r},\sigma)\,, \tag{2.31}$$

where $m^*(\mathbf{r})$ is the effective mass, $U_q(\mathbf{r})$ is the mean field (including the Coulomb contribution for protons), $\mathbf{W}_q(\mathbf{r})$ is the one-body spin-orbit potential, and λ runs over neutron and proton orbitals ($\lambda = n, l, j$, where n is the principal quantum number, l and j are the orbital and the total angular momentum). In order to obtain the Eqs. (2.31), one can minimize the total energy of the system with respect to the wave functions (normalized to unity) instead of minimizing with respect to the density, since the nucleon density depends uniquely on the wave functions (cf. Eq. (2.14)) [328, 282].
In a HF procedure, the energies and wave functions are determined, for each orbital, from

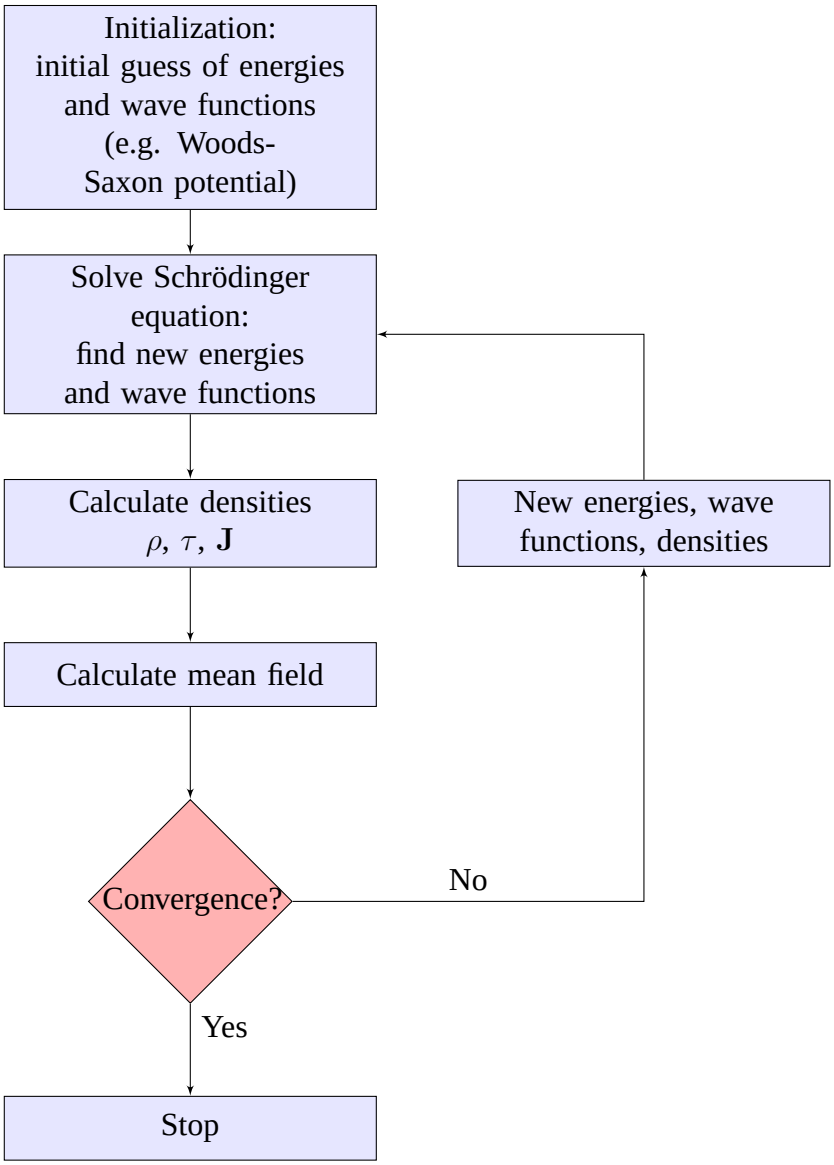

Figure 2.3: Flow chart of the HF procedure.

Eq. (2.31) by iteration until convergence is reached (i.e. self-consistently)[4]. We summarize the procedure in the flow chart Fig. 2.3.

Despite the fact that the HF approximation is a good tool to calculate the main properties of the nuclear structure, such as the ground state properties or the ordering of the sp levels, in particular for the case of closed-shell nuclei with a quite big gap between the last occupied state and the first non-occupied state, it fails in recovering some experimental evidences, such as the level density, the odd-even effect, or low-lying 2^+ states (see e.g. [44, 282]). To that extent one should go beyond the HF framework, and take into account additional correlations.

[4]The convergence condition can be made on the sp energies, i.e. when the difference between the energies calculated at the iteration $it + 1$ and at iteration it is less than the desired accuracy.

2.2 Pairing correlations

The word "correlation" often assumes different meanings according to the field of physics it refers to. In the following, we restrict the analysis to *pairing*, which is included in the simple BCS framework in obtaining the results of Chapter 3, and we leave to Appendix D the discussion about *particle-hole (ph)* correlations.

2.2.1 BCS model

Theory of nuclear pairing has a long history; for a review on this subject I address to Refs. [100, 97]. The presence of nuclear superfluidity turned out to be relevant also in neutron star physics, for example in influencing the thermal evolution of the stars, through the suppression of neutrino emission processes and the modification of the specific heat, and as a possible explanation of glitches (see e.g. Refs. [4, 268, 264, 78]).

Since the pairing theory proposed by Bardeen, Cooper and Schrieffer (BCS) [15], different applications have been made, both in finite nuclei, and in nuclear matter (see e.g. for a review [210, 97]).
A general way to include pairing in a MF description is to solve the Hartree- Fock- Bogolyubov (HFB) equations [43, 282] (whose applications can be found e.g. in the paper by Dobaczewski *et al.* [104]). In this framework, one introduces the concept of independent quasiparticles (qp), and the quasiparticle states are related to the sp states by the Bogolyubov transformation [282]:

$$\hat{b}_k^\dagger = \sum_l (U_{lk}\hat{a}_l^\dagger + V_{lk}\hat{a}_l) \ , \tag{2.32}$$

where l runs over the whole configuration space (i.e. l is larger than the number of nucleons), $\hat{b}_k^\dagger$ is the qp operator, $\hat{a}_l^\dagger$ and $\hat{a}_l$ are the creator and annihilator operator for a nucleon in the sp state, U_{lk} and V_{lk} are the matrix element of the U and V matrices which satisfy the conditions: (*i*) $U^\dagger U + V^\dagger V = 1$, (*ii*) $UU^\dagger + V^* V^T = 1$, (*iii*) $UV^\dagger + V^* U^T = 0$, (*iv*) $U^T V + V^T U = 0$. The transformation Eq. (2.32) can be written also in the compact form:

$$\begin{pmatrix} \hat{b} \\ \hat{b}^\dagger \end{pmatrix} = \begin{pmatrix} U & V^* \\ V & U^* \end{pmatrix}^\dagger \begin{pmatrix} \hat{a} \\ \hat{a}^\dagger \end{pmatrix} \ . \tag{2.33}$$

Thus, the quasiparticle wave functions Φ_{qp} are related to the sp wave functions Φ_l by:

$$\Phi_{qp,k} = \begin{pmatrix} \Phi_k^{(U)} \\ \Phi_k^{(V)} \end{pmatrix} = \begin{pmatrix} \sum_l U_{lk}\Phi_l \\ \sum_l V_{lk}\Phi_l \end{pmatrix} \ . \tag{2.34}$$

The minimization of the total energy of the system, under the constraint on particle number conservation, gives the so-called HFB equations:

$$\begin{pmatrix} h-\mu & \Delta \\ -\Delta^* & -h^*+\mu \end{pmatrix} \begin{pmatrix} \sum_l U_k\Phi_l \\ \sum_l V_k\Phi_l \end{pmatrix} = E_k \begin{pmatrix} \sum_l U_k\Phi_l \\ \sum_l V_k\Phi_l \end{pmatrix} \ , \tag{2.35}$$

where E_k is the quasiparticle energy, h stands for the expectation value of the standard Hamiltonian (kinetic plus 2-body interaction part), μ is the Lagrange multiplier (which

is the chemical potential), Δ is the gap Hamiltonian which has to be determined from the pair potential [282]. An alternative and simpler way is to construct a HF basis using the procedure drawn in the previous Section, and then solve the BCS equations, i.e. to use the so-called HF+BCS method, which is the one we have employed in Chapter 3; the chosen basis is the HF basis, in which the MF Hamiltonian H is diagonal. The BCS approximation consists in the diagonal approximation of the HFB equations; the pairing potential is diagonal in the same eigenstates of the MF Hamiltonian. In this case:

$$\Phi_{qp,k} = \begin{pmatrix} u_k \\ v_k \end{pmatrix} \Phi_l \ , \tag{2.36}$$

where u_k and v_k are variational parameters; v_k^2 represent the probabilities that a pairing state is occupied in a state k and $u_k^2 = 1 - v_k^2$. As a consequence, the matrix diagonalization problem turns into a system of two equations which have to be solved consistently, i.e. the particle number equation and the gap equation [282]:

$$N = \sum_k (2j_k + 1) v_{k,q}^2 \tag{2.37a}$$

$$\Delta_k = -\frac{1}{2} \sum_{k=0}^{k_c} v_{nn} u_k v_k \ , \tag{2.37b}$$

where v_{nn} is the pairing potential. Notice the difference in the summation in the two equations: in the first one, the summation must be carried over all considered states, while in the second case the definition of a cutoff is required to avoid divergence. Among the different pairing interactions present in the literature (see e.g. [24] for a list of Refs.), we have chosen for the application in Chapter 3 a contact pairing interaction of the form [131]:

$$\langle k | v_{nn} | k' \rangle = v_0 g(\rho) \ , \tag{2.38}$$

where v_0 is a constant and:

$$g(\rho) = 1 - \eta \frac{\rho}{\rho_0} \ , \tag{2.39}$$

being $\rho_0 = 0.16 \ \mathrm{fm}^{-3}$ the saturation density of symmetric nuclear matter, $\rho = \rho_n + \rho_p$ and η a parameter which localizes the interaction ($\eta = 0$ for a pure volume interaction, $\eta = 1$ for a pure surface interaction). In the specific case, one can thus rewrite the BCS equations at $T = 0$ in the following way (where I have also introduced the index $q = n, p$):

$$N_q = \sum_k (2j_k + 1) v_{k,q}^2 \qquad \text{particle number equation} \tag{2.40a}$$

$$\Delta_q(r) = \frac{v_0}{2} \, g(\rho) \tilde{\rho}_q(r) \qquad \text{gap equation} \ , \tag{2.40b}$$

where j_k is the quantum number for the sp total angular momentum, $v_0 \, g(\rho)$ is the pairing interaction, ρ the total density, being the isovector density:

$$\rho_q(r) = \frac{1}{4\pi} \sum_k (2j_{k,q} + 1) v_{k,q}^* v_{k,q} |\Phi_{k,q}(r)|^2 \ , \tag{2.41}$$

and $\tilde{\rho}_q(r)$ the abnormal density:

$$\tilde{\rho}_q(r) = -\frac{1}{4\pi}\sum_{k=0}^{k_c}(2j_k+1)u_{k,q}v_{k,q}|\Phi_{k,q}(r)|^2 \,, \tag{2.42}$$

where again the summation in Eq. (2.41) is carried over all considered states, while in Eq. (2.42) is carried over a selected number of states. A possible choice for the cutoff is to consider only a certain number of states around the Fermi energy, where the gap is expected to be present. Therefore, one can redefine the pairing interaction Eq. (2.38) in such a way:

$$\langle k|v_{nn}|k'\rangle = v_0 g(\rho)\theta(k,k') \,, \tag{2.43}$$

where different choices for the function $\theta(k,k')$ correspond to different choices for the energy cutoff[5].

If there is no interaction, $\Delta = 0$ and $v_k^2 = 1$, $u_k^2 = 0$ (the usual step function for occupied and unoccupied states). If a gap is present, then the particle number equation, together with the condition $v_k^2 + u_k^2 = 1$, gives [282]:

$$\begin{aligned} v_k^2 &= \frac{1}{2}\left[1 - \frac{\epsilon_k - \mu}{E_k}\right] \\ u_k^2 &= \frac{1}{2}\left[1 + \frac{\epsilon_k - \mu}{E_k}\right] \,. \end{aligned} \tag{2.44}$$

As an example, in Fig. 2.4, the occupation factors obtained in the HF+BCS code at $T = 0$ for the ^{120}Sn are displayed. For neutrons, we observe the smoothing in the occupation number curve as a consequence of the presence of pairing, while for protons, the behaviour is typical of a step function; this because ^{120}Sn is a closed-shell nucleus for protons, therefore, no pairing is expected for protons.

In the extension at finite temperature of the HFB and BCS model, the above equations keep the same structure [137]. The main effect is that the quasiparticles now obey to a temperature-dependent Fermi-Dirac distribution. This does not alter the definition of the pair potential but rather the definition of the density (both the particle and the abnormal one). In practice, in the BCS model, it can be shown [137] that the extension to $T \neq 0$ is done by replacing the occupation factor v_k^2 by:

$$v_k^2(1 - f_k) + u_k^2 f_k \,, \tag{2.45}$$

being f_k the Fermi function defined on the quasiparticle energy E_k:

$$f_k = \frac{1}{1 + e^{\frac{E_k}{k_B T}}} \,. \tag{2.46}$$

[5] In Chapter 3 we have chosen for the cutoff the following prescription: $\theta(k,k') = 1$ if $E_k, E_{k'} < E_c$, otherwise it is smoothed out with the Gaussian function $\exp\left(-[(E_k - E_c)/a]^2\right)$, with $E_c = 8$ MeV and $a = 1$ MeV, being E_k the quasiparticle energy $E_k = \sqrt{[(\epsilon_k - \mu)^2 + \Delta_k^2]}$.

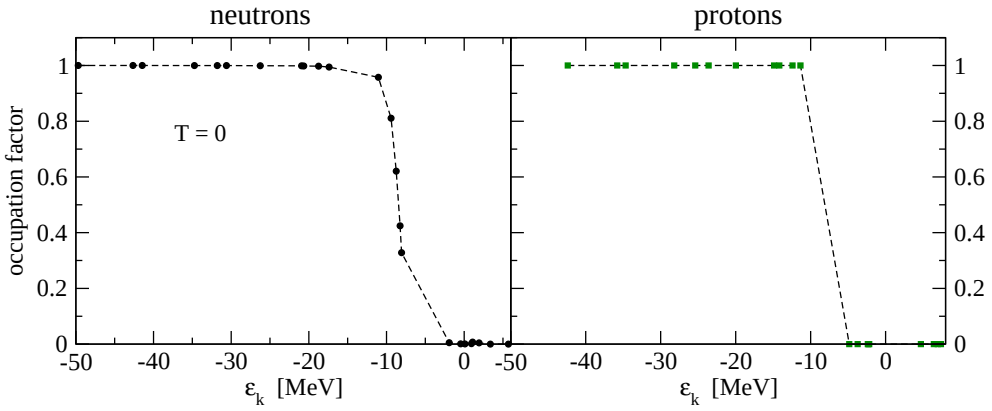

Figure 2.4: Occupation factor at $T = 0$ for neutrons (on the left) and for protons (on the right) for ^{120}Sn as a function of HF energies, for a pure surface interaction.

The particle number and gap equations Eqs. (2.40) now read [137]:

$$N_q = \sum_k (2j_k + 1) \left[v^2_{k,q}(1 - f_{k,q}) + u^2_{k,q} f_{k,q} \right] \tag{2.47}$$

$$\Delta_q(r) = \frac{v_0}{2}\, g(\rho)\tilde{\rho}_q(r)\ , \tag{2.48}$$

and:

$$\tilde{\rho}_q(r) = -\frac{1}{4\pi} \sum_{k=0}^{k=k_c} (2j_k + 1) u_{k,q} v_{k,q} (1 - 2f_{k,q}) |\Phi_{k,q}(r)|^2\ . \tag{2.49}$$

It has been also shown that in the case of $T \neq 0$, the pairing gap displays a "phase transition" behaviour (cf. Fig. 3.9, and Refs. [137, 176]) around $k_B T_c = 0.5669\Delta$, i.e. after the critical temperature pairing correlations are destroyed.

In practice, to solve the HF+BCS equations, at the end of each HF step (Fig. 2.3), a BCS procedure is then connected (Fig. 2.5). Convergence condition for the BCS procedure can be made on the average pairing gap, i.e. one can require the average gap to agree with the one extracted from experiments (e.g. in ^{120}Sn we have required the neutron pairing gap to be 1.3 MeV). The chemical potential is found via a Newton-Raphson method [327]. The first guess on the gap can be chosen according to the empirical formula $\Delta = 12\ A^{-1/2}$ [44].

2.3 Level density parameter and effective mass

The main source of information on nuclear structure is given by the nuclear masses and excitation spectra. The low-energy spectra are dominated by correlation effects that generate pairing and collective (rotational and vibrational) modes, superimposed to the single particle motion. Since the number of collective modes is smaller than the particle degrees of freedom, at sufficiently high excitation energy, the Fermi gas model may be appropriate to describe the main features of the nuclear spectrum.

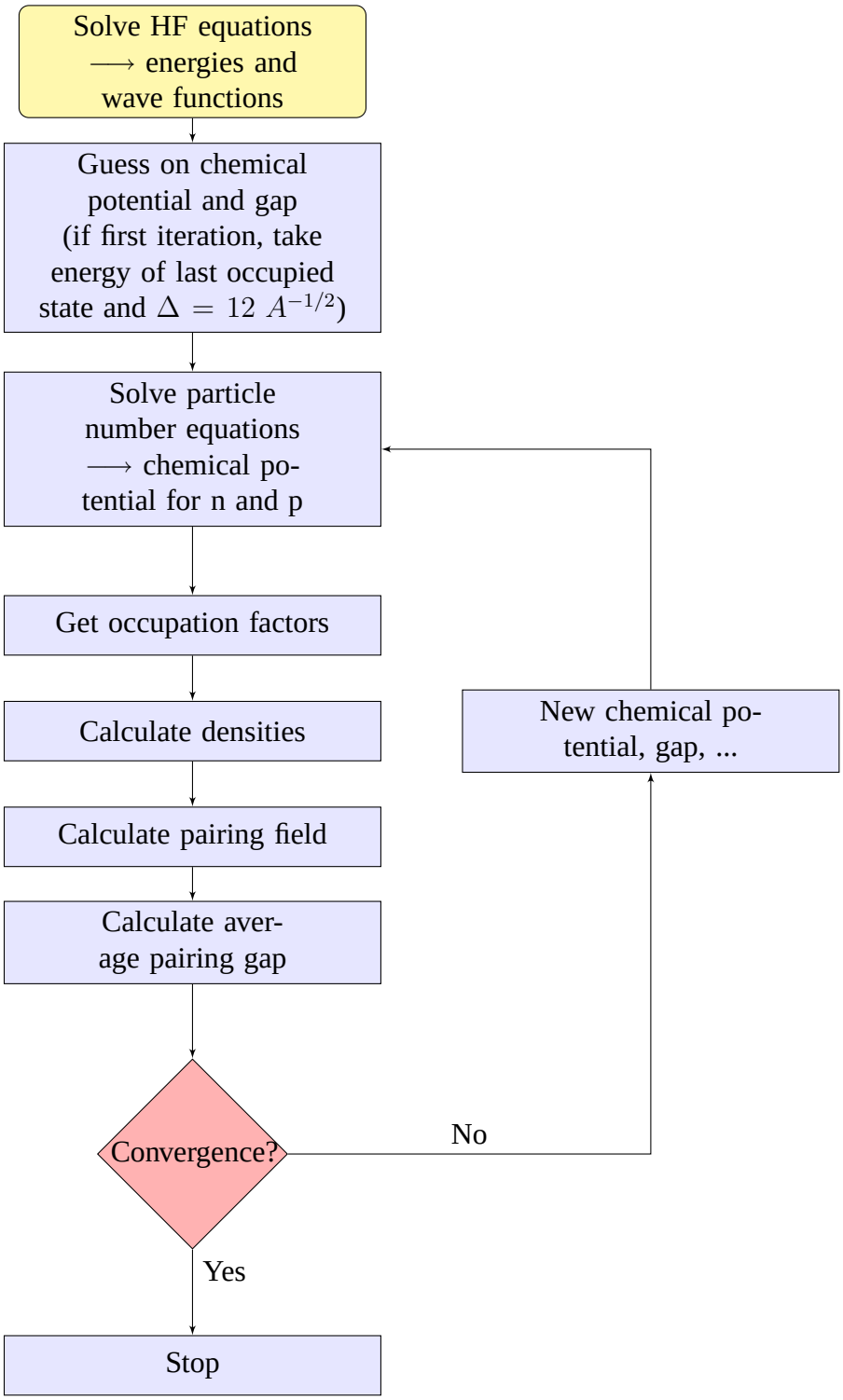

Figure 2.5: Flow chart of the BCS procedure.

The level density (density of states) is the physical quantity used to enumerate the different number of ways in which the excitation energy E^* (i.e. the difference between the energy E of the considered state and the energy E_{GS} of the ground state: $E^* := E - E_{GS}$) can be distributed among single particle states [44]. Many studies have been conducted to evaluate the nuclear level density and different techniques based on the statistical approach have been proposed to calculate it. However, combinatorial models which use the sp level distribution suffer of uncertainties and poorly reproduce experimental data because of the dependence of the choice of the sp potential. Various phenomenological modifications to the original Bethe's formula [32] have been proposed, accounting for pairing, shell and deformation effects.
For a Fermi gas and for symmetric systems ($N = Z = A/2$), the level density is given by [44, 34]:

$$\rho(E^*) = \frac{\sqrt{\pi}}{12} \frac{e^{2\sqrt{aE^*}}}{a^{1/4}(E^*)^{5/4}} , \tag{2.50}$$

where a is the so-called *level density parameter*, which in the Fermi gas model reads:

$$\frac{a}{A} = \frac{\pi^2}{6} g(\epsilon_F) \approx \frac{A}{15} \,\mathrm{MeV}^{-1}, \tag{2.51}$$

with $g(\epsilon_F) \approx \frac{3}{2}\frac{A}{\epsilon_F}$ the density of the sp levels near the Fermi surface, and ϵ_F the Fermi energy:

$$\epsilon_F = \frac{\hbar^2 k_F^2}{2m} \approx 30 \,\mathrm{MeV} , \tag{2.52}$$

where m is the bare mass. In this model it is then very easy to relate the level density to the nucleon mass.
However, the Fermi gas model is not appropriate to describe the low-energy part of the spectrum, because it does not take into account size effects, pairing correlations, effects of angular momentum and deformation, and collective excitations. If one takes in Eq. (2.52) the bare mass, the theoretical level density calculated for a Fermi gas is $\approx A/15$ MeV^{-1}, which significantly differs from that extracted from experiments, which is $\approx A/8$ MeV^{-1}. The agreement with the "experimental" value is even worst if one calculate a using the effective mass calculated in the Skyrme HF approximation, where $m^*/m \simeq 0.7$, which would give $a \approx A/22$ MeV^{-1}. It has been shown in Ref. [270] that this discrepancy disappears if one takes into account the surface peaking of m^* which is produced by dispersion corrections. In fact, only supposing an effective mass $\gtrsim 1$ at the Fermi surface (e.g. $m^*/m = 1.4$), one would obtain $a \approx A/10$ MeV^{-1}, which is closer to the value $\approx A/8$ MeV^{-1}. In other words, since the level density also depends upon the effective mass around the Fermi surface, the larger effective mass found empirically (e.g. [55]) and explained theoretically (e.g. [29, 147, 174]) tends to increase the level density. The inclusion of a surface-peaked effective mass in order to improve the density of states in a MF description will be the subject of Chapter 3.

In principle the level density parameter should depend on density, isospin asymmetry and temperature (see e.g. [301, 81]). We will focus only on the temperature dependence.

In order to get a temperature dependence of the level density parameter, one has to define the nuclear temperature [44]:

$$T^{-1} = \frac{1}{\rho(E^*)} \frac{\mathrm{d}\rho}{\mathrm{d}E^*} \,, \tag{2.53}$$

so that in the Fermi gas model one obtains the following relations which link the temperature T, the excitation energy E^* and the entropy S of the system:

$$S = 2aT \tag{2.54a}$$
$$S = 2\sqrt{aE^*} \tag{2.54b}$$
$$E^* = aT^2 \,. \tag{2.54c}$$

However, if the level density parameter is not a constant, but temperature or excitation energy dependent, the relations (2.54) cannot be satisfied by a unique a, but by different a which have to coincide as T goes to zero. Therefore one can define three level density parameters (see e.g. [96, 81]):

$$a_{ST} = \frac{S}{2T} \tag{2.55a}$$
$$a_{SE} = \frac{S^2}{4E^*} \tag{2.55b}$$
$$a_{ET} = \frac{E^*}{T^2} \,. \tag{2.55c}$$

Thus, one should be careful to compare the level density parameter at finite temperature extracted from experiments to the theoretical one. For instance, if in experiments E^* and T are determined independently one from each other (e.g. T can be obtained from the slope of the evaporation spectra of light particles and E^* from the linear momentum transfer [96]), one thus obtain a_{ET}, but if a is deduced by means of statistical model calculations (i.e. adjusted in such a way that the multiplicities experimentally measured are reproduced by the ones obtained in the statistical calculations using a given a), then a_{SE} is the extracted level density parameter [96, 81].

Different studies on the temperature- and mass-dependence of the level density parameter have been proposed (see e.g. Refs. [20, 270, 301, 195, 139, 2, 96, 81, 255]), but a clear and satisfactory link between the "experimental" level density parameter and the effective mass is still to be exploited. I address to Appendix C for a comparison with some different parameterizations of the level density parameter proposed in the literature.

2.3.1 Effective mass in nuclei

The static MF model and the nuclear shell model has been proven to be a very successful framework to describe states close to the nuclear Fermi energy. In this model, each nucleon moves independently in a smooth potential which is static but non-local in the space variables due to finite-range and spatial non-locality of the nuclear force. Nuclear potentials of this type lead to a nice overall agreement between calculated and measured important observables like binding energies and charge distributions as long as it is quite good in reproducing single particle spectra. However, this model fails to reproduce the

level density.
One has to keep in mind that the nucleus exhibits also some phenomena characteristic of a collective behaviour, such as the fission process and the large quadrupole moments. The fluctuation of the mean field potential gives rise to collective modes, in particular surface vibrations. Taking into account the coupling of these modes with the sp motion, the shell model acquires a dynamical content and the average potential becomes also non local in time, i.e. it is characterized by an energy dependence. The dynamics of the shell model affects different nuclear properties as the fragmentation and the spectroscopic factors of the sp states, their density, the sp spreading width and the imaginary part of the optical potential [55, 146, 147].
The effective mass is a powerful concept used to characterize the quasiparticle properties of a particle inside a strongly interacting medium like the nucleus because it is used to describe space and time non-locality (or, equivalently, momentum and frequency dependence) of the mean field. For simplicity, it is better to give the definition of the effective mass in nuclear matter, introducing $\mathcal{V}(k,\omega)$, the most general momentum and energy (or frequency ω) dependent average potential in which nucleons move. The energy of a state of momentum $\mathbf{k}$ and frequency (energy) ω can be thus written as:

$$\omega(k) = \frac{\hbar^2 k^2}{2m} + \mathcal{V}(k,\omega)\ . \tag{2.56}$$

We can define an effective mass m^* by the dispersion relation in analogy to the free particle case:

$$d\omega = \frac{\hbar^2 k}{m^*} dk. \tag{2.57}$$

The effective mass m^* coincides with the nucleon mass m if the nuclear potential is local and energy independent. The above dispersion relation can be written as:

$$\begin{aligned} \frac{\mathrm{d}\omega}{\mathrm{d}k} &= \frac{\hbar^2 k}{m} + \frac{\partial \mathcal{V}(k,\omega)}{\partial k} + \frac{\partial \mathcal{V}(k,\omega)}{\partial \omega}\,\frac{\partial \omega}{\partial k} \\ \frac{\mathrm{d}\omega}{\mathrm{d}k}\left[1 - \frac{\partial \mathcal{V}(k,\omega)}{\partial \omega}\right] &= \frac{\hbar^2 k}{m}\left[1 + \frac{m}{\hbar^2 k}\frac{\partial \mathcal{V}(k,\omega)}{\partial k}\right]\ , \end{aligned} \tag{2.58}$$

where now the effective mass m^* accounts for two terms, the k-mass and the ω-mass:

$$\frac{m^*}{m} = \frac{m_k}{m}\,\frac{m_\omega}{m} \tag{2.59}$$

$$\frac{m_k}{m} = \left[1 + \frac{m}{\hbar^2 k}\,\frac{\mathrm{d}\mathcal{V}(k,\omega)}{\mathrm{d}k}\right]^{-1} \tag{2.60}$$

$$\frac{m_\omega}{m} = \left[1 - \frac{\mathrm{d}\mathcal{V}(k,\omega)}{\mathrm{d}\omega}\right]\ . \tag{2.61}$$

The k-mass comes from the spatial non-locality or momentum dependence of the mean field, and it can be already derived at a MF level. The ω-mass, which is also the inverse of the so-called spectroscopic factor that indicates to which extent the exact wave function of the nucleus is in a single particle state, is related to the time non-locality or frequency dependence of the mean field.

2.3.2 Temperature dependence of the nucleon effective mass

Investigations of the temperature dependence of the effective mass in nuclei have been made by Bortignon *et al.* [47], Hasse and Schuck [152], and by Donati *et al.* [106]. In Ref. [47] an analysis was carried out for the nucleus ^{208}Pb in the Random Phase Approximation (RPA) framework, showing a decrease of the ω-mass with temperature in the range $0 < T < 4$ MeV. Hasse and Schuck [152] obtained the radial profile of the effective mass for different temperatures, in order to derive the level density parameter a/A as a function of temperature; the enhancement of the m^* for systems with $A = 160$ displayed in Fig. 3 of Ref. [152] is shown to disappear for $T > 4$ MeV.
In the paper by Donati *et al.* [106], the temperature dependence of the nucleon effective mass was calculated in the nuclei ^{98}Mo, ^{64}Zn and ^{64}Ni, and a first study of the implication of such a dependence on the gravitational collapse of the core of massive star was carried out by means of a one-zone code. The claimed T-dependence, due to the coupling of the mean field sp levels to the collective surface vibrations of the nucleus, was calculated in the quasiparticle random phase approximation[6](QRPA), the sp energies and wave functions having been calculated making use of an empirical potential of the Woods-Saxon type. The effective mass m^* has been considered as a product of two terms, the k-mass, and the ω-mass. The typical energy scale of the rigidity of the mean field related to the k-mass is of the order of the energy difference between two major shells $\hbar\omega_0 \approx 41\ A^{1/3}$ [44], i.e. ≈ 8 MeV for medium-heavy nuclei[7]. As an example, in Fig. 2.6, the results of Brückner-Hartree-Fock calculations of the k-mass are displayed as a function of temperature [329]; the points correspond to the numerical results, while the solid line corresponds to a fit where we have supposed the following Gaussian-like profile for $m_k(T)$:

$$\frac{m_k(T)}{m} = x_1 + x_2\ e^{-(T/T_{0,k})^2}\ , \tag{2.62}$$

where the best fit is given for the values of the parameters: $x_1 = 0.72$, $x_2 = 0.05$, $T_{0,k} = 7.25$ MeV.

Instead, the energy of low-lying collective vibrations related to the ω-mass is about $1 - 3$ MeV, which is the range encountered in the collapsing homologous core up to $\sim 0.1\rho_0$, where nuclei are expected to be still present. Even if temperatures of more than 7 MeV can be reached and exceeded at bounce, the (T, ρ) conditions would be favourable for nuclei to dissolve to nuclear matter. Thus, the question of the temperature dependence of m^* in our case can be formulated in terms of the temperature dependence of the ω-mass, keeping the k-mass temperature-independent[8]. In particular, in Ref. [106], the value of m_k was fixed to 0.76.
In Ref. [106], a decrease with temperature was obtained for m_ω in the range $0 < T < 2$ MeV (see Table 2.1, which is also Table 1 in Ref. [106]), and the authors parameterized

[6]The Random Phase Approximation (RPA) approach will be described in Appendix D. The difference with respect to the Quasiparticle RPA framework is that the latter one includes pairing.

[7]The value $\hbar\omega_0 \approx 41\ A^{1/3}$ comes from the fact that in the harmonic oscillator picture the oscillatory frequency ω_0 is adjusted to reproduce the nuclear mean square radius [44].

[8]We have actually tested in a one-dimensional Newtonian simulation the effect of the inclusion of the temperature dependence of the k-mass, according to the parameterization in Eq. (2.62), and we found no significant differences in the collapse trajectory.

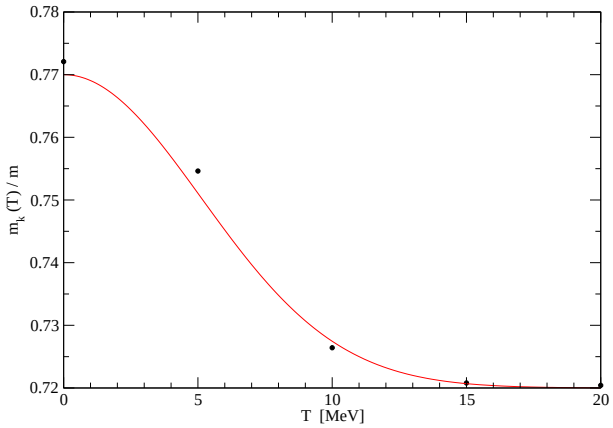

Figure 2.6: k-mass as a function of temperature. The points correspond to the results obtained by Brückner-Hartree-Fock calculations (courtesy of I. Vidaña [329]), while the solid line is the result of a Gaussian-like fit $m_k(T)/m = x_1 + x_2\ e^{-(T/T_{0,k})^2}$, where the best fit is given for the values of the parameters: $x_1 = 0.72$, $x_2 = 0.05$, $T_{0,k} = 7.25$ MeV.

this temperature dependence with the analytical expression:

$$\frac{m_\omega(T)}{m} = 1 + [m_\omega(T=0) - 1]\ e^{-T/T_0}\ , \tag{2.63}$$

where $m_\omega(T=0)$ is the ω-mass calculated at zero temperature and T_0 is obtained by the best fitting and gives the typical scale of variation of the m_ω with respect to T. One can argue that the results on ^{64}Ni seem to be contradictory with the claimed decrease of m^* with T. Actually, the value of m_ω is an average value:

$$\langle m_\omega/m \rangle = \frac{\sum_\lambda (2j_\lambda + 1)\ m_\omega}{\sum_\lambda (2j_\lambda + 1)}\ , \tag{2.64}$$

where λ runs over the levels of the major shell below and above the Fermi surface. If one looks in details the behaviour of the ω-mass for each level, m_ω decreases (for all levels) with the temperature [105]. In the study of Giovanardi *et al.* [132], the best fit for the exponential profile of m_ω was found to be $T_0 \approx 1.1$ MeV in semi-infinite nuclear matter. Even if the two kinds of system differ (the semi-infinite nuclear matter can only approximate finite size effects), the order of magnitude of the typical scale of T_0 found in the two cases agrees.

In analogy to the results of the Fermi gas model and assuming that only the kinetic part of the symmetry energy depends on the effective mass, it was argued that the temperature dependence of E_{sym} can be obtained by the following analytical expression:

$$E_{sym} = s(T)\ \left(1 - 2\frac{Z}{A}\right)^2\ , \tag{2.65}$$

where Z and A are the charge and mass number of the nucleus, and $s(T)$ is the symmetry coefficient at finite temperature, parameterized as:

$$s(T) = s(T=0) + \frac{\hbar^2 k_F^2}{6}\ \left[\frac{1}{m^*(T)} - \frac{1}{m^*(T=0)}\right]\ , \tag{2.66}$$

Nucleus	$T = 0$	$T = 1$ MeV	$T = 2$ MeV	T_0 [MeV]
^{98}Mo	1.70	1.36	1.26	1.89
^{64}Zn	1.80	1.45	1.30	1.97
^{64}Ni	1.45	1.20	1.20	2.05

Table 2.1: Values of $m_\omega(T)/m$ as a function of temperature for the nuclei ^{98}Mo, ^{64}Zn and ^{64}Ni. The last column gives the best fitting value of T_0 (in MeV) obtained according to Eq. (2.63) (from [106]).

being $k_F = 1.35$ fm^{-1} the Fermi momentum and $s(T = 0) \approx 30$ MeV the symmetry coefficient at zero temperature [106]. The decrease of m^* in the considered interval of temperature was found to correspond to an increase of the nuclear symmetry energy, E_{sym}. Thus, the temperature dependence of the nucleon effective mass affects the nuclear energy of the system.

After the study made by Donati *et al.* [106], two more investigations of the temperature dependence of the nuclear symmetry energy have been presented [98, 99], both based on shell model Monte Carlo (SMMC) calculations, the model of choice to take into account nuclear correlations beyond those treated at the QRPA level. The temperature dependence of the symmetry energy coefficient[9] $s(T)$ has been obtained calculating, for different temperatures, the expectation value of the energy per baryon $E(\rho, T, x)$ for different isobaric pairs ($x \equiv Z/A$):

$$\begin{aligned} E_{sym}(T) &= E(\rho, T, x_1) - E(\rho, T, x_2) \\ &= s(T) \left[\left(1 - 2\frac{Z_1}{A}\right)^2 - \left(1 - 2\frac{Z_2}{A}\right)^2 \right] . \end{aligned} \tag{2.67}$$

In Ref. [98], several isobaric pairs with mass numbers in the range $A = 54 - 64$ were studied. Although the results obtained for the nuclei ^{64}Zn and ^{64}Ni were in agreement with those of Donati *et al.*, in their conclusions the authors claimed to "find no systematic temperature dependence of the symmetry energy coefficient, b_{sym}, for $T \leq 1$ MeV. This contradicts a recent suggestion that b_{sym} increases by 2.5 MeV at this temperature" [98]. An improved SMMC calculation, however, was presented several years later in Ref. [99], where some known problems of the previous paper (small model space and g-extrapolation procedure to circumvent the notorious sign problem of SMMC) have been fixed. Nine isobaric pairs with $A = 56 - 66$ were analysed and this time the authors concluded that their "SMMC studies are consistent with an increase of the symmetry energy with temperature, supporting the argumentation of Donati *et al.*" [99]. Indeed, upon averaging over the various pairs, they found a variation $\overline{\delta b}_{sym} = (6.2 \pm 1.8)\%$ in the temperature interval $T = 0.33 - 1.23$ MeV, which is in reasonable agreement with the QRPA results of Donati *et al.*, namely an increase of the symmetry energy of $\sim 8\%$ in the interval $T = 0 - 1$ MeV.

Despite the agreement regarding the temperature dependence of the symmetry coefficient, in the concluding section of Ref. [99], where the authors quickly discussed possible consequences for core-collapse supernovae, they obtained changes of electron capture rates

[9] In Ref. [98], $s(T)$ is labelled as b_{sym}, while in Ref. [99] it is labelled as a_{sym}.

due to the T-dependence of b_{sym} that "appear to be rather mild so that one does not expect significant changes for the collapse trajectory" [99]. Even if we agree that no dramatic effect on the dynamics of the collapse is to be expected, one should be more cautious in dismissing any significant consequence of the T-dependence of E_{sym} without a collapse simulation. Indeed, not only the reaction Q-values (as considered in Ref. [99]), but also the equation of state of bulk dense matter, the free nucleon abundances, the degree of dissociation into α-particles and the nuclear internal excitations are affected by changes in the symmetry energy, so that mild changes in the rates may still result in non-negligible alterations of the collapse dynamics.

Chapter 3

Nuclear density functional with a surface-peaked effective mass

In this Chapter I will describe how we have introduced a surface-peaked effective mass in the Energy Density Functional framework, in order to improve the density of states. This is done in an effective way by adding a new term in the functional.
At first, the theoretical framework is presented; then the results on the mean field properties in the case of the spherical nuclei ^{40}Ca and ^{208}Pb, as well as pairing gap and finite temperature properties in the semi-magic nucleus ^{120}Sn, are discussed and analysed.

In finite nuclei, the single particle states around the Fermi energy are known to be strongly affected by the dynamical particle-hole correlations [216, 220]. The energy of the single particle states is modified and thus the level density around the Fermi energy is changed, which in turn has an impact on low-energy properties such as pairing correlations [97, 352], collective modes [149] as well as on temperature-related properties such as the entropy, the critical temperature, the specific heat [79]. In nuclear astrophysics, a good description of the density of states around the Fermi energy (which is related to the nucleon effective mass) turned out to be relevant also for the energetics of core-collapse supernovae [106, 111], as also depicted in Chapters 5 and 6.

Despite the important role of the density of states in self-consistent mean field theories, most of these models such as those based on Skyrme [302], Gogny [25] and M3Y interactions [254] or on the relativistic approaches like RMF [294] or RHF [211], have a density of states around the Fermi energy that is too low. The dynamical correlations, which lead to an increase of the effective mass at the surface, are implemented beyond the mean field. Indeed, the effective mean field theories have an average effective mass m^*/m, the k-mass, around 0.6-0.8.

The different microscopic calculations of the particle-vibration coupling (PVC) have been performed at the first order in perturbation, due to their heavy computational features [29, 26, 53, 27, 324, 47, 281, 351]. However, the induced effects of the PVC on the mean field itself is non-negligible. Since the effective mass is enhanced at the surface of nuclei [324], it impacts the single particle states and the pairing correlations which, in turn, modify the PVC and the effective mass.

We therefore propose an effective shortcut for treating the effects of the PVC directly in the Energy Density Functional (EDF) approach.

3.1 Nuclear energy density functional (EDF)

The EDF derived from Skyrme interaction will be considered following the notation used in Bender *et al.* [24] and Chabanat *et al.* [76, 77], as reported in Chapter 2, Eqs. (2.13)-(2.21).

3.1.1 Mean field equations in spherical symmetry

For spherical doubly-closed-shell nuclei, the single particle wave functions $\Phi_{\lambda,q}$ in Eq. (2.31) can be factorized into a radial part and an angular part as (cf. Eq. (26) of Ref. [328])[1]:

$$\Phi_{\lambda,q}(\mathbf{r},\sigma,\tau) = \frac{\phi_{\lambda,q}(r)}{r}\,\mathcal{Y}_{l,j,m}(\theta,\phi,\sigma)\,\chi_q(\tau)\;, \tag{3.5}$$

where σ is the spin and τ the isospin, and:

$$\mathcal{Y}_{l,j,m}(\theta,\phi,\sigma) = \sum_{m_l,m_s}\langle l\frac{1}{2}m_l m_s|jm\rangle\,Y_{l,m_l}(\theta,\phi)\,\chi_{m_s}(\sigma)\;, \tag{3.6}$$

where $Y_{l,m_l}(\theta,\phi)$ are the spherical harmonics, and m is the magnetic quantum number. The radial wave function $\phi_{\lambda,q}(r)$ satisfies the following equation (cf. Eq. (35) of Ref. [328]):

$$\begin{aligned}
&-\frac{\hbar^2}{2m_q^*}\,\frac{\mathrm{d}^2\phi_{\lambda,q}(r)}{\mathrm{d}r^2} - \frac{\mathrm{d}}{\mathrm{d}r}\left(\frac{\hbar^2}{2m_q^*}\right)\,\frac{\mathrm{d}\phi_{\lambda,q}(r)}{\mathrm{d}r}\\
&\quad+\left[\frac{\hbar^2}{2m_q^*}\frac{l(l+1)}{r^2}+\frac{1}{r}\frac{\mathrm{d}}{\mathrm{d}r}\left(\frac{\hbar^2}{2m_q^*}\right)\right]\phi_{\lambda,q}(r)\\
&\quad+[U_q(r)+U_q^{so}(r)\langle\hat{\mathbf{l}}\cdot\hat{\sigma}\rangle+\delta_{q,p}V_{Coul}(r)]\,\phi_{\lambda,q}(r)=\epsilon_{\lambda,q}\phi_{\lambda,q}(r)\;,
\end{aligned} \tag{3.7}$$

where $U_q^{so}(r)$ is the spin-orbit potential [328, 24] and $V_{Coul}(r)$ is the Coulomb potential (direct plus the exchange term treated in the Slater approximation) [328, 77]:

$$U_q^{so}(r)\langle\hat{\mathbf{l}}\cdot\hat{\sigma}\rangle = \frac{1}{r}W_q(r)\,\left[j_\lambda(j_\lambda+1)-l_\lambda(l_\lambda+1)-\frac{3}{4}\right] \tag{3.8}$$

$$V_{Coul}(r) = \frac{e^2}{2}\int\frac{\rho_p(\mathbf{r}')\mathrm{d}\mathbf{r}'}{|\mathbf{r}-\mathbf{r}'|}-\frac{e^2}{2}\left(\frac{3}{\pi}\right)^{1/3}\rho_p^{1/3}(r)\;. \tag{3.9}$$

[1]The spherical case is recovered by noticing that, in spherical symmetry [328]:

$$-i\,\mathbf{W}_q(\mathbf{r})\cdot(\nabla\times\hat{\sigma}) = \frac{1}{r}\,W_q(r)\,\hat{\mathbf{l}}\cdot\hat{\sigma} \tag{3.1}$$

$$\mathbf{J}(\mathbf{r}) = \frac{\mathbf{r}}{r}J(r) \tag{3.2}$$

$$\nabla^2 = \frac{1}{r}\frac{\partial^2}{\partial r^2}-\frac{\hat{\mathbf{l}}^2}{r^2} \tag{3.3}$$

$$\nabla = \frac{\mathbf{r}}{r}\frac{\mathrm{d}}{\mathrm{d}r}\;. \tag{3.4}$$

In the Skyrme functional $W_q(r)$ is given by [77]:

$$W_q(r) = \frac{1}{2}W_0\frac{\mathrm{d}}{\mathrm{d}r}(\rho+\rho_q) + \frac{1}{8}(t_1-t_2)J_q(r) - \frac{1}{8}(t_1x_1-t_2x_2)J(r)\ . \tag{3.10}$$

To get rid of the first derivative of the wave function one introduces the following transformation on the radial wave function [322]:

$$\phi_{\lambda,q}(r) = \sqrt{\frac{m_q^*(r)}{m}}\,\psi_{\lambda,q}(r)\ , \tag{3.11}$$

and, if one defines an equivalent potential [322]:

$$\begin{aligned} V_q^{\mathrm{eq}}(r,\epsilon) &= \frac{m_q^*(r)}{m}\Big[V_q(r) + U_q^{so}(r)\langle\hat{\mathbf{l}}\cdot\hat{\sigma}\rangle + \delta_{q,p}V_{Coul}(r)\Big] \\ &\quad + \left[1-\frac{m_q^*(r)}{m}\right]\epsilon_{\lambda,q}\ , \end{aligned} \tag{3.12}$$

where:

$$V_q(r) = U_q^{\mathrm{Sky}}(r) + U_q^{\mathrm{eff}}(r)\ , \tag{3.13}$$

$$\begin{aligned} U_q^{\mathrm{eff}} &= -\frac{1}{4}\frac{2m_q^*(r)}{\hbar^2}\left(\frac{\hbar^2}{2m_q^*(r)}\right)'^2 + \frac{1}{2}\left(\frac{\hbar^2}{2m_q^*(r)}\right)'' \\ &\quad + \left(\frac{\hbar^2}{2m_q^*(r)}\right)'\frac{1}{r}\ , \end{aligned} \tag{3.14}$$

the radial Schrödinger equation, Eq. (3.7), becomes:

$$\left[-\frac{\hbar^2}{2m}\frac{\mathrm{d}^2}{\mathrm{d}r^2} + \frac{\hbar^2}{2m}\frac{l(l+1)}{r^2} + V_q^{\mathrm{eq}}(r,\epsilon)\right]\psi_{\lambda,q}(r) = \epsilon_{\lambda,q}\psi_{\lambda,q}(r)\ . \tag{3.15}$$

The term $U_q^{\mathrm{Sky}}(r)$ in Eq. (3.13) is the mean field deduced from Skyrme.
The reason why one wants to express the Schrödinger equation without the dependence on the first derivative of the wave function comes from the choice of the numerical technique used to solve the Schrödinger equation. In fact, rewriting the equation Eq. (3.7) only in terms of the wave function and its second order derivative, one can implement the Numerov method which converges very fast [322]. The Numerov method can be used to solve equations of the form:

$$\left(\frac{\mathrm{d}^2}{\mathrm{d}x^2} + f(x)\right)y(x) = 0\ , \tag{3.16}$$

where, in the case of Schrödinger equation Eq. (3.15):

$$f(x=r) = -\frac{l(l+1)}{r^2} - \frac{2m}{\hbar^2}V_q^{\mathrm{eq}}(r,\epsilon) + \frac{2m}{\hbar^2}\epsilon\ . \tag{3.17}$$

Starting from a first approximation of the eigenvalues and eigenstates (e.g. the ones given by a Woods-Saxon potential), one can iteratively calculate the new mean field, sp energies and wave functions until convergence is reached (i.e. the relative difference between the

energies obtained in two consecutive iterations is less than the precision required), by means of the following procedure:

$$y_{n+1} = \frac{\left(2 - \frac{5h^2}{6} f_n\right) y_n - \left(1 + \frac{h^2}{12} f_{n-1}\right) y_{n-1}}{\left(1 + \frac{h^2}{12} f_{n+1}\right)} \,, \tag{3.18}$$

where n stands for the iteration counter and h is the integration step (for the present application: $h \equiv \mathrm{d}r$).

3.1.2 Extension of the Skyrme-EDF

In this Section, we propose an effective shortcut for treating the effects of the PVC directly in the EDF. The coupling of the collective modes to the single particle motion induces a dynamical type of correlation that in principle could not be easily implemented in an effective nuclear interaction or in a nuclear EDF. These correlations are mainly located at the surface of nuclei which makes easier the implementation in energy-density functionals. A parameterization of the ω-mass as a gradient of the nuclear profile has shown to give good results within a nuclear shell model [212] and the first order expansion of the self-energy near the Fermi energy induces a renormalization of the single particle Green function as well as a correction to the mean field, which almost compensates the effective component (Eq. (3.14)) of the equivalent potential (Eq. (3.12)) [212].

In order to include a surface-peaked effective mass induced by the PVC in the EDF approach, one has to add new terms in the functional. Since their exact form is not known *a priori*, we have chosen a correction term designed in such a way to produce: *(i)* a surface-peaked effective mass (energy independent); *(ii)* a compensation of the correction and effective component of the equivalent potential (as in Ref. [212]).
For simplicity, we at first propose a correction term which depends only on isoscalar quantities:

$$\mathcal{H}_0^{\mathrm{corr}}(\mathbf{r}) = C_0^{\tau(\nabla\rho)^2} \tau(\mathbf{r}) \left(\nabla\rho(\mathbf{r})\right)^2 + C_0^{\rho^2(\nabla\rho)^2} \rho(\mathbf{r})^2 \left(\nabla\rho(\mathbf{r})\right)^2 \,. \tag{3.19}$$

The first term in Eq. (3.19), introduced in Refs. [354, 355], induces a surface-peaked effective mass while the second term is introduced to moderate the effect of the first one in the mean field.

The effective mass is obtained from the functional derivative of the energy H with respect to the kinetic energy density τ and is expressed as (q runs over neutrons and protons: $q = n, p$):

$$\frac{\hbar^2}{2m_q^*(\mathbf{r})} \equiv \frac{\delta H}{\delta \tau_q} = \frac{\hbar^2}{2m} + C_q^\tau \rho_q(\mathbf{r}) + C_0^{\tau(\nabla\rho)^2} (\nabla\rho(\mathbf{r}))^2 \,, \tag{3.20}$$

where $C_q^\tau = (C_0^\tau \pm C_1^\tau)/2$, and the + (-) sign holds for neutrons (protons). The mean field is obtained from the functional derivative of H with respect to the isovector densities, and reads:

$$U_q(\mathbf{r}) \equiv \frac{\delta H}{\delta \rho_q} = U_q^{\mathrm{Sky}}(\mathbf{r}) + U^{\mathrm{corr}}(\mathbf{r}) \,, \tag{3.21}$$

where now, in addition to the standard Skyrme terms, we have the ones coming from the correction term induced by Eq. (3.19). The term $U^{\rm corr}(\mathbf{r})$ is defined as:

$$\begin{aligned} U^{\rm corr}(\mathbf{r}) &= -2C_0^{\tau(\nabla\rho)^2}\Big(\tau(\mathbf{r})\nabla^2\rho(\mathbf{r}) + \nabla\tau(\mathbf{r})\nabla\rho(\mathbf{r})\Big) \\ &- 2C_0^{\rho^2(\nabla\rho)^2}\Big(\rho(\mathbf{r})(\nabla\rho(\mathbf{r}))^2 + \rho(\mathbf{r})^2\nabla^2\rho(\mathbf{r})\Big) \ . \end{aligned} \tag{3.22}$$

The equivalent potential in the radial Schrödinger equation (cf. Eqs. (3.12), (3.13) and (3.15)) is thus modified in the following way:

$$V_q(r) = U_q^{\rm Sky}(r) + U^{\rm corr}(r) + U_q^{\rm eff}(r) \ , \tag{3.23}$$

where all the terms have been previously defined.

In the original work of Ma and Wambach [212], the term $U^{\rm corr}(r)$ was derived directly from the Green's function with energy dependent self-energies while, in our approach, $U^{\rm corr}(r)$ is derived from the new term (3.19) in the EDF. A one-to-one correspondence between EDF and the Green's function approach is not possible. However, since the terms $U^{\rm corr}(r)$ and $U_q^{\rm eff}(r)$ compensate each other in the Green's function approach [212], we want in the EDF to reproduce the same behaviour. We obtain approximate compensation between $U^{\rm corr}(r)$ and $U_q^{\rm eff}(r)$ by imposing the following relation between the new coefficients:

$$C_0^{\rho^2(\nabla\rho)^2} = 12 \text{ fm } C_0^{\tau(\nabla\rho)^2} \ . \tag{3.24}$$

We have investigated the sensitivity of the results to the value of the proportionality constant and we have checked that the reasonable values lie in the range 10-20 fm, after which the compensation is no longer efficient. We have performed the test for the following Skyrme forces: SkM* [21], BSk14 [140] and SLy4 [76, 77].

Notice that a surface-peaked effective mass could also be obtained from a modified Skyrme interaction. This different approach potentially leads to an improved agreement with experimental single particle energies [113]. Since the new term explored in Ref. [113] is simultaneously momentum and density dependent, the functional obtained is quite different from Eq. (3.19): the number of terms is much larger and the correction to the effective mass is a polynomial in the density. It would be interesting to carry out a more detailed comparison of these two different approaches in a future study.

3.2 Mean field properties

In the following, we study the influence of the correction introduced by the new term $\mathcal{H}_0^{\rm corr}$ for two representative nuclei: ^{40}Ca and ^{208}Pb, using BSk14 interaction [140], which is adjusted to a large number of nuclei (2149). The effective mass in symmetric matter at saturation density is $0.8m$ and the isospin splitting of the effective mass in asymmetric matter qualitatively agrees with the expected behaviour deduced from microscopic Brückner-Hartree-Fock theory [320]. In the following, we study the effect of the correction term on top of BSk14 interaction without refitting the parameters. The refit is in principle necessary since the correction term impacts the masses and changes the single particle energies (as we will see later). Since this work is thought to be exploratory, we

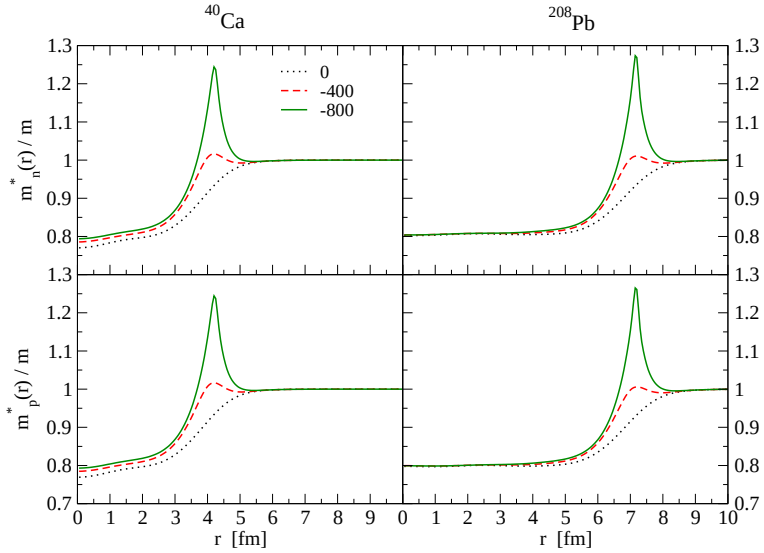

Figure 3.1: m^*_q/m as a function of radial coordinate for ^{40}Ca and ^{208}Pb, for $C_0^{\tau(\nabla\rho)^2} = 0$, -400, -800 MeV fm^{10}.

want to improve the level density and discuss the effects on other quantities like the pairing, the entropy, the specific heat. The correction term (3.19) could however potentially brings a better systematics in the comparison to experimental single particle centroids; this would be an interesting outlook with respect to this work.

The neutron and proton effective masses are plotted in Fig. 3.1 for different values of the coefficient $C_0^{\tau(\nabla\rho)^2} = 0$, -400, -800 MeV fm^{10}. Notice that the reference $C_0^{\tau(\nabla\rho)^2} = 0$ is that of the original Skyrme interaction BSk14. Increasing the absolute value of the coefficient $C_0^{\tau(\nabla\rho)^2}$ from 0 to 800 MeV fm^{10}, we observe an increasing of the effective mass m^*/m at the surface, producing a peak for large values of $C_0^{\tau(\nabla\rho)^2}$, while at the center of the nucleus the effective masses get closer to the value given by the standard Skyrme parameterization. Fig. 3.1 can be compared with Fig. 1 of Ref. [212]. Due to the different surface-peaked functions (here $(\nabla\rho)^2$ instead of a single ∇ dependence in Ref. [212]), the width of the effective mass at the surface is larger in Ref. [212] than in the present work. For values of the coefficient $C_0^{\tau(\nabla\rho)^2}$ larger in absolute value than -800 MeV fm^{10}, the potentials $U^{\rm corr}(r)$ and $U_q^{\rm eff}(r)$ (Eqs. (3.22), (3.14)) induce large gradients of the mean-field (3.23) in a tiny region close to the surface of the nuclei, which in turn produce an instability in the HF iterations.

A surface peaked effective mass could also be deduced from the particle-vibration coupling within the HF+RPA framework [324]. In the latter work, the effective mass is shown to be peaked not only at the surface of the nuclei, but also for an energy window around the Fermi energy of $\pm$ 5 MeV. Such an energy dependence could not be implemented straightforwardly in the EDF framework. We could however evaluate the state-averaged effective mass, $\langle m^*_q/m\rangle_\lambda$, defined as:

$$\langle m^*_q/m\rangle_\lambda = \int d\mathbf{r}\ \phi^*_{\lambda,q}(\mathbf{r})\frac{m^*_q(\mathbf{r})}{m}\phi_{\lambda,q}(\mathbf{r})\ , \tag{3.25}$$

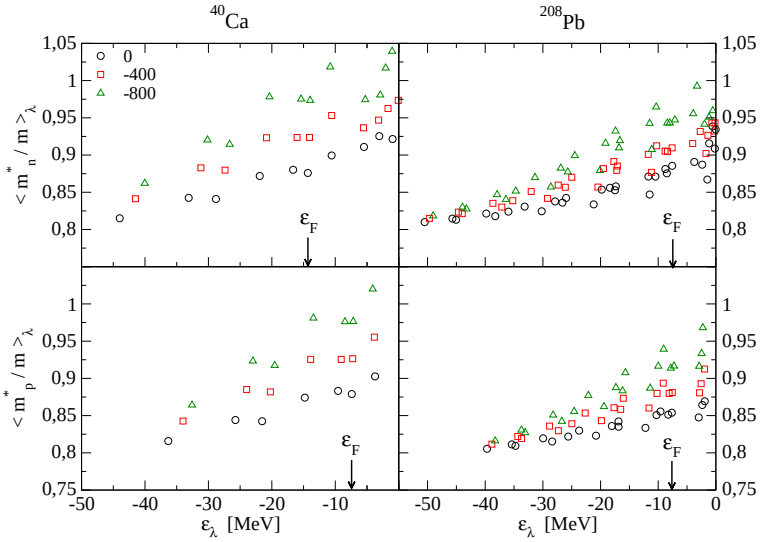

Figure 3.2: Energy dependence of the expectation value of $\langle m_q^*/m\rangle_\lambda$ for bound states for ^{40}Ca and ^{208}Pb, for $C_0^{\tau(\nabla\rho)^2} = 0$, -400, -800 MeV fm^{10}. The arrows indicate the position of the Fermi energy for $C_0^{\tau(\nabla\rho)^2} = 0$, defined as the energy of the last occupied state. The correction induced by the surface-peaked effective mass produces an increase of the Fermi energy by 400 keV at most.

where the index λ stands for the considered state. The state-averaged effective masses $\langle m_q^*/m\rangle_\lambda$ are represented in Fig. 3.2 as a function of the energy of the bound-states, and for different values of the parameter $C_0^{\tau(\nabla\rho)^2}$. As the value of the coefficient $|C_0^{\tau(\nabla\rho)^2}|$ gets larger, the state-averaged effective masses $\langle m_q^*/m\rangle_\lambda$ approach 1 around the Fermi energy while they get closer to the original effective masses for deeply bound states. In conclusion, even if we did not introduce an explicit energy dependence of the surface-peaked effective mass, we still find that the expected behaviour of $\langle m_q^*/m\rangle_\lambda$ as a function of energy (cf. Fig. 6 in Ref. [212] and Ref. [324]) is qualitatively reproduced.

In order to evaluate the impact of the new term on the density of states, we display in Fig. 3.3 the neutron and proton number of states as a function of the excitation energy, defined as:

$$N(E) = \int_0^E dE'\, g(E')\,, \tag{3.26}$$

where g(E) is the density of states,

$$g(E) \equiv \frac{\mathrm{d}N(E)}{\mathrm{d}E} = \sum_{\substack{\lambda_1<F\\ \lambda_2>F}} (2j_{\lambda_2}+1)\,\delta(E-(\epsilon_{\lambda_2}-\epsilon_{\lambda_1}))\,, \tag{3.27}$$

and ϵ_{λ_1} (ϵ_{λ_2}) represent the single-particle energies below (above) the Fermi surface. The expected relation between the surface peaked effective mass and the density of states is clearly shown in Fig. 3.3: the number of states at given excitation energy increases as the coefficient $C_0^{\tau(\nabla\rho)^2}$ goes from 0 to -800, meaning that the density of states also increases as $|C_0^{\tau(\nabla\rho)^2}|$ gets larger.

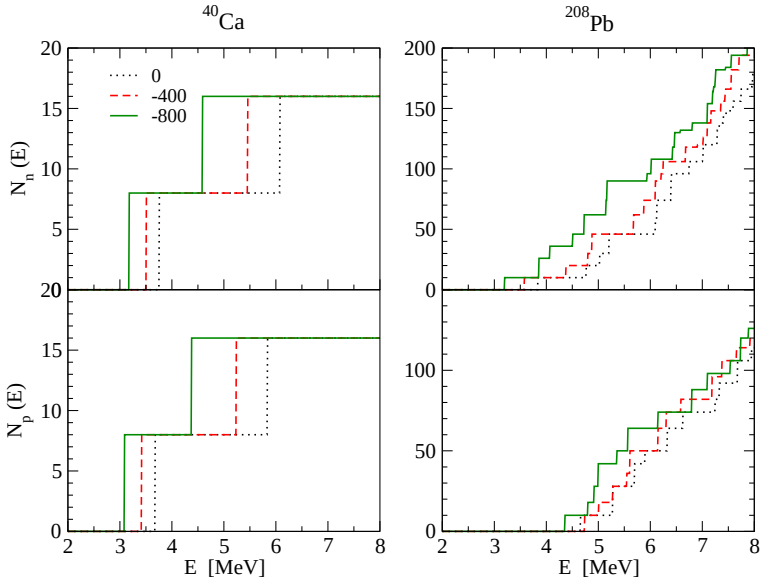

Figure 3.3: Number of states as a function of the excitation energy for ^{40}Ca and ^{208}Pb, for $C_0^{\tau(\nabla\rho)^2} = 0$, -400, -800 MeV fm^{10}.

Let us now discuss qualitatively the impact of the correction term (3.19) on global properties on nuclei starting with the density profiles. The neutron and proton densities are shown in Fig. 3.4. Since for ^{40}Ca the neutron density is very similar to the proton one, we have chosen to represent only the neutron one. We observe that the extension of the density profile is slightly increased as the value of the parameter $|C_0^{\tau(\nabla\rho)^2}|$ gets larger. Since the number of particles has to be conserved, lower values of the density in the bulk of nuclei for larger values of the coefficient $|C_0^{\tau(\nabla\rho)^2}|$ are compensated by a slight increase of the size of the nucleus. These small differences in the density profile influence the charge root mean square radius r_{ch} (see Table 3.1), which slightly increases as the value of the parameter $|C_0^{\tau(\nabla\rho)^2}|$ gets larger. Moreover, because of the isoscalar nature of the correction (3.19), neutrons and protons are affected in an identical way, as one can see from the constant value of the neutron skin radius, r_{skin}, given in Table 3.1.

Let us now analyse the influence of $\mathcal{H}_0^{\rm corr}$ at the level of the mean field $V_q(r)$ defined in Eq. (3.23). The different components of the central part of the mean field, $U_q^{\rm Sky}(r)$, $U_q^{\rm eff}(r)$, and $U^{\rm corr}(r)$, see Eqs. (3.14) and (3.22), are represented in Fig. 3.5 for neutrons, protons, and for ^{40}Ca and ^{208}Pb nuclei. The value of the coefficient is fixed to be $C_0^{\tau(\nabla\rho)^2} = -400$ MeV fm^{10}. As expected, there is a reasonable compensation between $U_q^{\rm eff}(r)$ and $U^{\rm corr}(r)$. As a consequence, the mean field $V_q(r)$ is nearly not affected by the presence of a surface-peaked effective mass for the values of the coefficient $C_0^{\tau(\nabla\rho)^2}$ chosen in the domain going from 0 to -800 MeV fm^{10}, except close to the surface where a small change in the slope is observed. We have then shown that in the EDF framework, the correction term (3.19) reproduces the result obtained in Ref. [212].

We now compare our results to the recent ones of Zalewski *et al.*[354, 355] where correction terms such as (3.19) as well as others have been studied. The main differences between our approach and that of Refs. [354, 355] are: *(i)* the moderating term is not

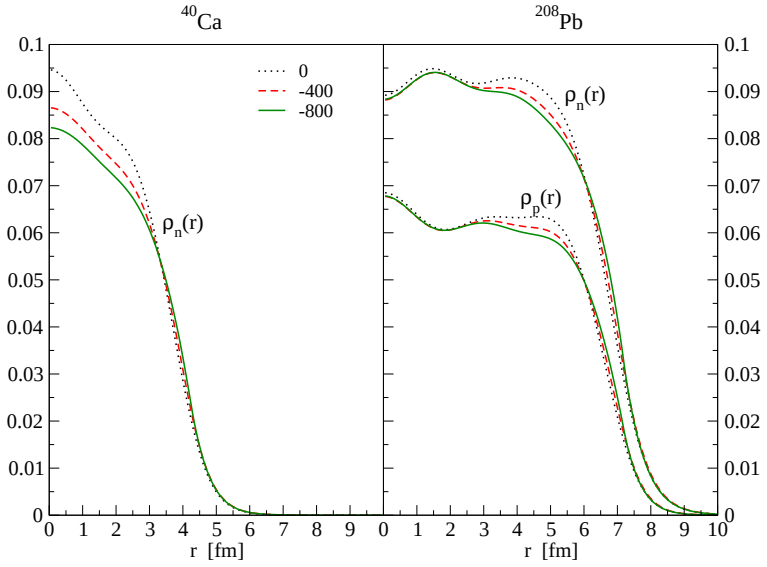

Figure 3.4: Neutron density as a function of radial coordinate for ^{40}Ca and neutron and proton densities as a function of the radial coordinate for ^{208}Pb, for $C_0^{\tau(\nabla\rho)^2} = 0$, -400, -800 MeV fm^{10}.

present in Refs. [354, 355], *(ii)* the effective mass in the bulk of nuclei is close to $0.8m$ in our case, while in the Refs. [354, 355] it assumes the value 1 since they started with SkX-Skyrme interaction [51] , *(iii)* we have not refitted the parameters of the interaction contrarily to Refs. [354, 355]; indeed, at variance with our approach, the functional is readjusted in Refs. [354, 355] such that the condition

$$\int d\mathbf{r}\ \frac{\rho_0(r)}{A}\ \frac{m^*(r)}{m} = 1 \tag{3.28}$$

is satisfied. An important dependence of the spin-orbit splitting and of the centroids as a function of the coefficient of the correction term has been observed in Ref. [354]. In our case, as shown in Figs. 3.6 and 3.7 for both ^{40}Ca and ^{208}Pb nuclei, we do not find such an important effect. Only a weak dependence on the coefficient $C_0^{\tau(\nabla\rho)^2}$ of the spin-orbit splitting is observed and an almost independence of the spin-orbit centroids. This contradiction between the two results might come from the readjustment of the Skyrme parameters performed in Ref. [355], where the spin-orbit is not changed but the parameters of the Skyrme interaction are changed. This might induce a modification of the density profile and, in turn, of the spin-orbit splitting. In fact, in Ref. [355] another procedure is adopted, the *non-perturbative* one, and the behaviour of the spin-orbit splitting and of the spin-orbit centroids is quite different from that shown in Ref. [354]. The *non-perturbative* prescription of Ref. [355] shows almost no change of the spin-orbit splittings and centroids with respect to the strength of the surface-peaked effective mass. This shows that the spin-orbit splittings and their centroids might not be impacted by the presence of a surface-peaked effective mass in a direct way, but eventually, indirectly through the readjustment procedure of the functional.

Finally, we have studied how the binding energies vary as a function of the correction term (3.19). The results are presented in Table 3.2. The binding energy of ^{40}Ca and ^{208}Pb

	^{40}Ca		^{208}Pb	
$C_0^{\tau(\nabla\rho)^2}$ $[\mathrm{MeVfm}^{10}]$	r_{ch} [fm]	r_{skin} [fm]	r_{ch} [fm]	r_{skin} [fm]
0	4.01	-0.04	6.05	0.16
-200	4.05	-0.04	6.08	0.16
-400	4.08	-0.04	6.10	0.16
-600	4.10	-0.04	6.12	0.16
-800	4.10	-0.04	6.12	0.16

Table 3.1: Charge rms radius, r_{ch}, and neutron skin radius, r_{skin}, for ^{40}Ca and ^{208}Pb and for different values of the coefficient $C_0^{\tau(\nabla\rho)^2}$. The charge rms radius is calculated according to Eq. (110) in Ref. [24].

$C_0^{\tau(\nabla\rho)^2}$	^{40}Ca	^{208}Pb
0	-8,781	-8,071
-200	-8.591	-7.983
-400	-8.442	-7.910
-600	-8.322	-7.849
-800	-8.227	-7.801

Table 3.2: Binding energies per nucleon in ^{40}Ca and ^{208}Pb (in MeV) for different values of the coefficient $C_0^{\tau(\nabla\rho)^2}$.

increases as the parameter $|C_0^{\tau(\nabla\rho)^2}|$ gets larger. We can therefore expect that the readjustment of the parameters of the Skyrme interaction shall essentially make the interaction more attractive.

3.3 Pairing properties

Most of the nuclei are superfluid and it could be shown that in the weak coupling limit of the BCS approximation, the pairing gap at the Fermi surface Δ_F and the pairing interaction v_{pair} are related in uniform matter through the relation [210]:

$$\Delta_F \approx 2\epsilon_F \exp[2/(N_0 v_{pair})], \tag{3.29}$$

where ϵ_F is the Fermi energy, $N_0 = m^* k_F/(\hbar^2\pi^2)$ is the density of states at the Fermi surface. Then a small change of the effective mass m^* can result in a substantial change of the pairing gap.

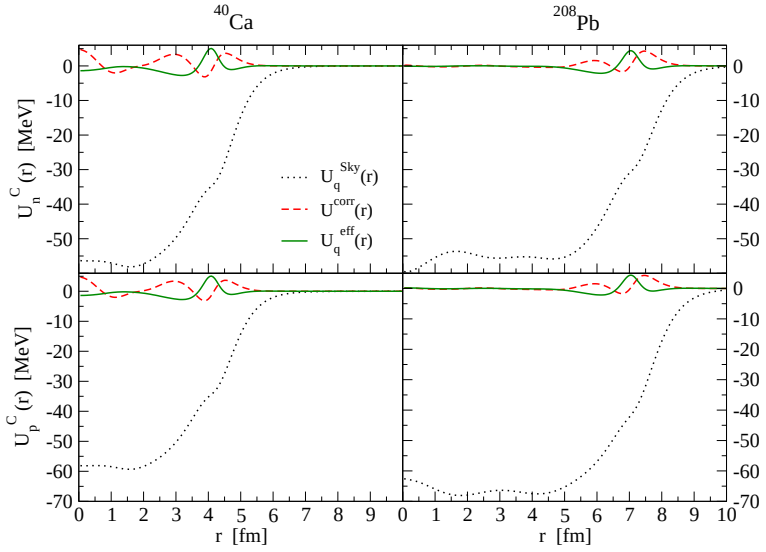

Figure 3.5: Central part of the neutron and proton mean field as a function of radial coordinate for ^{40}Ca and ^{208}Pb, for $C_0^{\tau(\nabla\rho)^2} = -400$ MeV fm^{10}.

In the following, we will consider ^{120}Sn because it is an excellent candidate to study pairing correlations [24]: ^{120}Sn is spherical and only neutrons are participating to the S-wave Cooper-pairs. An accurate description of the pairing properties can be obtained already at the level of the spherical HF+BCS framework [24]. In this Section, we study qualitatively the relation between the increase of the effective mass at the surface and its consequences on the pairing properties, both at zero and at finite temperature.

We adopt a density-dependent contact interaction v_{nn} given by [131]:

$$\langle k|v_{nn}|k'\rangle = v_0 g(\rho)\theta(k,k') \ , \tag{3.30}$$

where the strength v_0 of the pairing interaction is adjusted to obtain an average neutron pairing gap equals to 1.3 MeV in ^{120}Sn. $g(\rho)$ is a density-dependent function (see below) and $\theta(k,k')$ is the cutoff introduced to regularize the ultraviolet divergence in the gap equation. We choose for $\theta(k,k')$ the following prescription[2]: $\theta(k,k') = 1$ if $E_k, E_{k'} < E_c$, otherwise it is smoothed out with the Gaussian function $\exp\left(-\left[(E_\lambda - E_c)/a\right]^2\right)$. Hereafter, we choose $E_c = 8$ MeV and $a = 1$ MeV. Notice that to be compatible with HFB calculations, the cutoff is implemented on the quasiparticle energy,

$$E_{\lambda,q} = \left[(\epsilon_{\lambda,q} - \mu_q)^2 + \Delta^2_{\lambda,q}\right]^{1/2} \ , \tag{3.31}$$

[2]We have actually checked different prescriptions for the cutoff, such as a step function equals to 1 for bound states and 0 for unbound states, or a Gaussian smoothing around the Fermi energy, implementing the cutoff either on the HF energies or on quasiparticle energies, and we have finally decided to adopt a prescription on the quasiparticle energies, to be able to compare the results with the ones obtained in the HFB calculations. The impact of the cutoff is not negligible (see e.g. [225]). For example, for $C_0^{\tau(\nabla\rho)^2} = -800$ MeV fm^{10}, $\eta = 1$, and $E_c = 5$ MeV, the neutron gap at $T = 0.1$ MeV varies from 1.53 MeV if the cutoff is implemented on the quasiparticle energies to 1.96 MeV if the cutoff is implemented on the HF energies, while the HF sp energies themselves differ of about 10 keV. This could be explained noticing that, changing the cutoff, the number of the considered states in averaging the gap differs, and that has a non-negligible impact on the gap.

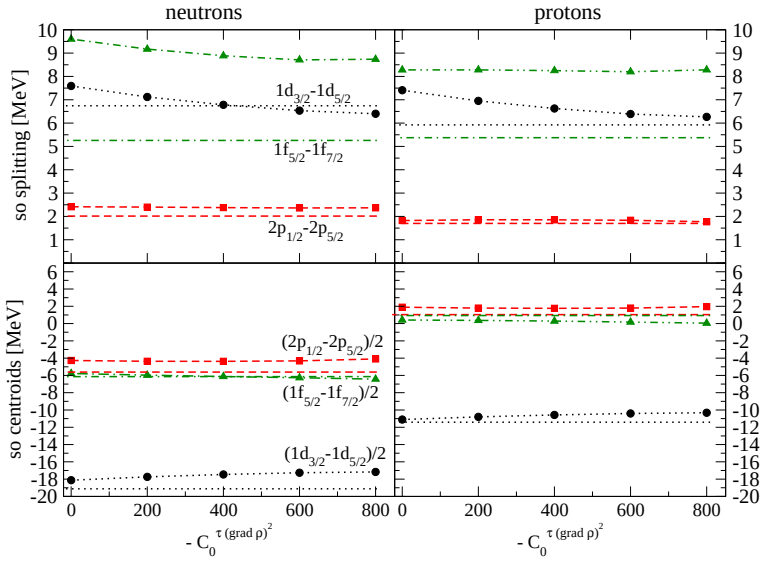

Figure 3.6: Spin orbit splitting and centroids for ^{40}Ca as a function of the coefficient $C_0^{\tau(\nabla\rho)^2}$. The experimental values, drawn with a straight line, are taken from [261].

where $\epsilon_{\lambda,q}$ is the HF energy, μ_q the chemical potential, and $\Delta_{\lambda,q}$ the average pairing gap for the state λ (see Eq. (3.35)). The density-dependent term $g(\rho)$ is simply defined as in Eq. (2.39), and the isoscalar particle density, $\rho = \rho_n + \rho_p$, is the generalization at finite temperature of Eq. (2.41), defined as:

$$\rho_q(r) = \frac{1}{4\pi}\sum_{\lambda}(2j_\lambda+1)\left[v^2_{\lambda,q}(1-f_{\lambda,q}) + u^2_{\lambda,q}f_{\lambda,q}\right]|\phi_{\lambda,q}(r)|^2\,, \tag{3.32}$$

where the $u_{\lambda,q}$ and the $v_{\lambda,q}$ are the variational parameters, and $f_{\lambda,q}$ is the Fermi function for the quasiparticle energy $E_{\lambda,q}$ (Eq. (3.31)) [137]:

$$f_{\lambda,q} = \frac{1}{1+e^{E_{\lambda,q}/k_BT}}\,, \tag{3.33}$$

where k_B is the Boltzmann constant. The local pairing field is then given by Eq. (2.40b), and the abnormal density is defined, generalizing Eq. (2.42) at finite temperature, as (Eq. (2.49)):

$$\tilde{\rho}_q(r) = -\frac{1}{4\pi}\sum_{\lambda}(2j_\lambda+1)u_{\lambda,q}v_{\lambda,q}(1-2f_{\lambda,q})|\phi_{\lambda,q}(r)|^2\,. \tag{3.34}$$

The self-consistent gap equation Eq. (2.40b) should be solved consistently with the particle conservation equation (3.32). The average pairing gap for the state λ used in the definition of the quasiparticle energy Eq. (3.31) is defined as:

$$\Delta_{\lambda,q} = \int d\mathbf{r}|\phi_{\lambda,q}(r)|^2\Delta_q(r). \tag{3.35}$$

In the HF+BCS framework we adopt, Eqs. (3.32) and (2.40b) are solved at each iteration. The number of iterations performed depends on the convergence of the pairing gap equation (2.40b); it goes from about 200 up to about 1000 near the critical temperature.

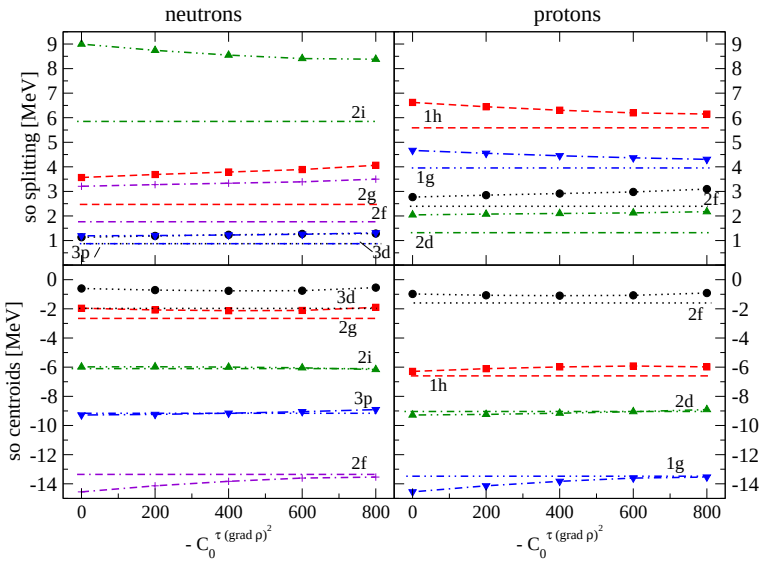

Figure 3.7: Spin orbit splitting and centroids for ^{208}Pb as a function of the coefficient $C_0^{\tau(\nabla\rho)^2}$. The experimental values, drawn with a straight line, are taken from [328].

3.3.1 Pairing properties at $T = 0$

In the following, we study the influence of the correction term (3.19) on the pairing properties at $T = 0$. A realistic calculation for nuclei shall treat consistently the pairing interaction in the particle-particle channel and that in the particle-hole channel. The bare interaction in the particle-particle channel shall then be replaced by the induced one which accounts for a 50% correction [138]. However, for the moment we will not investigate this question. We want, at a simpler level, to clarify the role of the correction term (3.19) on the pairing properties, and we will show that there is indeed a correlation in space between the enhancement of the effective mass and that of the probability distribution of the Cooper pairs.

$C_0^{\tau(\nabla\rho)^2}$		η	
[MeV fm^{10}]	0	0.5	1
0	1.30	1.30	1.30
-200	1.33	1.36	1.47
-400	1.37	1.43	1.62
-600	1.42	1.52	1.79
-800	1.49	1.60	1.96

Table 3.3: Average neutron pairing gap $\tilde{\Delta}_n$ for ^{120}Sn for different values of the coefficient $C_0^{\tau(\nabla\rho)^2}$.

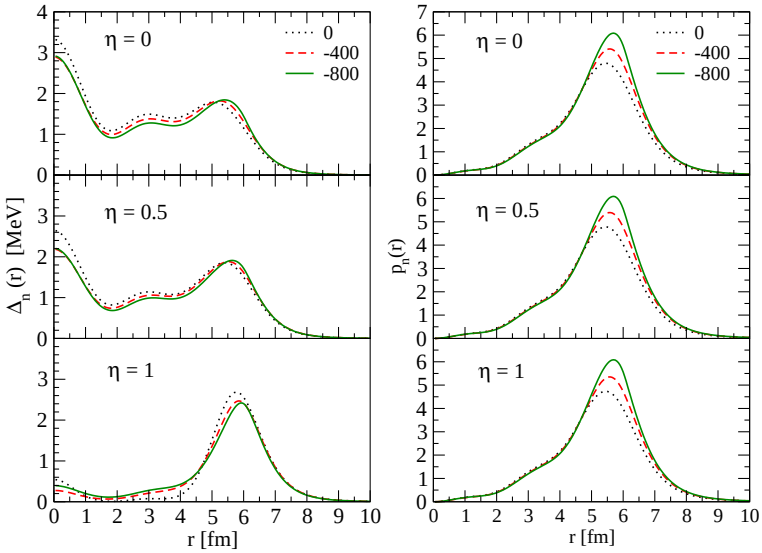

Figure 3.8: Neutron pairing gap (on the left) and probability distribution of the Cooper pairs (on the right) for ^{120}Sn as a function of radial coordinate, for $C_0^{\tau(\nabla\rho)^2} = 0$, -400, -800 MeV fm^{10}, and for different types of pairing interaction (volume, mixed, surface).

In order to reproduce the value of the average gap $\tilde{\Delta}_n = 1.3$ MeV in ^{120}Sn, we have adjusted Eq. (2.40b) for three kinds of pairing interaction (volume, mixed, and surface), for the functional without the correction term (3.19). We obtain for the values (η, v_0): (0; -259 MeV fm^3), (0.5; -391 MeV fm^3), (1; -800 MeV fm^3). In Table 3.3 we report the values for the average neutron pairing gap $\tilde{\Delta}_n$, calculated as the average gap over the abnormal density,

$$\tilde{\Delta}_n \equiv \frac{1}{\tilde{N}} \int d\mathbf{r}\ \tilde{\rho}_n(\mathbf{r}) \Delta_n(\mathbf{r}) \tag{3.36}$$

where $\tilde{N} = \int d\mathbf{r}\ \tilde{\rho}_n(\mathbf{r})$, and for several values of the coefficient $C_0^{\tau(\nabla\rho)^2}$. In Table 3.3, it is shown that the effect of the correction term (3.19) on the pairing gap is non-negligible. The pairing gap is increased by 200 to 700 keV as the coefficient $|C_0^{\tau(\nabla\rho)^2}|$ gets larger. A large dependence with respect to the kind of the pairing interaction (volume, mixed, surface) is also observed. The largest effect of the correction term (3.19) is obtained for the surface pairing gap. From the results presented in Table 3.3 we notice that the correction term (3.19) in the functional has an important influence on the average pairing gap.

In order to study the effect of the correction term on the pairing properties in a more realistic case, we have chosen to renormalize the pairing interaction, for each value of the coefficient $C_0^{\tau(\nabla\rho)^2}$, in such a way to get always at zero temperature $\tilde{\Delta}_n = 1.3$ MeV. We obtain, at $T = 0$, for $C_0^{\tau(\nabla\rho)^2} = -400$ MeV fm^{10}, the values (η, v_0): (0; -248 MeV fm^3), (0.5; -362 MeV fm^3), (1; -670 MeV fm^3), and, for $C_0^{\tau(\nabla\rho)^2} = -800$ MeV fm^{10}, the values (η, v_0): (0; -235 MeV fm^3), (0.5; -337 MeV fm^3), (1; -593 MeV fm^3). We represent in Fig. 3.8 the pairing field and the probability distribution of Cooper-pairs defined as

$$p(r) = -4\pi r^2 \tilde{\rho}(r)\ , \tag{3.37}$$

versus the radial coordinate for different values of the parameter $C_0^{\tau(\nabla\rho)^2}$. On the left panel, we display the pairing field profiles, which do not change very much with the coefficient $C_0^{\tau(\nabla\rho)^2}$; this is due to our renormalization procedure, which requires the average pairing gap to be 1.3 MeV. The right panel of Fig. 3.8 clearly shows the correlation in space between the enhancement of the effective mass and that of the probability distribution of the Cooper-pairs, i.e. the enhancement of the probability distribution is located where the effective mass is surface-peaked.

In conclusion, it has been shown in this Section that the effect of the surface-peaked effective mass on the pairing properties is non-negligible. As for approaches where the pairing interaction is empirically adjusted on some nuclei, we absorbed this effect through a renormalization of the pairing interaction. For non empirical approaches where the pairing interaction is not adjusted on nuclei properties but directly to that of the bare $^1S_0$ potential [225, 226, 31, 153, 194], the enhancement of the average pairing gap induced by the surface-peaked effective mass shall be treated consistently with the induced pairing interaction [138].

3.3.2 Pairing properties at finite temperature

The density of states around the Fermi energy shall influence the temperature-related quantities such as the entropy and the specific heat [79], and at the same time the density of states is also affected by the temperature [333, 106, 132]. We explore the effect of the new term on ^{120}Sn in the framework of HF+BCS at finite temperature, using the pairing interaction where the strength has been renormalized at $T = 0$ for each value of the coefficient $C_0^{\tau(\nabla\rho)^2}$. In Fig. 3.9 we show the neutron pairing gap as a function of temperature, for the three different kinds of pairing interaction (volume, mixed, surface). The results on the left are obtained keeping the coefficient $C_0^{\tau(\nabla\rho)^2}$ constant, while, on the right, we plot the results obtained letting $C_0^{\tau(\nabla\rho)^2}$ vary exponentially with temperature, according to the following relation:

$$C_0^{\tau(\nabla\rho)^2}(T) = C_0^{\tau(\nabla\rho)^2} \times e^{-T/T_0}\,, \tag{3.38}$$

with $T_0 = 2$ MeV. The choice of this kind of temperature dependence relies on the work by Donati *et al.* [106], where a study of the ω-mass in the framework of QRPA for temperatures up to some MeV was carried out on some neutron rich nuclei. The variation of m_ω with respect to temperature was parameterized with an exponential profile and the typical scale of the variation of m_ω with temperature was found to be around 2 MeV (see Section 2.3.2 for more details). We want then to see if, modifying the coefficient $C_0^{\tau(\nabla\rho)^2}$ as in Eq. (3.38), we obtain the same decrease of the effective mass as a function of temperature, as in Donati *et al.*[106]. To that extent, as an example case, in Fig. 3.10 (upper panels), the neutron effective mass m^*/m is plotted, as a function of r for different temperatures, for ^{120}Sn, in the case of $C_0^{\tau(\nabla\rho)^2} = -800$ MeV fm^{10}, and for a pure surface (left panels) or volume (right panels) pairing interaction. One can clearly see the decrease of the effective mass with T at the surface. To estimate if the reduction of m^* at the surface is really exponential as expected from the variation of the coefficient $C_0^{\tau(\nabla\rho)^2}(T)$ (Eq. (3.38)), in Fig. 3.10 (lower panels), the values of the peak of the effective mass as a

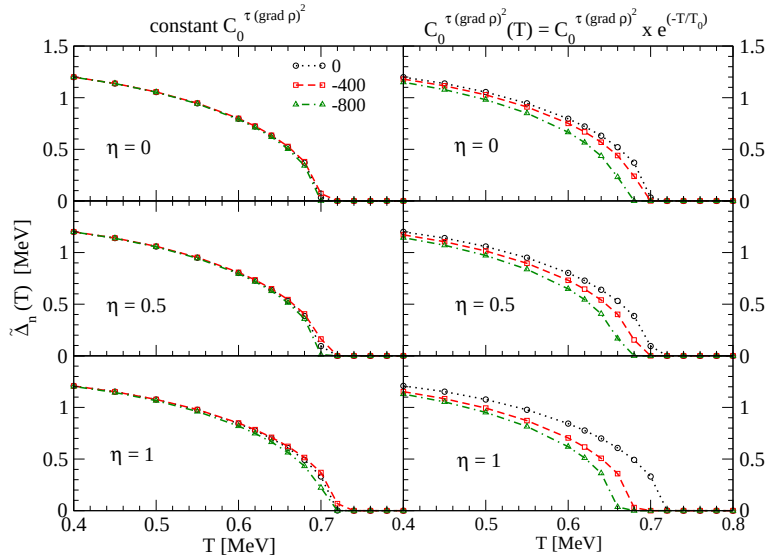

Figure 3.9: Neutron pairing gap for ^{120}Sn as a function of temperature for different values of the coefficient $C_0^{\tau(\nabla\rho)^2}$ and for different types of pairing interaction (volume, mixed, surface). The results on the left are obtained keeping $C_0^{\tau(\nabla\rho)^2}$ constant ($C_0^{\tau(\nabla\rho)^2}$ = 0, -400, -800 MeV fm^{10}), while the results on the right are obtained using for $C_0^{\tau(\nabla\rho)^2}$ the prescription in Eq. (3.38).

function of temperature are displayed, together with an exponential fit of the form:

$$\frac{m^*(T)}{m} = a + b\, e^{-T/T_0} \ , \tag{3.39}$$

which seems to well reproduce the calculations. The parameters $a = 0.94$, $b = 0.25$, $T_0 = 1$ MeV result from the fit procedure. The value of a and b are very close to the ones in the parameterization by Donati *et al.*(i.e. $a = 1$ and $b = m_\omega(T = 0) - 1$); the temperature scale (T_0) is 1 MeV, which is lower that the 2 MeV supposed in Eq. (3.38). However, the shown results are limited to the case of neutrons in ^{120}Sn, and the points are taken in correspondence of the peak of the effective mass, while one would expect a smoother decrease of the effective mass (i.e. a higher value of the scale T_0) if a state-average value of m^* is considered. Moreover, the EDF framework adopted is different from the approach employed in Ref. [106] (for example, in this case we calculate the total effective mass m^*, while in the case of Donati *et al.*only the variations of m_ω were taken into account). Notice that in semi-infinite nuclear matter, the typical scale was found to be 1.1 MeV [132]; the reduction of the scale might be due to the semi-infinite model which is still far from a realistic finite nucleus case.

We observe in all cases in Fig. 3.9 the typical behaviour associated to the existence of a critical temperature T_c after which pairing correlations are destroyed [137]. In particular, as expected, T_c is not modified by the new term for the case of constant coefficient, since we absorbed the effect of the new term through the renormalization procedure. Instead, the effect of a temperature dependent coefficient $C_0^{\tau(\nabla\rho)^2}(T)$ is to reduce the critical temperature; indeed, the chosen dependence (3.38) shifts the critical temperature of ~ 40 keV in the case of volume interaction and of ~ 60 keV in the case of surface interaction. The

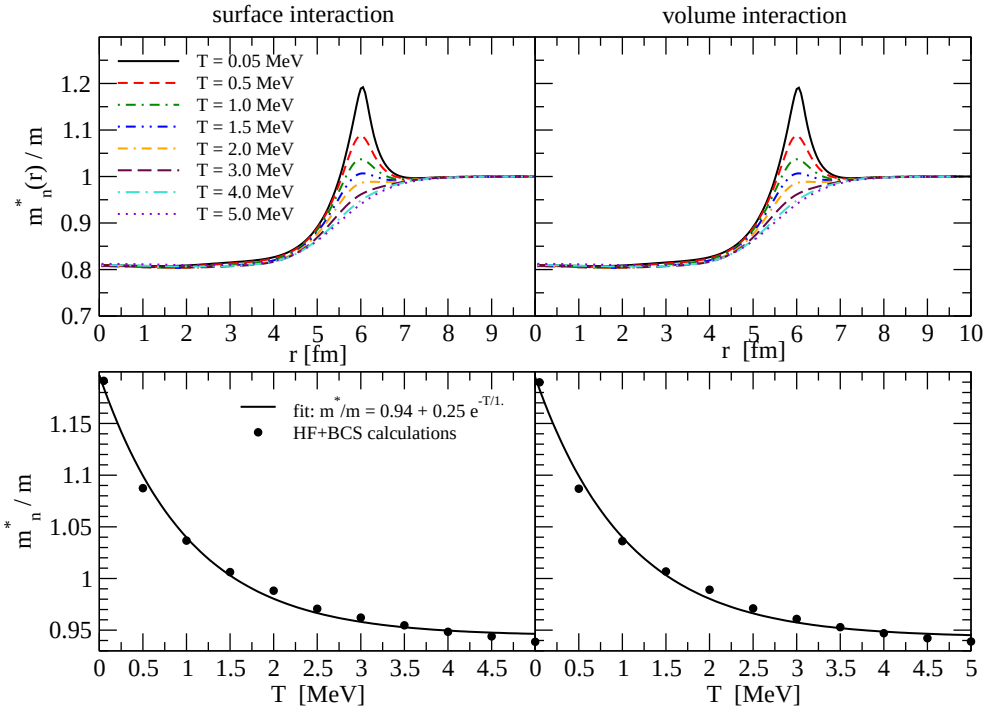

Figure 3.10: Neutron effective mass in ^{120}Sn as a function of radius for different temperatures (upper panels), and peak of neutron effective mass as a function of temperature together with an exponential fit (lower panels), for $C_0^{\tau(\nabla\rho)^2} = -800$ MeV fm^{10}. On the left (right) the results for a pure surface (volume) interaction are displayed.

relation $T_c \simeq \tilde{\Delta}_n(T=0)/2$ is still verified; more precisely, the ratio $T_c/\tilde{\Delta}_n(T=0)$ is $\simeq 0.55$ (for volume interaction) and $\simeq 0.57$ (for surface interaction) for the case of T-independent $C_0^{\tau(\nabla\rho)^2}$, while with the T-dependent prescription (3.38) it varies from $\simeq 0.55$ (for volume interaction) to $\simeq 0.51$ (for surface interaction). In conclusion, we remark that through its temperature dependence, the surface-peaked effective mass has an effect on the critical temperature, that could also be extracted experimentally [144, 292]. This perspective motivates the application of the present work to realistic cases at finite temperature.

Finally, in Fig. 3.11 we show the total entropy and specific heat as a function of temperature for volume and surface interaction, and for three values of $C_0^{\tau(\nabla\rho)^2}$ (0, -800 MeV fm^{10}, and $C_0^{\tau(\nabla\rho)^2}(T)$ for the case -800 MeV fm^{10}). The entropy of the system is calculated as: $S_{tot} = S_n + S_p$, being:

$$S_q = -k_B \sum_\lambda \left[f_{\lambda,q} \ln(f_{\lambda,q}) + (1 - f_{\lambda,q}) \ln(1 - f_{\lambda,q}) \right] , \tag{3.40}$$

where $f_{\lambda,q}$ is defined as in Eq. (3.33). The specific heat is then defined as:

$$C_V = T \frac{\partial S_{tot}}{\partial T} . \tag{3.41}$$

We observe the change of the slope in the entropy curve, which causes the discontinuity in the specific heat in correspondence of the critical temperature. In agreement with the pre-

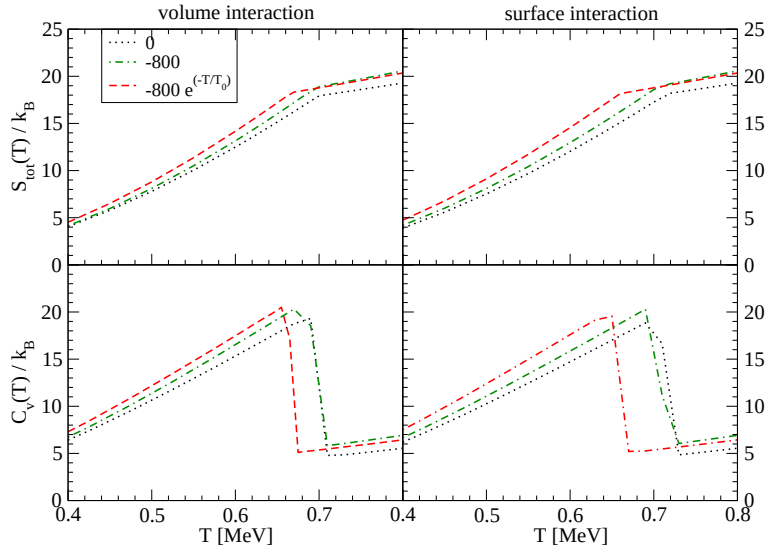

Figure 3.11: Total entropy, S_{tot}, and specific heat, C_V (in units of the Boltzmann constant), for ^{120}Sn as a function of temperature, for $C_0^{\tau(\nabla\rho)^2} = 0$, -800 MeV fm^{10}, -800 e^{-T/T_0} MeV fm^{10}, and for volume (on the left) and surface (on the right) pairing interaction.

vious results, T_c is shown to be modified by a temperature-dependent $C_0^{\tau(\nabla\rho)^2}$, the effect is stronger in the case of surface interaction, and the temperature dependent coefficient acts as to reduce T_c.

3.4 Conclusions and Outlooks

We have studied the influence of the correction term (3.19) on various nuclear properties. The isoscalar correction term (3.19) has been shown to produce a surface-peaked effective mass in the nuclei under study (^{40}Ca and ^{208}Pb), without modifying significantly the mean field profiles. The increase of m^*/m at the surface is up to about 1.2 - 1.3 for the maximum value of the strength of the correction we used. As the effective mass gets enhanced at the surface of nuclei, the density of states increases. Then, we have studied the impact of such a term on the neutron pairing gap in the semi-magic nucleus ^{120}Sn, within an HF+BCS framework, and it turned out that its effect is non-negligible; if the pairing interaction is not renormalized consistently with the new term, the average gap increases from 200 keV to 700 keV under variation of the strength of the correction term and depending on the volume/surface character of the interaction. In a recent work [13], it has been stressed that the surface enhancement of the pairing field induced by the PVC might also play a role on the size of the Cooper-pairs at the surface of nuclei. In uniform matter, the coherence length is indeed inversely proportional to the pairing gap. The surface enhancement of the pairing field could then make the Cooper-pairs smaller at the surface of nuclei.
Finally, we have explored some finite temperature properties in ^{120}Sn, within a HF+BCS framework at finite temperature. We observed for the neutron pairing gap that the critical temperature at which pairing correlations vanish is shifted if a T-dependence in the new

coefficient is considered. As a consequence, the entropy and specific heat profiles are affected by the introduction of the new term.

In the future, we shall go on with a global refitting of all the parameters of the functional, including the new correction term (3.19). We expect to reproduce the deviation between the experimental and theoretical masses and single-particle levels.

Part II
Astrophysical models

Chapter 4

Introduction - Supernova simulations

In this Part of the thesis I will describe the astrophysical models we use to investigate specific microphysics inputs in core-collapse SN. We perform the analysis by means of one-dimensional hydrodynamical codes, which are easier to handle, faster to run and can well reproduce core-collapse phase before core bounce and the propagation of the shock wave when multi-dimensional effects come into play.

As already depicted in the Introduction, supernovae simulations are a challenging task. However, since analytical models cannot reproduce all the complex details of the SN mechanism, most of our current understanding of the picture relies on numerical simulations, both Newtonian and Relativistic. A full GR simulation, with sophisticated microphysics and implemented in multi-dimensions, is not yet available, but is in development in several groups. Codes with detailed microphysics and neutrino transport usually rely on Newtonian gravity or are implemented in spherical symmetry; while multi-dimensional GR codes are often computed with a rather crude approximation for the microphysics. The full hydrodynamical GR in three-dimensions is already implemented (e.g. in the CoCoNuT code [359], where a refined microphysics and the inclusion of neutrino treatment is underway), and sophisticated microphysics in one-dimensional full GR code is present e.g. in the codes from the Basel group.

Our first attempt to simulate the supernova mechanism has been done by means of a one-zone code, in order to discuss a particular issue related to the temperature dependence of the nuclear symmetry energy and the electron capture during core-collapse. The results of this work, described in Chapter 5, motivated us to perform a more detailed analysis with a one-dimensional code. In Chapter 6 a one-dimensional spherically symmetric Newtonian code with neutrino transport and treatment of electron capture will be presented, and the improvements to this code will be analysed. In Chapter 7, a one-dimensional Relativistic code is described. I have two versions of this code, both based on the same formulation of the hydrodynamical equations: one working with a polytropic equation of state, and one working with the Lattimer and Swesty EoS and which includes a multi-group treatment of neutrinos, but without neutrino transport.

4.1 Numerical schemes

The hydrodynamical equations governing the dynamics of the core collapse (both in Newtonian and in GR) constitute a system of non-linear hyperbolic equations, which can be implemented and solved numerically by replacing the partial derivatives by finite differences on a discrete grid in space and time. Hyperbolic equations describe initial value problems, since the space of relevant solutions depends on the value the solution takes at some initial time. If we consider a quasi-linear partial differential equation of the second-order generally written as:

$$a_{11}\frac{\partial^2 y}{\partial (x^1)^2} + 2a_{12}\frac{\partial^2 y}{\partial x^1 \partial x^2} + a_{22}\frac{\partial^2 y}{\partial (x^2)^2} + f\left(x^1, x^2, y, \frac{\partial y}{\partial x^1}, \frac{\partial y}{\partial x^2}\right) = 0\,, \qquad (4.1)$$

the traditional classification of a partial differential equation is based on the sign of the determinant $\Delta := a_{11}a_{22} - a_{12}^2$. If $\Delta < 0$, Eq. (4.1) is strictly hyperbolic (e.g. wave equation); if $\Delta = 0$, Eq. (4.1) is parabolic (e.g. diffusion equation); if $\Delta > 0$, Eq. (4.1) is elliptic (e.g. Poisson equation) [279]. Hydrodynamical equations behave like Burger equation, i.e. the momentum equation of an isothermal gas in which pressure gradients are neglected: they lead to discontinuous solutions even from smooth initial data. This is the case of core-collapse SN, which are well known to produce shocks.

Finite difference schemes are based on a discretization of the space-time plane with a mesh of discrete points (x_j, t^n), $j = 1, 2, \ldots$, $n = 0, 1, \ldots$. These time-marching procedures permit to obtain approximations to the solution in the mesh points u_j^n from the approximation obtained in the previous time step u_j^{n-1}. Finite difference methods for solving time-dependent flows have been based either on the Lagrangian (fixed mass coordinate) or the Eulerian (fixed space coordinate) form of the equations, either on explicit or implicit scheme for advancing in time (see e.g. [244, 279]).

In the Lagrangian formulation, the independent space variable refers to a coordinate system fixed in the fluid and undergoing the motion of the fluid; particles in the fluid are characterized by their Lagrangian (or *comoving*) variables while their positions in space are dependent quantities one has to solve for. The time variation of the properties of a Lagrangian fluid element is described by the Lagrangian derivative (or *comoving*, or *substantial*, or *fluid-frame* time derivative) $\mathrm{D}/\mathrm{D}t$.
In the Eulerian formulation, the independent space variables refer to a coordinate system fixed in space (i.e. the *laboratory frame*); the fluid moves through this system, and it is identified by a time-dependent velocity field which has to be found by solving the initial value problem. The time and space variation of a property of the fluid is described by the time derivative $\partial/\partial t$, taken at fixed position, and the space derivative $\partial/\partial x^i$, computed at fixed t.
The main reason for the choice of the Lagrangian scheme is that neutrino transport equations can be written and implemented in an easier way in the comoving frame, even if the Eulerian scheme is more convenient if the extension to the multi-dimensional case is foreseen. The relation which links the Lagrangian time derivative of a quantity y to the

derivatives in the Eulerian frame[1]is [280, 244]:

$$\frac{\mathrm{D}y}{\mathrm{D}t} = \frac{\partial y}{\partial t} + (\mathbf{v}\cdot\nabla)y \ . \tag{4.2}$$

For advancing in time, explicit or implicit scheme can be implemented (for a description and analysis of these schemes, see e.g. [279]). If one considers a physical variable $y(t)$ varying according to the differential equation $\mathrm{d}y/\mathrm{d}t = f(y)$, the simplest explicit finite differencing can be written as:

$$\frac{y^n - y^{n-1}}{t^n - t^{n-1}} = f(y^{n-1}) \ . \tag{4.3}$$

where the function f is evaluated at the time $n-1$. Therefore, in the explicit scheme, the quantity we want to solve for, y^n at the time t, is only related to its old value y^{n-1}.
On the other hand, the simplest implicit finite differencing can be written as:

$$\frac{y^n - y^{n-1}}{t^n - t^{n-1}} = f(y^n) \ , \tag{4.4}$$

where the difficulty stands in the fact that the value of the variable y^n depends implicitly on itself through the function f. If $f(y^n)$ is not so different from $f(y^{n-1})$, the two discretization procedures are similar; this happens for small time steps, but for larger time steps the two solutions diverge. Explicit schemes, in fact, give meaningful solutions only if the time step is smaller than a characteristic timescale determined by the function f, as required by the Von Neumann stability analysis [280], while implicit schemes are unconditionally stable and thus can work for large time steps (i.e. relatively few numbers of time steps). However, the price to pay is that, depending on the function f, implicit schemes may require computationally expensive solutions, since an algebraic system of equations needs to be solved (i.e. a matrix inversion procedure is needed). Thus, these algorithms are suitable for systems of moderate size; in hydrodynamical simulations, they are usually employed in one-dimension (in the case of SN simulation, implicit hydrodynamics is used for example in Refs. [306, 350, 200, 203, 309]).

The codes we use work with different schemes: the Newtonian code with neutrino transport developed by P. Blottiau and Ph. Mellor is implemented with finite difference implicit scheme based on the Lagrangian coordinates, while the Relativistic code by the Valencia group is written with finite difference explicit scheme based on the Eulerian form of the equations.

4.1.1 The formulation of hydrodynamical equations in Newtonian and GR frameworks

The fluid hydrodynamical equations governing the dynamics of the core collapse are the continuity equation, the Euler equation of motion (i.e. the momentum equation), and

[1]In the following, if both frames are used at the same time, the superscript "LF", "0" or "FRF" will refer to the Lagrangian or comoving or fluid rest frame, while the subscript "EF" or "Lab" will refer to the Eulerian or lab frame or coordinate frame.

the energy equation. I report here the main equations; then I will detail how we deal with the different frameworks (Eulerian/Lagrangian, Newtonian/Relativistic) in the following Chapters.

In the Lagrangian formulation, the system of conservation equations, for an ideal fluid in Newtonian hydrodynamics, can be written as (see e.g. [280, 244]):

$$\frac{\mathrm{D}\rho}{\mathrm{D}t} + \rho\,(\nabla\cdot\mathbf{v}) = 0 \qquad \text{the continuity equation} \tag{4.5a}$$

$$\rho\,\frac{\mathrm{D}\mathbf{v}}{\mathrm{D}t} + \nabla P = \rho\,\mathbf{g} \qquad \text{the Euler equation} \tag{4.5b}$$

$$\rho\,\frac{\mathrm{D}\left(\epsilon+\frac{1}{2}v^2\right)}{\mathrm{D}t} + \nabla\cdot(P\,\mathbf{v}) = \rho\,\mathbf{g}\cdot\mathbf{v} \qquad \text{the energy equation ,} \tag{4.5c}$$

where $|\mathbf{g}| = -\frac{GM}{r^2}$ is the gravity acceleration, $\rho = \rho_b$ is the baryon density, P the pressure and ϵ the internal energy. The continuity equation comes from the conservation of mass for the fluid in the volume V [244]:

$$\frac{\mathrm{D}}{\mathrm{D}t}\int_V \rho\,\mathrm{d}V = 0\,. \tag{4.6}$$

By means of the Reynolds theorem[2]:

$$\int_V \left[\frac{\mathrm{D}\rho}{\mathrm{D}t} + \rho(\nabla\cdot\mathbf{v})\right]\mathrm{d}V = 0\,, \tag{4.9}$$

and thus Eq. (4.5a). The Euler equation, Eq. (4.5b), comes from the principle of momentum conservation which states that the time rate of change of the momentum associated with the material element equals the total force acting on it (the gravity $\mathbf{g}$ in this case). The energy equation, Eq. (4.5c), is obtained from the conservation of the *total* energy. It is a restatement of the first law of thermodynamics; in fact, subtracting the mechanical energy equation $\rho\mathbf{v}\cdot\mathrm{D}\mathbf{v}/\mathrm{D}t$ (i.e. $\mathbf{v}$ times Eq. (4.5b)), and using the continuity equation, Eq. (4.5c) becomes:

$$\frac{\mathrm{D}\epsilon}{\mathrm{D}t} + P\frac{\mathrm{D}(1/\rho)}{\mathrm{D}t} = T\frac{\mathrm{D}s}{\mathrm{D}t}\,, \tag{4.10}$$

in the case $\mathrm{D}s/\mathrm{D}t = 0$, i.e. the flow of an ideal fluid must be adiabatic. However, there can be an increase in entropy across a discontinuity, i.e. shock. This can be interpreted consistently from a physical point of view admitting the possibility of dissipative processes in the fluid.

[2]The Reynolds theorem [244] states that, being F a scalar, vector or tensor field such as:

$$\mathcal{F}(t) = \int_V F(\mathbf{x},t)\,\mathrm{d}V\,, \tag{4.7}$$

then the fluid-frame time derivative of $\mathcal{F}$ is:

$$\frac{\mathrm{D}\mathcal{F}}{\mathrm{D}t} = \int_V \left[\frac{\mathrm{D}F}{\mathrm{D}t} + F(\nabla\cdot\mathbf{v})\right]\mathrm{d}V\,. \tag{4.8}$$

In the Eulerian coordinates, in spherical symmetry, the system (4.5) reads:

$$\frac{\partial \rho}{\partial t} + \frac{1}{r^2}\frac{\partial (r^2\, \rho\, v)}{\partial r} = 0 \tag{4.11a}$$

$$\frac{\partial v}{\partial t} + v\frac{\partial v}{\partial r} + \frac{1}{\rho}\frac{\partial P}{\partial r} = -\frac{GM}{r^2} \tag{4.11b}$$

$$\frac{\partial \left(\rho\epsilon + \frac{1}{2}\rho v^2\right)}{\partial t} + \frac{1}{r^2}\frac{\partial \left[r^2\left(\epsilon + \frac{1}{2}v^2 + \frac{P}{\rho}\right)\rho\, v\right]}{\partial r} = -\rho\,\frac{GM}{r^2}\, v\ . \tag{4.11c}$$

In GR, different formulations have been proposed. In the 60's May and White [233, 234] have worked out a first Lagrangian formulation which has been implemented in their pioneering one-dimensional code. A first Eulerian multi-dimensional formulation has been introduced by Wilson [339, 341] (for a review see e.g. Refs [118, 120]).
In 1991, Martí, Ibáñez, and Miralles [229] proposed a new formulation of the Eulerian GR equations, in order to exploit the conservative nature of the equations, which allows to avoid the use artificial viscosity in treating discontinuous solutions (see next Section). Indeed, the system of conservation laws (Eqs. (4.5)) can be written as:

$$\frac{\partial \mathbf{U}}{\partial t} + \nabla \cdot \mathbf{F}(\mathbf{U}) = \mathbf{S}(\mathbf{U})\ , \tag{4.12}$$

where $\mathbf{U}(\mathbf{x}, t)$ is the vector of the *conserved* quantities which depends on the spatial and time coordinate $(\mathbf{x}, t)$; $\mathbf{F}$ is the conserved flux, since in the integral formulation of Eq. (4.12) the time variation of the integral of $\mathbf{U}$ over a volume V is given by the net flux of $\mathbf{U}$ across the surface enclosing V. The right-hand side of Eq. (4.12), the source term $\mathbf{S}$, contains the source/sink of the vector $\mathbf{U}$. In this framework, the hyperbolic system of the conservation equations in GR can be written as [14, 118]:

$$\frac{1}{\sqrt{-g}}\left[\left(\frac{\partial(\sqrt{\gamma}\,\mathbf{U})}{\partial t} + \frac{\partial(\sqrt{-g}\,\mathbf{F})}{\partial x^i}\right)\right] = \mathbf{S}\ , \tag{4.13}$$

where: $g := \det(g_{\mu\nu})$ and $\gamma := \det(\gamma_{ij})$ (the metric tensors). In the spherically symmetric case:

$$\frac{1}{\sqrt{-g}}\left[\left(\frac{\partial(\sqrt{\gamma}\,\mathbf{U})}{\partial t} + \frac{1}{r^2}\frac{\partial(\sqrt{-g}\,r^2\,\mathbf{F})}{\partial r}\right)\right] = \mathbf{S}\ . \tag{4.14}$$

In Chapter 7 we use the same notation as in Romero *et al.*[285]. The equations are equivalent to the Valencia formulation ones presented in Banyuls *et al.*[14] (see e.g. Appendix A in Ref. [258] for a proof).

4.1.2 Shock treatment: Artificial viscosity vs High Resolution Shock Capturing scheme

Fluid flows often face with internal discontinuities, i.e. shocks. The correct modelling of the shock is one of the main issue involved in SN simulations. As a consequence, standard finite-difference schemes have been modified to get a high-order accuracy and a proper treatment of discontinuities. From the numerical point of view, two different techniques have been employed in treating shocks: the *shock tracking* and *shock capturing*

methods.
Historically, the shock tracking has been widely used in the literature, either first order accurate (e.g. Lax method), or second order accurate; these methods are generally not very accurate around shock and introduce spurious oscillations [279]. In order to avoid oscillations near discontinuities the hydrodynamical equations have been modified introducing an *artificial viscosity*, i.e. a dissipative term which can smooth shock transition and spread it into a finite number of cells of the grid. The introduction of this term changes the equation of motion and the energy equation (Eqs. (4.5b)-(4.5c)) in such a way that $P \rightarrow P + Q$, where Q is the so-called artificial viscosity (or pseudoviscosity). The idea was first suggested by Von Neumann [280]; it has the advantage to be easy to implement, not too much computational expensive and efficient (tuning the parameter governing the expression for the artificial viscosity Q one can spread the shock into a small number of zones). Von Neumann and Richtmyer originally proposed the following prescription for the viscous term [280]:

$$Q = \begin{cases} -\rho(k\Delta x)^2 \left(\frac{\partial v}{\partial x}\right)^2 & \left(\frac{\partial v}{\partial x} < 0 \text{ or } \frac{\partial \rho}{\partial t} > 0\right) \\ 0 & (\text{otherwise}) \end{cases} , \tag{4.15}$$

where v is the fluid velocity, ρ the density, Δx the spatial interval and k a constant but adjustable parameter which controls the number of zones in which the shock wave is spread. Since then, different expressions for the viscosity term have been applied (see e.g. [280, 316, 256]); for example, in Ref. [256] the artificial viscosity in the Lagrangian frame has been defined as:

$$Q_L = \begin{cases} c_0^2 l^2 \rho \left(\frac{\partial v}{\partial x}\right)^2 - c_1 \rho c_s l \frac{\partial v}{\partial x} & \left(\frac{\partial v}{\partial x} < 0\right) \\ 0 & (\text{otherwise}) \end{cases} , \tag{4.16}$$

where c_0, c_1 are dimensionless constants, l is related to the shock width and c_s is the speed of sound. Both the proposed expressions for the artificial viscosity have the following properties: *(i)* they come into play only when gas is compressed ($\partial v/\partial x < 0$), which is a prerequisite and a characteristic property of shock formation; *(ii)* is very small in regions far from the shock (velocity gradients are big only across shocks).

However, it is not straightforward to make the right choice for Q, since it has to be chosen in such a way to account for the necessary dissipation in order to prevent spurious oscillations, but at the same time it has to be efficient only at shock front, without altering too much the hydrodynamical equations. Moreover, this technique suffers of some drawbacks, such as excess Q heating, or errors in propagating shock over non-uniform mesh or in spherical geometry, as pointed out by Noh [256], who concluded in his paper that these errors are not attributable to any particular finite-difference method but rather intrinsic to the artificial viscosity method itself.

Although refined Q methods, including an artificial heat flux which can minimize the excess Q heating, together with adaptive mesh technique, can improve the treatment of the shock, the shock capturing methods (also known as Godunov-type methods [134]), which are designed for a non-linear hyperbolic system of conservation laws and which avoid the use of the artificial viscosity, have been more and more used. In these kind of approaches, it is convenient to write the homogeneous system of hyperbolic equations in the conservative form:

$$\frac{\partial \mathbf{U}}{\partial t} + \frac{\partial \mathbf{F}(\mathbf{U})}{\partial x^i} = 0 , \tag{4.17}$$

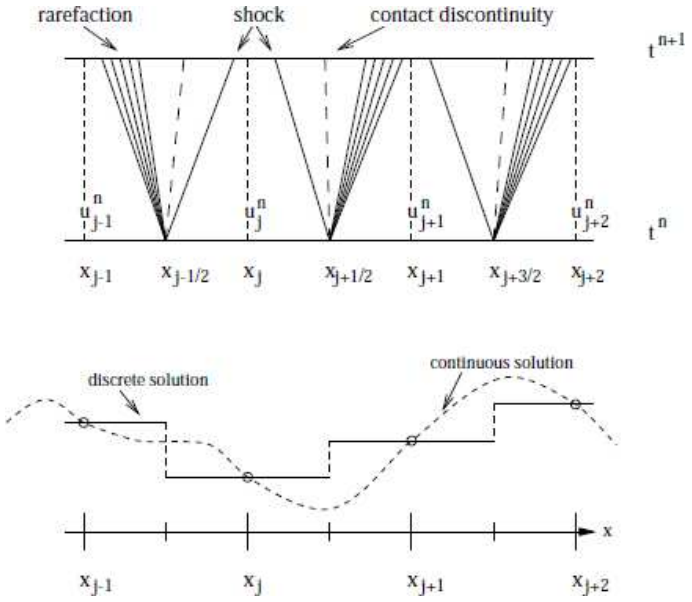

Figure 4.1: Godunov scheme. In the bottom panel, a Riemann problem is constructed as a consequence of the discretization procedure ($u_j^n \equiv U_j^n$, the state vector at x_j and t^n). In the top panel, at t^n, the discontinuities decay into three elementary waves: shock wave, rarefaction wave and contact discontinuity (from [118]).

which satisfies the initial value problem $\mathbf{U}(\mathbf{x}, t = 0) = \mathbf{U}_0(\mathbf{x})$, being $\mathbf{U}(\mathbf{x}, t)$ the state vector and $\mathbf{F}(\mathbf{U})$ the flux. An initial value problem with discontinuous data:

$$\mathbf{U}_0(x) = \begin{cases} \mathbf{U}_0^L & (x < 0) \\ \mathbf{U}_0^R & (x > 0) \end{cases} , \tag{4.18}$$

where the superscript L (R) stands for "left" ("right") with respect to the interface, is a Riemann problem. In any numerical finite volume scheme, a continuous function is represented as a series of piecewise constant on the grid with discontinuities at the cell interfaces (see Fig. 4.1, bottom panel). Godunov [134] pointed out that each discontinuity at cell interface can be seen as a local Riemann problem [118]; so the global solution to the conservation equations is a series of solutions to the local Riemann problem at the interfaces. Each discontinuity decays into three waves which propagate the solution to the next time step: a shock wave, propagating forward, where all the variables related to the state $\mathbf{U}$ are discontinuous, a contact discontinuity, which carries a jump in density, and a rarefaction wave, propagating backward, where all the variables are continuous (Fig. 4.1).

The analytical solution of the complete Riemann problem is computationally expensive, so often linearized approximate Riemann solvers are employed. Some of these methods, such as the Roe's one [284] which is adopted in the Relativistic code, require the knowledge of the characteristic speeds and fields (see also Chapter 7).
The Lax Wendroff theorem states that if flux conservative schemes have a solution, they converge to the so-called *weak solution* of the original system of equations [280]. The weak solutions are the generalized solutions (i.e. the solutions of the integral form of the flux conservative formulation) with a finite number of discontinuities ([118, 120] and Refs. therein). They differ from the *classical solutions*, which are the continuous and

differentiable solutions satisfying the initial value problem.
It is then useful to write Eq. (4.17) in the form:

$$\frac{\partial \mathbf{U}}{\partial t} + \mathcal{B}(\mathbf{U})\frac{\partial \mathbf{U}}{\partial x^i} = 0 \ , \tag{4.19}$$

where $\mathcal{B}$ is the Jacobian matrix:

$$\mathcal{B}(\mathbf{U}) = \frac{\partial \mathbf{F}(\mathbf{U})}{\partial \mathbf{U}} \ . \tag{4.20}$$

In this way the equations are casted into a set of linear equations for the characteristic variables $\mathbf{w}$ ($\mathbf{U} = R\,\mathbf{w}$) of the form (see e.g. [121, 279]):

$$\frac{\partial \mathbf{w}}{\partial t} + \Lambda(\mathbf{U})\frac{\partial \mathbf{w}}{\partial x^i} = 0 \ , \tag{4.21}$$

being Λ the diagonal matrix of the eigenvalues λ_α, related to $\mathcal{B}$ through:

$$\mathcal{B} = R\,\Lambda\,R^{-1} \ , \tag{4.22}$$

where R is the matrix of the right eigenvectors. The system is (strictly) hyperbolic if the eigenvalues are (distinct and) real. In other words, there exist characteristic directions along which $\mathbf{w}$ are conserved:

$$\mathbf{w}_\alpha(\mathbf{x}, t) = \mathbf{w}_\alpha(\mathbf{x} - \lambda_\alpha t, 0) \ , \tag{4.23}$$

and the solutions of the Eq. (4.17) are:

$$\mathbf{U}(\mathbf{x}, t) = \sum_\alpha \mathbf{w}_\alpha(\mathbf{x} - \lambda_\alpha t, 0)\,\mathbf{r}_\alpha \ , \tag{4.24}$$

being $\mathbf{r}_\alpha$ the right eigenvectors of $\mathcal{B}$. Therefore, once the solution at $t = 0$ and the set of eigenvectors are given, the solution $\mathbf{U}$ is known in the spacetime $(\mathbf{x}, t)$.

In Roe's approach, each component of the flux vector at the interface $j+1/2$ is written as [284, 285]:

$$\hat{F}_{j+1/2} = \frac{1}{2}\left\{ F(\mathbf{U}^L_{j+1/2}) + F(\mathbf{U}^R_{j+1/2}) - \sum_{\alpha=0,\pm} |\lambda_\alpha| \Delta w_\alpha \mathbf{r}_\alpha \right\} \ , \tag{4.25}$$

where Δw_α are the jumps in the local characteristic variables across the cell interface, λ_α and $\mathbf{r}_\alpha$ are the eigenvalues and the component of the right eigenvector of the Jacobian matrix. The first two terms come from the finite difference framework and the last term in the Eq. (4.25) comes from the free evolution of the solution along the three waves (shock, rarefaction, discontinuity waves) and represents the numerical viscosity of the scheme, which is no more introduced *ad hoc* to smooth the shock profile as in the artificial viscosity scheme, but it comes out naturally when writing the hydrodynamical equations in an eigensystem structure.
To get the values of the quantities at the cell interface a reconstruction procedure has to be adopted. Among the different cell-reconstruction procedures, we will use in Chapter 7 the slope-limiter one.

In the models presented in this thesis, for the Newtonian code a shock tracking with artificial viscosity is implemented, while the Relativistic code from the Valencia group relies on the shock capturing scheme.

4.2 Role of neutrino transport in CCSN simulations

The treatment of neutrinos and neutrino transport are among the most difficult tasks in a CCSN simulation, and require a huge amount of computational time. One of the problems related to the implementation of neutrino transport is that the transport and hydrodynamical timescales differ, so the time step of the simulation must be chosen carefully. The correct treatment of neutrino physics is undoubtedly very important all along the simulation: prior to trapping and bounce, the lepton number determines the position of the formation of the shock wave; then, after the shock, $\approx 10^{51}$ erg are released at neutrino outburst; finally, the amount of energy absorbed in the heating region, which is decisive for the success of the delayed mechanism, is sensitively related to the local neutrino distribution (indeed, the neutrino absorption cross section strongly depends on the neutrino energy).

In the one-zone approach described in Chapter 5, a treatment of neutrino transport is impossible. The zero-dimensional (sphere of uniform density) model cannot contain any gradients which are needed for transport or diffusion equations.
In the one-dimensional Newtonian code described in Chapter 6, instead, the neutrino transport is included in the multi-group flux-limited diffusion approximation. In the one-dimensional Relativistic code described in Chapter 7, even if no transport is implemented, the equation for the neutrino evolution is already written in a multi-group form, which is well suited for a subsequent inclusion of the transport equations and accounts already reasonably well for the presence of neutrinos in dense matter.

4.2.1 Methods for neutrino transport - brief overview

Due to the difficulty in modelling and implementing neutrino transport, and since the resolution of the full Boltzmann equation for transport is computationally very expensive, different approximations have been used in numerical simulations.

One of the simplest methods is the *leakage scheme*, which considers neutrinos as sinks of energy, momentum and lepton number (see e.g. Ref. [57] for a comparison of these methods to the multi-flux multi-group schemes). The neutrinos are treated in two limit conditions: either they escape freely, and thus are just a sink, or they are trapped and in equilibrium with matter. Therefore, no transport is calculated (see e.g. [162, 326, 160, 161], or the review by Cooperstein [91]).

A better description of neutrino transport could be implemented through diffusion methods. The common idea is that neutrinos, interacting with matter, have a mean free path smaller than the typical length scale of the system; this lets the hydrodynamical part and neutrino transport decouple one from each other. As a consequence, the local distribution of neutrinos can be assumed to be not so far from isotropy and a diffusion equation can be used to treat the transport problem. However, this approximation cannot deal with the limit case of free streaming particles and, in optically thin regions (i.e. region quasi-transparent to neutrinos), this treatment gives supraluminal speeds for energy transport. To avoid this problem, the *flux limited* approach [193], which employs an interpolation for the energy flux between the optically thin and optically thick region (i.e. regions quasi-opaque to neutrinos), can be used. Although this scheme reproduces the correct limits, the choice of the interpolation in the in-between regime is quite arbitrary (examples are

given in Chapter 6 and in Appendix G). Among the methods which apply the flux limiting scheme, there is the *multi(energy)-group flux-limited diffusion* scheme (MGFLD), extensively described by Bruenn [56]. It treats the energy dependent transport in diffusion approximation casting the neutrino energies in bins (typically $\sim$20, from few MeV to hundreds MeV). This model is employed in the Newtonian code described in Chapter 6.

In principle, one must also take into account the angular dependence of the neutrino distribution function. However, unlike the spherically symmetric case where neutrino transport has been treated with high accuracy, multi-dimensional neutrino transport has not yet been faced in the full complexity. One of the employed techniques is the 2D *ray-by-ray* approximation [61, 64], which consists to assume the neutrino distribution function to be axially symmetric in the radial direction, i.e. one solves several 1D problems in angular wedge with periodic boundary conditions. The ray-by-ray approach (including some GR corrections) is used for example by the MPA-Garching group (in the PROMETHEUS-VERTEX code), and by the Oak-Ridge-Florida group (in their CHIMERA code), together with a 2D effective GR gravitational potential for solving the hydrodynamics. A 2D multi-angle, multi-group transport, where the 2D Boltzmann equation is discretized and simplified without GR correction, in a MGFLD approximation, is instead employed by the Princeton-Tucson group, again with a 2D effective GR gravitational potential for the treatment of the hydrodynamics (in the VULCAN code).
Other approximations are present in the literature; for example in Refs. [209, 205] the authors neglect the energy redistribution of the neutrino energy in phase space.
Solutions of the Boltzmann equation are also provided within *Monte Carlo* methods, which calculate the neutrino distribution function by a statistical approach (see e.g. [317]). However, in order to construct an accurate distribution function, a quite large amount of sample particles has to be followed, which makes the computation time consuming. A comparison between the flux-limited and the Monte Carlo transport is given in Ref. [171]. A solution of the Boltzmann equation is also presented by Mellor [236] and Mellor *et al.* [237].

4.3 Presupernova models

Presupernova models are the required inputs of CCSN simulations. A first approximation of presupernova model is constituted by a $4/3$ polytrope, where the pressure of the system is only density dependent. This is enough to have a hydrodynamical collapse and bounce and it is often used as a test case, but, since one has no information on the composition of the system, no refined microphysics can be computed.

However, more realistic simulations require to start from a presupernova profile which is the end product of stellar evolution calculations. To-date available progenitor models[3]are computed by means of Newtonian spherically symmetric codes which follow the star life from hydrogen burning on the main sequence up to the onset of core collapse [336, 257, 348, 82, 155, 345, 207, 156, 208]. Recent models were also computed including rotation and magnetic field [164, 156]. In our simulations, we will consider non-rotating supernova progenitors.

[3]Many presupernova models in text format are directly available on the authors' websites; a collection of these models can also be found at the website: http://stellarcollapse.org.

Even if the importance of the Relativistic effects in a CCSN simulation has been pointed out, the initial profiles calculated using Newtonian hydrodynamics are a good approximation. Indeed, the initial pre-collapsing core is Newtonian since the M/R ratio[4]is $M/R \sim 10^{-3}$, and the initial infall velocities are of the order of $10^{-3}c$.

Most of the presupernova models already have a negative velocity field, as it should be at the beginning of the collapse; thus, giving the presupernova as input of the simulation, and implementing a deleptonization process, which helps to reduce the pressure in the system, nothing artificial should be done to initiate the collapse.
However, to match the presupernova profile into the CCSN simulation, one has to recompute the pressure (or temperature) profile consistently with the EoS employed in the simulation, keeping the density and the electron fraction fixed. The match of the given profiles (density, pressure, etc) with the computational grid is done interpolating (linear or spline[5]) the initial data.

To give an insight of the differences among presupernova profiles, the density, electron fraction, temperature and pressure profiles are plotted in Fig. 4.2 as a function of radius. Two sets of different presupernova models of solar metallicity[6]are displayed: one from Woosley and Heger (thick lines, labelled by "sXX", being XX the star ZAMS mass, i.e. the mass of the star lying on the main sequence before mass losses which can occur during the giant phase), and one from Limongi and Chieffi (thin lines, labelled by "m0XX", being XX the star ZAMS mass). The discontinuities exhibited in the curves correspond to the change in the structure, e.g. the onset of a different burning shell. The iron core is usually defined by the steep change in the Y_e profile from $Y_e \sim 0.48$ to $Y_e \sim 0.5$. In Table 4.1 I summarize the main properties of the presupernova profiles shown in Fig. 4.2. Roughly speaking, the Limongi and Chieffi models predict less massive, less extended and more symmetric iron cores, with lower central densities. Moreover, in the Limongi and Chieffi models we observe a monotonicity in the results. Differences could arise from the different input physics adopted; for example, in the case of Limongi *et al.*calculations, the nuclear network is fully coupled to the equations describing the physical structure of the star, so that both the physical and chemical evolutions due to the nuclear reactions are solved simultaneously, while in the case of Heger calculations, the structure and chemical evolution of the star are solved separately [206]. One of the main differences between the two groups is that the Limongi and Chieffi profiles do not have an initial velocity field. Even if the different groups computing presupernova progenitors have an overall agreement on the presupernova conditions (*core convergence*), uncertainties are still present in the models, for example regarding mass loss during blue and red supergiant phases, treatment of convection, role of rotation, nuclear cross sections and computation of nuclear energy generation (size of nuclear network, NSE/QSE approximations), weak interactions rates (which determine the Y_e profile) [206].

[4]The "M/R ratio" is expressed in the geometric units (see Appendix A). One has to compare the size of the core with the Schwarzschild radius, defined as $R_s = 2GM/c^2$.

[5]Spline interpolation consists in a form of interpolation where the interpolant is a special type of piecewise polynomial, e.g. of the order 3, called a spline. Linear spline interpolation reduces to the usual linear interpolation. To compute spline interpolation, different libraries are available, or a recipe for Fortran language is also given in [271].

[6]I recall that in stellar astrophysics it counts for the metallicity any element heavier than ^{4}He. Solar metallicity corresponds to $Z = 0.02$, where Z is the relative abundance of "heavy" elements with respect to hydrogen plus helium abundance.

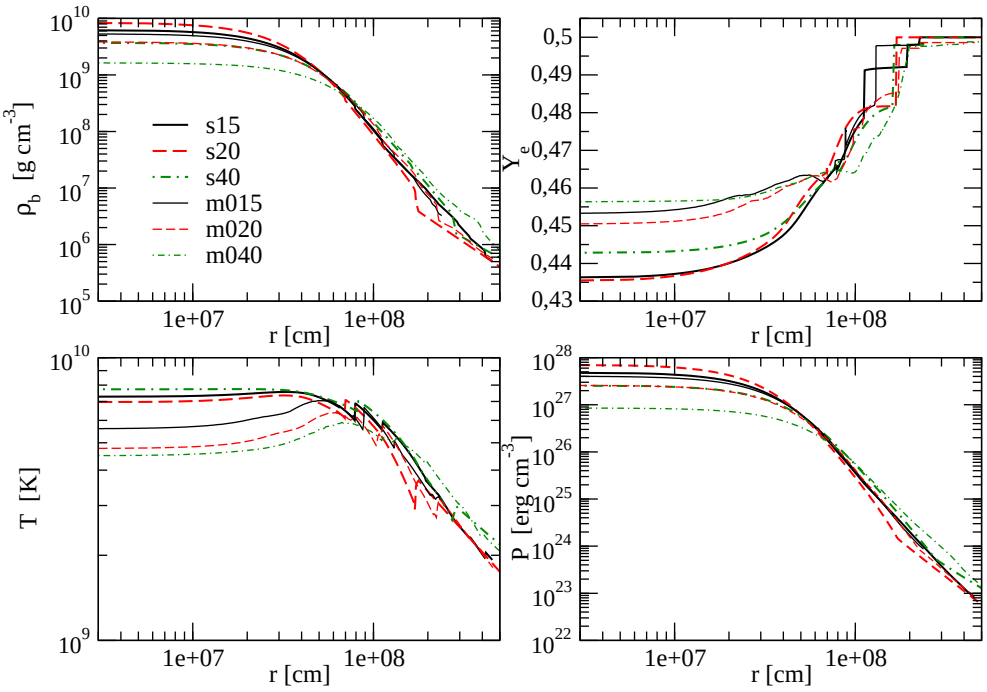

Figure 4.2: Comparison of presupernova core profiles calculated by Woosley and Heger [345] (thick lines, models sXX) and by Limongi and Chieffi [207] (thin lines, models mXXX). As a function of radial coordinate, the baryon density (upper left panel), the electron fraction (upper right panel), the temperature (lower left panel) and the pressure (lower right panel), in cgs units, are plotted.

We have also investigated the influence of the EoS on the presupernova profiles [122]. In fact, as already mentioned, it is important to reconstruct the profile at the beginning of the first iteration of the code consistently with the EoS employed. As an example, we display in Fig. 4.3 the pressure as a function of density for different EoS, taking as input for the EoS the density, temperature and electron fraction from the s20 model. For comparison, we have chosen to consider a 4/3 polytrope (green dotted line), the LS EoS with $K = 220$ MeV (black solid line), a neutron-proton-electron (npe) EoS (red dashed line) as derived in Appendix E, and a modified npe EoS labelled npe^* (blue dashed-dotted lines), where the baryon contribution has been cut for low densities (cf. Appendix E). We note a factor $\gtrsim 4$ between the pressure obtained using the LS EoS and the polytropic EoS at low density (i.e. at the edge of the iron core), and a factor ~ 2 between the pressure calculated with the LS EoS and the npe EoS. This corroborates the importance of being consistent in the EoS in mapping the presupernova profiles onto the hydrodynamical code. The changes in the slope observed for all curves (except the polytropic one) result from the discontinuities in the (ρ, T, Y_e) inputs (see Fig. 4.2), apart from the discrepancies among the EoS due to the different composition (the npe gas does not contain any cluster).

Model	ZAMS Mass $[M_\odot]$	M_{Fe} $[M_\odot]$	R_{Fe} $[10^8$ cm]	ρ_c $[10^9$ g cm$^{-3}]$	T_c $[10^9$ K]	Y_e
s15 [345]	15.0	1.62	2.28	6.16	7.28	0.4363
s20 [345]	20.0	1.46	1.69	8.31	6.97	0.4354
s40 [345]	40.0	1.78	2.46	3.69	7.73	0.4428
m015 [207]	15.0	1.38	1.30	5.33	5.60	0.4532
m020 [207]	20.0	1.47	1.75	3.85	4.77	0.4504
m040 [207]	40.0	1.51	1.98	1.63	4.50	0.4564

Table 4.1: Main properties of the presupernova profiles from Woosley and Heger [345] and from Limongi and Chieffi [207]. The position of the iron core is defined by the steep change in Y_e profile from $Y_e \sim 0.48$ to $Y_e \sim 0.5$.

4.4 Contribution of this thesis to the development of the hydrodynamical models

As a first step, I have worked in implementing the effect of the temperature dependence of the nucleon effective mass in nuclei in different CCSN simulations, from one of the most simple models, a one-zone model [50, 106, 110, 111], to a more advanced one, a spherical symmetric Newtonian code with neutrino transport, developed at CEA/DAM [41]. The effective mass in nuclei is affected by the damping of the particle-vibration coupling in the range of temperature around 1-2 MeV which are the typical temperatures encountered during core collapse. In the liquid-drop model framework, the impact of the temperature dependent effective mass can be included through the terms for the internal nuclear excitation and the symmetry energy coefficient. Moreover, the symmetry energy enters in the electron capture rates in nuclei. We have therefore implemented this "thermal" effect in the Q-value of the capture reaction.
We have also worked in implementing a routine version of the Lattimer and Swesty EoS [192] in the Newtonian code.

Afterwards, a full General Relativistic hydrodynamical code, without neutrino transport, has been provided by J. Novak and J. Pons. I have worked on this code including a trapping scheme for the treatment of neutrinos and I have generated a Newtonian version of this code.

In the future, we aim at developing the microphysics part in the GR code, in order to study the effect of the temperature dependent nuclear symmetry energy, the effect of different EoS, and, as a long time project, neutrino transport.

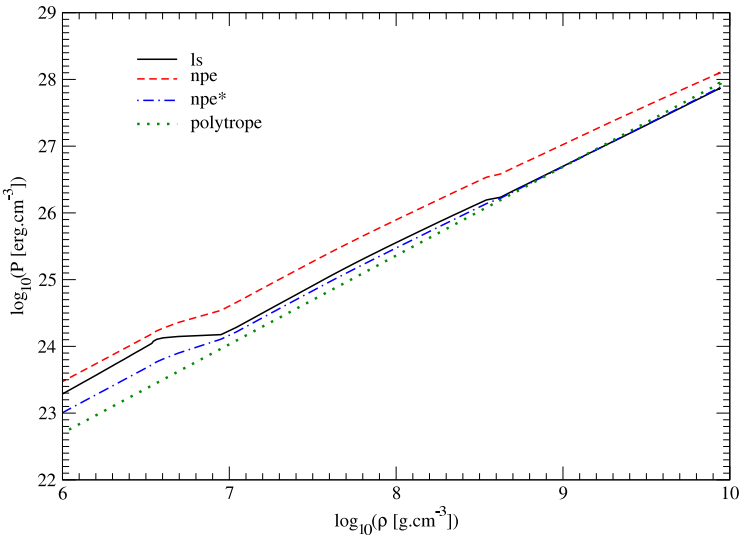

Figure 4.3: Comparison of the pressure obtained with different EoS along the density, temperature and electron fraction profile from the model s20. We have chosen to consider the following EoS: a 4/3 polytrope (green dotted line), the LS EoS ($K = 220$ MeV) (black solid line), a neutron-proton-electron (npe) EoS (red dashed line), and a modified npe EoS labelled npe^* (blue dashed-dotted line), where the baryon contribution has been smoothed out at low densities.

Chapter 5

One-zone simulation

In this Chapter a one-zone model developed in order to make a preliminary study of the deleptonization during core-collapse, including the temperature dependence of the nucleon effective mass is described.
I will present the physical model and the results we have obtained in such a framework, namely: including a temperature dependence of the effective mass in the one-zone simulation, we have found a systematic reduction of the deleptonization during collapse, which in turn has a non-negligible effect on the shock wave energetics.
All the details about this work can be found in Refs. [110, 111] and Refs. therein.

The advantage of this kind of approach is that it is analytical, and thus very easy to compute and very fast to run. Moreover, it contains the important physics and it has proven effective to make a preliminary study of the core deleptonization before core bounce [109, 126, 277]. Even if the numerical results of such a model are significative for their order of magnitude, not their precise values, which are limited by the oversimplified zero-dimensional approach, this analysis, as it will be shown, could justify a further investigation in more detailed simulations, where it is possible to model the formation of the shock wave.

The first study of the implication of the temperature dependence of the nuclear symmetry energy on the gravitational collapse making use of a one-zone code has been done by Donati *et al.* [106]. Such a temperature dependence was obtained in Ref. [106] studying the temperature dependence of the nucleon effective mass m^* in some neutron rich nuclei which are expected to be present in the core of an evolved massive star, in particular: ^{98}Mo, ^{64}Zn and ^{64}Ni. The decrease of m^* with temperature found in the range $0 < T < 2$ MeV (which is significant for the core-collapse phase) induces a corresponding increase of the nuclear symmetry energy, E_{sym}, which enters in the electron capture cross sections. In analogy to the results of the Fermi gas model, it has been argued that the temperature dependence of E_{sym} can be fitted by a simple analytical expression (cf. Section 2.3.2 in Part I of this thesis):

$$E_{sym} = s(T) \left(1 - 2\frac{Z}{A}\right)^2 , \tag{5.1}$$

where Z and A characterize the nucleus and $s(T)$ is the symmetry coefficient at finite

temperature, parameterized as Eq. (2.66):

$$s(T) = s(T=0) + \frac{\hbar^2 k_F^2}{6} \left[\frac{1}{m^*(T)} - \frac{1}{m^*(T=0)} \right] , \tag{5.2}$$

being $k_F = 1.35$ fm^{-1} the Fermi momentum and $s(T=0) \approx 30$ MeV the symmetry coefficient at zero temperature [106]. The physical connection between the temperature dependence of the nucleon effective mass and the stellar collapse relies on the fact that the rate of electron capture depends in a very sensitive way on the difference between the neutron and proton chemical potentials $\hat{\mu} := \mu_n - \mu_p$ (cf. Eqs. (5.12), (5.13) and (5.22)). Larger value of $\hat{\mu}$ makes the capture more difficult, since it increases the energy required to change a proton into a neutron. Thus, the final value of lepton fraction at trapping is increased, i.e. the neutronization process during core collapse is inhibited. As explained in the general Introduction, the amount of deleptonization during the collapse phase is very important in order to determine the position of the formation of the shock wave. Moreover, the shock wave formed at the edge of the homologous core has to reach the edge of the iron core in order to let the star explode. On its way out, the shock wave loses energy in dissociating the nuclei into free neutrons and α particles; the amount of energy lost is of about 17 foe per solar mass crossed[1], i.e. (cf. Eq. (1.1) and Eq. (1.7)):

$$\begin{aligned} E_{diss} &\approx 17\, \Delta M_{crossed} = 17\, [M_{ch}(Y_{l,in}) - M_{ic}(Y_{l,tr})] \text{ foe} \\ &\approx 98\, [(Y_{l,in})^2 - (Y_{l,tr})^2] \text{ foe} , \end{aligned} \tag{5.3}$$

where masses are expressed in solar mass units, $Y_{l,in}$ corresponds to the lepton fraction at the onset of the collapse, and $Y_{l,tr}$ indicates the lepton fraction at trapping, i.e. after which β equilibrium is established and the total lepton fraction remains constant. Thus, larger values of $Y_{l,tr}$ result in less energy dissipated, i.e. stronger shock wave. In order to quantify this "thermal" effect, we define the *gain* in dissociation energy of the shock wave, $\delta_T E_{diss}$, where δ_T stands for the "thermal" variation of a quantity due to the temperature dependence of the symmetry energy, for example: the thermal change in final lepton fraction is $\delta_T Y_{l,tr} = Y_{l,tr}|_T - Y_{l,tr}|_0$ and the thermal gain in dissociation energy is $\delta_T E_{diss} = E_{diss}|_0 - E_{diss}|_T$.

Already in Ref. [106] it has been shown that the temperature dependence of the nuclear symmetry energy yields a lower rate of deleptonization along the collapse and, as a consequence, a higher value of $Y_{l,tr}$ and a smaller value of dissociation energy of about 0.5-0.6 foe, a non-negligible amount when one considers that the explosion energy (kinetic energy of the ejecta) of SN 1987A was observed to be ~ 1 foe [37].

After the study performed by Donati *et al.* [106], other investigations of the temperature dependence of the nuclear symmetry energy have been done, as explained in Section 2.3.2. Although we agree that no dramatic effect on the dynamics of the collapse is to be expected, one should be cautious in dismissing any significative consequence of the T-dependence of E_{sym} without a collapse simulation. Indeed, not only the reaction Q-values (as considered in Ref. [99]), but also the equation of state of bulk dense matter, the free nucleon abundances, the degree of dissociation into α-particles and the nuclear internal

[1]The estimation of the dissociation energy comes out considering that the energy required to dissociate a nucleus is about 8.8 MeV/nucleon, and: $1 M_\odot \approx 1.2 \times 10^{57}$ nucleons. Thus, the energy required to dissociate 1 $M_\odot$ is $\approx 10^{58}$ MeV, i.e. $\approx 1.7 \times 10^{52}$ erg = 17 foe.

excitations are affected by changes in the symmetry energy. Moreover, the dynamics of the collapse depends in a very non-linear way on the strength of nuclear electron capture[2], so that mild changes in the rates may still result in non-negligible alterations of the overall energetics.

Our aim is thus to investigate with a collapse simulation the extent to which the temperature dependence of the nuclear symmetry energy, found by Donati *et al.* [106] and confirmed by Dean *et al.* [99], can affect the deleptonization of the collapsing stellar core.

5.1 Model for the collapse

Our one-zone model (i.e. sphere of uniform density) is developed along the classic approach of Refs. [109, 126, 277]. Since the publication of the first investigation of the temperature dependence of the nuclear symmetry energy in a collapse model made by Donati *et al.* [106], remarkable progresses have been made in the SMMC calculations of electron capture rates, that, of course, we have to take into account. On the one hand, the new values obtained with improved SMMC techniques for capture on nuclei present in lower-density matter ($A < 65$) [184] have been implemented in modern evolutionary stellar calculations yielding new presupernova models [154], which are significantly different than those used so far as initial conditions in collapse simulations. On the other hand, the unblocked GT strengths found with the hybrid model for the neutron-rich nuclei typical of higher-density matter ($A > 65$) [183] have been used in numerical (1-dimension) collapse simulations, both Newtonian and Relativistic. When compared to the results from the commonly used Bruenn parameterization of nuclear electron capture [56], which quenches capture on heavy nuclei as required by the IPM and thus allows capture on free protons to dominate some crucial phases of the collapse, the simulations with the new rates show significant differences in the dynamics of the shock wave and in the neutrino luminosity [187, 165, 166].

Altogether, the results obtained in the collapse simulations of Ref. [106] have to be revisited in four main aspects, all related to electron capture on nuclei:

1. by using the approach of BBAL [34], the effect of the temperature-dependent symmetry energy on the deleptonization has been overestimated. Indeed, the BBAL rates for capture on nuclei are calculated applying the Fermi approximation to a shell model description of the GT transition. This statistical limit (which actually does not apply to the collapse scenario, where the shell structure is still dominant and the nuclear density of states is far from thermal [183]) involves an integration over the initial proton states and this multiplies the final capture rates by a factor containing the nucleon effective mass[3]. This linear dependence of the nuclear rates on m^* obviously amplifies the thermal effects, but it is absent if a more realistic, non-statistical description of capture is adopted.

2. the BBAL rates for electron capture (on both nuclei and free protons) used in Ref. [106] were calculated at $T = 0$, but since we are looking for a small thermal

[2]The parameter study of Ref. [166], for example, shows that each increase of the rate of capture by a factor 10 corresponds roughly to the same decrease ($\sim 0.1 M_\odot$) of the mass of the homologous core.

[3]The integration requires the nuclear density of states, which in the Fermi gas model is proportional to the nucleon mass [34].

effect we cannot neglect the influence of the Fermi distribution functions, which describe the occupation numbers of initial and final particle states at finite temperature [109, 126].

3. the multiplying factor $\gamma^2 = 0.1$, introduced in Ref. [106] to account for the Pauli blocking of GT transitions, is not anymore realistic according to the new results from the hybrid model [183]. These new findings, however, are not yet obtained in a consistent SMMC calculation so that, in our opinion, the actual strength of nuclear electron capture is still an open issue and the correct value of γ^2 is not yet pinned down.

4. the initial conditions adopted in Ref. [106] for the collapse have to be revisited, to account for the new results obtained for the presupernova core when implementing the improved SMMC capture rates in evolutionary stellar codes [154].

The model is an improvement over the one used in Ref. [106] in two respects: first, the treatment of electron capture is revisited in order to answer the issues 1. and 2. previously mentioned; then, the trapping of neutrinos is treated more realistically and provides the final lepton fraction after trapping, when the collapse is adiabatic. Moreover, the capture strength on nuclei is kept as a free parameter, γ^2, as discussed in issue 3., and the presupernova initial conditions are the improved ones mentioned in issue 4.
In the following, we describe the main features of our collapse model:

1. The dynamical evolution of density with time due to gravity decouples from the thermodynamical equations for the changes in entropy and lepton fractions. Indeed, the variation of the density ρ scales with time as [34]:

$$\frac{\mathrm{d}(\ln \rho)}{\mathrm{d}t} = 100\ \rho_{10}^{1/2}\ , \tag{5.4}$$

where ρ_{10} is in units of 10^{10} g cm^{-3}. Therefore, we can follow the relevant thermodynamical variables (entropy, temperature, electron and neutrino fractions, particle abundances, nuclear composition) as a function of density, along the so called collapse trajectories.

2. We adopt the equation of state for hot dense matter derived in BBAL [34], which is based on a compressible liquid drop model. The ensemble of nuclear species is approximated by a mean heavy nucleus in a sea of dripped-out free neutrons and (fewer) protons. Electrons are treated as a non-interacting ideal gas of ultra-relativistic particles. The energy per particle of a nucleus is given by ($x = Z/A$):

$$\begin{aligned} W_N(A, Z, V_N, n_n) &= [(1-x)m_n c^2 + x m_p c^2 + W(k, x)] \\ &\quad + W_{coul}(A, Z, V_N, n_n) + W_{surf}(A, Z, V_N, n_n)\ , \end{aligned} \tag{5.5}$$

being the size (Coulomb and surface) and the bulk contribution, around saturation density, parameterized in terms of the nuclear saturation density ρ_0, the incompressibility modulus $K \approx 240$ MeV, the volume coefficient $w_0 \approx 16$ MeV and the

symmetry coefficient $s(T)$ ($s(0) \approx 30$ MeV):

$$\begin{aligned} W_{bulk}(k,x) &= -w_0 + \frac{1}{2}\,K\,\left(1-\frac{k}{k_0}\right)^2 + 4\,s(T)\,\left(\frac{1}{2}-x\right)^2 \\ &\approx -w_0 + 4\,s(T)\,\left(\frac{1}{2}-x\right)^2 \qquad (5.6) \\ W_{surf}(A,x) &= w_s\,A^{-1/3} \qquad (5.7) \\ & \quad w_s = 290\,x^2\,(1-x)^2 \\ W_{Coul}(\rho,x,A) &= w_c\,A^{2/3} \qquad (5.8) \\ & \quad w_c = \frac{3}{4}\,x^2\,\left[1-\frac{3}{2}\left(\frac{\rho}{\rho_0}\right)^{1/3}+\frac{1}{2}\left(\frac{\rho}{\rho_0}\right)\right]\,, \end{aligned}$$

where k is the momentum, related to the number density as $n = k^3/(1.5\pi)$, and $k_0 = k(\rho_0)$. From the minimization of the energy (which, in this case, can be done full analytically) one obtains an expression for the mean nucleus [34]:

$$A = 194\,(1-x)^2\left[1-0.236\left(\frac{\rho_{10}}{100}\right)^{1/3}\right]^{-1}\,, \qquad (5.9)$$

while the nuclei abundance is determined by the mass conservation relation: $\sum_i X_i = 1$. The fractions of free nucleons are determined from nuclear statistical equilibrium:

$$\begin{aligned} X_n &= 79\,\frac{(k_B T)^{3/2}}{\rho_{10}}\,e^{\mu_n/(k_B T)} \qquad (5.10) \\ X_p &= X_n\,e^{-\hat{\mu}/(k_B T)}\,. \qquad (5.11) \end{aligned}$$

The free nucleons are supposed to follow a Maxwell-Boltzmann distribution, since, as noticed in Refs. [34, 126, 188], in the density-temperature range considered, their low abundances, $X_n \lesssim 10-20\%$ and $X_p \sim 10^{-3}-10^{-4}$, allow to consider them as a "dilute" gas. The neutron chemical potential μ_n and $\hat{\mu} := \mu_n - \mu_p$ are given by[4] [22, 34]:

$$\begin{aligned} \mu_n &= -w_0 + 4\,s(T)\,\left(\frac{1}{2}-x\right) - \frac{4}{3}\,s(T)\,\left(\frac{1}{2}-x\right)^2 \\ &\quad -2\,\frac{\omega_s}{A^{1/3}}\,\left(\frac{1-2x}{1-x}-\frac{1}{3}\right) \qquad (5.12) \\ \hat{\mu} &= 8\,s(T)\left(\frac{1}{2}-x\right) - \frac{\omega_s}{A^{1/3}}\left(\frac{1}{x}+\frac{2}{x}\frac{1-2x}{1-x}\right)\,. \qquad (5.13) \end{aligned}$$

Thus, the symmetry energy appears in the bulk nuclear energy and, as a consequence, in the neutron chemical potential, μ_n, and in the neutron-proton energy

[4]The neutron and proton chemical potentials do not include the rest mass; thus, in computing the Q-value of the reactions, one must pay attention to include explicitly the neutron-proton mass difference.

difference, $\hat{\mu}$. These are crucial quantities in determining the free particle abundances, the nuclear capture Q-values and the entropy changes due to the departure from β-equilibrium of the collapsing core before neutrino trapping.

3. Thermal dissociation of nuclei into α-particles and nucleons

$$(A, Z) + \gamma \rightarrow \frac{Z}{2}\,\alpha + (A - 2Z)\,n + Q_{diss} \tag{5.14}$$

is also taken into account through the Saha equation [295]:

$$\frac{n_\alpha^{Z/2} n_n^{A-2Z}}{n_A} = \frac{g_\alpha^{Z/2} g_n^{A-2Z}}{g_A} \left(\frac{k_B T}{2\pi\hbar^2}\right)^y \left(\frac{m_\alpha^{Z/2} m_n^{A-2Z}}{m_A}\right)^{3/2} e^{-\frac{Q_{diss}}{k_B T}}\,, \tag{5.15}$$

where we have taken [34, 295] $g_n = 2$ and $g_A = 1$ and being:

$$y = \frac{3}{2}\left[\frac{Z}{2} + (A - 2Z) - 1\right] \tag{5.16}$$

$$\begin{aligned} Q_{diss} &= \frac{Z}{2}\,m_\alpha + (A - 2Z)\,m_n - m_A \\ &= -28.3 M_\alpha - B.E.\,, \end{aligned} \tag{5.17}$$

$$\begin{aligned} B.E. &= m_A - Z\,m_p - (A - Z)\,m_n = A\,W_{bulk} + W_{size} \\ &= A\left[-w_0 + 4\,s(T)\left(\frac{1}{2} - x\right)^2\right] + \frac{3}{2}\,w_s\,A^{2/3}\,. \end{aligned} \tag{5.18}$$

However, it has been found that accounting for α particles has a negligible effect on the collapse trajectories, as also noticed in Appendix F of Ref. [34].

4. Entropy terms are included for the translational degrees of freedom of all the particles (mean heavy nucleus, free classical nucleons, relativistic degenerate leptons) as well as for the internal nuclear excitations, treated in the Fermi gas approximation [34, 126, 295]:

$$s_{tot} = s_{tr} + s_{el} + s_N + s_\nu \tag{5.19}$$

$$s_{tr} = \frac{(1 - \delta_{diss})\,X_h}{A}\,\tilde{s}_A + \frac{\delta_{diss}\,X_h}{4}\,\tilde{s}_\alpha + X_n\,\tilde{s_n} + X_p\,\tilde{s_p} \tag{5.20a}$$

$$s_{el} = Y_e\,\tilde{s}_{el} \tag{5.20b}$$

$$s_N = \frac{(1 - \delta_{diss})\,X_h}{A}\,\tilde{s}_N \tag{5.20c}$$

$$s_\nu = Y_\nu\,\tilde{s}_\nu\,, \tag{5.20d}$$

$$\tilde{s}_A = 6.19 + \ln\left[\frac{A^{5/2}\,(k_BT)^{3/2}}{(1-\delta_{diss})\,X_h\,\rho_{10}}\right] \tag{5.21a}$$

$$\tilde{s}_\alpha = 9.65 + \ln\left[\frac{(k_BT)^{3/2}}{\delta_{diss}\,X_h\,\rho_{10}}\right] \tag{5.21b}$$

$$\tilde{s_n} = 6.88 + \ln\left[\frac{(k_BT)^{3/2}}{X_n\,\rho_{10}}\right] \tag{5.21c}$$

$$\tilde{s_p} = 6.87 + \ln\left[\frac{(k_BT)^{3/2}}{X_p\,\rho_{10}}\right] \tag{5.21d}$$

$$\tilde{s}_{el} = \pi^2\frac{k_BT}{\mu_e} \tag{5.21e}$$

$$\tilde{s}_N = A\,\frac{\pi^2}{2}\,\frac{k_BT}{\epsilon_F}\,m^*(T) \tag{5.21f}$$

$$\tilde{s}_\nu = \pi^2\frac{k_BT}{\mu_\nu}\,, \tag{5.21g}$$

being δ_{diss} the fraction of nuclei dissociated in α particles and neutrons, and $\epsilon_F \approx 34$ MeV is the Fermi energy[5]. Neutrino contributions are set to zero prior to neutrino trapping.
The nuclear excitation energy is proportional to the nucleon effective mass [33], which is the quantity whose temperature dependence has been originally calculated and fitted by an analytical expression in Ref. [106]. We have found that the corresponding entropy term has a non-negligible effect on the collapse trajectories.

5. Neutrino trapping is set to start at a given trapping density, ρ_{tr}. The typical "standard" value is $\rho_{10,tr} = 43$ (ρ_{10} being the density in units of 10^{10} g cm^{-3}), but we keep it as a model parameter. As long as $\rho < \rho_{tr}$, neutrinos are allowed to stream freely out of the core and the neutrino fraction is $Y_\nu = 0$. When $\rho \geq \rho_{tr}$, neutrino diffusion is treated along the lines of Ref. [277]: a degenerate sea of neutrinos with $Y_\nu \neq 0$ is allowed to build up by the inclusion of a diffusion term which decreases with density. Moreover, the inverse reactions induced by the sea of neutrinos are included in the electron capture rates [326], so that weak interactions can reach equilibrium. In this way, complete neutrino trapping is reached gradually at a density somewhat larger than ρ_{tr} ; both the total lepton fraction, $Y_l = Y_e + Y_\nu$, and the entropy tend naturally to constant values, after which the collapse proceeds adiabatically and in β-equilibrium. This is a major improvement over Ref. [106], where neutrinos were always streaming out freely ($Y_\nu = 0$), so that equilibrium could never be reached and the final lepton fraction was just the value of the electron fraction taken at $\rho = \rho_{tr}$ along the collapse trajectory, namely $Y_e = Y_e(\rho_{tr})$.

6. Electron capture is implemented on both free protons and heavy nuclei with stan-

[5] In the BBP EoS [22], from which the BBAL EoS is derived, the approximation $T = 0$ has been done. This is justified by the fact that during core collapse $k_BT \approx 1 - 2$ MeV $\ll \epsilon_F$. As a consequence, in a first approximation, finite temperature effects should not contribute very much in finding the equilibrium composition [34, 295] of the system. The only T-dependence we have introduced in the BBAL EoS is the temperature dependence of the nuclear symmetry energy, derived from the temperature dependent nucleon effective mass.

dard two-level transitions, as fully developed in Ref. [126]; the phase space integral is calculated numerically, although its approximation by Fermi integral (as in Eq. (1) of Ref. [187]) turns out to be accurate enough. For this kind of transitions, the nuclear capture rate λ_N is a function of density, temperature and two other quantities: the excitation energy of the nuclear GT resonance, Δ_N, and the reaction Q-value. The first is taken as a model parameter, while $Q = \hat{\mu} + \Delta_N$. We have actually used a regularized expression for the GT excitation energy which takes into account that electron capture has a threshold energy [326]:

$$\Delta_h = \min \left[\Delta_N, \max \left\{ 0, \frac{1}{2}(\mu_e - \hat{\mu} - 1.297 - \mu_\nu) \right\} \right] . \tag{5.22}$$

We have also multiplied the nuclear strength λ_N by a free parameter, γ^2. As shown in Ref. [187], the Q-dependence of the capture rates obtained with the hybrid model can be reasonably fitted by the two-level expression, with $\Delta_N = 2.5$ MeV and an appropriate GT matrix element; we normalize λ_N so that our expression coincides with Eq. (1) of Ref. [187] (Eq. (1.29)) when $\gamma^2 = 1$.

7. The temperature dependence of the symmetry energy is treated as in [106], where it was expressed in terms of the T-dependence of the nucleon effective mass, $m^* = m^*(T)$, calculated for different nuclei. The results for each nucleus were fitted with a formula containing two parameters: the value at $T = 0$ of the so-called ω-mass, $m_\omega(0)$, and the temperature scale of this dependence, T_0. The standard average values are $m_\omega(0) = 1.7$ and $T_0 = 2$ MeV, but we keep them as model parameters allowed to vary in a meaningful physical range ($1.4 \lesssim m_\omega(0) \lesssim 1.8$ and $1.9 \lesssim T_0 \lesssim 2.1$ MeV [106]), to account for their dependence on the nucleus studied.

More details can be also found in Refs. [34, 109, 126, 277, 50, 110]; in particular, we adopted the following differential equations for the collapse trajectories:

- the electron fraction evolution:

$$\frac{\mathrm{d}Y_e}{\mathrm{d}\rho_{10}} = - \frac{1}{100\ \rho_{10}^{3/2}} \left[\lambda_{fp}\, X_p + \lambda_{bp}\, \frac{X_h}{A} \right] , \tag{5.23}$$

where X_p and X_h are the free proton and nuclei abundances, λ_{fp} and λ_{bp} are the electron capture rates on free protons and bound nuclei (cf. Eq. (85) of Fuller [126]). From trapping density onwards, the neutrino-induced inverse reactions are included by multiplying the electron capture rates by the factor $1 - e^{-\Delta/T}$ (for free protons; Δ equals the difference in mass between neutrons and protons) and $1 - e^{-\Delta_h/T}$ (for nuclei; Δ_h is the excitation energy of the daughter nucleus), as in Eqs. (15) and (16) of Ray *et al.* [277].

- the temperature evolution is (cf. Eqs. (92) and (93) of Ref. [126] before trap-

ping[6]and Eqs. (33) and (35) of Ref. [277] after trapping):

$$\begin{aligned}\frac{\mathrm{d}T}{\mathrm{d}\rho_{10}} &= -\frac{G_\rho}{G_T} - \left\{\frac{G_Y}{G_T}\right. \\ &+ \frac{1}{TG_T}\left[(\mu_e-\mu_n+\mu_p-1.297-\bar{\epsilon}_{\nu,bp})\,\frac{X_h\,\lambda_{bp}}{AX_p\lambda_{fp}+X_h\lambda_{bp}}\right. \\ &+ \left.\left.(\mu_e-\mu_n+\mu_p-1.297-\bar{\epsilon}_{\nu,fp})\,\frac{X_p\,A\,\lambda_{fp}}{AX_p\lambda_{fp}+X_h\lambda_{bp}}\right]\right\}\frac{\mathrm{d}Y_e}{\mathrm{d}\rho_{10}} \quad (5.24)\end{aligned}$$

where G_j are the partial derivatives of the entropy with respect to the variable j, μ_i are the chemical potentials of the species i, $\bar{\epsilon}_\nu$ are the average energies of neutrinos produced by electron capture on free protons (fp) and nuclei (bp) (all the expressions can be found in [110]).

- the neutrino fraction evolution is (cf. Eq. (29) of Ref. [277]):

$$\frac{\mathrm{d}Y_\nu}{\mathrm{d}\rho_{10}} = -\frac{\mathrm{d}Y_e}{\mathrm{d}\rho_{10}} + \left(\frac{\mathrm{d}Y_\nu}{\mathrm{d}\rho_{10}}\right)_{diff}, \quad (5.25)$$

where, after trapping:

$$\begin{aligned}\frac{\mathrm{d}Y_e}{\mathrm{d}\rho_{10}} &= -\frac{1}{100\,\rho_{10}^{3/2}}\left[\lambda_{fp}\,X_p\,(1-e^{-\Delta/T})\right. \\ &\quad \left.+\lambda_{bp}\,\frac{X_h}{A}\,(1-e^{-\Delta_h/T})\right] \quad (5.26)\\ \left(\frac{\mathrm{d}Y_\nu}{\mathrm{d}\rho_{10}}\right)_{diff} &= -\frac{17}{13}\,(3.5\times10^{-4})\,\frac{\mu_\nu^3}{\rho_{10}}\frac{(\rho_{10,tr}/\rho_{10})^{17/6}\,\rho_{10}^{-1}}{[1+(4/13)\,(\rho_{10,tr}/\rho_{10})^{17/6}]} \quad (5.27)\end{aligned}$$

Eq. (5.27) simulates the diffusion of neutrinos that cannot be extensively treated in the zero-dimensional approach. The term μ_ν is the neutrino chemical potential, which is calculated assuming neutrinos as massless ultra-relativistic particles: $\mu_\nu = 14\,(Y_\nu\rho_{10})^{1/3}$. Before trapping we take $Y_\nu = 0$ (no neutrinos are taken into account in the model).

The collapse trajectories are determined starting from a set of initial conditions on the density, ρ_{in}, the temperature, T_{in}, and the electron fraction, $Y_{e,in}$ (until trapping density is reached, $Y_\nu = 0$). According to the improved results of Ref. [154] for the central properties of the presupernova core which evolves from a $15M_\odot$ star (about the size of the progenitor of SN 1987A), we will take the initial values $\rho_{10,in} = 0.936$, $T_{in} = 0.625$ MeV and $Y_{e,in} = 0.432$, which differ significantly from those adopted in Ref. [106]. The differential equations are then integrated and the collapse trajectories of the different thermodynamical quantities are found. In particular, the total lepton fraction $Y_l = Y_l(\rho)$ tends to a constant value, $Y_{l,tr}$, as the density increases above ρ_{tr} and neutrino trapping is completed.

[6]In Eq. (92) of Ref. [126], the terms AX_p in the denominators should each be multiplied by a factor λ_{fp}.

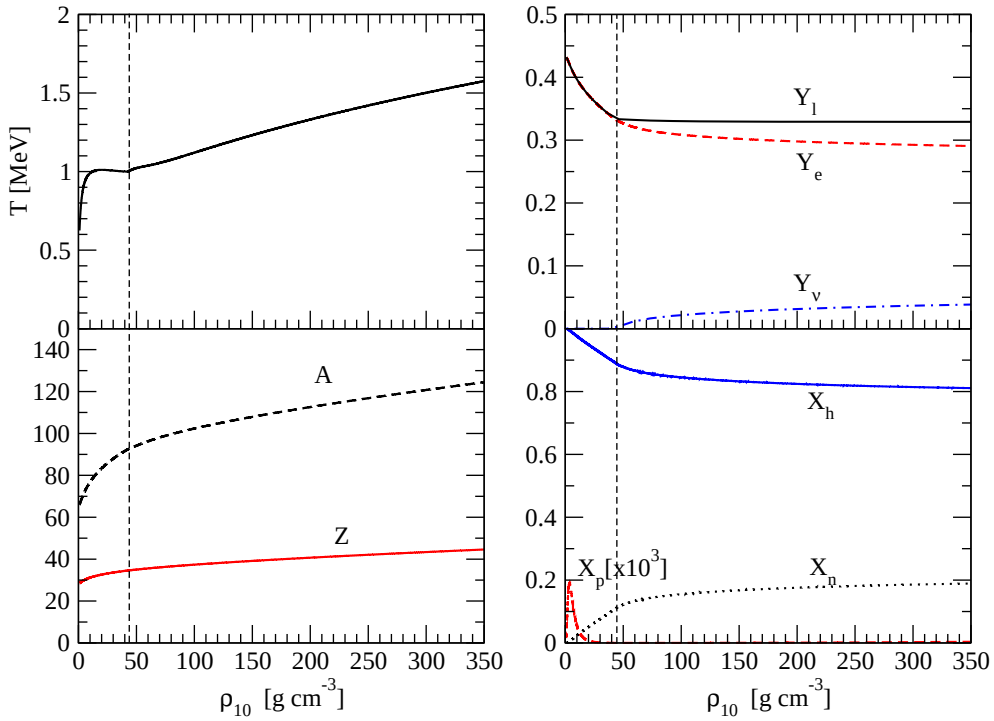

Figure 5.1: Temperature (upper left panel), lepton fractions (upper right panel), and composition (lower panels) as a function of density, obtained without the temperature dependence of the symmetry energy. The dotted vertical line indicates the trapping density ρ_{tr}. The parameters of the model are the standard ones: $\rho_{tr,10} = 43$, $m_\omega(0) = 1.7$, $T_0 = 2$ MeV, $\Delta_N = 2.5$ MeV.

5.2 Results

Before discussing the results obtained implementing the temperature dependent nuclear symmetry energy, in Fig. 5.1 the temperature, composition and lepton fractions along the collapse, traced by the increasing density, are shown, for the case of constant nuclear symmetry energy (i.e. $E_{sym} = E_{sym}(T = 0)$), in order to give an insight of the typical T, Y_e and (A, Z) ranges encountered in the collapse. The model parameters are set to their "standard" values: $\rho_{10,tr} = 43$, $m_\omega(0) = 1.7$, $T_0 = 2$ MeV, $\Delta_N = 2.5$ MeV.

We now make a parameter study of the core neutronization as a function of the nuclear strength in the range $0 \leq \gamma^2 \leq 5$. We point out that $\gamma^2 = 0$ corresponds to electron capture on free protons *only*, while $\gamma^2 = 5$ is very large and probably unrealistic. The older, blocked GT rates of Fuller [126] correspond to $\gamma^2 = 0.1$, while the new unblocked rates of Ref. [183] are associated to $\gamma^2 = 1$ (cf. Eq. (1.29)). Improved future calculations could change the presently accepted value of the nuclear strength, but (barring discovery of past errors or unexpected breakthroughs) we think that $0.5 \lesssim \gamma^2 \lesssim 2$ should represent a reasonable physical range.

For each choice of parameters, we have run the collapse simulation twice: once implementing the temperature dependence $E_{sym} = E_{sym}(T)$ and obtaining $Y_{l,tr}|_T$, once setting $E_{sym} = E_{sym}(0)$ and obtaining $Y_{l,tr}|_0$.

From the collapse trajectories of the lepton fraction, $Y_l = Y_l(\rho)$, we can infer the density range where the temperature dependence of the symmetry energy is most relevant.

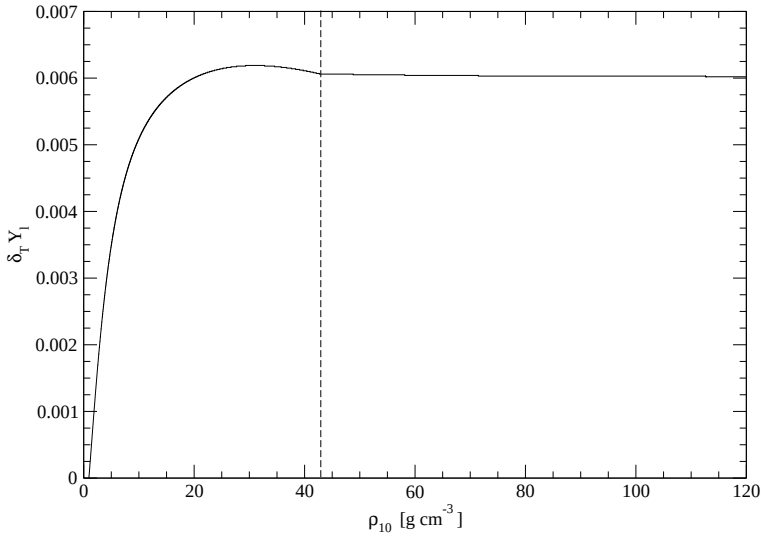

Figure 5.2: Thermal variation of the lepton fraction collapse trajectories, $\delta_T Y_l$, as a function of the density of the collapsing core, ρ_{10} (in units of 10^{10} g cm^{-3}). The dotted line indicates the trapping density, ρ_{tr}. The curve corresponds to standard parameters of the model ($\rho_{\rm tr,10} = 43$, $m_\omega(0) = 1.7$, $T_0 = 2$ MeV, $\Delta_N = 2.5$ MeV).

Regarding the thermal variation of the capture rates, we obtain similar results as those shown in Fig. 7 of Ref. [99]: the thermal effect is maximum at the onset of collapse ($\rho_{10} \sim 1$) and decreases with increasing density; when trapping sets in ($\rho_{10} \sim 40$), the difference in the capture rates due to $E_{sym}(T)$ is already negligible. However, since this is a cumulative and non-linear effect on the lepton fraction, a difference between the collapse trajectories, $\delta_T Y_l(\rho) = Y_l(\rho)|_T - Y_l(\rho)|_0$, gradually builds up as the density increases. This is shown in Fig. 5.2, where the thermal variation of the lepton fraction collapse trajectories, $\delta_T Y_l$, is given as a function of the density of the collapsing core. We notice that, even though the thermal variation actually reaches its final equilibrium value, $\delta_T Y_{l,tr}$, only when neutrino trapping is fully achieved (around $\rho_{10} \sim 250$), the whole effect is seen to build up before trapping sets in. In particular, it is mostly in the low-density range $1 \lesssim \rho_{10} \lesssim 20$ that the temperature dependence of the symmetry energy affects significantly the neutronization process.

Surprisingly, although Fig. 5.2 corresponds to standard parameters of the model, the curve $\delta_T Y_l(\rho)$ is found to change very little under physically reasonable variations of the model parameters, as it will be shown in the following.

The results for the final lepton fractions and the associated thermal changes are shown in Table 5.1 for different values of γ^2. We point out how the general magnitude of the final lepton fraction is a very slowly decreasing function of γ^2. Increasing the strength by a factor ten, from the blocked to the unblocked capture rates, decreases the final lepton fraction by $\sim 13\%$, which is in reasonable agreement with the $\sim 10\%$ change obtained in Newtonian one-dimensional simulations [166]. We also notice that the thermal effect under study *systematically* reduces the final neutronization, namely $Y_{l,tr}$ is increased by an almost constant value, $\delta_T Y_{l,tr} \simeq 0.006$, irrespective of the value of the strength γ^2. Although small, this effect is not negligible, as it can be seen after.

γ^2	$Y_{l,tr}\|_0$	$Y_{l,tr}\|_T$	$\delta_T Y_{l,tr}$	$\delta_T E_{diss}$ [foe]
0	0.3996	0.4054	0.0058	0.45
0.1	0.3802	0.3861	0.0060	0.44
0.5	0.3460	0.3519	0.0059	0.41
1	0.3291	0.3351	0.0060	0.39
2	0.3114	0.3175	0.0061	0.38
5	0.2808	0.2868	0.0060	0.34

Table 5.1: Results of the collapse simulation for different values of the strength of nuclear electron capture, γ^2. We show the final lepton fractions after trapping obtained without, $Y_{l,tr}|_0$, and with, $Y_{l,tr}|_T$, the temperature dependence of the symmetry energy; the thermal change of final lepton fraction, $\delta_T Y_{l,tr}$; the corresponding gain in dissociation energy of the shock, $\delta_T E_{diss}$ (in foe). The model parameters are the standard ones ($\rho_{10,tr} = 43$, $m_\omega(0) = 1.7$, $T_0 = 2$ MeV, $\Delta_N = 2.5$ MeV).

In order to determine the relevance of our results to supernova explosions, we need a quantity with a more direct physical meaning and which can be compared to relevant observables. As in Ref. [106], we use the gain in shock dissociation energy which is defined as $\delta_T E_{diss} = 98\,[(Y_{l,tr}|_T)^2 - (Y_{l,tr}|_0)^2] = 98\ \delta_T Y_{l,tr}^2$ (in foe). Although based on a schematic model for the shock formation and propagation [52], this expression provides a reasonable order of magnitude estimate of $\delta_T E_{diss}$. In a similar fashion, one could consider the change in initial (i.e. post-bounce) shock energy, $\delta_T E_{\rm shock}$, which also follows from changes in the final lepton fractions affecting the size of the homologous core. In the schematic approach of Ref. [126], however, the expression for the initial shock energy, $E_{\rm shock} = E_{\rm shock}(Y_{l,tr})$, has a maximum for $Y_{l,tr} = \frac{10}{13} Y_{in} = 0.3323$. Since the final lepton fractions corresponding to $\gamma^2 = 1$ are close to this extremum (cf. Table 5.1), the thermal effect $\delta_T E_{\rm shock}$ turns out to be quite small ($\sim 10^{-2}$ foe); we will not consider it in the following.

Since $\delta_T Y_{l,tr}$ is small, the thermal gain in dissociation energy can be written as $\delta_T E_{diss} \simeq 196\ Y_{l,tr}|0 \times \delta_T Y_{l,tr}$. This shows that in general $\delta_T E_{diss}$ depends on $\delta_T Y_{l,tr}$, but its magnitude is fixed by the final neutronization reached by matter, $Y_{l,tr}|_0$, which is determined by the nuclear capture strength γ^2. In the last column of Table 5.1, we show the results for the gain in dissociation energy. For standard parameters and $\gamma^2 = 1$, we find $\delta_T E_{diss} = 0.39$ foe. Moreover, since $\delta_T Y_{l,tr}$ is constant, the gain in dissociation energy has the same very slow dependence on the strength parameter as the final lepton fraction. This is well seen in Fig. 5.3, where $\delta_T E_{diss}$ is given as a function of γ^2. The points are the results of the collapse simulation, while the line in the log-log graph represents a power-law best fit, with a very small exponent $a = -0.065$. In the physical meaningful range for the strength ($0.5 \lesssim \gamma^2 \lesssim 2$), the gain in dissociation energy varies only by $\pm 4\%$, in the interval $\delta_T E_{diss} \sim 0.38 - 0.41$ foe.

Although the previous discussion indicates a quite stable value $\delta_T E_{diss} \sim 0.4$ foe, we want to study the robustness of such a result under reasonable variations of the model parameters, compatible with present theoretical uncertainties about the values of $\rho_{10,tr}$, Δ_N, $m_\omega(0)$ and T_0. In Table 5.2, we show $\delta_T E_{diss}$ for different values of γ^2: each column represents the case in which only one of the parameters, $\rho_{10,tr}$ or Δ_N, is changed from

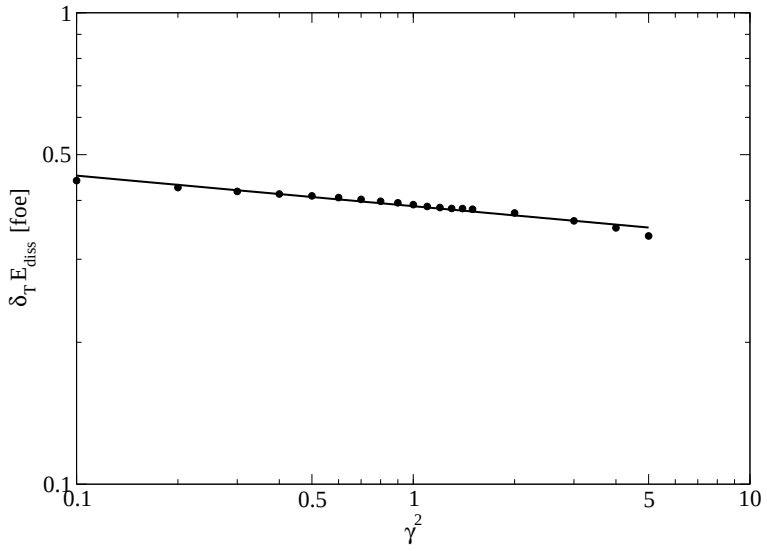

Figure 5.3: Gain in dissociation energy of the shock, $\delta_T E_{diss}$ (in foe), as a function of the strength of nuclear electron capture, γ^2. The calculated points correspond to standard parameters of the model ($\rho_{\rm tr,10} = 43$, $m_\omega(0) = 1.7$, $T_0 = 2$ MeV, $\Delta_N = 2.5$ MeV). The line represents a power-law fit, with exponent $a = -0.065$.

its standard value to the value indicated. In Fig. 5.4, instead, we show a contour plot for $\delta_T E_{diss}$ (in foe) as a function of the two parameters $m_\omega(0)$ and T_0, the other ones being fixed at their standard values. The solid level lines are for $\gamma^2 = 1$, the dotted ones for $\gamma^2 = 0.1$ and the shaded area indicates the physically meaningful range found in Ref. [106] for the thermal parameters of the symmetry energy.

The results of Table 5.2 and Fig. 5.4 show that, under reasonable variations of the model parameters, the gain in dissociation energy of the shock changes only by about $\pm 10\%$, in the range $\delta_T E_{diss} \sim 0.35 - 0.45$ foe. This proves the robustness of our conclusions: the temperature dependence of the symmetry energy yields a systematic energy gain (less dissipation of shock energy), whose order of magnitude is $\delta_T E_{diss} \sim 0.4$ foe[7].

5.3 Conclusions and Outlooks

In this Chapter a zero-dimensional code aimed at simulating the core-collapse up to neutrino trapping has been presented.
This analysis has shown that the discussed temperature dependence of the nuclear symmetry energy acts in such a way to reduce systematically the neutronization during collapse. As a consequence, we have pointed out that, under reasonable variations of the model parameters (different strength of the nuclear electron capture, neutrino trapping density, excitation energy of the GT resonance), the gain in dissociation energy of the shock changes

[7] As in Ref [106], we have set the volume energy coefficient and the volume symmetry energy coefficient in the BBAL EOS to the values $w_0 = -16.5$ MeV and $s(0) = 29.3$ MeV respectively. Different values give a different energy gain, but do not alter our general conclusions (for example, with $w_0 = -16$ MeV and $s(0) = 31.3$ MeV we find $\delta_T E_{diss} \sim 0.3$ foe).

γ^2	$\Delta_N = 2$	$\Delta_{\rm N} = 3$	$\Delta_N = 4$	$\rho_{10,tr} = 35$	$\rho_{tr,10} = 55$
0	0.45	0.45	0.45	0.43	0.46
0.1	0.43	0.45	0.46	0.44	0.44
0.5	0.40	0.42	0.43	0.42	0.38
1	0.38	0.40	0.42	0.42	0.36
2	0.37	0.38	0.40	0.40	0.34
5	0.28	0.35	0.38	0.37	0.28

Table 5.2: Dependence of the results from the parameters of the model. We show the gain in dissociation energy of the shock, $\delta_T E_{diss}$ (in foe), for different values of the strength of nuclear electron capture, γ^2. In each column we change only the value of one parameter, either the excitation energy of the GT resonance, Δ_N (in MeV), or the trapping density, $\rho_{10,tr}$, while the other parameters are the standard ones ($\rho_{10,tr} = 43$, $m_\omega(0) = 1.7$, $T_0 = 2$ MeV, $\Delta_N = 2.5$ MeV).

only by about $\pm 10\%$, in the range $\delta_T E_{diss} \sim 0.35 - 0.45$ foe.

Such an effect is obviously not a dramatic one, when one considers that the total energy sapped from the shock by photo-dissociation of nuclei is larger by almost two orders of magnitude [33]. Indeed, even changing the nuclear strength (i.e. changing by hand the γ^2 coefficient) by a factor of ten through the unblocking of GT transitions does not qualitatively alter the final outcome of the failed explosion, at least in one-dimensional simulations [165]. Actually, recent developments of three-dimensional simulations of core-collapse supernovae indicate that the roles of neutrinos, fluid instabilities, rotation and magnetic fields are probably critical to obtain successful explosions [346]. However, when compared to the typical kinetic energies of a supernova explosion, $K_{\rm expl}$, which are imparted by the shock wave to the ejecta, a gain in shock energy of $\delta_T E_{diss} \sim 0.4$ foe is not negligible (for SN 1987A, observation gave $K_{\rm expl} \sim 1$ foe [37]). Moreover, $\delta_T E_{diss}$ is two orders of magnitude larger than the total electromagnetic output [33]. On general grounds, since both the explosion energy $K_{\rm expl}$ and the much smaller electromagnetic output have small values resulting from differences of very large quantities (gravitational energy, initial post-bounce shock energy, neutrino losses, nuclear photo-dissociation), it follows that the explosion observables can be sensitive to subtle microphysical features. In particular, systematic nuclear effects can be of particular importance, as noted also in the conclusions of Ref. [166].

These results motivate us to study the temperature dependence of the nuclear symmetry energy in more sophisticated simulations, at least in a one-dimensional code, where the position of the shock can be quantitatively evaluated and the dynamics treated in a more proper way.

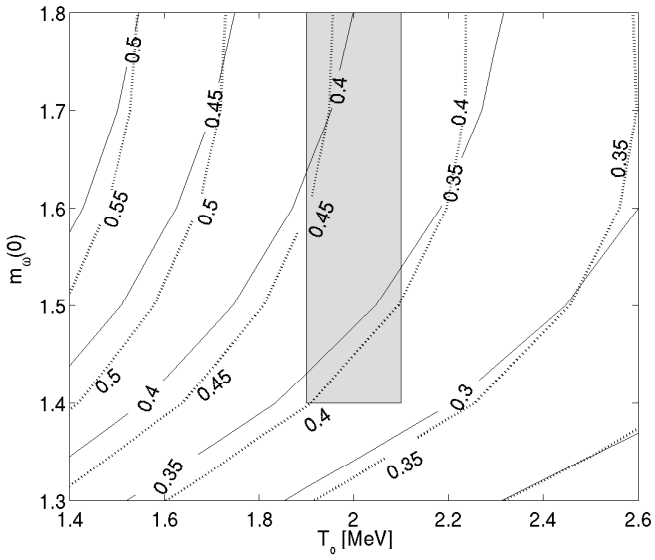

Figure 5.4: Gain in dissociation energy of the shock, $\delta_T E_{diss}$ (level lines labelled in foe), as a function of the parameters $m_\omega(0)$ and T_0. The solid contour lines correspond to $\gamma^2 = 1$, the dotted contour lines to $\gamma^2 = 0.1$. The other parameters are the standard ones ($\rho_{10,tr} = 43$, $\Delta_N = 2.5$ MeV). The shaded area shows the physical range found in Ref. [106] for the parameters $m_\omega(0)$ and T_0.

Chapter 6

Newtonian model of core-collapse with neutrino transport

This Chapter is devoted to the results obtained in the Newtonian one-dimensional simulation of core-collapse supernova. The structure of the code, as well as the the improvements made, are presented. I focus on the results obtained including the temperature dependence of the nuclear symmetry energy.

The original hydrodynamical code was developed by P. Blottiau and Ph. Mellor at CEA/DAM [41]. It is a spherically symmetric one-dimensional code with multi-group flux-limited neutrino transport; the treatment of electron capture and neutrino interactions follows the lines of the work by Bruenn [56].

6.1 Hydrodynamics

The code is written in Lagrangian coordinates, i.e. the star is divided in different zones which evolve at constant mass (cf. Section 4.1.1), and assumes spherical symmetry. The star is formed by a core, divided into about 40 zones, and an envelope, constituted of about 60 zones; the total number of zones is typically $N_{zone} = 100$. Moreover, a number of energy bins is needed to treat neutrinos. The number of energy bins, N_{bin}, originally 20, has been increased to 40, in order to assure the convergence of the integrals calculated for the transport; the price to pay is to have computationally more expensive calculations.

The system of hydrodynamical equations to be solved for each mass shell consists of a system of conservations laws for the mass, the momentum and the energy (cf. Eqs. (4.5)). The radiation equations are solved simultaneously with the fluid equations. In the specific

case, this system can be written as [41, 244] (cf also Eqs. (4.5)):

$$\frac{\mathrm{D}\rho}{\mathrm{D}t} + \rho \, \frac{1}{r^2}\frac{\partial (r^2 v)}{\partial r} = 0 \tag{6.1a}$$

$$\frac{\mathrm{D}v}{\mathrm{D}t} = -\frac{\nabla P}{\rho} + \frac{\partial \Phi}{\partial r} + \frac{1}{\rho} Q_M^0 = -4\pi r^2 \, \frac{\mathrm{d}P}{\mathrm{d}m} - \frac{Gm}{r^2} + \frac{1}{\rho} Q_M^0 \tag{6.1b}$$

$$\frac{\mathrm{D}\epsilon}{\mathrm{D}t} + P \frac{\mathrm{D}(1/\rho)}{\mathrm{D}t} = Q_{th} + \frac{1}{\rho} Q_E^0 \tag{6.1c}$$

$$\frac{\mathrm{D}Y_e}{\mathrm{D}t} = R_{Y_e}^0 \tag{6.1d}$$

$$P = P(\rho, T, Y_e) \, , \tag{6.1e}$$

where $\rho \equiv \rho_b$ is the baryon density, T the temperature, Y_e the electron fraction, P the pressure, m the enclosed mass, $R_{Y_e}^0$ is the change in the electron fraction due to microphysical processes (mainly electron capture), and the EoS closes the system[1]. Q_M^0 and Q_E^0 are the variations in the momentum and energy due to neutrinos (i.e. the momentum and energy exchanged by the fluid with the radiation field, see Section 6.3), and $Q_{th} := \mathrm{D}\epsilon_{th}/\mathrm{D}t$ represents the variation in the energy due to nuclear reactions, i.e. the energy coming from dissociation reactions (Eqs. (6.14)-(6.15)), plus the energy storage in excited states (Eq. (6.10)).
Moreover, N_{bin} equations must be added to Eqs. (6.1) for the radiative transfer (see Section 6.3).

The advancing in time is implicit, i.e. a matrix system of $(N_{bin}+3) \times N_{zone} + 1$ has to be solved (being N_{zone} the number of zones in which the star is divided, N_{bin} the number of neutrino energy bins, 3 stands for the Euler, energy and electron fraction evolution equation, and the additional equation is for the last interface velocity).

A numerical treatment of how to solve the above equations is given e.g. in the Mihalas and Mihalas textbook [244]. I just recall (see Fig. 6.1, where the spherical star is drawn) that, typically, thermodynamical variables (like pressure, density) are taken at the center of the cell, while hydrodynamical variables (like velocity, fluxes) are computed at the cell interface. Thus, if values calculated at cell center (interface) are required at the cell interface (center), a reconstruction procedure must be adopted, the simplest one being taking the average value (weighted over the mass) between two adjacent cells.

Boundary conditions

For the solution of the Eqs. (6.1), boundary conditions are needed. The following boundary conditions are imposed:

$$\begin{aligned} m(r=0,t) &= 0 \\ v(r=0,t) &= 0 \\ P(r=R,t) &= P_{ext} = const \, , \end{aligned} \tag{6.2}$$

[1] We note that in this case we do not make any distinction between the gravitational mass and the baryonic mass, since in the Newtonian case they coincide: $m_g = m_b$ (unlike in the Relativistic case, see Chapter 7). For the electron fraction source term, $R_{Y_e} = R_{Y_e}^0$, i.e. it is the one calculated in the comoving frame (I recall that the superscript "0" refers to the comoving frame).

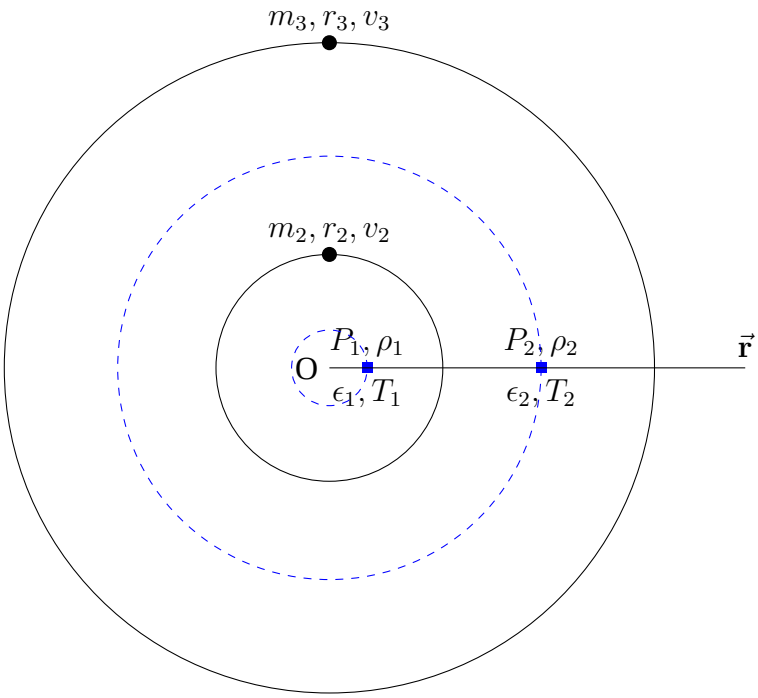

Figure 6.1: Sketch of the first two zones of the star. Thermodynamical quantities are computed at cell center (squares) while hydrodynamical quantities and fluxes are defined at cell interface (circles). The quantities m_1, r_1, v_1 are taken in O.

i.e., for each time step, the mass and the velocity at the center of the star are zero; the pressure at the edge of the star (R being the radius of the star) is taken as constant (and small). The choice to impose a constant pressure at the star surface is justified by the fact that, if the progenitor is big enough, the external shells are barely influenced by the dynamics of the core.

6.1.1 Artificial viscosity

The Newtonian code employs the artificial viscosity technique to treat the shock. As a consequence, the momentum and energy equations, Eqs. (6.1b) and (6.1c), must be re-written as:

$$\frac{\mathrm{D}v}{\mathrm{D}t} = -4\pi r^2 \frac{\mathrm{d}(P+Q)}{\mathrm{d}m} - \frac{Gm}{r^2} + \frac{1}{\rho} Q_M^0 \tag{6.3a}$$

$$\frac{\mathrm{D}\epsilon}{\mathrm{D}t} + (P+Q)\frac{\mathrm{D}(1/\rho)}{\mathrm{D}t} = Q_{th} + \frac{1}{\rho} Q_E^0 \,, \tag{6.3b}$$

where Q stands for the viscosity pressure, or pseudoviscosity. The choice of this term is quite delicate and depends on the specific problem (cf. Section 4.1). In this case, an expression analogue to the one proposed by Noh [256] (cf. Eq. (4.16)) has been adopted:

$$Q = \begin{cases} (\Gamma-1)\rho \left(c_0 \sqrt{\epsilon - \epsilon_{th}} \left|\Delta v\right| + c_1 \left(\Delta v\right)^2 \right) & (\mathrm{div}\ v < 0) \\ 0 & (\mathrm{otherwise}) \end{cases} \,, \tag{6.4}$$

where ϵ is the total internal energy, ϵ_{th} is the thermal energy (see next Section), $\Delta v = v_{j+1} - v_j$ is the difference in the velocity of two neighbouring cells, and the choice of the value of the coefficients c_0 and c_1 is: $c_0 = 0.5$ and $c_1 = 0.5$. The condition on the divergence of the velocity, which in spherical symmetry reads:

$$\mathrm{div}\ v = \frac{1}{r^2}\frac{\partial(r^2\ v)}{\partial r} = 4\pi\ \rho\frac{\mathrm{d}(r^2 v)}{\mathrm{d}m} < 0\ , \tag{6.5}$$

assures that the matter is in the compression phase. We notice that, far from shock, Q is small since the velocity profile is not steep, thus Δv is small.

6.2 Equation of state

The star is divided into two distinct regions: the core and the envelope. The complex structure and composition of the envelope, determined by the different nuclear burning stages, are simplified by dividing it into shells, where we impose the existence of a mean representative nucleus, chosen following the results of the common stellar evolution codes (see e.g. [345]). Going from the edge of the inner core towards the surface, we distinguish: a silicon shell (where we impose $A = 28$, $Z = 14$), an oxygen shell ($A = 16$, $Z = 8$), a helium shell ($A = 4$, $Z = 2$), and a hydrogen outer shell ($A = 2$, $Z = 1$). The electron fraction is fixed to 0.5. The matter is treated as an ideal gas of baryons, electrons and photons. Thus, in the following, the discussion about the EoS will focus on the EoS which describes the matter in the core.

The EoS originally employed in the code was the one derived by Bethe *et al.*(BBAL) [34], matched to the nuclear EoS derived in Bonche and Vautherin [45] and by Suraud [304] above $\sim 2 \times 10^{13}$ g cm^{-3}. We have decided to keep, at first, this choice for the EoS. Indeed, we want at first to investigate the effect of the temperature dependence of the nuclear symmetry energy in a one-dimensional code with conditions as closer as possible to the ones used in our one-zone code, in order to perform a systematic comparison. We can thus choose to run the code with the BBAL EoS, with $E_{sym} = E_{sym}(0)$, or $E_{sym} = E_{sym}(T)$. I have also worked to implement the routine version of the Lattimer and Swesty EoS; in the latter, it is not yet possible to study the effect of the temperature dependent nuclear symmetry energy derived in Donati *et al.* [106].

The BBAL EoS is implemented according to the analytical expressions described in Chapter 5. At variance with the one-zone code, where the independent variables are chosen to be the density, the temperature and the electron fraction, the hydrodynamical code works with (ρ, ϵ, Y_e) as independent variables. A routine which recovers the temperature from the internal energy has therefore been supplied. Since the EoS is analytical, also the routine which recovers the temperature is analytical (i.e. the required derivatives of the thermodynamical quantities are calculated analytically).

The total pressure and specific internal energy of the system contain the baryon, lepton and photon contribution, which can be added up independently as:

$$P = P_b + P_l + P_{ph} \tag{6.6}$$

$$\epsilon = \epsilon_b + \epsilon_l + \epsilon_{ph}\ , \tag{6.7}$$

where, detailing the different contributions:

- Baryon contribution: the BBAL EoS [34] assumes the particles to form an ideal classical gas:

$$P_b = \left(\frac{X_h}{A} + \frac{X_\alpha}{4} + X_n + X_p\right) n_b k_B T \tag{6.8}$$

$$\epsilon_b = \frac{3}{2}\frac{P_b}{\rho_b} + \epsilon_{b,th} \tag{6.9}$$

$$\epsilon_{b,th} = \frac{E_{th}}{A m_u} = \frac{1}{m_u}\frac{\pi^2}{4}\frac{(k_B T)^2}{\epsilon_F}\frac{m^*}{m} , \tag{6.10}$$

  where $\epsilon_{b,th}$ represents the nuclear thermal excitation energy, which can be derived in the Fermi gas model (cf. Eq. (5.21f) in Chapter 5 for the corresponding entropy contribution). The effective mass of nucleons in nuclei (both for protons and neutrons) was taken to be [35]:

$$\frac{m^*(\rho, x)}{m} = 1 + 10.67 x^2 (1-x)^{4/3} \left[1 - \frac{3}{2}\left(\frac{\rho}{\rho_0}\right)^{1/3} + \frac{1}{2}\left(\frac{\rho}{\rho_0}\right)\right] ; \tag{6.11}$$

  this expression, derived in the liquid drop model framework, has been claimed to be in agreement with more microscopic calculations by Bonche and Vautherin [45] and to reproduce the value $m^*/m \approx 2$ in the case of iron. We have replaced the above expression for the effective mass with the temperature dependent effective mass (Eq. (2.63)) as explained in Chapter 5.

- Lepton contribution: electrons are considered as relativistic particles. Neutrino pressure and energy are calculated considering neutrinos as ultra-relativistic degenerate (massless) particles.

- Photon contribution: photon pressure and energy are simply given by [34, 295]:

$$P_{ph} = \frac{1}{3} a T^4 \tag{6.12}$$

$$\epsilon_{ph} = \frac{a T^4}{\rho} , \tag{6.13}$$

  with $a = 7.565 \times 10^{-15}$ erg^{-3} cm^{-3}.

The thermal dissociation of nuclei into α-particles and nucleons,

$$(A, Z) + \gamma \rightarrow \frac{Z}{2}\,\alpha + (A - 2Z)\, n + Q_{diss} , \tag{6.14}$$

is taken into account as well as the thermal dissociation of ^{4}He in protons and neutrons:

$$^4\mathrm{He} + \gamma \rightarrow 2\,p + 2\,n + Q_{diss} , \qquad Q_{diss} = 28.3\ \mathrm{MeV} , \tag{6.15}$$

according to the Saha equation [34, 295].

For the high density region, a match to a nuclear EoS has been done, ensuring the continuity in the pressure profile. Above a given density ($\approx 2 \times 10^{13}$ g cm^{-3}), the EoS

derived by Bonche and Vautherin [45, 46] and by Suraud [304] was taken to model the transition from nuclei to nuclear matter. Above the matching point, the EoS is calculated along adiabatic paths (i.e. at constant entropy), and we keep only the informations about the thermodynamical quantities (P, ϵ), and not about the composition of the system. In Ref. [45], the EoS is derived using mean field (HF) approximation and a Skyrme NN interaction; neutrinos are considered in β equilibrium, which is a valid approximation in the density range of validity of the EoS. The pressure is well approximated by a polytropic-like expression, with a density dependent adiabatic index. In our model, the density dependent Γ changes from 1.29 to 2, up to 3 for very high density. The transition densities are parameters of the model, which can be tuned to test their impact on the results. Typically, the match to the Bonche and Vautherin EoS is done at $0.02\ \mathrm{fm}^{-3}$, and the stiffening of the EoS is taken to be respectively at 0.1 fm^{-3} (Γ from 1.29 to 2) and 0.12 fm^{-3} (Γ from 2 to 3).
Of course, once we change the EoS, we cannot include anymore our expression for the temperature dependent symmetry energy. However, the match to the high density EoS has been done for densities and temperatures at which the claimed T-dependence of the nucleon effective mass is no longer efficient ($T > 2$ MeV, and/or density at which nuclei are no more expected to be present).

6.3 Neutrino transport

Neutrino transport is treated in the diffusion approximation, in the flux-limited diffusion approximation scheme. The transport is written in the comoving frame, which comprises a set of inertial frames, having a velocity that instantaneously coincides with that of the particles; this frame is identical to the Lagrangian frame for hydrodynamics (and, in the relativistic case, is the "proper" frame). It is the "natural" frame, where the microscopic description of the properties of the matter applies, the details of the matter-radiation interaction are easier handled and the material properties are isotropic, which simplifies the implementation.

Even if, in principle, the Boltzmann transport equation (BTE) for each neutrino species should be exactly solved, most of neutrino transport calculations in SN simulations have been carried out in this approximation. The BTE for the spherically symmetric case, neglecting $\mathcal{O}(v/c)$ terms, reads [56, 237]:

$$\frac{1}{c}\frac{\partial f}{\partial t} + \frac{\mu}{r^2}\frac{\partial (r^2 f)}{\partial r} + \frac{1}{r}\frac{\partial [(1-\mu^2) f]}{\partial \mu} = \mathcal{C}[f]\ , \tag{6.16}$$

where $f = f(t, r, \mu, \omega)$ is the neutrino distribution function (being r the distance of the considered fluid element from the center of the star in Lagrangian coordinates, μ the cosine angle between the propagation direction of the neutrino and the outward radial direction, ω the neutrino energy), which is defined in such a way that the mean number of neutrinos at time t, at position r (within a volume $\mathrm{d}V$ and a solid angle $\mathrm{d}\Omega$) and with energy between ω and $\omega + \mathrm{d}\omega$ is given by: $f \mathrm{d}V \mathrm{d}\Omega \omega^2 \mathrm{d}\omega/(2\pi\hbar c)^3$ and $\mathcal{C}[f] = (\mathrm{d}f/\mathrm{d}t)_{coll}$ is the collision integral, which contains all of the informations about the changes in f due to reactions (absorption, emission), and collisions.

The diffusion approximation equation is then written as [48]:

$$\frac{1}{c}\frac{\partial f}{\partial t} = \nabla \cdot (D \nabla f) + \frac{1}{c}\left(\frac{\mathrm{d}f}{\mathrm{d}t}\right)_{coll} , \tag{6.17}$$

where D is the diffusion coefficient. In the initial stage of collapse, only electron neutrinos coming from electron capture are present; we therefore consider only one neutrino species, ν_e. Antineutrinos and other neutrino flavours, ν_μ and ν_τ, shall be generated after the shock [202, 173, 251]. In order to avoid difficulties in the transition from the diffusion regime to the free streaming limit, flux-limiting schemes have been employed. In the code, the prescription by Bowers and Wilson [48, 49] has been adopted. The diffusion coefficient, usually equal to $\lambda_\nu/3$ (where λ_ν stands for the mean free path), has been re-expressed as:

$$D = \frac{\lambda_\nu}{3 + \lambda_\nu \left|\frac{\partial \log f}{\partial r}\right| \xi\left(\lambda_\nu \left|\frac{\partial \log f}{\partial r}\right|\right)} , \tag{6.18}$$

where $\xi(x)$ is a function which can be chosen in various way: $\xi(x) = 1$ corresponds to the "minimal flux limiter", while we have used the expression [48]:

$$\xi(x) = 1 + \frac{3}{1 + x/2 + x^2/8}, \quad x = \lambda_\nu \left|\frac{\partial \log f}{\partial r}\right| , \tag{6.19}$$

which gives the expected limit behaviours: if $\left|\frac{\partial \log f}{\partial r}\right| \lambda_\nu \ll 1$ (optically thick region), D approaches the value $\lambda_\nu/3$, while for $\left|\frac{\partial \log f}{\partial r}\right| \lambda_\nu \gg 1$ one recovers the free streaming case[2]with the particle velocity $v = c$ if the collision integral is zero.

However, in Ref. [237], it has been pointed out that this prescription does not ensure an accurate interpolation in the transition regime. Nevertheless, the authors have checked numerically the agreement of the diffusion approximation together with the assumption Eq. (6.18) with the exact solution of the transport equation, finding an "acceptable qualitative agreement when matter through which neutrinos diffuse is at rest". Therefore, we keep this prescription.

The equation of transport Eq. (6.17) is solved for each energy bin:

$$\frac{1}{c}\frac{\partial f_i}{\partial t} = \nabla \cdot (D \nabla f_i) + \frac{1}{c}\left(\frac{\mathrm{d}f_i}{\mathrm{d}t}\right)_{coll} \qquad i = 1, \ldots, N_{bin} . \tag{6.22}$$

The collision integral contains emission and absorption terms due to electron capture on free nucleons and nuclei, elastic scattering on free nucleons and nuclei, and can include

[2] If $\left|\frac{\partial \log f}{\partial r}\right| \lambda_\nu \gg 1$, $\xi(x) \simeq 1$, and thus:

$$D \approx \frac{\lambda_\nu}{3 + \frac{\lambda_\nu}{f}\left|\frac{\partial f}{\partial r}\right|} . \tag{6.20}$$

Eq. (6.17) then becomes:

$$\frac{1}{c}\frac{\partial f}{\partial t} \approx \vec{\mathbf{k}} \cdot \nabla f + \ldots , \tag{6.21}$$

where $\vec{\mathbf{k}}$ is the direction of propagation.

also neutrino-electron scattering, as treated in Bruenn's paper [56] (I recall the main expressions in Appendix G). The number of neutrino energy bins, originally 20, has been increased to 40; neutrino energies span from 10^{-2} MeV to 300 MeV, in geometrical progression, centered around 10 MeV in $N_{bin}/2$.

If one considers also first order terms in v/c [74, 56], other contributions should be added to the left-hand side of the Eq. (6.16) (cf. Eq. A1-A4 in [56]). As a result of the MGFLDA (see also Appendix G), expanding the distribution function f in a Legendre series and keeping only the zero and first-order moment ($\psi^{(0)}$ and $\psi^{(1)}$), and neglecting $\mathcal{O}(v^2/c^2)$ terms (i.e. velocity-dependent terms) in the BTE, one ends up with an additional term which corresponds to the change in the neutrino distribution function due to compression or expansion of the matter:

$$\frac{1}{3c}\frac{\partial \log\rho}{\partial t}\left(\omega\frac{\partial\psi^{(0)}}{\partial\omega}\right) \ . \tag{6.23}$$

This term is exhaustively discussed in Bruenn [56], Appendix B, where it has been pointed out that to treat consistently the energy exchange between matter and neutrinos for an arbitrary neutrino mean free path, only a fraction $\eta(r,\omega)$ of neutrinos must be affected by the compression/expansion term; the $1-\eta(r,\omega)$ neutrino distribution function evolves according to the MGFLDA equation without the term in Eq. (6.23). The implementation in the code follows this line.

The change in electron fraction is then given by integrating the number of neutrinos emitted (or absorbed) in capture processes (scattering processes just change the direction or the energy of neutrinos, but do not have any effect on the number variation). This is a consequence of the lepton number conservation, i.e. the emission (absorption) of an electron-type neutrino gives rise to a loss (gain) of an electron. Thus [56]:

$$\frac{\mathrm{D}Y_e}{\mathrm{D}t} = R^0_{Y_e} = -\frac{1}{N_A\,\rho}\frac{4\pi c}{(2\pi\hbar c)^3}\int_0^\infty \omega^2\left\{j(\omega)[1-f(\omega)] - \frac{1}{\lambda^{(a)}(\omega)}f(\omega)\right\}\mathrm{d}\omega\,, \tag{6.24}$$

where $j(\omega)$ and $1/\lambda^{(a)}(\omega)$ account for emission and neutrino absorption (see Appendix G and Ref. [56])[3], i.e. the change in the electron fraction (actually, also antineutrinos should be considered, but their contribution will be neglected in the following) is given by the 0th-order moment of the collision integral integrated over the energy.

The energy sapped by neutrinos is given by the 1st-order moment of the collision integral [56]:

$$Q^0_E = \left(\frac{\mathrm{D}E}{\mathrm{D}t}\right)_\nu = -\frac{4\pi c}{(2\pi\hbar c)^3}\int_0^\infty \omega^3\left(\frac{\mathrm{d}f}{\mathrm{d}t}\right)_{coll}\mathrm{d}\omega \tag{6.25}$$

where $(\mathrm{d}f/\mathrm{d}t)_{coll}$ (always evaluated in the comoving frame) must contain both absorption/emission and scattering terms. The momentum transfer between neutrinos and matter is given by the first-order moment of the neutrino distribution function (cf. Eqs. (7.88)-(7.90)) and it is related to the derivative of the neutrino pressure with respect to the spatial coordinate:

$$Q^0_M = Q^0_{\nu,M} = -\frac{\partial P_\nu}{\partial r}\ , \tag{6.26}$$

[3] Actually, in Eq. (B12) in Bruenn [56], f is replaced by $\psi^{(0)}(\omega)$, since the distribution function has been expanded into a Legendre series, whose zero-order term is $\psi^{(0)}(\omega)$.

where[4][56]:

$$P_\nu = \frac{4\pi}{(2\pi\hbar c)^3}\frac{1}{3}\int_0^\infty \omega^3 f(\omega)\mathrm{d}\omega \ . \tag{6.27}$$

The term $\frac{\partial P_\nu}{\partial r}$ keeps track of the MGFLDA employed, and it contains in the energy integral the flux limiter $\xi(x)$ (cf. Eqs. (A58)-(A60) in Bruenn [56]).

The implementation of the transport equations is done coupling them with the hydrodynamical equations in an implicit scheme. In fact, even if the large number of unknowns (which of course increase with increasing number of energy bins and of spatial zones) would prefer an explicit scheme, the neutrino diffusion terms would impose a severe Courant time-step condition, since $\Delta t_{Courant} \propto 1/\lambda_\nu$ (especially at the beginning of the simulation, the neutrino mean free path is very large, so the Courant time step would be very small).

Boundary conditions

The boundary conditions on the fluxes, for each energy bin, are taken at the center and at the surface of the star:

$$\begin{aligned} F_{\nu,i}(r=0,t) &= 0 \\ F_{\nu,i}(r=R,t) &= 0 \qquad i=1,\dots N_{bin} \ . \end{aligned} \tag{6.28}$$

6.4 Flow chart

In Fig. 6.2 the flow chart for the Newtonian code is sketched. The main feature that has to be noticed is the coupling of the hydrodynamics to the neutrino transport, so that in the matrix inversion procedure one gets all the independent variables (such as velocity, energy, electron and neutrino fraction). In the "Time update" step, a check on the characteristic time step for transport is done.

6.5 Results

In this Section the results obtained by means of the Newtonian code described above are presented. We will focus on the collapse phase.

All the runs are carried out starting from a Woosley and Weaver presupernova model with a 1.3 $M_\odot$ core [348], while in the original work by Blottiau [41] the presupernova model was taken from Ref. [336]. The core is divided into about 40 zones. This might introduce concerns about the precision of the grid; however, even if it might be difficult to exactly locate the position of shock formation (as we will argue in the following), this grid spacing allows us to correctly reproduce the features of the collapse with neutrino transport in less than one day computation time.

As far as concerning the EoS, we employ the BBAL EoS [34], matched with the high density EoS derived in Suraud [304], as explained in Section 6.2. We also present

[4] As in Eq. (B12), in Eq. (A52) in Ref. [56], f is replaced by the 0-th order term of the Legendre series $\psi^{(0)}(\omega)$.

a simulation done with the Lattimer and Swesty EoS [192], routine version, with $K = 180$ MeV, for comparison with the literature and with the results obtained with the BBAL EoS.

For the microphysics inputs, we take into account, if not explicitly mentioned otherwise, the electron capture on free protons and on nuclei, including the backward reactions, and the neutrino scattering on nuclei and free nucleons, according to the Bruenn's prescription (see Appendix G). We consider only electron neutrinos, since other neutrino flavours are expected to actively influence the dynamics only in the post-bounce phase. After β equilibrium is naturally achieved (at $\rho \approx 10^{13}$ g cm^{-3}), the electron capture rates are no longer calculated.
The neutrino transport is implemented in the multi-group flux-limited diffusion approximation fashion.

6.5.1 Impact of the electron capture rates on nuclei

In order to explore the sensitivity of the model to uncertainties in the nuclear electron capture rates, we have performed a parameter study, each time varying only the strength of the electron capture on nuclei, leaving the other parameters unchanged. In particular, we have set $E_{sym} = E_{sym}(0)$. This is actually the analogous of varying the parameter γ^2 in the model described in Chapter 5.
For sake of completeness and further discussions, I report the expressions of the emissivity and absorptivity for the electron capture rates on nuclei as given by Bruenn [56]:

$$\begin{aligned} j(\omega) &= \frac{G_F^2}{(\hbar c)^4 \pi} n_b \frac{X_h}{A}\, g_A^2\, |M_{GT}|^2\, f_e(\omega + Q')\, (\omega + Q')^2 \\ &\quad \times \left[1 - \frac{(m_e c^2)^2}{(\omega + Q')^2}\right]^{1/2} \qquad (6.29) \\ \frac{1}{\lambda^{(a)}(\omega)} &= \frac{G_F^2}{(\hbar c)^4 \pi} n_b \frac{X_h}{A}\, e^{(\mu_n - \mu_p - Q')/k_B T}\, g_A^2\, |M_{GT}|^2\, [1 - f_e(\omega + Q')]\, (\omega + Q')^2 \\ &\quad \times \left[1 - \frac{(m_e c^2)^2}{(\omega + Q')^2}\right]^{1/2} , \qquad (6.30) \end{aligned}$$

where all the terms are described in Appendix G. The typical GT matrix element $|M_{GT}|^2$ is estimated in Refs. [128, 56] by the term $\frac{2}{7} N_p N_h$, where the number of particles (related to the number of protons) and holes (related to the number of neutrons) available for the capture are:

$$N_p(Z) = \begin{cases} 0 & Z \leq 20 \\ Z - 20 & 20 < Z \leq 28 \\ 8 & Z > 28 \end{cases} , \qquad (6.31)$$

$$N_h(N) = \begin{cases} 6 & N \leq 34 \\ 40 - N & 34 < N \leq 40 \\ 0 & N > 40 \end{cases} . \qquad (6.32)$$

Eqs. (6.31)-(6.32) are meant to reproduce the zero-order shell model results [56]. If one takes into account the calculations in Ref. [130] (FFN1985 from now on), the $|M_{GT}|^2$ can

be estimated by (cf. Eq. (28) in [130])[5]:

$$|M_{GT}|^2 = \begin{cases} 2.5 & N < 40\,, Z > 20\,, \mu_e + m_e c^2 < |\hat{\mu} + 1.29| + \Delta_N \\ 10 & N < 40\,, Z > 20\,, \mu_e + m_e c^2 > |\hat{\mu} + 1.29| + \Delta_N \\ 10^{1-2.23/T[\mathrm{MeV}]} & \text{otherwise}\,, \end{cases} \tag{6.35}$$

where the strength for electron capture depends on thermal unblocking and the condition on the chemical potentials accounts for the capture threshold energy. The excitation energy Δ_N is fixed to 3 MeV [34, 56].

In Fig. 6.3 we display the velocity (upper left panel), density (upper right panel), electron fraction (lower left panel) profiles as a function of the enclosed mass, and central lepton fraction (lower right panel) as a function of the central density at bounce. We define the bounce as the maximum scrunch, i.e. when the maximum central density is reached. The bounce occurs around 210-220 ms (depending on the model) after starting the simulation; this can be understood considering in a first approximation the collapse as a free fall, whose Newtonian timescale is given by [295]:

$$t_{ff} \simeq \sqrt{\frac{1}{24\pi G\rho}}\,, \tag{6.36}$$

which, for initial central density $\rho \approx 10^{10}$ g cm^{-3}, gives $t_{ff} \approx 210$ ms.
In Fig. 6.3 solid black lines correspond to the standard Bruenn parameterization of the emissivity and absorptivity [126, 56]; dashed red lines correspond to FFN1985 capture rates; dashed-dotted green lines and dashed-dotted-dotted blue lines results are obtained holding the product $N_p N_h$ constant, and equal to 1 and 10, respectively. This is a simple and easily reproducible way to change the strength of the capture rates. The same prescription was adopted, e.g., in Ref. [166].
We notice that, for example, changing the product $N_p N_h$ by a factor of ten, the final lepton fraction changes from 0.345 to 0.308, i.e. by $\sim 11\%$, and the enclosed mass at bounce from 0.82 to 0.71, i.e. by $\sim 13\%$, which is in reasonable agreement with the conclusions of Ref. [166]. However, the absolute values of the position of the shock wave shown in Ref. [166] are different from ours, namely, the shock forms systematically inwards in the case of Ref. [166]. The differences might come from different input physics, such as EoS (cf. Section 6.5.3), progenitor model, neutrino processes such as neutrino-electron scattering we are not including, but the expected trend with respect to the capture rates agrees. A supplementary variance when comparing the models might also come from the uncertainties in defining the time at bounce; in Fig. 6.3, the velocity profiles display clearly positive velocities, i.e. the shock is already formed.
If now one looks at the Y_e profiles, they present the same kind of behaviour noticed in Ref. [183]: increasing the strength of the capture rates results in smaller Y_e at center and

[5] In Eq. (28) in [130] the expression for the comparative half-life $(ft)_{ij}$ is given. This quantity is related to the allowed weak-interaction matrix elements (GT and Fermi) by [127]:

$$(\log ft)_{GT} = 3.596 - \log |M_{GT}|^2 \tag{6.33}$$
$$(\log ft)_{F} = 3.791 - \log |M_{F}|^2\,. \tag{6.34}$$

Capture rates	$\rho_{c,bounce}$ $[10^{14}$ g cm$^{-3}]$	$M_{b,encl,bounce}$ $[M_\odot]$	$Y_{e,c,bounce}$	$Y_{l,c,bounce}$
Bruenn 1985	2.83	0.86	0.299	0.372
FFN1985	2.81	0.84	0.290	0.355
$N_pN_h = 1$	2.79	0.82	0.282	0.345
$N_pN_h = 10$	2.67	0.71	0.259	0.308

Table 6.1: Central density, enclosed mass, electron and lepton fractions at bounce, for the different strengths of the electron capture on nuclei.

higher Y_e in the outer part of the core. If we now look at the Y_l profiles (lower right panel), and we compare the case of fixed N_pN_h (dashed-dotted green lines and dashed-dotted-dotted blue lines) to the case of the standard Bruenn parameterization (solid black lines and dashed red lines), the different equilibrium values after trapping come from the fact that, when the standard Bruenn parameterization is employed, the capture on nuclei is blocked for neutron rich nuclei, and the capture on free protons dominates. Due to the low free protons abundance, the total capture rates on free protons are smaller than the ones on nuclei [183], thus a smaller amount of electrons are captured and as a consequence the final lepton fraction is higher.

For clarity, in Table 6.1, I summarize some key quantities at bounce for different strength of the electron capture rates on nuclei.

If we now analyse the behaviour of the core dynamics and density as a function of time, we see in Fig. 6.4 the different cell radii (left panel) and the central density (right panel) as a function of post bounce time. We notice that only the core is concerned by the collapse (radii bigger than $\sim$ 1000 km are nearly unaffected); the figure shows the central bounce and subsequent oscillations. The central density reaches the maximum value at bounce, then oscillates as a consequence of the re-expansion of the matter. I have taken the case where FFN1985 are employed as an example case.

6.5.2 Impact of the temperature dependence of the symmetry energy

To evaluate the impact of the temperature dependent effective mass (through the temperature dependent nuclear symmetry energy), we have run the simulation twice, in analogy with the procedure adopted in Chapter 5: once implementing the temperature dependence $E_{sym} = E_{sym}(T)$ and obtaining $Y_l|_T$ and once setting $E_{sym} = E_{sym}(0)$ and obtaining $Y_l|_0$. We thus act on the bulk part of the EoS and on the Q-value of the electron capture rates on nuclei as explained in Chapter 5. In Fig. 6.5 we plot the velocity (upper left panel), density (upper right panel), electron fraction (lower left panel) profiles as a function of the enclosed mass, and central lepton fractions (lower right panel) as a function of the central density at bounce, for the FFN1985 capture rates on nuclei. In the lower right panel, the inset shows a zoom of the final lepton fraction as a function of the central density.

We notice a reduction of the deleptonization in the case of temperature dependent nuclear symmetry energy. The final lepton fraction is increased from $Y_l|_0 = 0.355$ to $Y_l|_T = 0.359$; thus $\delta Y_{l,T} = 0.004$, which is in agreement with what we have found in

Capture rates	$\rho_{c,bounce}$ $[10^{14}$ g cm$^{-3}]$	$M_{b,encl,bounce}$ $[M_\odot]$	$Y_{l,c,bounce}$
Bruenn 1985, $E_{sym}(0)$	2.83	0.86	0.372
Bruenn 1985, $E_{sym}(T)$	2.61	0.93 (0.07)	0.377 (0.005)
FFN1985, $E_{sym}(0)$	2.81	0.84	0.355
FFN1985, $E_{sym}(T)$	2.58	0.92 (0.08)	0.359 (0.004)
$N_pN_h = 1$, $E_{sym}(0)$	2.79	0.82	0.345
$N_pN_h = 1$, $E_{sym}(T)$	2.57	0.90 (0.08)	0.348 (0.003)
$N_pN_h = 10$, $E_{sym}(0)$	2.67	0.71	0.308
$N_pN_h = 10$, $E_{sym}(T)$	2.49	0.81 (0.1)	0.311 (0.003)

Table 6.2: Central density, enclosed mass, lepton fraction at bounce, for the different strengths of the electron capture on nuclei, and for $E_{sym} = E_{sym}(0)$ or $E_{sym} = E_{sym}(T)$. The values in parenthesis are the differences due to the claimed thermal effect in the enclosed mass $\delta_T M_{encl} = M_{b,encl,bounce}|_T - M_{b,encl,bounce}|_0$ and lepton fraction $\delta_T Y_l = Y_{l,c,bounce}|_T - Y_{l,c,bounce}|_0$ at bounce.

Chapter 5. The corresponding effect on the dynamics is non-negligible and surprisingly big: the formation of the shock wave is shifted from 0.84 to 0.92, i.e. $\sim 9\%$. This is not only due to the reduction of the deleptonization; in fact, not only the reaction Q-values, but also the EoS of the bulk matter, and the particle abundances, are affected, and this might change the overall dynamics.

In the case of the FFN1985 capture rates, we plot, in Fig. 6.6, the neutrino distribution functions as a function of neutrino energy at different times along the collapse, for the innermost zone (left panels), the zone located in the middle of the core (central panels) and the one at the outer edge of the core (right panels). The upper (lower) panels show the results obtained for the run where $E_{sym} = E_{sym}(0)$ ($E_{sym} = E_{sym}(T)$) is implemented. We see a similar behaviour in both cases: the neutrino distribution function is constructed up to a Fermi-Dirac distribution in the innermost zone, while for the outer zone of the core the neutrinos do not reach a Fermi-Dirac distribution, since they are not yet thermalized with matter, i.e. the density in not high enough to completely trap them. The peak of the distribution, when the Fermi-Dirac is not yet achieved, is around 10 MeV.

To prove that the effect due to the temperature dependence of the nuclear symmetry energy is systematic, and acts for different strengths of the electron capture rates on nuclei, we plot in Fig. 6.7 the velocity and Y_l profiles at bounce for different strength of electron capture rates on nuclei: from top to bottom panels, the standard Bruenn prescription [56] is employed, either with N_pN_h from Fuller 1982 [126] (Eqs. (6.31)-(6.32)), or keeping the factor N_pN_h fixed and equal to 1 and 10. We observe in all cases the same *systematic* behaviour: the deleptonization is slightly reduced when the temperature dependence of the symmetry energy is considered, and the shock wave formation is shifted outwards.

For clarity, in Tab. 6.2, I summarize some key quantities at bounce, for the run where $E_{sym} = E_{sym}(0)$ or $E_{sym} = E_{sym}(T)$ has been set.

6.5.3 Lattimer and Swesty EoS routine

We have also performed simulations using the routine version of the Lattimer and Swesty EoS [192], version v2.7. The results in Fig. 6.8 are shown for FFN1985 capture rates on nuclei. The α particle binding energy has not been corrected; however, as discussed in Appendix F, this does not have a big impact on the thermodynamical quantities.

In Fig. 6.8 we plot the velocity (upper left panel), density (upper right panel), electron fraction (lower left panel) profiles as a function of the enclosed mass, and central lepton fractions (lower right panel) as a function of the central density at bounce. The bounce is located around 0.69 $M_{\odot}$, which is in reasonable agreement with the Newtonian simulations showed, e.g., in Ref. [166]. Therefore, the fact that in the previous results the shock is forming at ~ 0.8 enclosed mass, i.e. systematically outwards with respect to the simulations e.g. in Ref. [166], might come from the EoS adopted (BBAL together with the Suraud EoS).

6.6 Conclusions and Outlooks

In this Chapter we have presented simulations performed with a Newtonian one-dimensional code with neutrino transport.

We have improved the code originally developed by P. Blottiau and Ph. Mellor including the temperature dependence of the nuclear symmetry energy via the temperature dependent nucleon effective mass in the BBAL EoS, as explained above. We wanted first to compare the effect of this new term, which enters in the EoS and modifies the Q-value of the electron capture on nuclei, with the results obtained with the one-zone code described in Chapter 5. Using the one-zone code, in fact, the determination of the position of the formation of the shock wave can be only qualitative. Despite differences due to the model, the results on the deleptonization and on the final value of the lepton fraction generally agree, and confirm the behaviour that the inclusion of a temperature dependence of nuclear symmetry energy shifts the formation of the shock wave outward of a non-negligible amount. In particular, we found that $\delta_T Y_l$ varies from 0.003 to 0.005 depending on the strength of the electron capture rates on nuclei. This small difference results in a surprisingly big difference of the enclosed mass at bounce, which varies from 0.06 to 0.1 $M_{\odot}$.

Moreover, we have implemented a routine version of the LS EoS, finding values of the total lepton fraction after trapping and enclosed mass at bounce in global agreement with the literature.

In the future, we foresee to test different EoS, and implement neutrino processes other than the ones listed above; the implementation of the neutrino-electron scattering is already underway. It would be very instructive then to compare the obtained results with the Relativistic code described in Chapter 7, in order to evaluate the effect of the neutrino transport in the simulations.

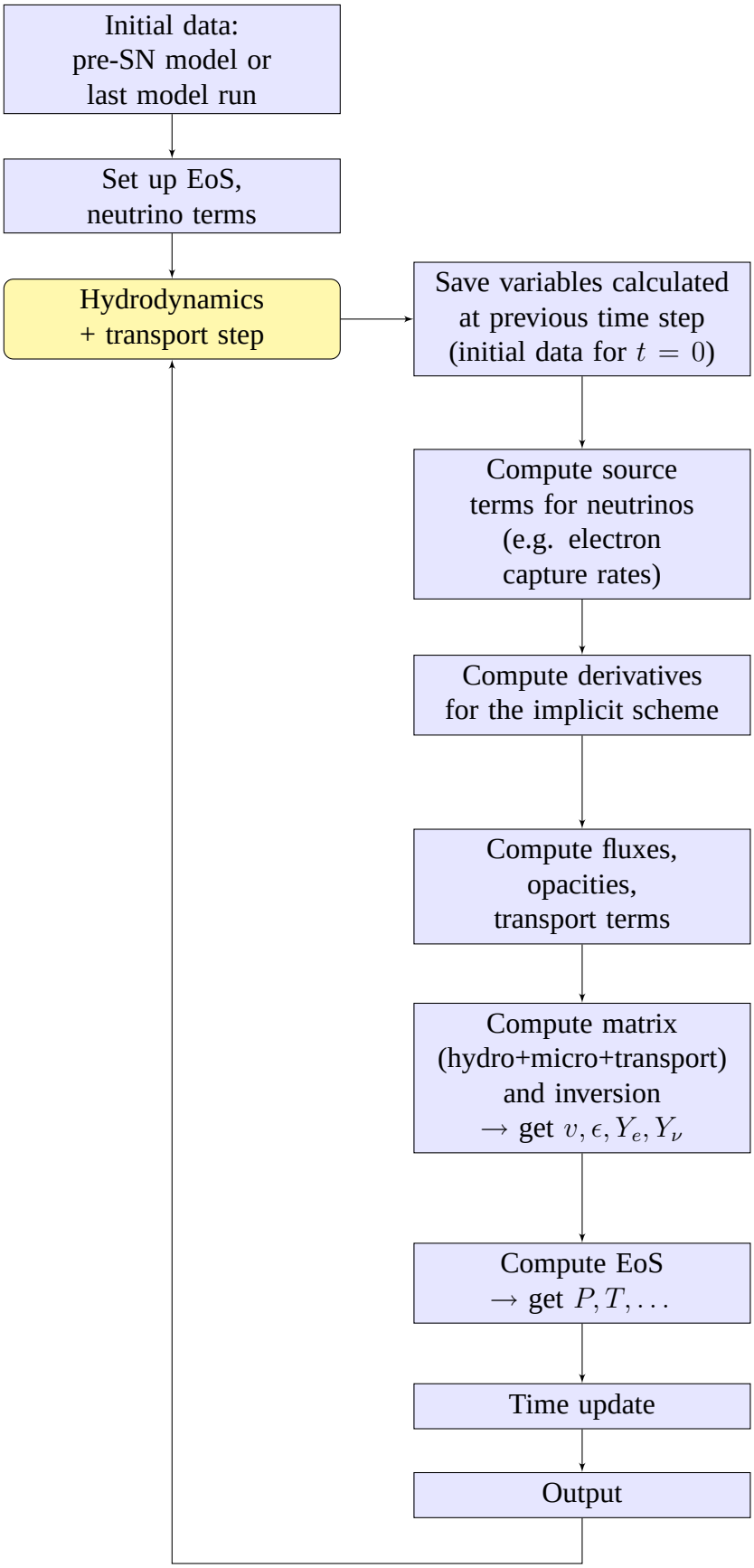

Figure 6.2: Flow chart of the Newtonian code.

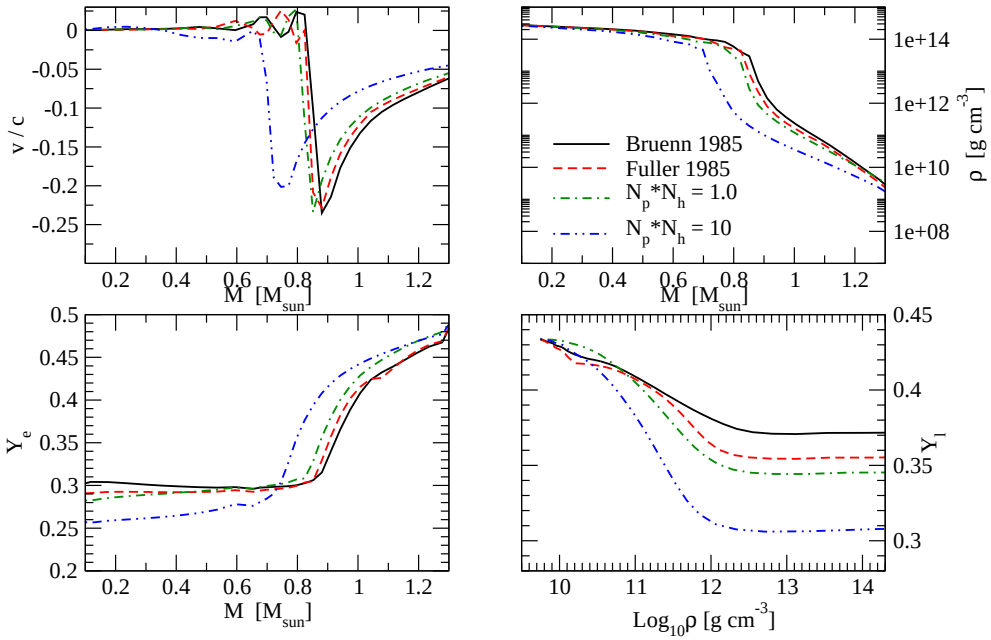

Figure 6.3: Velocity (upper left panel), density (upper right panel), electron fraction (lower left panel) profiles as a function of the enclosed mass, and central lepton fraction (lower right panel) as a function of the central density at bounce. Solid black lines and dashed red lines correspond, respectively, to the Bruenn 1985, FFN1985 capture rates on nuclei. Dashed-dotted green lines and dashed-dotted-dotted blue lines results are obtained keeping the product $N_p N_h$ in Eqs. (6.29)-(6.30) fixed and equal to 1 and 10.

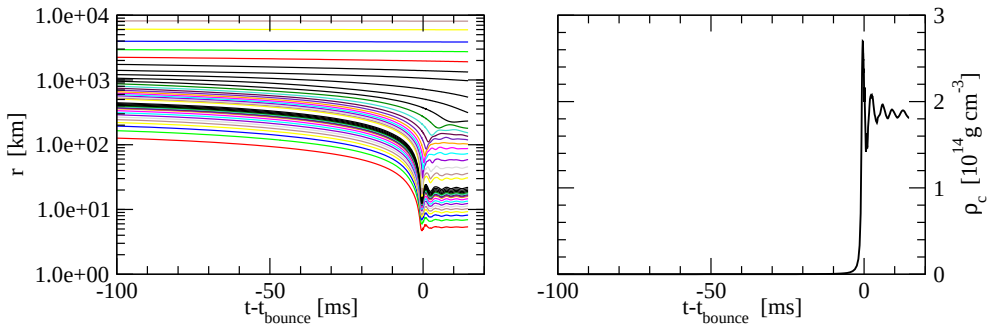

Figure 6.4: Different cell radii (left panel) and central density (right panel) as a function of post bounce time.

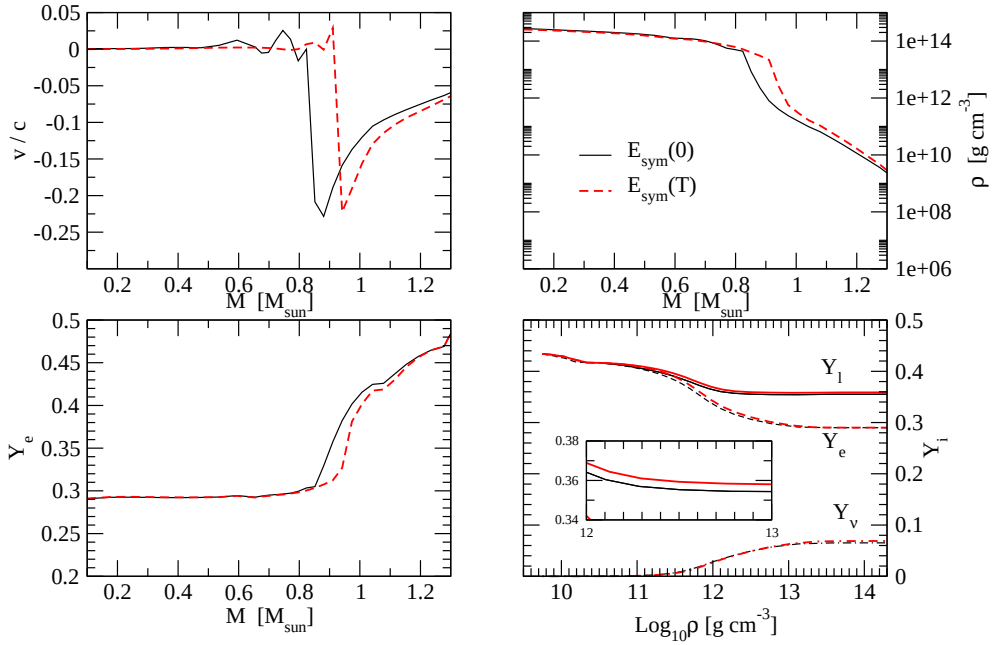

Figure 6.5: Velocity (upper left panel), density (upper right panel), electron fraction (lower left panel) profiles as a function of the enclosed mass, and central lepton fractions (lower right panel) as a function of the central density at bounce. In the lower right panel, the inset shows a zoom of the final lepton fraction as a function of the central density. Except for the lower right panel, solid black lines correspond to the case $E_{sym} = E_{sym}(0)$, while dashed red lines correspond to the case $E_{sym} = E_{sym}(T)$. In the lower right panel, thin black lines correspond to the case of constant symmetry energy, while thick red lines correspond to the case of temperature dependent symmetry energy; solid (dashed / dashed-dotted) lines indicate the central lepton (electron / neutrino) fraction. The capture rates on nuclei are the FFN1985 ones.

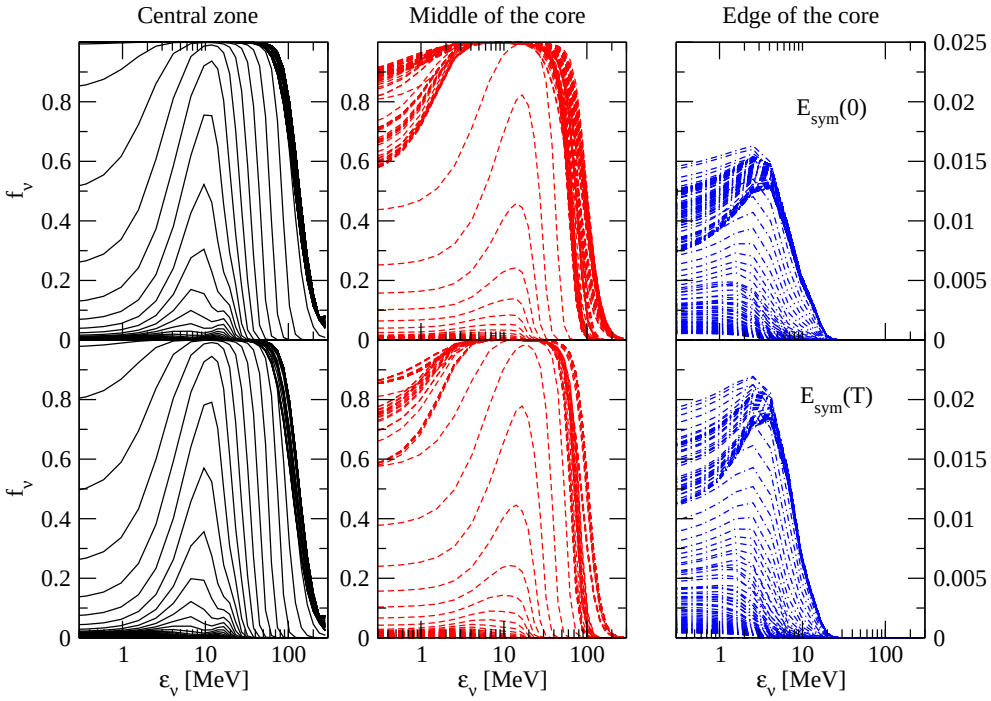

Figure 6.6: Neutrino distribution functions as a function of neutrino energy at different times along the collapse, for the innermost zone (left panels), the zone located in the middle of the core (central panels) and the one at the outer edge of the core (right panels). For the upper panels: $E_{sym} = E_{sym}(0)$, while for the lower panels: $E_{sym} = E_{sym}(T)$. The capture rates on nuclei are the FFN1985 ones.

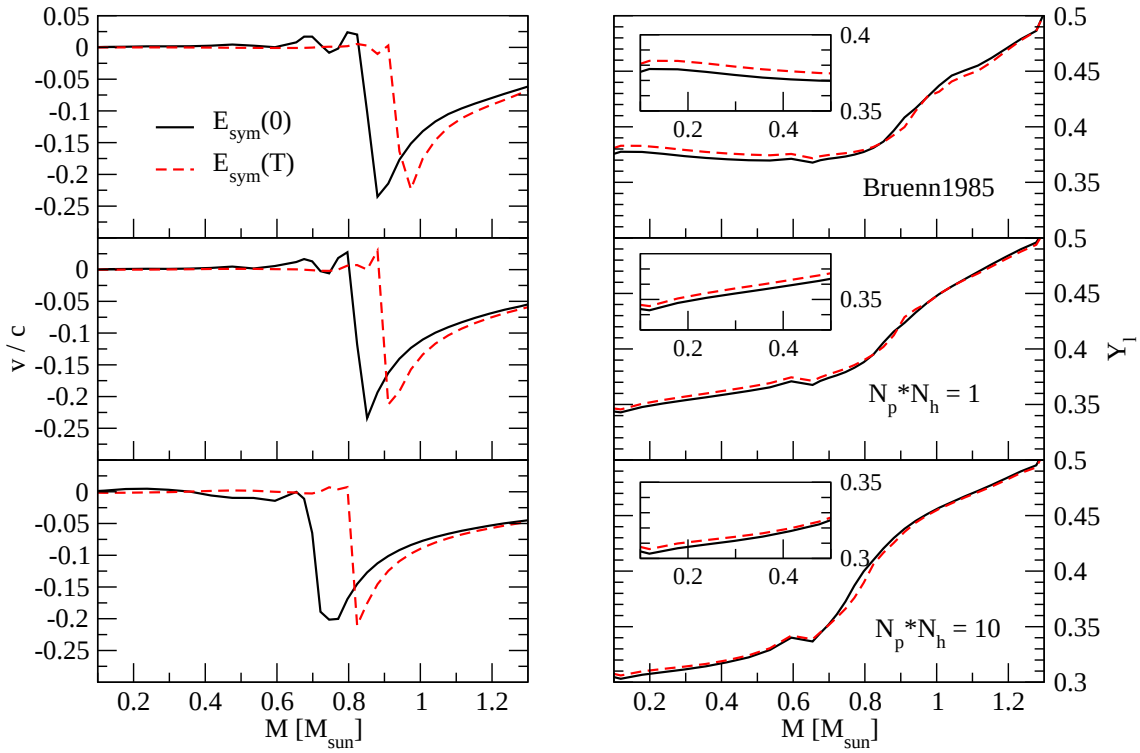

Figure 6.7: Velocity (left panels), and lepton fraction (right panels) profiles as a function of the enclosed mass at bounce. The insets show a zoom of the final lepton fraction as a function of the enclosed mass. Solid black lines correspond to the case $E_{sym} = E_{sym}(0)$, while dashed red lines correspond to the case $E_{sym} = E_{sym}(T)$. In the upper panels, $N_p N_h$ are taken as in the standard Bruenn prescription (Eqs. (6.31)-(6.32)), in the middle (lower) panels $N_p N_h$ is kept fixed and equal to 1 (10).

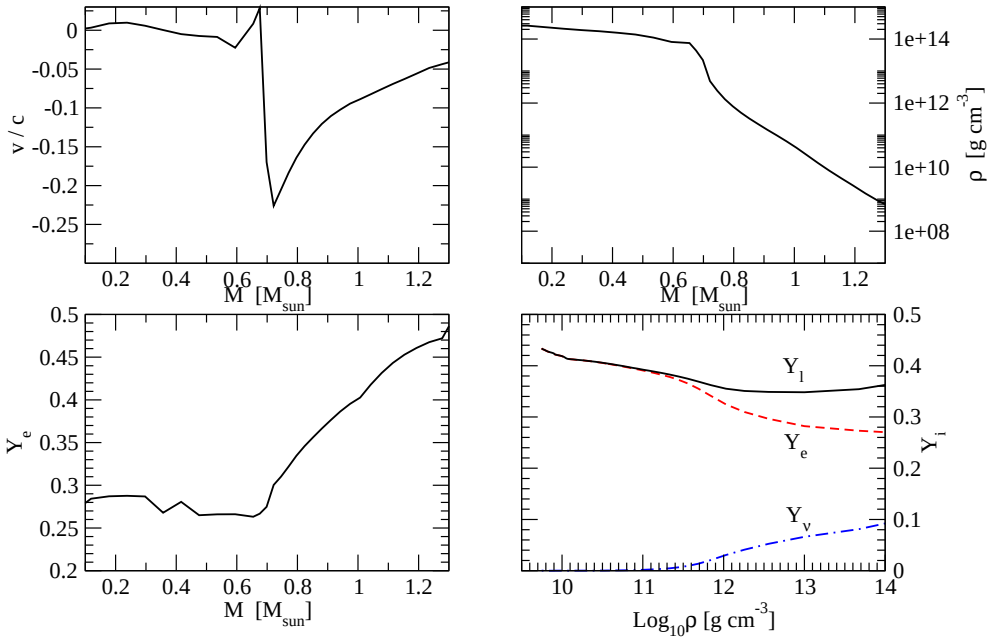

Figure 6.8: Velocity (upper left panel), density (upper right panel), electron fraction (lower left panel) profiles as a function of the enclosed mass, and central lepton fractions (lower right panel) as a function of the central density at bounce, for the run with the LS EoS ($K = 180$ MeV) and FFN1985 capture rates on nuclei.

Chapter 7

General Relativistic model of core-collapse

In this Chapter the model of the core-collapse made by means of a fully General Relativistic hydrodynamical code with a shock capturing scheme is described. The general structure of the code, as well as the modifications we have made, will be discussed. It will be explained how we have included a trapping scheme for neutrinos and obtained a Newtonian version of the code. The treatment of neutrino transport is not as advanced as in the Newtonian code; we will leave for future studies the inclusion of a transport scheme. Since no transport is implemented, the code has the advantage to be quite fast to run (it can be even run on a laptop).

GR effects are all but negligible in compact star physics. A measure of the importance of GR is given by the parameter $R_s/R = \frac{GM}{Rc^2}$, where R_s is the Schwarzschild radius and R the star radius; for neutron stars $R_s/R \sim 0.2$. In the core-collapse mechanism there is an interplay of hydrodynamics and neutrino transport which are both affected by GR effects: GR simulations are expected to modify the hydrodynamics at high densities, giving for example higher central densities and a more compact central residue with respect to the Newtonian simulations. GR effects act also over the initial shock strength, the long-term evolution of the shock position, the neutrino energies and the luminosity [60, 202, 102].

The original code we use for simulating core-collapse was developed by the Valencia group [285]. The first version, described in the paper by Romero *et al.* [285], and which runs only with a polytropic EoS, has been provided by Jérôme Novak (Luth, Meudon). An updated version of this code, which includes a more realistic EoS (a routine version of the Lattimer and Swesty EoS [192]), and the treatment of the electron capture *à la Bruenn*, was developed by José Pons and collaborators [286]. In both models, spherical symmetry is assumed, and rotation and magnetic field effects are neglected. I have worked both on the original version of the code and on its updated version.

For this Chapter, I will usually adopt the geometric units $c = G = 1$.

7.1 Hydrodynamics

7.1.1 ADM $\{3+1\}$ formalism and RGPS coordinates

Before writing the hydrodynamical equations implemented in the code, I briefly recall the main ingredients of the formalism in which we set in; I refer to the review by E. Gourgoulhon [141, 142] and Refs. therein for a proper and detailed treatment. A deeper insight on the Arnowitt-Deser-Misner (ADM) formalism is also given in Dimmelmeier's and Ott's PhD thesis [101, 262].

General Relativity describes gravitation in terms of the curvature of the spacetime. Matter is described by the 4-vector current $\mathbf{J}$ and stress-energy tensor $\mathbf{T}$, which satisfy:

$$\nabla \cdot \mathbf{J} = \mathcal{R} \tag{7.1}$$

$$-\mathbf{u} \cdot \nabla \cdot \mathbf{T} = \mathcal{Q}\,, \tag{7.2}$$

being ∇ the covariant derivatives (which is the usual nabla in a flat spacetime), $\mathbf{u}$ the 4-velocity (time-like vector[1]). $\mathcal{R}$ is the production rate of particles per unit time and volume, and $\mathcal{Q}$ is the energy and momentum production rate per unit time and volume, which depends on the frame of reference, since the energy is not a Lorentz invariant, unlike the particle number.

The main relation which links the gravitational field and the matter is the Einstein equation [246]:

$$\mathbf{R} - \frac{1}{2}\, R\, \mathbf{g} = \frac{8\pi\, G}{c^4}\, \mathbf{T} \tag{7.3}$$

which can be written in the covariant components as:

$$R_{\mu\nu} - \frac{1}{2}\, R\, g_{\mu\nu} = \frac{8\pi\, G}{c^4}\, T_{\mu\nu}\,, \tag{7.4}$$

where $R = \mathrm{Tr}\ \mathbf{R}$, $\mathbf{R}$ is the Ricci tensor, and $\mathbf{g}$ is the metric. The Newtonian limit of the Einstein equation is the Poisson equation $\nabla^2\Phi = 4\pi G\rho$ which links the gravitational field Φ to the mass density ρ.

In order to solve the system of equations (7.4), one has to turn it into a system of differential (scalar) equations, which can be done when projecting onto a coordinate system. Since there is no *a priori* choice of the coordinate system, one possible choice is to "privilege" a coordinate ($x^0 = t$, the time coordinate) and turn the system of 10 equations Eq. (7.4) into a Cauchy problem, i.e. a time-evolution problem where a set of initial data is given.

Defined a couple $(\mathcal{M}, \mathbf{g})$, where $\mathcal{M}$ is a general spacetime described by the 4- dimensional metric tensor $g_{\mu\nu}$ of signature $(-,+,+,+)$, the $\{3+1\}$ formalism decomposes (i.e. *slices*, or *foliates*) the manifold into a series of space-like hypersurfaces Σ_t, such as: $\mathcal{M} = \cup_{t\in\mathbb{R}}\Sigma_t$, where all tangent vectors to the hypersurface are space-like, and the orthogonal vectors are time-like. On each hypersurface one can define a coordinate system $\{x^i\},\ i = 1,2,3$, so that the coordinate system $\{x^\mu\},\ \mu = 0,1,2,3$ defines the whole

[1] A time-like vector $\mathbf{u}$ is characterized by: $\mathbf{u}\cdot\mathbf{u} < 0$, while a space-like vector $\mathbf{n}$ is characterized by: $\mathbf{n}\cdot\mathbf{n} > 0$.

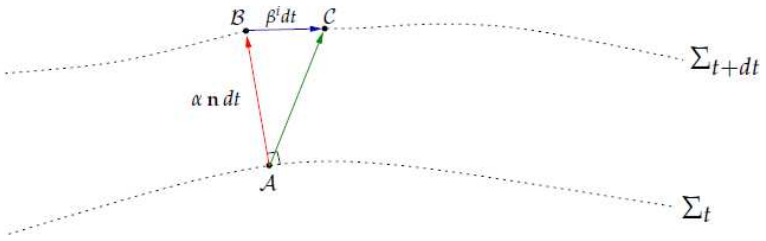

Figure 7.1: Schematic representation of the $\{3+1\}$ foliation of the spacetime, which is decomposed into hypersurfaces Σ_t. The lapse function α connects the hypersurface Σ_t with the hypersurface $\Sigma_{t+\mathrm{d}t}$. The Eulerian observer moves along the orthogonal direction with respect to Σ_t (from A to B), and not along the $x^i = const$ curves, whose path goes from A to C, being the position of C on $\Sigma_{t+\mathrm{d}t}$ determined by the shift vector β^i (from [262]).

manifold. The foundation of the $\{3+1\}$ formalism is to project the Einstein equation onto (and perpendicularly to) Σ_t.
Being $\mathbf{n}$ the orthonormal vector to the hypersurface Σ_t pointing towards $\Sigma_{t+\mathrm{d}t}$, the *lapse* function α is defined by the relation between the proper time $\mathrm{d}\tau$ (i.e. the time interval between two events on the observer's world line) measured by an Eulerian observer (fixed with respect to Σ_t) and $\mathrm{d}t$:

$$\mathrm{d}\tau = \alpha \, \mathrm{d}t \, , \tag{7.5}$$

and the *shift* 3-vector β^i (which represents the coordinate shift) is defined by (see Fig. 7.1):

$$x^i(t + \mathrm{d}t) = x^i(t) + \beta^i \, \mathrm{d}t \, . \tag{7.6}$$

The invariant line element, generally expressed as $\mathrm{d}s^2 = g_{\mu\nu}\mathrm{d}x^\mu \, \mathrm{d}x^\nu$, where $\mathrm{d}x$ is the spatial separation between two events, is given by

$$\mathrm{d}s^2 = -(\alpha^2 - \beta_i\beta^i) \, \mathrm{d}t^2 + 2 \, \beta_i \mathrm{d}x^i \, \mathrm{d}t + \gamma_{ij} \, \mathrm{d}x^i \, \mathrm{d}x^j \, , \tag{7.7}$$

where γ_{ij} is the spatial 3-metric of the 4-metric $g_{\mu\nu}$ and describes the geometry on a time slice Σ_t:

$$g_{\mu\nu} = \begin{pmatrix} -\alpha^2 + \beta_i\beta^i & \beta_i \\ \beta_j & \gamma_{ij} \end{pmatrix} \, , \tag{7.8}$$

being $\beta_i = \gamma_{ij}\beta^j$, and:

$$g^{\mu\nu} = \begin{pmatrix} -\frac{1}{\alpha^2} & \frac{1}{\alpha^2} \, \beta^i \\ \frac{1}{\alpha^2} \, \beta^j & \gamma^{ij} - \frac{1}{\alpha^2}\beta^i\beta^j \end{pmatrix} \, . \tag{7.9}$$

The description of how the hypersurfaces Σ_t are embedded into the spacetime is made through the extrinsic curvature tensor $\mathbf{K}$, which gives the curvature radius of Σ_t in the spacetime $\mathcal{M}$. It is related to the converge (or divergence) of $\mathbf{n}$, the vectors orthonormal to Σ_t (see e.g. [141] for more details). The Cauchy problem is defined by the initial data on a slice Σ_t (e.g. $\Sigma_{t=0}$) and the boundary conditions at each $\Sigma_{t'>t}$.

For the choice of the foliation of the spacetime and the spatial coordinates (i.e. for the determination of the lapse function and the shift vector), we will adopt the *radial gauge polar slicing* (RGPS), and in spherical symmetry we will also label the coordinates $\{0,1,2,3\}$ as $\{t,r,\theta,\phi\}$.
The choice of the foliation (*polar slicing*), suitable for the treatment of a gravitational collapse since it "avoids" singularity, means the choice of the lapse function α; the choice of the coordinates $\{x^i\}$ (*radial gauge*) means choosing the shift vector β_i in such a way that the shift vector is null $\beta_i = 0$, and γ_{ij} is diagonal and of the form:

$$\gamma_{ij} = \begin{pmatrix} A^2(r,t) & 0 & 0 \\ 0 & r^2 & 0 \\ 0 & 0 & r^2\,\sin^2\theta \end{pmatrix} . \tag{7.10}$$

These are Schwarzschild-type coordinates; α and $A(r,t)$ are given by:

$$\alpha = \alpha(r,t) := e^{\Phi} \tag{7.11}$$

$$X = X(r,t) := A(r,t) := \left(1 - \frac{2Gm(r,t)}{rc^2}\right)^{-1/2} . \tag{7.12}$$

In the Schwarzschild metric, m is the enclosed gravitational mass (more general, m is the mass-energy), and Φ is the metric potential (the gravitational potential in the non-relativistic limit). The metric $g_{\mu\nu}$ is given by:

$$g_{\mu\nu} = \begin{pmatrix} -\alpha^2 & 0 & 0 & 0 \\ 0 & X^2 & 0 & 0 \\ 0 & 0 & r^2 & 0 \\ 0 & 0 & 0 & r^2\,\sin^2\theta \end{pmatrix} . \tag{7.13}$$

and:

$$g^{\mu\nu} = \begin{pmatrix} -\frac{1}{\alpha^2} & 0 & 0 & 0 \\ 0 & \frac{1}{X^2} & 0 & 0 \\ 0 & 0 & \frac{1}{r^2} & 0 \\ 0 & 0 & 0 & \frac{1}{r^2\,\sin^2\theta} \end{pmatrix} . \tag{7.14}$$

The determinant of $\mathbf{g}$ (which we use in the following) is: $\det\,\mathbf{g} = -\alpha^2 X^2 r^4 \sin^2\theta$. We will also indicate: $\sqrt{-g} := \sqrt{-\det\,\mathbf{g}} = \alpha X r^2 \sin\theta$.

Eulerian observer and fluid velocity

It is crucial to define the quantities as measured by an Eulerian observer, since they enter directly in the hydrodynamical equations, written in Eulerian form. The Eulerian observer is at rest in hypersurfaces Σ_t; its world lines are normal to the hypersurface. Given an orthonormal basis: $(\mathbf{n},\mathbf{e}_1,\mathbf{e}_2,\mathbf{e}_3)$ of the "physical space" ("physical" because measurable by an observer), which can be expressed in terms of the RGPS coordinates as:

$$\begin{aligned} n^\mu &= \left(\frac{1}{\alpha},0,0,0\right) \qquad & e_2^\mu &= \left(0,0,\frac{1}{r},0\right) \\ e_1^\mu &= \left(0,\frac{1}{X},0,0\right) \qquad & e_3^\mu &= \left(0,0,0,\frac{1}{r\sin\theta}\right) , \end{aligned} \tag{7.15}$$

the 4-velocity $\mathbf{u}$ of the fluid decomposed on this orthonormal basis is:

$$\mathbf{u} = u^0 \mathbf{n} + u^i \mathbf{e}_i \ , \tag{7.16}$$

where u^0 is the Lorentz factor between the Eulerian observer and a "Lagrangian" observer (moving with the fluid) W; in RGPS coordinate (t, r, θ, ϕ):

$$\begin{aligned} W &= u^0 \ ; \\ u^t &= \frac{1}{\alpha} u^0 = \frac{W}{\alpha} \ . \end{aligned} \tag{7.17}$$

W is also the ratio between the proper time of the Eulerian observer and the "Lagrangian" (comoving frame) one: $W = \mathrm{d}\tau_{Eul}/\mathrm{d}\tau_{Lag}$, where $\mathrm{d}\tau_{Eul}/\mathrm{d}t = \alpha$ and $\mathrm{d}\tau_{Lag}/\mathrm{d}t = 1/u^t$. This relation is particularly useful when dealing with transport or neutrino source, since the neutrino sources are calculated in the comoving frame, so a change of coordinate must be done.
Since we work in spherical symmetry, the fluid is supposed moving in radial direction, therefore the θ and ϕ components of the fluid velocity are zero.
The 3-(physical) radial velocity measured by the Eulerian observer is thus related to the fluid velocity by[2]:

$$v = v^i = \frac{u^i}{W} \ , \tag{7.19}$$

and W satisfies the relation (since $\mathbf{u} \cdot \mathbf{u} = -1$):

$$W = \frac{1}{\sqrt{1 - v_i v^i}} = \frac{1}{\sqrt{1 - v^2}} \ . \tag{7.20}$$

The coordinate radial velocity in the $\{\mathbf{e}_\mu\}$ basis is related to the physical velocity by[3]:

$$V = V^i = \frac{\mathrm{d}r}{\mathrm{d}t} = \frac{u^r}{u^t} = \frac{\alpha}{X} v \ . \tag{7.21}$$

[2]This expression is valid in RGPS case, where the shift vector is zero; otherwise the 3-velocity reads:

$$v^i = \frac{u^i}{W} + \frac{\beta^i}{\alpha} \ . \tag{7.18}$$

[3]In other words, the Eulerian observer measures the distance $\mathrm{d}l = X \mathrm{d}r$ covered during its proper time $\mathrm{d}\tau_{Eul} = \mathrm{d}\tau = \alpha \mathrm{d}t$. So, the velocity he measures is:

$$v = \frac{\mathrm{d}l}{\mathrm{d}\tau} = \frac{X}{\alpha} V \ . \tag{7.22}$$

As we will see in the next Section, the hydrodynamical equations will be written in RGPS coordinates, so that when we write, for example, ρu^μ, for the second component we should write: $\rho u^r = \rho u^t V = \rho \frac{W}{\alpha} V = \rho \frac{W}{X} v$, being v the physical velocity (i.e. measured by the (Eulerian) observer).

7.1.2 Hydrodynamical equations as a system of conservation laws

In the perfect fluid scheme, the evolution of matter is described by the Eqs. (4.13): which derive from the local baryon number and energy conservation [285]:

$$\nabla_\mu J^\mu = 0, \tag{7.23}$$
$$\nabla_\mu T^{\mu\nu} = 0\,, \tag{7.24}$$

where $\rho = \rho_b = m_u n_b$ is the baryon density, ∇_μ is the covariant derivative,

$$J^\mu = \rho u^\mu\,, \tag{7.25}$$

u^μ is the four-velocity of the fluid, $T^{\mu\nu}$ is the stress-energy tensor:

$$T^{\mu\nu} = \rho h u^\mu u^\nu + P g^{\mu\nu} \tag{7.26}$$

being P the pressure, and h is the specific enthalpy defined by:

$$h = 1 + \epsilon + \frac{P}{\rho}\,, \tag{7.27}$$

with ϵ the specific internal energy.

In RGPS coordinates the conservation equations Eqs. (7.23)-(7.24) read (the Greek indices run over (t, r, θ, ϕ), and using the notation in [285, 258]):

$$\nabla_\mu J^\mu = \frac{1}{\sqrt{-g}}\frac{\partial}{\partial x^\mu}\left(\sqrt{-g}\rho u^\mu\right) = 0 \tag{7.28}$$
$$\nabla_\mu T^{\mu\nu} = \frac{1}{\sqrt{-g}}\frac{\partial}{\partial x^\mu}\left(\sqrt{-g}T^{\mu\nu}\right) + \Gamma^\nu_{\alpha\mu}\,T^{\mu\alpha} = 0\,, \tag{7.29}$$

where all the quantities have been previously defined except the Christoffel symbols, related to the derivative of the metric[4]:

$$\Gamma^\nu_{\alpha\mu} = \frac{1}{2}g^{\nu\beta}\left(\frac{\partial}{\partial x^\alpha}g_{\mu\beta} + \frac{\partial}{\partial x^\mu}g_{\alpha\beta} - \frac{\partial}{\partial x^\beta}g_{\alpha\mu}\right)\,. \tag{7.30}$$

The source terms, identically zero if the particle number and the energy is strictly conserved, are different from zero if a source/sink of particles/energy is introduced; this is the case when considering external forces (e.g. gravity) or neutrino processes (e.g. electron capture).

In the Valencia formulation, and following the paper by Romero *et al.*, the hydrodynamical evolution equations can be written in the flux-conservative form[5][285]:

$$\frac{\partial \mathbf{U}}{\partial t} + \frac{1}{r^2}\frac{\partial}{\partial r}\left[\frac{r^2\alpha}{X}\mathbf{F}(\mathbf{U})\right] = \mathbf{S}(\mathbf{U})\,, \tag{7.31}$$

[4]The divergence of the tensor can be also defined without introducing the Christoffel symbols [141].

[5]For a derivation of the evolution equation with the same notation as presented here, we refer to the paper by O'Connor and Ott, Appendix A [258].

where the *conserved* variables are the conserved baryon density D, momentum $S^r = S$, the energy density τ and electron fraction DY_e, which are related to the primitive variables baryon density ρ, (physical) velocity v, specific internal energy ϵ, electron fraction Y_e as:

$$\mathbf{U} = \begin{pmatrix} D \\ S \\ \tau \\ DY_e \end{pmatrix} ; \quad \begin{array}{l} D = \rho\, X\, W \\ S = \alpha T^{tr} = \rho h W^2 v \\ \tau = \alpha^2 T^{tt} - D = \rho h W^2 - P - D \\ DY_e = \rho\, X\, W\, Y_e\ . \end{array} \tag{7.32}$$

The neutrino fraction evolution, i.e. the equation for DY_ν, will be discussed later. It was not present in the original version of the code, and it was added in the modified code by J. Pons and collaborators. I have also made some modifications to this equation.
The fluxes are given by:

$$\mathbf{F}(\mathbf{U}) = \begin{pmatrix} Dv \\ Sv + P \\ S - Dv \\ DY_e v \end{pmatrix}, \tag{7.33}$$

and the source terms are[6]:

$$\mathbf{S}(\mathbf{U}) = \begin{pmatrix} 0 \\ (Sv - \tau - D)\left(8\alpha X \pi r P + \alpha X \frac{m}{r^2}\right) + \alpha X P \frac{m}{r^2} + \frac{2\alpha P}{Xr} + (vQ_{\nu,E} + Q_{\nu,M}) \\ Q_{\nu,E} + vQ_{\nu,M} \\ R_{Y_e} \end{pmatrix}, \tag{7.34}$$

where the source/sink terms Q_ν and R_{Y_e} are associated with neutrinos (e.g. electron capture).
I recall that v is the physical velocity measured by the Eulerian observer, which is related to the coordinate velocity V as:

$$v = \frac{X u^r}{\alpha u^t} = \frac{X}{\alpha} V\ , \tag{7.35}$$

and the Lorentz factor is $W = (1 - v^2)^{-1/2}$.

This system is closed by an EoS, of the form :

$$P = P(\rho, T, Y_e)\ , \tag{7.36}$$

and the equations for the gravitational mass $m(r,t)$ and the metric potential $\Phi(r,t)$, which are given by[7][141]:

$$\frac{\partial m}{\partial r} = 4\pi r^2 (\tau + D)\ , \tag{7.37}$$

$$\frac{\partial \Phi}{\partial r} = X^2 \left[\frac{m}{r^2} + 4\pi r (P + Sv)\right]\ . \tag{7.38}$$

[6]For the flux and source terms, to recover the correct units, one has to remember that we are working with $c = G = 1$ units.

[7]More precisely, the equation for m derives from the Hamiltonian constraint which gives an equation for the 3-tensor of extrinsic curvature, and the equation for Φ comes from the momentum constraints with the relations for the extrinsic curvature components imposed by the RGPS.

In GR one has to distinguish between the gravitational mass (7.37) and the baryonic mass (the one which must be conserved):

$$\frac{\partial m_b}{\partial r} = 4\pi r^2 D. \tag{7.39}$$

At each time step the metric is computed; Eqs. (7.37), (7.38), (7.39) are integrated from $r = 0$ to $r = R(t)$ (the radius of the core, since only the central part is considered)[8], reconstructing the mass at the interfaces with a parabola formula, and using the following boundary conditions:

$$\begin{aligned}
m(r=0) &= 0 && \text{(7.40a)}\\
m_b(r=0) &= 0 && \text{(7.40b)}\\
m(r=R(t)) &= M_g \text{ the gravitational mass} && \text{(7.40c)}\\
m_b(r=R(t)) &= M_b \text{ the total baryonic mass} && \text{(7.40d)}\\
\Phi\left(r=R(t)\right) &= \frac{1}{2}\ln\left(1-\frac{2M_g}{R(t)}\right) \text{ the exterior Schwarzschild solution}^9 && \text{(7.40e)}
\end{aligned}$$

The binding energy of the star E_{bind} is defined as $E_{bind} = M_g - M_b$. Integrating the first and third components of Eq. (7.31), one gets at the surface :

$$\begin{aligned}
\frac{\partial M_b}{\partial t} &= -\frac{\alpha}{X} Dv\Big|_{R(t)} && \text{(7.41)}\\
\frac{\partial E_{bind}}{\partial t} &= -\frac{\alpha}{X}(S - Dv)\Big|_{R(t)} \ . && \text{(7.42)}
\end{aligned}$$

If the boundary conditions at the surface for the fluxes are zero and $\rho = 0$, $v = 0$, then the conservation of baryonic mass and energy is strictly satisfied.

I also recall that the speed of sound c_s is given by (see also Appendix F) [285]:

$$\begin{aligned}
hc_s^2 &= \chi + \frac{P}{\rho^2}\kappa, && \text{(7.43)}\\
\text{with: } \chi &= \left(\frac{\partial P}{\partial \rho}\right)_{\epsilon} && \text{(7.44)}\\
\text{and: } \kappa &= \left(\frac{\partial P}{\partial \epsilon}\right)_{\rho} \ . && \text{(7.45)}
\end{aligned}$$

7.1.3 Local characteristic approach, HRSC and Flux formula

As explained in Section 4.1.2, the hyperbolic character of the hydrodynamical equations can be exploited to employ Godunov-type methods to treat shocks and solve the series of local Riemann problems at each cell interface which result from the discretization procedure. The exact solution of the Riemann problem is feasible, but computational expensive especially in multi-dimensional hydrodynamics; thus, often, approximate Riemann solvers are used; the fluxes at cell interfaces can be calculated via flux formulæ.

The hydrodynamical step can be divided into the following sub-steps:

[8] The integration is performed via an algorithm adapted from [95] which computes an approximation to the integral in an interval $[a, b]$.

[9] The gravitational potential Φ (Eq. (7.38)) is defined with respect to an additive constant which can be determined matching the solution at $R(t)$ to the Schwarzschild solution Eq. (7.40e).

1. Advancing in time.
   At each time step, the (cell averaged[10]) conserved quantities are updated according to a version of the *method of line* (MoL):

$$\mathbf{U}_j^{n+1} = \mathbf{U}_j^n - \frac{1}{r_j^2(r_{j+1/2} - r_{j-1/2})} \left[\left(\frac{\alpha r^2}{X} \hat{\mathbf{F}} \right)_{j+1/2} - \left(\frac{\alpha r^2}{X} \hat{\mathbf{F}} \right)_{j-1/2} \right] + \mathbf{S}_j \,, \quad (7.47)$$

   where the sources are included in the hydrodynamical step if the unsplit method is used (see Section 7.1.4), and $\hat{\mathbf{F}}$ are the numerical fluxes.
   The advancing in time can be done in second-order accuracy, for example with a *predictor-corrector* method, i.e. at the beginning of the hydrodynamical step the state vector is advanced according to Eq. (7.47) using the values of the fluxes and sources from previous time step (block labelled "Predictor step" in the flow chart Fig. 7.3), then at the end of the hydrodynamical step the state vector is "corrected" according always to Eq. (7.47), but where now the fluxes and sources are averaged (arithmetic mean) between the "old" and "new" values (block labelled "Corrector step" in the flow chart).

2. Cell reconstruction.
   The cell reconstruction is needed to get the values of the primitive variables at each cell interface (see Fig. 7.3, block labelled as "Reconstruction at interfaces").

3. Computation of the fluxes.
   After the reconstruction, one has to solve the Riemann problem, or get an approximate solution by a flux formula (block labelled as "Compute fluxes" in Fig. 7.3). Finally, after the solution is known in terms of the conserved variables, the primitive ones have to be recovered (blocks labelled as "Conservative-to-primitive").

To compute the fluxes, the code [285] originally employs a Roe's solver; I have implemented also the calculation of the fluxes according to the HLLE solver, whose expressions will be given in the following:

- **Roe's solver**
  The Roe's flux formula [284] to compute the interfaces flux, for each component of the numerical flux, reads:

$$\hat{F}^{\rm Roe}_{j+1/2} = \frac{1}{2} \left\{ F(\mathbf{U}^L_{j+1/2}) + F(\mathbf{U}^R_{j+1/2}) - \sum_{\alpha=0,\pm} |\lambda_\alpha| \Delta w_\alpha \mathbf{r}_\alpha \right\} \,, \quad (7.48)$$

  where $\mathbf{U}^{L/R}_{j+1/2}$ are the left and right states, i.e. the reconstructed values of the conserved variables at the interfaces (see next Subsection), λ_α and r_α are the eigenvalues and the α-component of the right eigenvector of the Jacobian matrix:

$$\mathcal{B}_{j+1/2} = \left[\frac{\partial \mathbf{F}(\mathbf{U})}{\partial \mathbf{U}} \right]_{\mathbf{U}=(\mathbf{U}^L_{j+1/2} + \mathbf{U}^R_{j+1/2})/2} \,, \quad (7.49)$$

[10] The cell averages of the conserved quantities read:

$$\mathbf{U}_j^n := \bar{\mathbf{U}}_j^n = \frac{1}{r_j^2(r_{j+1/2} - r_{j-1/2})} \int_{r_{j-1/2}}^{r_{j+1/2}} \mathbf{U}(r, t^n)\, r^2 {\rm d}r \,. \quad (7.46)$$

Since in the code all quantities are evaluated at the cell-center, I will make the equivalence $\mathbf{U}_j^n = \bar{\mathbf{U}}_j^n$.

Δw_α are the jumps in the local characteristic variables across the cell interface:

$$\mathbf{U}^R_{j+1/2} - \mathbf{U}^L_{j+1/2} = \sum_{\alpha=0,\pm} \Delta w_\alpha \mathbf{r}_\alpha \ , \tag{7.50}$$

i.e.:

$$\Delta w_\alpha = \sum_{\alpha=0,\pm} \mathbf{l}_\alpha \left(\mathbf{U}^R_{j+1/2} - \mathbf{U}^L_{j+1/2} \right) \ , \tag{7.51}$$

where $\mathbf{l}_\alpha$ is the α-component of the left eigenvector of the Jacobian matrix[11].

- **HLLE solver**
  The Harten-Lax-van Leer-Einfeldt (HLLE) solver [151, 107] requires only the knowledge of the eigenvalues, since it considers only the fastest wave moving to the left and to the right; for each component of the flux:

$$\hat{F}^{\rm HLLE}_{j+1/2} = \frac{\xi_+ F(\mathbf{U}^L_{j+1/2}) - \xi_- F(\mathbf{U}^R_{j+1/2}) + \xi_+ \xi_- (\mathbf{U}^R_{j+1/2} - \mathbf{U}^L_{j+1/2})}{\xi_+ - \xi_-} \ , \tag{7.52}$$

  where:

$$\begin{aligned} \xi_- &= \min\left(\lambda^L_{-,j+1/2}, \lambda^R_{-,j+1/2}, 0\right) \\ \xi_+ &= \max\left(\lambda^L_{+,j+1/2}, \lambda^R_{+,j+1/2}, 0\right) . \end{aligned} \tag{7.53}$$

The eigenvalues associated to the material and acoustic wave are given by:

$$\lambda_- = \frac{v - c_s}{1 - v\, c_s} \ , \tag{7.54a}$$

$$\lambda_0 = v \ , \tag{7.54b}$$

$$\lambda_+ = \frac{v + c_s}{1 + v\, c_s} \ , \tag{7.54c}$$

and represent the characteristic speeds associated to the three kinds of waves (rarefaction, shock and contact discontinuity, cf. Section 4.1.2). These are the extension of the corresponding characteristic speeds in Newtonian fluid dynamics[12].

The right eigenvectors read [285]:

$$\mathbf{r}_- = \left[\frac{X(1-\lambda_- v)}{hW(1-v^2)},\ \lambda_-,\ 1 - \frac{X(1-\lambda_- v)}{hW(1-v^2)} \right] \tag{7.55a}$$

$$\mathbf{r}_0 = \left[\frac{X\frac{\kappa}{\rho}}{hW\left(\frac{\kappa}{\rho} - c_s^2\right)},\ \lambda_0,\ 1 - \frac{X\frac{\kappa}{\rho}}{hW\left(\frac{\kappa}{\rho} - c_s^2\right)} \right] \tag{7.55b}$$

$$\mathbf{r}_+ = \left[\frac{X(1-\lambda_+ v)}{hW(1-v^2)},\ \lambda_+,\ 1 - \frac{X(1-\lambda_+ v)}{hW(1-v^2)} \right] \ . \tag{7.55c}$$

[11] The left eigenvectors are implemented inverting the matrix of the right-eigenvectors.

[12] In the Lagrangian framework, one has $v = 0$, since the system moves together with the fluid (e.g. [228]).

Reconstruction of variables at interface: *slope limiter*

The reconstruction consists in getting the values of the desired variables at cell interfaces $j \pm 1/2$, once their value at the cell center j is known. Unlike the Newtonian code described in Chapter 6, all the quantities are defined at cell center, and must be reconstructed (i.e. interpolated) at cell interfaces where the fluxes are computed. In the code, the primitive variables are reconstructed first, then the conserved variables are computed from the primitive ones, by means of the relations (7.32).
There are many different reconstruction procedures available in the literature; among them, for example, the second-order slope limiter methods (see e.g. [315]) and the third-order piecewise-parabolic (PPM) reconstruction by Colella and Woodword [87].

To get values at interfaces, Romero *et al.*used a linear reconstruction with a minmod function as a slope limiter. If $\bar{\mathbf{U}}_j$ is the cell average of the conserved quantity $\mathbf{U}$, a second order linear reconstruction would give, for example for the left "L" value:

$$\mathbf{U}^L_{j+1/2} = \bar{\mathbf{U}}_j + \frac{\bar{\mathbf{U}}_{j+1} - \bar{\mathbf{U}}_j}{r_{j+1} - r_j} \left(r_{j+1/2} - r_j\right) , \tag{7.56}$$

which does not preserve monotonicity and thus can introduce oscillations which are undesirable in solving equations numerically. In the slope limiter method employed, the values of the conserved quantities at cell interfaces are given by [285]:

$$\begin{aligned} \mathbf{U}^L_{j+1/2} &= \bar{\mathbf{U}}^n_j + \sigma^n_j \left(r_{j+1/2} - r_j\right) \\ \mathbf{U}^R_{j+1/2} &= \bar{\mathbf{U}}^n_{j+1} + \sigma^n_{j+1} \left(r_{j+1/2} - r_{j+1}\right) , \end{aligned} \tag{7.57}$$

where the *slope limiter* function σ^n_j is given by (see Fig. 7.2):

$$\sigma^n_j = \text{minmod} \left(\frac{\bar{\mathbf{U}}^n_{j+1} - \bar{\mathbf{U}}^n_j}{r_{j+1} - r_j}, \frac{\bar{\mathbf{U}}^n_j - \bar{\mathbf{U}}^n_{j-1}}{r_j - r_{j-1}} \right) , \tag{7.58}$$

being the minmod function defined as:

$$\text{minmod}\,(a,b) = \begin{cases} a & \text{if } |a| < |b|,\ ab > 0 \\ b & \text{if } |a| > |b|,\ ab > 0 \\ 0 & \text{if } ab < 0\ . \end{cases} \tag{7.59}$$

The "L" and "R" values enter directly in the flux formula.

Courant condition

Since the code is explicit in the hydrodynamics, the time step Δt for the hydrodynamical evolution has to obey the Courant-Friedrichs-Lewy (CFL) condition (see e.g. [279]):

$$\Delta t = \min_j \left(C\, \frac{r_{j+1/2} - r_{j-1/2}}{\lambda_{+,j} - \lambda_{-,j}} \right) , \tag{7.60}$$

where j runs over the number of zones. The Courant factor C (we will run the simulation with $C = 0.5$, or $C = 0.8$) tells us by which amount Δt is reduced from the maximum

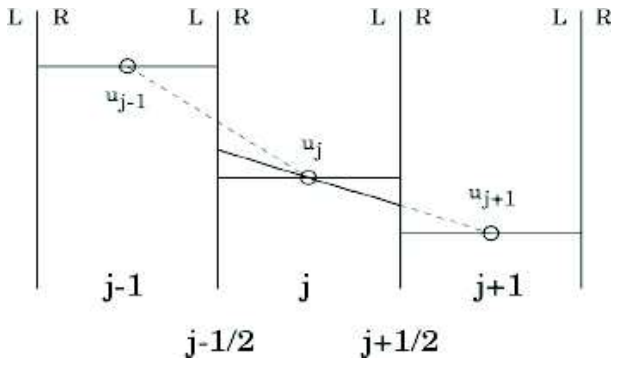

Figure 7.2: Minmod linear reconstruction. The reconstruction of the variables at each cell interface is done by a linear interpolation, using a slope limiter (minmod) function. "L" ("R") stands for the left (right) value at the cell interface (from [119]).

allowed by the CFL criterion. This value depends on the stability properties of the hydrodynamical equations and the discretization.
This condition means that the time step used to solve the equations must be smaller than the time for the wave to travel between adjacent grid points; otherwise, no physical solutions arise. Moreover, if the electron evolution equation together with a treatment of neutrinos is included, the source terms introduce a characteristic timescale (e.g. diffusion timescale) which would impose an upper limit on the numerical time step [169]. In order to avoid a restrictive CFL condition and to properly cover the different timescales, an implicit scheme for the neutrino source terms has to be employed.

7.1.4 Source terms

The source terms, i.e. the right-hand side of the system of "conservation" laws, arise when taking into account external forces such as gravity, or when introducing microscopic processes such as electron capture, or radiative transfer.
There are two ways of implementing the source terms: the *unsplit* and the *split* methods. In the first approach, the source terms are considered with the flux terms in the time-advancing procedure, i.e., the state vector is updated from its previous value $\mathbf{U}^n$ to its new value $\mathbf{U}^{n+1}$ at t^{n+1} over a unique step. In solving the Eq. (7.61), substeps can be introduced, via a predictor-corrector method (the one we adopt), or Runge-Kutta schemes. In the finite-difference scheme, this reads [118]:

$$\frac{\Delta \mathbf{U}_j}{\Delta t} = -\frac{1}{\Delta x}\left(\mathbf{F}_{j+1/2} - \mathbf{F}_{j-1/2}\right) + \mathbf{S}^n \,. \tag{7.61}$$

This is the case of the momentum equation without contributions from neutrinos.

The splitting (or *fractional-step*) methods consist in splitting the time-advancing step into two pieces: the advection part and the source part. Thus, in the hydrodynamical step, the homogeneous equation is solved (i.e. the source term is zeroed), updating the state vector from $\mathbf{U}^n$ to an intermediate value $\mathbf{U}^*$, then the source term is added updating the

state vector from $\mathbf{U}^*$ to the value $\mathbf{U}^{n+1}$ at t^{n+1}, as:

$$\begin{aligned}
&\frac{\Delta \mathbf{U}}{\Delta t} + \frac{\Delta \mathbf{F}(\mathbf{U})}{\Delta t} = 0 \Longrightarrow \mathbf{U}^* \text{ (PDE)} \\
&\frac{\Delta \mathbf{U}^*}{\Delta t} = \mathbf{S}(\mathbf{U}^*) \Longrightarrow \mathbf{U}^{n+1} \text{ (ODE)} \, .
\end{aligned} \tag{7.62}$$

This second approach is adopted in dealing neutrino contributions, i.e. in the electron fraction evolution equation and in adding the $Q_{\nu,E}$ and $Q_{\nu,M}$ contributions (see also Fig. 7.3), which will be discussed in Section 7.3.

7.1.5 Conserved-to-primitive variable reconstruction

The hydrodynamical equations Eqs. (7.31) evolve the conserved variables (7.32): D, S, τ, DY_e, DY_ν. Therefore, the primitive variables which are needed for the computation of the fluxes and of the microphysics, ρ, v, ϵ, Y_e, Y_ν, have to be recovered. In the case of a finite-temperature EoS, if the density is lower than a certain value (typically 10^6 g cm^{-3}, which is the value one can have at the edge of the core), the velocity is zeroed and the other primitive variables are set equal to the values they assume in the inner adjacent cell. This prevents the code to crash in calling the EoS which does not work at low density. A solution could be the inclusion of a different EoS at very low density; this is a part of our outlooks.

To recover the primitive variables, a Newton-Raphson method on the pressure is used, as described in Martí and Müller [230]. Starting from an initial guess for the pressure, the Newton-Raphson scheme calculates the zero of the function $f(p) = P - P_{old}$, where P_{old} is the pressure from the previous time step, and P is the updated value of the pressure calculated by the EoS, whose inputs (density, energy and electron fraction) are related to the conserved quantities and to P_{old} by:

$$\begin{aligned}
\rho &= \frac{D}{X\, W} \\
\epsilon &= \frac{\tau + D + P_{old}(1 - W^2)}{\frac{D}{X} W} - 1 \\
Y_e &= \frac{D Y_e}{D} \, ,
\end{aligned} \tag{7.63}$$

where:

$$W = \frac{1}{\sqrt{1 - v^2}} \tag{7.64}$$

and:

$$v = \frac{S}{\tau + D + \rho} \, . \tag{7.65}$$

The Newton-Raphson method requires also the derivative of f, which is given by:

$$\begin{aligned}
f' = \frac{\mathrm{d}f}{\mathrm{d}P_{old}} &= \left.\frac{\partial P}{\partial \rho}\right|_\epsilon \frac{\partial \rho}{\partial P_{old}} + \left.\frac{\partial P}{\partial \epsilon}\right|_\rho \frac{\partial \epsilon}{\partial P_{old}} - 1 \\
&= \left.\frac{\partial P}{\partial \rho}\right|_\epsilon \frac{D}{X} \frac{v^2\, W}{\tau + D + P_{old}} + \left.\frac{\partial P}{\partial \epsilon}\right|_\rho \frac{P_{old}\, v^2\, W^3}{\frac{D}{X}(\tau + D + P_{old})} \, ,
\end{aligned} \tag{7.66}$$

where $\frac{\partial P}{\partial \rho}$ and $\frac{\partial P}{\partial \epsilon}$ are output of the EoS. f' can be approximated as:

$$f' = v^2\, c_s^2 - 1\ , \tag{7.67}$$

being c_s the speed of sound calculated by the EoS.

7.2 Equation of State

The EoS closes the system of hydrodynamical equations Eqs. (7.31). It must be kept in mind once more that an hydrodynamical code usually work with (ρ, ϵ, Y_e) as independent variables, while the EoS works with (ρ, T, Y_e) as independent variables, so that $P = P(\rho, T, Y_e)$. Unless the case of a polytropic EoS, where the relation between the pressure and the energy is straightforward and no informations on the temperature are required, for most of finite-temperature EoS a root-finder which converts the energy (coming from the solution of the hydrodynamical equations) to the corresponding temperature (at fixed density and electron fraction) must be supplied.

The EoS is called at the beginning of the simulation during the initialization procedure (see Fig. 7.3) and in conserved-to-primitive reconstruction.

7.2.1 Polytropic EoS

The original version of the code works with a polytropic EoS of the form:

$$P(\rho) = K\ \rho^{\Gamma}\ , \tag{7.68}$$

where Γ is the adiabatic index (being related to the polytropic index according to: $n = 1/(\Gamma - 1)$), and K is a constant. To reproduce the stiffening of the EoS above nuclear densities, the adiabatic index was taken to be density-dependent, according to the relation [325, 285]:

$$\Gamma = \Gamma_{min} + \eta\,(\log\rho - \log\rho_0)\ , \tag{7.69}$$

with $\Gamma_{min} = 1.33$, $\rho_0 = 2.5 \times 10^{14}$ g cm^{-3}and with $\eta = 0$ if $\rho < \rho_0$ and $\eta = 1$ otherwise. In the paper by Romero *et al.* [285] two sets of parameters (Γ, η, ρ_0) have been studied; in Section 7.6.1 some profiles obtained with the choice for the parameters: $\Gamma = 1.33$, $\eta = 1$ $\rho_0 = 2.5 \times 10^{14}$ g cm^{-3}(which corresponds to "Model A" in [285]) are shown.
Even if this kind of EoS can well reproduce the hydrodynamical behaviour of a fluid dominated by electron degeneracy pressure (as it is the case for the first phase of a core collapse), it obviously contains no additional informations on the composition of the system, and therefore no microscopical processes can be analysed in such a framework.

7.2.2 Finite-temperature nuclear EoS

The Lattimer and Swesty [192] finite-temperature EoS was implemented in the Romero *et al.*code by J. Pons and collaborators. They have included in the code the routine version v2.6 of the LS EoS. I have replaced it with the v2.7 available on the Swesty's webpage,

modifying directly the routine to make it work at lower densities (cf. Appendix. F). The version v2.7 includes the possibility to charge the boundaries and Maxwell construction files for three different values of the incompressibility, namely $K = 180, 220, 375$ MeV, which allows us to make a first test of the sensitivity of the results of the simulation on this parameter. The inclusion of a table for the EoS has not yet been implemented; this will be one of our next steps in the improvement of the code. Even if the value of $K = K_\infty$ at the saturation density is well known from nuclear physics, and it would be instructive to carry out simulations varying the parameter K_{sym} (which is poorly known as discussed in Section 2.1.2), no tables are available to-date for different values of K_{sym}.

The EoS call first recovers the temperature from the energy density, using a Newton-Raphson method operating on the internal energy. To speed up the convergence of the routine, the guessed input value for temperature is that of the previous iteration. Then, the EoS routine is called with ρ, T, Y_e as input to calculate the thermodynamical variables (such as pressure, chemical potentials and the related derivatives to compute the speed of sound), and the composition, which is necessary to compute the capture rates. I recall that the EoS works with nuclear units (i.e. MeV and fm), so a unit conversion is also required. Moreover, when calling the EoS, for each cell, a check is done whether the density is below some minimum value (which is likely expected near the edge of the core); if this is the case, a $\Gamma = 4/3$ polytropic EoS is used to recover the pressure and the sound speed from the energy, by means of the well known relations [295]:

$$P = \frac{1}{3}\rho\epsilon \tag{7.70}$$

$$c_s = \frac{\sqrt{\Gamma(\Gamma-1)\epsilon}}{1+\Gamma\epsilon}\,. \tag{7.71}$$

7.3 Electron capture and treatment of neutrinos

A treatment of the deleptonization is present in the version of the code by J. Pons. Only the electron capture and the inverse reaction are considered as source (or sink) of neutrinos, in a multi-group fashion. Even if no transport is included, the multi-group implementation allows a first analysis of the neutrino spectra.

In the literature, e.g. in CoCoNuT code, or in the recent 1D code by O'Connor and Ott [258], the parameterized scheme *à la Liebendörfer* is often employed in order to describe the deleptonization process. This scheme, introduced in Ref. [199] consists in parameterizing the electron fraction evolution as a function of the density only: $Y_e = Y_e(\rho)$. The fit formula was obtained from a series of 1D simulations solving the full Boltzmann equation. It has the advantage, among others, to be computationally very fast. However, since the neutrinos are not explicitly treated (their contribution to the pressure is taken into account after trapping, and their chemical potential is equal to the one at β equilibrium), no information on their spectra can be extracted.

In order to implement a more refined treatment of the electron capture, via the calculation of the capture rates, one must add to the hydrodynamical equations in Ref. [285]

two other equations describing the evolution of the electron and neutrino fraction:

$$\frac{\partial(DY_e)}{\partial t} + \frac{1}{r^2}\frac{\partial}{\partial r}\left[\frac{\alpha}{X} r^2\, vDY_e\right] = R_{Y_e} \tag{7.72}$$

$$\frac{\partial(DY_\nu)}{\partial t} + \frac{1}{r^2}\frac{\partial}{\partial r}\left[\frac{\alpha}{X} r^2\, vDY_\nu\right] = R_{Y_\nu}\ , \tag{7.73}$$

where[13]:

$$R_{Y_e} = \frac{\alpha}{W}\, D\, R^0_{Y_e} \tag{7.75}$$

$$R_{Y_\nu}(\omega) = \frac{\alpha}{W}\, D\, R^0_{Y_\nu}(\omega) - \alpha\, X\, \frac{\mathrm{D}\log\rho}{\mathrm{D}t}\left(\frac{\partial K_\nu(\omega)}{\partial\omega}\right)\ , \tag{7.76}$$

and the superscript "0" indicates the quantities calculated in the comoving frame, and $R^0_{Y_e} = \mathrm{d}Y_e/\mathrm{d}t$. Both source terms, $R^0_{Y_e}$ and $R^0_{Y_\nu}$, are due to electron capture, and are related because of the local conservation of lepton number: if a neutrino is emitted (as a consequence of the electron capture), an electron is absorbed and viceversa (see Eqs. (7.81), (7.82)).
A remark has to be done for the neutrino evolution equation. In fact, as already mentioned in Chapter 6, to take into account the energy redistribution of neutrinos due to the compression/expansion of the matter, an additional term has to be included [56, 286]. This term is equivalent to the one in Eq. (6.23), which can be written, either on the left-hand side of the Eq. (7.73) [56] or on the right-hand side [286] ($c = 1$ units):

$$\frac{\mathrm{D}\log\rho}{\mathrm{D}t}\left(\frac{\partial K_\nu(\omega)}{\partial\omega}\right)\ , \tag{7.77}$$

where ω is the neutrino energy and K_ν the second moment of the specific intensity[14]:

$$K_\nu(\omega) = \frac{1}{4\pi^2(\hbar c)^3}\,\omega^3 \int_{-1}^{1} \mu^2 f(r,t,\omega,\mu)\mathrm{d}\mu\ , \tag{7.78}$$

being μ the cosine of the angle between the neutrino direction and the radial direction (see Appendix G). Since we work in spherical symmetry, we integrate over the angles; the integration over μ gives the $1/3$ factor in Eq. (6.23)[15], and the Eq. (7.78) becomes:

$$K_\nu(\omega) = \frac{4\pi}{3(2\pi\hbar c)^3}\,\omega^3 f(r,t,\omega,\mu)\ . \tag{7.79}$$

Note that D indicates the Lagrangian derivatives, thus: a change of coordinate must be done according to Eq. (4.2) (comoving to Eulerian frame), and it must be kept in mind that the neutrino equations are calculated in the fluid rest frame, so a further change of

[13] The source term for electrons (and for neutrinos) can be written in an equivalent way as [286, 258, 251]:

$$R_{Y_e} = \alpha\, X\, R^0_{Y_e}\ , \tag{7.74}$$

where now $R^0_{Y_e}$ must contain the density ρ to recover the correct units (cf. Eq. (7.81)). The metric factors αX come out from the $\sqrt{-g}$ term in Eq. (7.28).

[14] To recover the correct units, a factor $m_u = 1/N_A$ is needed.

[15] Eq. (6.23) is actually written for the first moment of Legendre expansion $\psi^{(0)}$.

coordinate (from the "physical" quantities measured by the Eulerian observer to the coordinate frame) introduces the metric factors in the Eq. (7.77)[16].

The implementation of the term (7.77) has been done in the "advancing in time" step, i.e. as a source in unsplit fashion, while the source coming from electron capture is treating in the split fashion after each hydro-step.

The capture terms read (cf. Eq. (6.24), where the integration over the angles has been already performed)[17]:

$$R^0_{Y_e} = -\int_0^\infty R^0_{Y_\nu}(\omega)\mathrm{d}\omega \tag{7.81}$$

$$R^0_{Y_\nu}(\omega) = \frac{1}{N_A\rho}\frac{c}{4\pi^2(\hbar c)^3}\omega^2\int_{-1}^{1}\left(\frac{\mathrm{d}f(\omega,\mu)}{\mathrm{d}t}\right)_{coll}\mathrm{d}\mu\ , \tag{7.82}$$

where (cf. Eq. (G.5)):

$$\left(\frac{\mathrm{d}f(\omega,\mu)}{\mathrm{d}t}\right)_{coll} = B_{AE}\ , \tag{7.83}$$

since only electron capture is considered in the collision integral.

The implementation of the emissivity and absorptivity has been done *à la Bruenn*, according to the expressions given in Appendix G, Sections G.2.1 and G.2.2. However, a further assumption has been made in [286]: neutrinos created in electron capture stay in β equilibrium. If the trapping holds, one can write Eq. (7.82), after integrating over μ, as follows (see Section G.2.2, Eqs. (G.38)-(G.40)) [286]:

$$R^0_{Y_\nu}(\omega) = \frac{1}{N_A\rho}\frac{c}{2\pi^2(\hbar c)^3}\omega^2\left(j(\omega)+\frac{1}{\lambda^{(a)}(\omega)}\right)\left[f^{eq}(\omega)-f(\omega)\right]\ , \tag{7.84}$$

being f^{eq} the neutrino distribution function at equilibrium (i.e. the neutrino chemical potential is the one at β equilibrium).

The implementation of the source term for neutrinos is done by an implicit method, i.e. the change in the neutrino distribution function f and the corresponding correction in the energy term $Q_{\nu,E}$ are found by inverting a matrix, as described in Bruenn [56].

This happens because the neutrino fraction:

$$Y_\nu(\omega) = \frac{1}{N_A\rho}\frac{1}{4\pi^2(\hbar c)^3}\omega^2\int_{-1}^{1}f(\omega,\mu)\mathrm{d}\mu\ , \tag{7.85}$$

which is evolved by the advection equation (actually, the neutrino related conserved quantity DY_ν is evolved), appears also on the right-hand side of the evolution Eq. (7.73) via the distribution function f.

[16] More precisely, from the Lagrangian to the Eulerian frame:

$$\frac{\mathrm{D}}{\mathrm{D}t} = \frac{\partial}{\partial t} + v\frac{\partial}{\partial r}\ , \tag{7.80}$$

and, from the fluid rest frame (FRF) to the coordinate frame: $\mathrm{d}\tau_{FRF} = \frac{\alpha}{W}\mathrm{d}t$, and: $\partial r_{FRF} = \frac{X}{W}\mathrm{d}r$.

[17] In the following equations, c appears explicitly in order to directly compare the equations with the ones in Chapter 6.

However, in the first phase of the collapse, the assumption of neutrino trapping is not valid. In this respect I have modified this part, considering, before neutrino trapping, only the emission term, $j(\omega)$, in the collision integral:

$$R^0_{Y_\nu}(\omega) = \frac{1}{N_A \rho} \frac{c}{2\pi^2 (\hbar c)^3} \omega^2 j(\omega) \; . \tag{7.86}$$

Thus, in this regime, neutrinos are only emitted and escape freely, i.e. $f = 0$ (the expressions in the general case are given in [269]). The neutrinos produced before trapping are not diffusing through the dense matter but are simply removed from the stars. In principle, they should move outwards according to a transport equation, at least in a diffusion approximation (as done in the Newtonian code described in Chapter 6), but as a first step, this hypothesis of trapping scheme should not be too bad. Moreover, in this framework, the equation for the neutrino (and electron) evolution becomes explicit, since now the distribution function appears only on the left-hand side of the evolution equation, and the implementation is easier.

Let us now define the neutrino trapping. In principle, the trapping regime should come out naturally when solving the transport equation. In our case, a possible choice for the neutrino trapping is to fix a condition on the neutrino diffusion time scale, evaluated from the neutrino mean free path (e.g. neutrinos can escape if they have a diffusion timescale smaller than the hydrodynamical timescale).
In order to impose the moment at which the trapping is established (i.e. when we have to switch from solving Eq. (7.86) to solving Eq. (7.84)), we have decided to follow the prescription in Kotake *et al.*[179], who fixed a trapping density of $\rho_{tr,1} = 3 \times 10^{11}$ g cm^{-3}before bounce, and $\rho_{tr,2} = 1 \times 10^{11}$ g cm^{-3}after bounce, to take into account the different hydrodynamical timescale of the problem. To test the sensitivity of the results to the trapping condition, we have performed simulations varying this trapping density, see Section 7.6.2. In this way we lose the energy dependence of the trapping condition, i.e. either all neutrinos (of any energy) escape, or are all trapped.

A different treatment is proposed by Ruffert *et al.*[288], who calculated the neutrino opacity for emission/absorption and scattering, and the neutrino emission rates. The authors assumed that the neutrino spectra can be represented by a Fermi-Dirac distributions for the temperature T and neutrino chemical potential μ_ν which is given by an interpolated expression between the free streaming case ($\mu_\nu = 0$) and the completed trapped case ($\mu^{eq}_\nu = \mu_e + \mu_p - \mu_n$). We could in the next step mix our prescription with this one to improve the treatment of trapping.

The correction to the energy and momentum equation due to neutrinos, $Q_{\nu,E}$ and $Q_{\nu,M}$ are given by:

$$Q_{\nu,M} = \alpha \, W \, Q^0_{\nu,M} \tag{7.87}$$

$$Q_{\nu,E} = \alpha \, W \, Q^0_{\nu,E} \; , \tag{7.88}$$

where:

$$Q^0_{\nu,M} = -\frac{\partial P_\nu}{\partial r} \tag{7.89}$$

$$Q^0_{\nu,E} = -\frac{4\pi}{(2\pi\hbar c)^3} \int_0^\infty \omega^3 \left(\frac{\mathrm{d}f}{\mathrm{d}t} \right)_{coll} \mathrm{d}\omega \; , \tag{7.90}$$

being the neutrino pressure calculated as [56]:

$$P_\nu = \frac{4\pi}{(2\pi\hbar c)^3}\frac{1}{3}\int_0^\infty \omega^3 f(\omega)\mathrm{d}\omega \ . \tag{7.91}$$

The gradient term $\frac{\partial P_\nu}{\partial r}$ has been evaluated numerically in the coordinate frame; this would lead to a slight inconsistency since the momentum transfer in radiation-transport is computed fully locally [258, 251].

7.4 Flow chart

In Fig. 7.3 I have drawn the flow chart of the Relativistic code. I point out some differences in the structure of the code with respect to the Newtonian one (cf. Section 6.4):

1. Implicit vs Explicit scheme: the main difference in the structure of the code is the treatment of the hydrodynamical equation: in the Newtonian code, everything is coupled: hydrodynamics and transport equations are solved together (in the matrix inversion one gets *all* the independent variables). In the Relativistic code, hydrodynamics and neutrino treatment are decoupled; the neutrino terms are calculated according to the operator-split method at the end of each hydrodynamical step.

2. Independent variables: in the Newtonian code, no "Conserved-to-primitive" (and viceversa) routine is needed. The physical variables (ρ, v, ϵ) are directly obtained as solutions of the matrix inversion.

3. Time step: in the Relativistic code, a routine computing the Courant condition must be called. In the Newtonian case, because of the implicit scheme, in principle any time step is allowed. However, since the transport equation is solved simultaneously with the hydrodynamical equations, a condition on the time step is regulated by the transport (diffusion timescale).

7.5 Newtonian version of the code

I have also worked to have a Newtonian version of the code. This is very interesting since it allows a direct comparison between the two different hydrodynamics, in GR and Newtonian framework.

The system of flux-conservative hyperbolic equations Eqs. (7.31) is unchanged in its general formulation:

$$\frac{\partial \mathbf{U}}{\partial t} + \frac{1}{r^2}\frac{\partial}{\partial r}\left[\frac{r^2\alpha}{X}\mathbf{F}(\mathbf{U})\right] = \mathbf{S}(\mathbf{U}) \ , \tag{7.92}$$

where now the chosen primitive physical variables are: the baryon density ρ, the (physical) velocity v, the specific internal energy ϵ, and the electron fraction Y_e. The same choice is done for example in Ref. [102], where the electron fraction is not included. I neglect, for the moment, the neutrino evolution equation; we will first concentrate on the

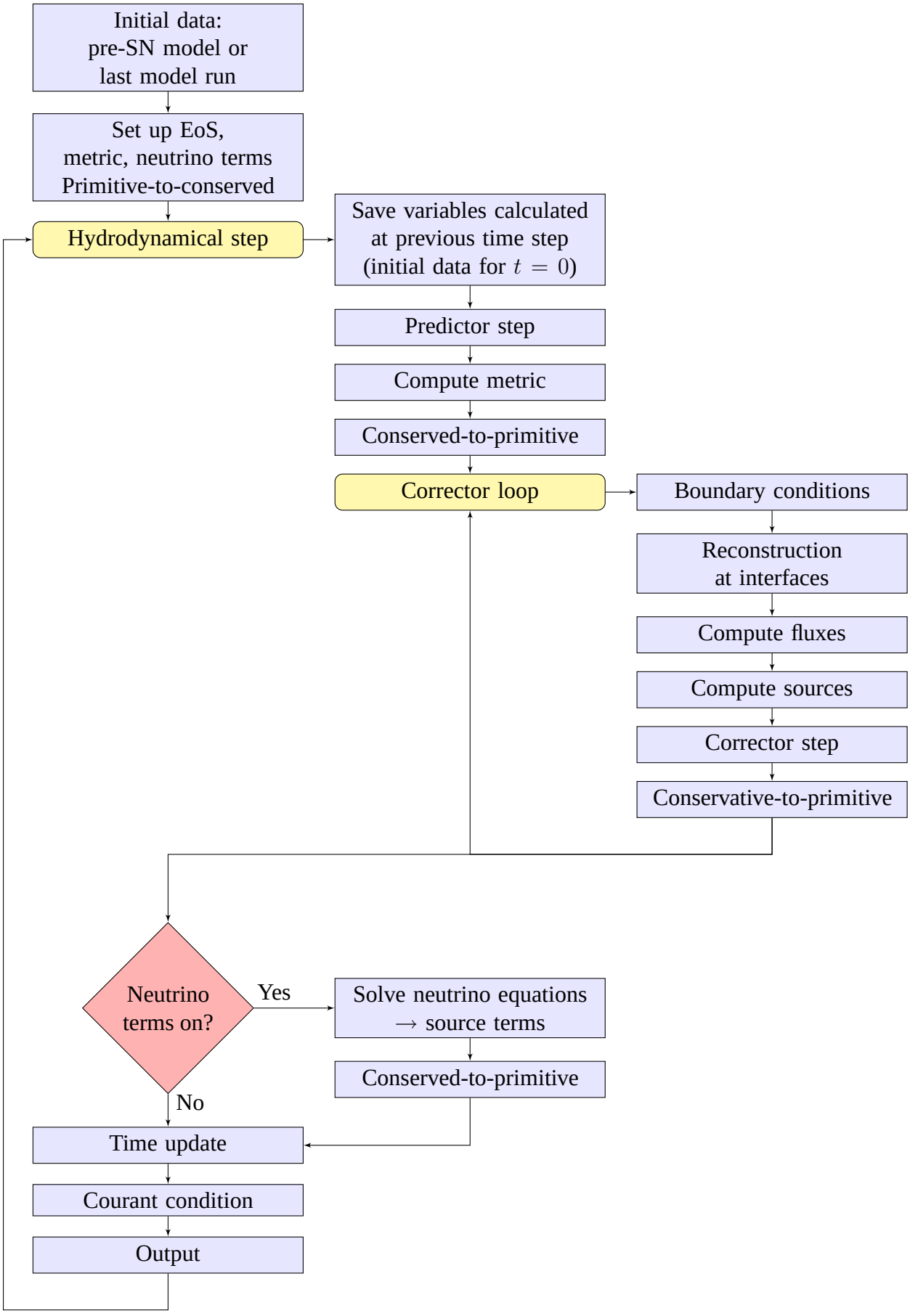

Figure 7.3: Flow chart of the Relativistic code.

hydrodynamical part without microphysical processes. When the neutrino evolution is considered, we have to keep in mind that in the Newtonian case the proper time is just the coordinate time. Thus, we obtain the following set of conserved variables: D, S, τ and DY_e, given by:

$$\mathbf{U} = \begin{pmatrix} D \\ S \\ \tau \\ DY_e \end{pmatrix}; \quad \begin{array}{l} D = \rho \\ S = \rho\, v \\ \tau = \rho\, \epsilon + \frac{1}{2}\, \rho v^2 \\ DY_e = \rho\, Y_e\, . \end{array} \tag{7.93}$$

To obtain the Newtonian limit, the following assumptions have been made: *(i)* I neglect terms of the order of v^2/c^2; *(ii)* I take the non relativistic limit $\rho v^2 \gg v^2\ (\rho\epsilon + P)$; *(iii)* to recover the correct expression in the energy equation, an expansion of the Lorentz factor W up to the second order $W = 1 + \frac{1}{2}v^2 + \mathcal{O}(v^4)$ is required. I have also checked that the equation found are equivalent to the ones employed by the Newtonian code described in Chapter 6.

The fluxes are then given by:

$$\mathbf{F}(\mathbf{U}) = \begin{pmatrix} Dv \\ Sv + P \\ S - Dv \\ DY_e v \end{pmatrix} \simeq \begin{pmatrix} \rho v \\ \rho v^2 + P \\ \left(\rho\epsilon + \frac{1}{2}\rho v^2 + P\right) \\ \rho Y_e v \end{pmatrix}, \tag{7.94}$$

and the source terms are:

$$\mathbf{S}(\mathbf{U}) = \begin{pmatrix} 0 \\ -\rho\frac{Gm}{r^2} + 2\frac{P}{r} + (vQ^0_{\nu,E} + Q^0_{\nu,M}) \\ -\rho v\frac{Gm}{r^2} + Q^0_{\nu,E} + vQ^0_{\nu,M} \\ R^0_{Y_e} \end{pmatrix}. \tag{7.95}$$

In the expressions for the momentum and energy source terms, I have explicitly written the gravitational constant G, so one can immediately recognize the usual gradient of gravitational potential $\frac{\partial\Phi}{\partial r}$ which comes into play.

It must be noticed that the baryonic mass and the gravitational one coincide, so m in this case refers to both.

For the computation of the fluxes, the eigenvalues and eigenvectors have been rederived. To that extent, I have followed the procedure explained in [133, 121]. Chosen a suitable vector of unknown ($\mathbf{w} = \rho, v, \epsilon$), the matrices:

$$\begin{aligned} \mathcal{A}^0 &= \frac{\partial \mathbf{U}}{\partial \mathbf{w}} = \begin{pmatrix} 1 & 0 & 0 \\ 0 & 1 & 0 \\ 0 & 0 & 1 \end{pmatrix} \\ \mathcal{A}^1 &= \frac{\partial \mathbf{F}}{\partial \mathbf{w}} = \begin{pmatrix} 0 & 1 & 0 \\ c_s^2 - \frac{\kappa}{\rho}(\tilde{h} - v^2) - v^2 & 2v - \frac{\kappa}{\rho}v & \frac{\kappa}{\rho} \\ v\left(c_s^2 - \frac{\kappa}{\rho}(\tilde{h} - v^2) - \tilde{h}\right) & \tilde{h} - \frac{\kappa}{\rho}v^2 & v^2\left(1 + \frac{\kappa}{\rho}\right) \end{pmatrix}, \end{aligned} \tag{7.96}$$

where: $\tilde{h} := \epsilon + \frac{1}{2}\rho v^2 + \frac{P}{\rho}$, have been calculated. The Jacobian matrix is given by: $\mathcal{B} = \mathcal{A}^1(\mathcal{A}^0)^{-1}$ [121]. The expressions for the solution of the eigenvalue problem have then been checked using Mathematica.

The eigenvalues are just the Newtonian limit of the ones in Eq. (7.54):

$$\lambda_- = v - c_s \tag{7.97a}$$
$$\lambda_0 = v \tag{7.97b}$$
$$\lambda_+ = v + c_s \, . \tag{7.97c}$$

The right eigenvectors in the Newtonian limit have been derived following e.g. the paper by Glaister [133]:

$$\mathbf{r}_- = \left[1,\ \lambda_-,\ \tilde{h} - c_s\, v\right] \tag{7.98a}$$
$$\mathbf{r}_0 = \left[1,\ \lambda_0,\ \tilde{h} - \frac{\rho c_s^2}{\kappa}\right] \tag{7.98b}$$
$$\mathbf{r}_+ = \left[1,\ \lambda_+,\ \tilde{h} + c_s\, v\right] \, . \tag{7.98c}$$

Again, the left eigenvectors needed to calculate the fluxes are computed via the inversion of the right-eigenvector matrix.

7.6 Results

In this Section we present some preliminary results and comparisons studying the sensitivity of the results when changing some values of the inputs. This is very helpful to understand the role and the impact of new implementations.

If not explicitly told, the simulations are run starting from the same 15 $M_\odot$ presupernova core from the Woosley and Heger models [345], the s15 with 1.62 $M_\odot$ core (cf. Section 4.3). The numerical grid which discretizes the core is made of 300 zones[18]non-equally spaced in radial coordinate (in the center, the grid is denser). The EoS employed in the "standard" model is the LS (routine version) with $K = 180$ MeV (for comparison with the literature).
When neutrinos are included, their spectrum between 0.5 and 380 MeV (originally 200 MeV) is discretized by 25 geometrically spaced energy bins, centered around 10 MeV. The choice of the maximum neutrino energy has been done in analogy with the literature (see e.g. [200]) and the choice of centering the distribution around 10 MeV has been done in analogy with the Newtonian code described in Chapter 6. Moreover, this choice is guided by the fact that the mean energy for neutrinos produced in electron capture during collapse is about 10 MeV.

In the following plots, when the velocity and the radius are displayed, I refer to the physical velocity (v in Romero *et al.*[285]) and the coordinate radius r. In the literature, it is often plotted the radial velocity per proper time, which is: v/X (cf. Section 7.1.1); this can generate differences in the absolute value of velocity when comparing with other works.

Before entering into the details of the parameter studies carried out, a general overview on the (ρ, T, Y_e) range spanned by the core during the collapse and early post-bounce phase is shown in Fig. 7.4. The density and temperatures are indicated in the (x,y) plane

[18]We have actually tried different discretizations; e.g. from 250 to 400 zones, checking that the results were in agreement.

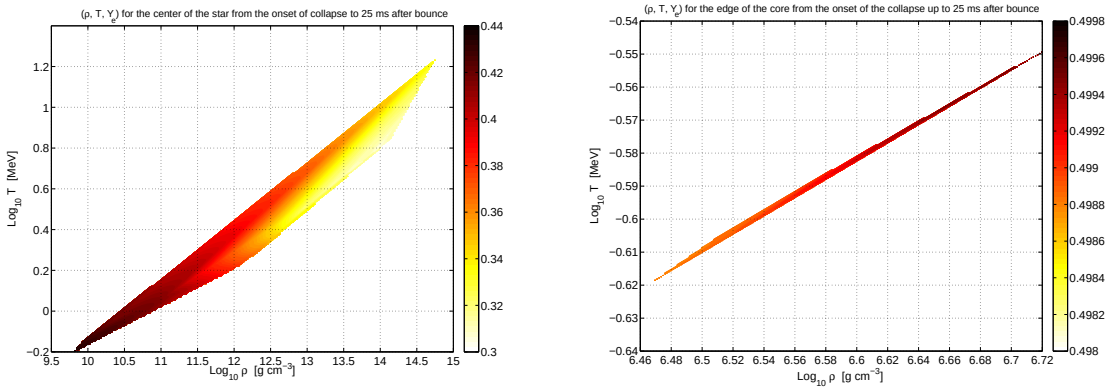

(a) (b)

Figure 7.4: (ρ, T, Y_e) range spanned by the core, in the center (left panel) and on the edge (right panel), in the case of "standard" trapping.

on a logarithmic scale, while the color scale corresponds to the values of Y_e. The left (right) panel refers to the center (edge) of the core of a 15 $M_\odot$ progenitor. One can notice that in the center of the star a wider range of (ρ, T, Y_e) conditions is encountered, supporting the argument that the outer layers of the star (which start after the core edge) are only slightly affected by the collapse dynamics.

7.6.1 Impact of the EoS

The first simulation we have run is a core collapse of a 4/3 polytrope, with a density dependent adiabatic index, and with the parameters described in Section 7.2. The presupernova is the same as in the paper by Romero *et al.*[285], i.e. a white dwarf having a gravitational mass of 1.3862 $M_\odot$. The velocity and density profiles obtained in Fig. 7.5 as a function of the radial coordinate at different times during collapse and bounce are of course the same as in Romero *et al.*The central density suddenly increases at the shock; it is often used as a criterion to localize the shock in time. We observe that the shock is well reproduced, and that it will go out of the core; this is not surprising since no microphysics is included in the simulation, so nothing stops the shock in its way out.

Then, the impact only of the incompressibility modulus has been evaluated; in particular we have chosen to run the simulation of core collapse for the three different values of the incompressibility modulus available with the LS EoS, namely $K = 180, 220, 375$ MeV. To this extent, three simulations have been run, all starting from the same s15 presupernova core without electron capture (i.e. the source term for the electron capture is switched off).

In Fig. 7.6 the velocity, density, entropy and adiabatic index (Γ) profiles at bounce are plotted as a function of the radial coordinate. The bounce time is defined as the time when in the inner core the entropy is larger than 3 (in unity of k_B)[19]. The bounce, which is expected to occur around 200 ms after starting the simulations, in our case happens later, around 320 ms. This is because the electron capture (which contributes to accelerate the

[19]In Chapter 6 we have adopted the convention to define the bounce as the time when maximum central density is reached, i.e. maximum scrunch. In the literature both are used.

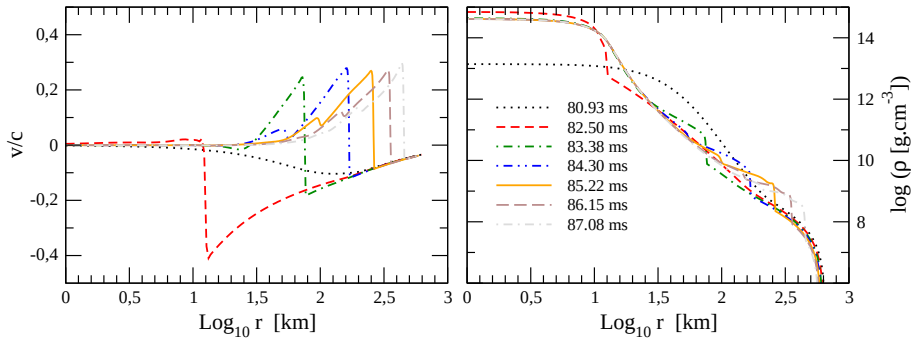

Figure 7.5: Snapshots of velocity and density profiles as a function of the radial coordinate obtained with a polytropic EoS.

Model	$\rho_{c,bounce}$ $[10^{14}$ g cm$^{-3}]$	$M_{b,encl,bounce}$ $[M_\odot]$	$Y_{e,c,bounce}$	$Y_{l,c,bounce}$
$K = 180$ MeV	5.05	0.70	0.332	0.401
$K = 220$ MeV	4.73	0.69	0.330	0.400
$K = 375$ MeV	3.84	0.72	0.326	0.398

Table 7.1: Central density, enclosed mass, electron and lepton fraction at bounce, for the s15 model with "standard" trapping, for the three values of incompressibility modulus: $K = 180, 220, 375$ MeV.

collapse) is turned off, so a number of initial oscillations take place before the "real" collapse, initiated by the initial velocity profile of the presupernova model (see Section 4.3), happens. We do not observe a big impact of the incompressibility modulus on the velocity profiles; in fact, the size of the homologous core is mainly determined by the electron fraction, which does not vary in these simulations (Y_e is only advected).
On the other hand, we observe, as expected, the impact of the K parameter on the density and adiabatic index profile, since the adiabatic index is related to the incompressibility modulus: smaller the incompressibility modulus, softer the EoS (smaller Γ), bigger the central density at bounce.

I have also run the simulations for different incompressibility modulus with deleptonization, fixing a trapping density as in Kotake *et al.*. In Fig. 7.7 the same quantities as in Fig. 7.6 are plotted. Again, we do not observe a big impact of the incompressibility modulus on the velocity and entropy profiles, while the K parameter acts mainly on the density and adiabatic index profile. Also in Refs. [313, 303], it has been observed that "numerical results of core collapse and bounce with different incompressibilities turn out to be similar up to 200 ms after bounce". If we look at the value of the enclosed mass at bounce, it is slightly higher in the case of a stiffer EoS ($K = 375$ MeV), as we can see from Table 7.1, where, for clarity, I have summarized some key quantities at bounce.

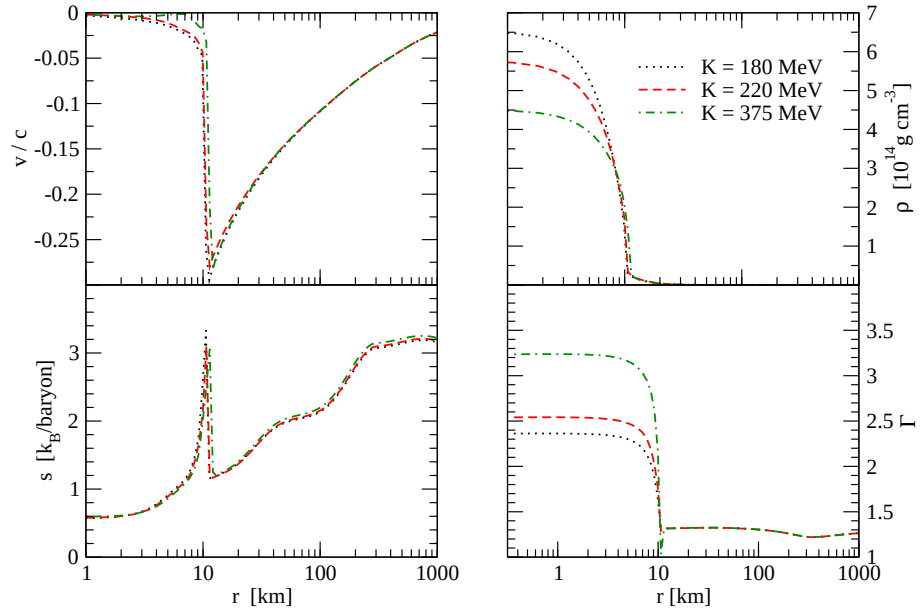

Figure 7.6: Velocity (upper left panel), density (upper right panel), entropy (lower left panel) and adiabatic index (Γ, lower right panel) profiles at bounce, as a function of the radial coordinate, for $K = 180, 220, 375$ MeV.

7.6.2 Impact of neutrino trapping and electron capture

In this Section we will comment on the results obtained varying the treatment of the neutrino trapping or the capture rates. The simulations are run starting from the s15 presupernova core and with the LS EoS with $K = 180$ MeV.

"Standard case"

The first set of plots are made assuming the trapping *à la Kotake* and the electron capture rates *à la Bruenn*. We fix a trapping density at 3×10^{11} g cm^{-3}before bounce and at 1×10^{11} g cm^{-3}after bounce. This is our "standard" case; we then make a parameter study comparing the different results to the "standard" ones.

In Fig. 7.8, the velocity (upper left panel), density (upper right panel), entropy (middle left panel), lepton fractions (middle right panel), mass fractions (lower left panel), rms neutrino energy (lower right panel) are plotted as a function of the radial coordinate, at the time of bounce. As already mentioned, this time has been defined as the time when the entropy in the inner core reaches 3 k_B/baryon. In the literature, one could also find the definition of the bounce as the time of maximum scrunch (maximum central density), or as the time when the nuclear density is reached. For comparison with works employing the LS EoS, we have decided to keep the definition based on the entropy[20]; different definitions can give slightly different bounce time. We notice the steepening of the profiles at the bounce, which is located around 10 km and (see Fig. 7.14) at around 0.7 $M_\odot$. In the

[20]In the Newtonian code, when the BBAL together with the Suraud EoS in employed, we do not really have an information on the entropy, since the employed high density EoS is calculated along isoentropic lines.

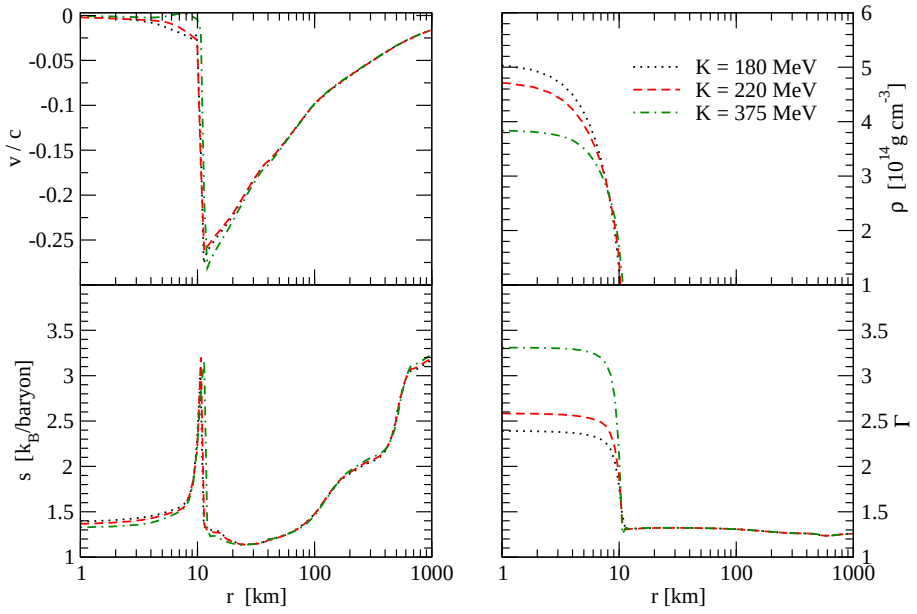

Figure 7.7: Velocity (upper left panel), density (upper right panel), entropy (lower left panel) and adiabatic index (Γ, lower right panel) profiles at bounce, as a function of the radial coordinate, for $K = 180, 220, 375$ MeV, in the case of "standard" trapping.

literature we can find the position of the formation of the shock around 0.6 or even 0.5 $M_\odot$ for a relativistic core collapse simulation. However, differences can arise from different progenitor models, neutrino treatment, or different network of microphysical processes considered. For example the neutrino-electron scattering is thought to act in moving the position of the shock wave inward of about 0.1 $M_\odot$ [33]. The dashed lines plotted together with the velocity profile is the speed of sound (in units of c); the position of the shock is defined by the sonic point, i.e. the point where the speed of sound equals the infall velocity. The electron fraction at the center has reached 0.33; this value is slightly higher with respect to the one, e.g., in Ref. [200], where Y_e at center is 0.28-0.30. The results however agree, considering that in our case, for example, neutrino-electron scattering which would contribute to decrease Y_e is not implemented, and the neutrino trapping scheme is less refined than in Ref. [200]. The lower left panel displays the mass fractions (nuclei, α, free neutrons and free protons): we notice that, in the innermost zones, the matter is mainly composed by free nucleons; the density is high enough to have dissociated the clusters. The neutrino root mean square (rms) energy shown in the lower right panel is defined as [244]:

$$\langle \epsilon_\nu \rangle_{rms} = \frac{\int_0^\infty \omega^4 f(\omega) \mathrm{d}\omega}{\int_0^\infty \omega^2 f(\omega) \mathrm{d}\omega} \,, \tag{7.99}$$

being ω the neutrino energy and f its distribution function. In the multi-group implementation the integrals are replaced by a summation over the energy bins. The sudden decrease of the rms energy around 70 km is due to our treatment of trapping; in fact, in the density plot (upper right panel) we can see that this point corresponds to $\rho \simeq 10^{11}$ g cm^{-3}which is around the trapping density; for $\rho < \rho_{tr}$, neutrinos are just removed from

the star; thus their distribution function is set to zero.

We now show what happens after bounce. In Fig. 7.9 we plot, as a function of the radial coordinate, the velocity (upper left panel), density (upper right panel), entropy (middle left panel), lepton fractions (middle right panel), mass fractions (lower left panel), rms neutrino energy (lower right panel) as a function of the radial coordinate, 3 ms after the core bounce. We notice that the shock has moved outwards from 10 to 100 km, i.e., from about 0.7 to about 1.15 $M_\odot$ (baryonic enclosed mass). The electron and lepton fractions exhibit a strong decrease between around 50 and 100 km; this is a consequence of the presence of the shock, which increases the temperature in the shocked region behind it and thus increases the electron capture rates. I point out however that the electron, neutrino and lepton fraction profiles are in very good agreement with Fig. 2 in Kotake *et al.*[179] (they use a slightly different progenitor, from Weaver and Woosley, but still a 15 $M_\odot$ progenitor). Again we notice a strong dissociation region behind the shock, and the sudden decrease of the neutrino rms energy due to the trapping condition. The velocity profile displays a double peak. This could be associated to wave reflection effects [200], or to a numerical instability: the reason for that might be searched in the recovering of the primitive variables procedure: one in fact encounters discontinuities around shock, and since the EoS (which is called in the conservative-to-primitive routine) is employed in its routine version, these discontinuities might impact the output of the EoS call. Moreover, the trapping condition introduces another discontinuity in the simulation because of its "step function"-like definition. In the bottom left panels, we observe that nuclei are destroyed in the high entropy region behind the shock, but there is already a thin zone at around 10 km where nuclei exist; this spatial zone corresponds to the location where the future neutron star crust is expected to lie.

We now comment the time evolution of the simulation. Since different simulations can give different time at bounce, I synchronize the plots at the bounce time. In Fig. 7.10, as a function of post-bounce time (the 0 abscissa corresponds to the time of bounce, which occurs at 225 ms after the simulation starts), the central electron fraction (left panel) and central density (right panel) are displayed. Around bounce time the curves exhibit a steep profile which corresponds to the central bounce. The shape of the profiles in Fig. 7.10 are in good agreement, e.g., with Ref. [265], where simulations with CoCoNuT (1D case) and a similar treatment of the electron capture are carried out for a 40 $M_\odot$ progenitor.

In Fig. 7.11 the shock radius R_s, defined as the position of the maximum of the velocity divergence, is plotted. For comparison, I have superimposed the curves obtained for different incompressibility modulus. We observe oscillations starting at around 5 ms after bounce; the shock however seems to stall, as expected, between 100 and 150 km. I plan to perform longer-term simulations in order to determine more precisely this value.

To show at what extent the GR effects are important, the lapse function α (left panels) and the metric X (right panels) (cf. Eqs. (7.11) and (7.12)) are displayed in Fig. 7.12 as a function of radius (upper panels) and as a function of post bounce time (lower panels). The plots show that the metric factors are noticeably different from 1 from bounce on, and for the innermost zones. This consideration also tells that using the Newtonian framework to build the presupernova models is a very good assumption.

In Fig. 7.13, the neutrino distribution function is plotted for the central zone as a function of neutrino energy, for different densities after the trapping density. This figure gives an idea on how the neutrino distribution function is built up after trapping. We

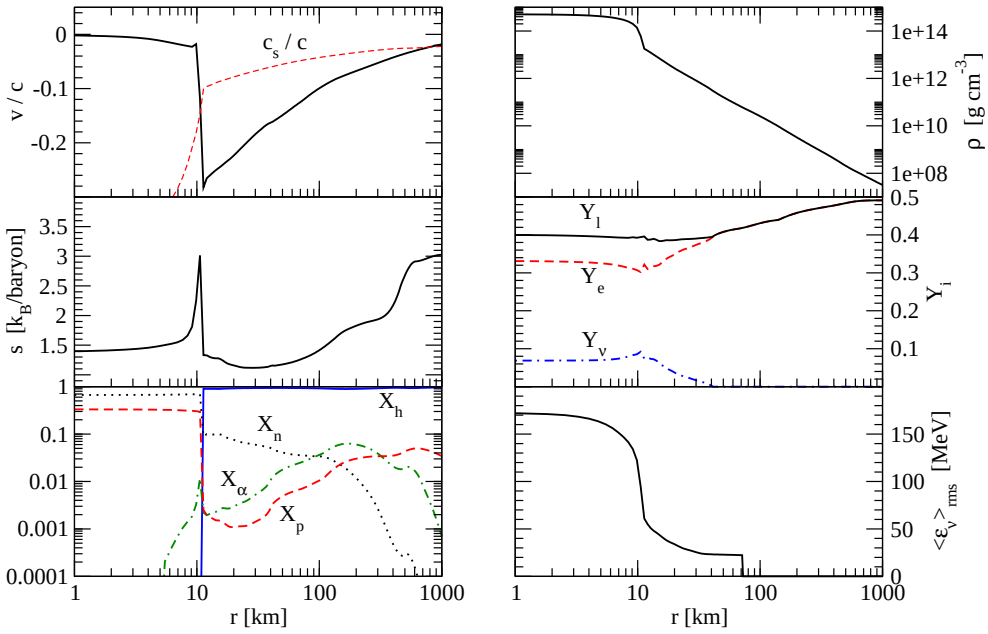

Figure 7.8: Velocity (upper left panel), density (upper right panel), entropy (middle left panel), lepton fractions (middle right panel), mass fractions (lower left panel), rms neutrino energy (lower right panel) as a function of the radial coordinate at bounce, in the case of "standard" trapping.

see, as the density increases, how f_ν goes towards the Fermi-Dirac distribution, which is expected when neutrinos are completely thermalized.

Parameter study varying the trapping density

We perform now a parameter study varying the trapping density. In Fig. 7.14 we compare the "standard" case with the case where Eq. (7.84) is solved from the beginning, i.e. neutrino produced in electron capture are kept trapped since the simulation starts. The velocity and Y_e profiles (left panels) at bounce, which occurs at 254 ms, and the central values of lepton fractions and entropy as a function of the central density (right panels) are compared. We notice that the lepton fraction is constant (conservation of lepton number) and that a non-zero neutrino fraction is constructed if neutrinos are trapped. This has a non-negligible impact on the collapse dynamics, since the higher lepton fraction drives the formation of the shock outwards, as a function of the enclosed mass (from $0.70\ M_\odot$ in the "standard" case to $0.81\ M_\odot$). This can be understood thinking about the simple relation $M_{hc} \simeq 5.8 Y_l^2\ [M_\odot]$ (Eq. (1.1)), i.e. the difference in the mass of the homologous core is $\Delta M_{hc}/M_{hc} \simeq 2\Delta Y_l/Y_l$. Thus, if we estimate the expected change in the position of the shock wave in terms of the enclosed mass: $\Delta M_{hc} \simeq 0.12$, which is in agreement with what we obtain.

We now change the trapping density; we have decided to increase the density at which neutrinos are kept trapped by an order of magnitude, i.e. from 3×10^{11} g cm^{-3}before bounce and at 1×10^{11} g cm^{-3}after bounce to 3×10^{12} g cm^{-3}before bounce (which occurs in this case at 224 ms) and at 1×10^{12} g cm^{-3}after bounce. In Fig. 7.15 the velocity (upper left panel), electron fraction (lower left panel) as a function of the enclosed baryon mass,

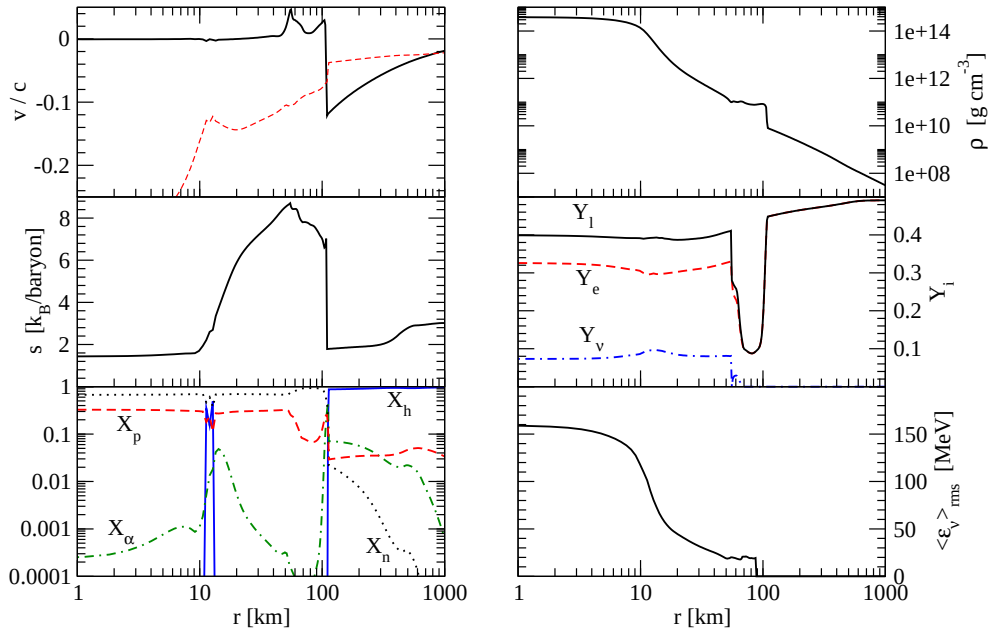

Figure 7.9: Velocity (upper left panel), density (upper right panel), entropy (middle left panel), lepton fractions (middle right panel), mass fractions (lower left panel), rms neutrino energy (lower right panel) as a function of the radial coordinate 3 ms after bounce, in the case of "standard" trapping.

and central lepton fractions (upper right panel) and central entropy (lower right panel) as a function of the central density at the time of bounce are displayed. Since in the second case we let neutrinos escape freely for a longer time, the capture is allowed for a longer time, which in turn gives lower Y_e (and Y_l) and a shock bounce at a smaller enclosed mass (from $0.70\ M_\odot$ in the "standard" case to $0.63\ M_\odot$). If again we estimate the difference in the mass of the homologous core as a consequence of the different value of the lepton fraction at trapping, $\Delta M_{hc}/M_{hc} \simeq 2\Delta Y_l/Y_l$, we find: $\Delta M_{hc} \simeq 0.1$, since $\Delta Y_l \simeq 0.04$. In fact, if the trapping is imposed at 3×10^{11} g cm^{-3}, the central final lepton fraction is 0.401, while if the trapping is imposed at 3×10^{12} g cm^{-3}, the final lepton fraction is 0.362.

Parameter study varying the electron capture rates on nuclei

To show the sensitivity of the final lepton fraction to the electron capture rates, we have run the simulations with the "standard" trapping condition varying the strength of the electron capture. In Fig. 7.16 I plot the central lepton fractions as a function of central density, for different capture rates: the "standard" Bruenn parameterization (solid black line), considering the capture only on nuclei, according to the Bruenn parameterization (dashed red line), considering the capture only on free protons (dotted-dashed green line), or taking into account the capture both on free protons and on nuclei, but keeping fixed the product N_pN_h equal to 0.1 (dotted blue line), 1 (dashed-dotted-dotted maroon line), or 10 (dashed-dashed-dotted orange line). Since the term $\frac{2}{7}N_pN_h$ represents the typical matrix element for the capture (see Section G.2.2), changing by hand N_pN_h means, in a

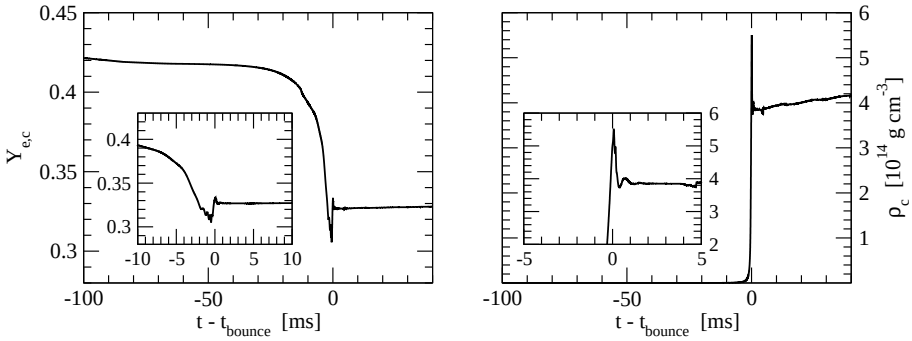

Figure 7.10: Central electron fraction (left panel) and central density (right panel) as a function of the coordinate time from bounce. The insets show a zoom of the profiles around the bounce time.

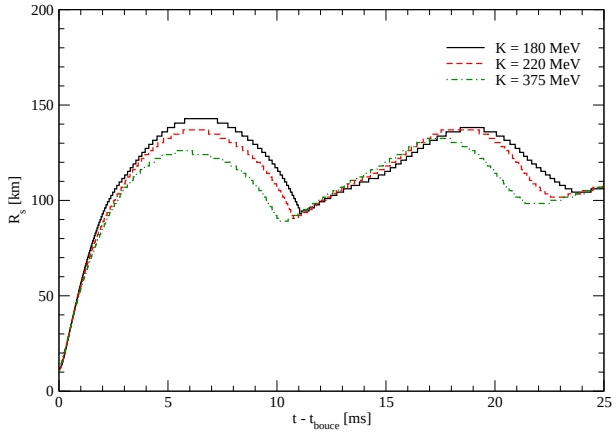

Figure 7.11: Shock radius as a function of post bounce time, for K =180 (solid black line), 220 (dashed red line), 375 MeV (dotted-dashed green line).

way, changing the strength of the capture rates on nuclei. This simple and reproducible way to tune the matrix element was already adopted in Ref. [166] and in Chapter 6. We notice that the initial behaviour of Y_l for the "standard" case is similar to the case where only capture on nuclei is considered; then, as a consequence of the Pauli blocking, the capture on free protons dominates. Changing the product $N_p N_h$ from 0.1 to 10, the final lepton fraction decreases by ~ 0.01. The change in the slope for the dashed-dotted and the dotted curves (capture only on free protons and case $N_p N_h = 0.1$ i.e. the capture on nuclei is strongly inhibited) is a consequence of the condition on the blocking factors η_{np} and η_{pn} (see Section G.2.1).

The apparent opposite behaviour of Y_l for different capture rates with respect to what obtained in Chapter 6 (cf. Fig. 6.3) might be attributable to two reasons: (i) transport: in the GR model there is no transport, (all) neutrinos escape, and that contributes to rapidly decrease the lepton fraction from the beginning (i.e. Y_l is lower in GR case with respect to the Newtonian code from the beginning); (ii) GR effects contribute to increase the density and temperature of the system (the potential well is deeper in GR than in Newtonian dynamics, see e.g. Shapiro and Teukolski textbook [295]), so that the capture rates might be

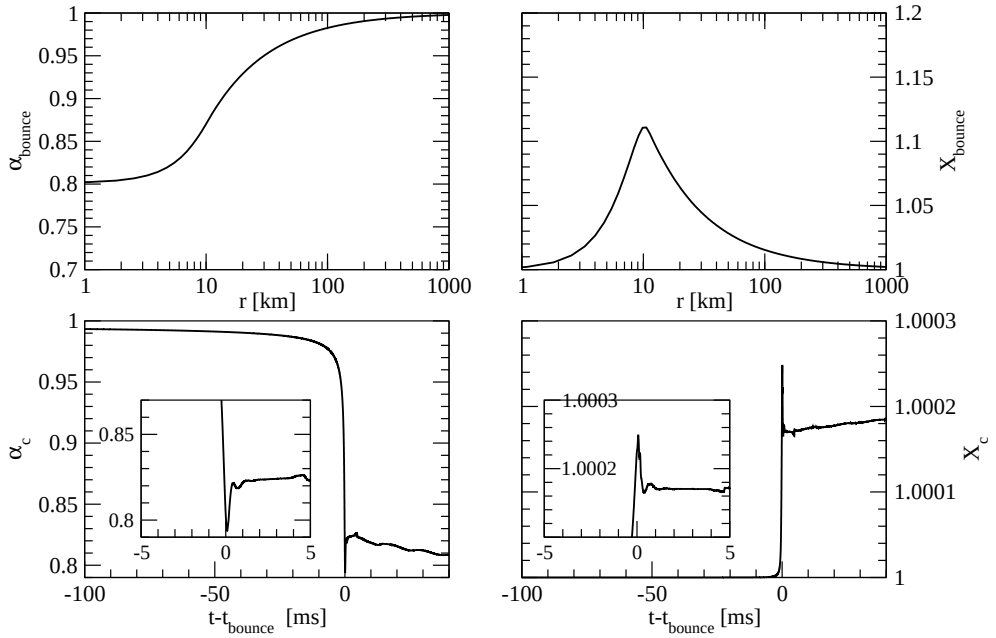

Figure 7.12: Lapse function α (left panels) and metric X (right panels) as a function of radius (upper panels) and post bounce time (lower panels). The insets in the lower panels show a zoom around the bounce time.

affected in this respect. Indeed, the final lepton fraction is a consequence of the previous cumulative effects before trapping, when, at lower densities, mostly the capture on nuclei dominates.

Progenitor model comparison

We have also run the simulation for different progenitor models, other than the s15 (15 $M_\odot$) described previously, namely the s20 (20 $M_\odot$), the s40 (40 $M_\odot$) models (see Section 4.3).

The results are compared in the "standard" trapping case. There are no big differences between the profiles at bounce. In fact, all iron cores are alike, even if not identical; the non monotonicity of the quantities, like the initial central density, depends on the details of the stellar evolution history. If we compare the velocity, density, entropy and lepton fractions at bounce, they look very similar, as one can see from Fig. 7.17, where the results for the s15, s20 and s40 models are shown. Since the three sets of profiles for Y_l, Y_e and Y_ν are alike, we plot only the lepton fraction profiles. The discrepancies in the entropy profiles in the exterior zones might be due to the different composition of the progenitor, i.e. to the prior different stellar evolution paths. The curves stop at different enclosed mass because the dimensions of the iron core of the progenitor models are different (see Table 4.1). In particular, the central density at bounce changes from 5.05×10^{14} g cm^{-3}for the s15 model, to 5.21×10^{14} g cm^{-3}for the s20 model, to 5.04×10^{14} g cm^{-3}for the s40 model. A weak dependence on the progenitor model for the maximum central density was also obtained, for example, by Ott [262] and Dimmelmeier *et al.* [103]. Even if one cannot make an exact comparison of the absolute values of the central density (rotation

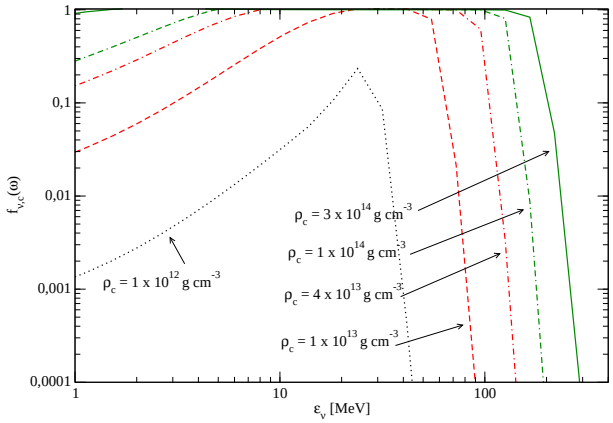

Figure 7.13: Neutrino distribution function at core center as a function of neutrino energy, for different central densities.

Model	$\rho_{c,bounce}$ $[10^{14}$ g cm$^{-3}]$	$M_{b,encl,bounce}$ $[M_\odot]$	$Y_{e,c,bounce}$	$Y_{l,c,bounce}$
s15 ("std" trapping)	5.05	0.70	0.332	0.401
s20 ("std" trapping)	5.21	0.73	0.335	0.405
s40 ("std" trapping)	5.04	0.68	0.327	0.394

Table 7.2: Central density, enclosed mass, electron and lepton fraction at bounce, for the s15, s20 and s40 progenitor models, with the "standard" trapping condition.

and axisymmetry are not included in our case), in Fig. 8 of Ref. [103] the maximum central density is shown to be mainly dependent on the EoS more than on the mass of the progenitor model. The value we obtain for the central density at bounce for the s40 model is in very good agreement with Ref. [265].

In order to show in a clearer way the (even if small) differences in the central density, the latter is plotted as a function of time for the three progenitors in Fig. 7.18. Since the bounce time is not the same for the three simulations, I synchronize them at the core bounce time. We see that the curves are nearly indistinguishable at bounce, while after bounce the central density is slightly less for the more massive model.

To summarize, Table 7.3 lists the results discussed above.

7.6.3 Comparison between GR and Newtonian results

In order only to compare the GR and the Newtonian hydrodynamics, we run the code twice, without and with neutrino contribution in the "standard" case, for the same s15 presupernova model, using the LS EoS with $K = 180$ MeV.

Let us analyse first the comparison obtained without electron capture, so that we could address the differences only to the hydrodynamics itself. In Fig 7.19 a comparison between the two runs, at bounce, is displayed. We plot the velocity, density, entropy and temperature profiles as a function of the enclosed (baryonic) mass. GR effects shift the

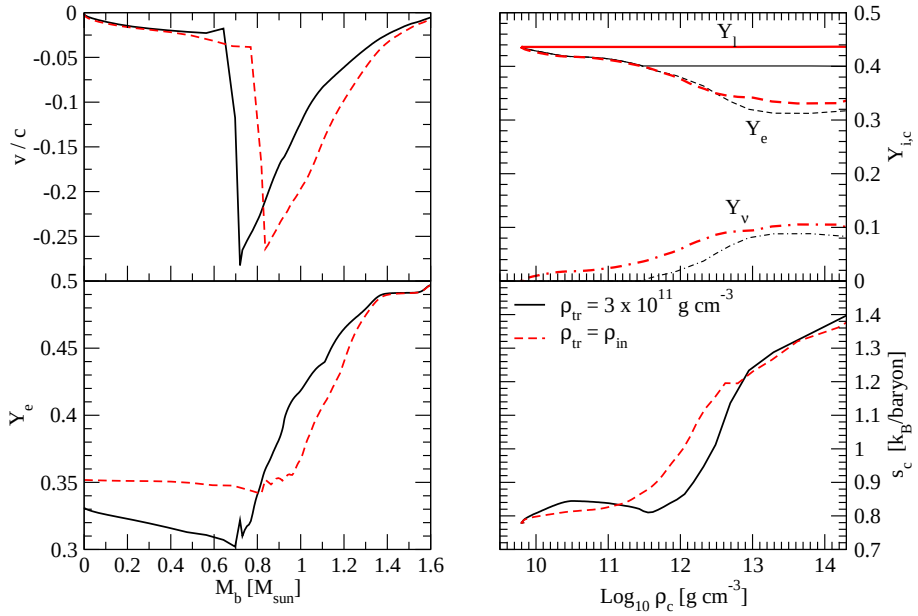

Figure 7.14: Velocity (upper left panel) and electron fraction (lower left panel) profiles as a function of the baryon enclosed mass at bounce, and lepton fractions (upper right panel) and entropy (lower right panel) as a function of the central density. Black solid lines correspond to $\rho_{tr} = 3 \times 10^{11}$ g cm^{-3}(before bounce), red dashed lines to the case where neutrino are kept trapped from the beginning. In the upper right panel, thin lines correspond to the "standard" case, while thick lines correspond to the case where neutrino are kept trapped from the beginning.

position of the formation of the shock wave $\sim 0.1\ M_\odot$ inwards ($\sim$ 20% smaller enclosed mass), in agreement with the conclusions of Ref. [202]. Moreover, the central density in the GR case is higher, from about 4×10^{14} g cm^{-3}(Newtonian) to about 6×10^{14} g cm^{-3}(GR). We observe the same behaviour for the temperature profile: in the GR case, the temperature at bounce is slightly higher than in the Newtonian case, while the entropy is nearly unaffected.

We now comment the plots obtained in the "standard" trapping treatment. In Fig 7.20 a comparison between the two runs, at bounce, is drawn. The velocity (upper left panel), density (upper right panel), entropy (middle left panel), lepton fractions (middle right panel), mass fractions (lower left panel), rms neutrino energy (lower right panel) are plotted as a function of the radial coordinate at bounce. Again, GR effects shift the position of the formation of the shock wave to innermost shells, correspondent to $\sim$ 16% smaller enclosed mass. Moreover, the rms neutrino energy are smaller at the center in the Newtonian case.

For sake of clarity, in Table 7.3 I summarize the results given above.

A nice comparison between GR and Newtonian code outputs is given e.g. in [60, 202]. Even if it is not possible to compare directly with Ref. [202] (differences arise e.g. in transport scheme and progenitor model), we can notice however that the general trend of the plots (see e.g. their Fig. 1) is reproduced by our simulations: position of formation of the shock shifted inwards of about 20%, slightly lower central value of density, Y_e, and rms neutrino energy in the Newtonian case.

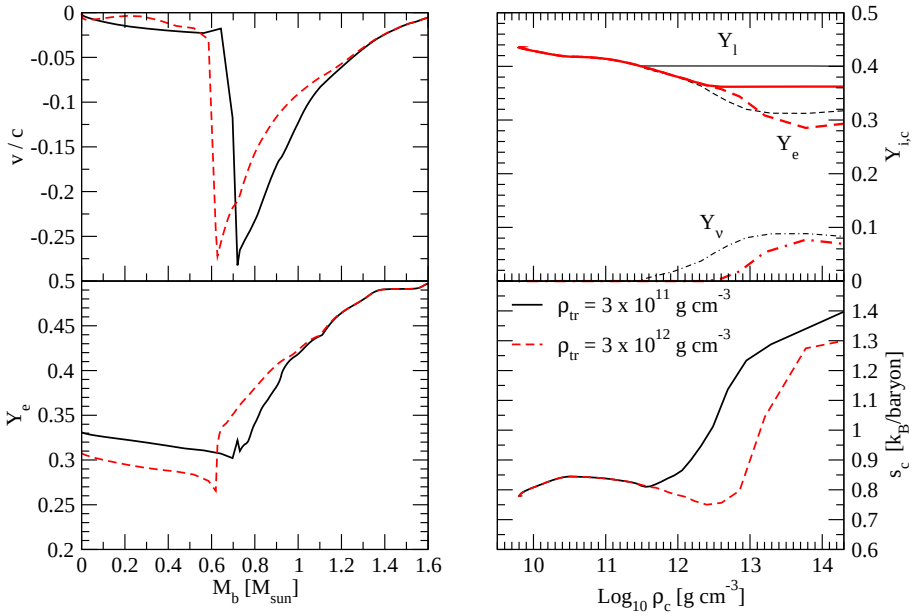

Figure 7.15: Velocity (upper left panel) and electron fraction (lower left panel) profiles as a function of the baryon enclosed mass at bounce, and lepton fractions (upper right panel) and entropy (lower right panel) as a function of the central density. Black solid lines correspond to $\rho_{tr} = 3 \times 10^{11}$ g cm^{-3}(before bounce), red dashed lines to $\rho_{tr} = 3 \times 10^{12}$ g cm^{-3}(before bounce). In the upper right panel, thin black lines correspond to the standard case, while thick red lines correspond to the case $\rho_{tr} = 3 \times 10^{12}$ g cm^{-3}(before bounce).

7.7 Conclusions and Outlooks

In this Chapter we have described the one-dimensional GR code whose original version was written by Romero and collaborators. An updated version with a multi-group treatment of deleptonization and the routine version of the LS EoS was implemented by J. Pons and collaborators.

Starting from this last version, we have modified the electron capture treatment including a neutrino trapping condition, defined by a trapping density. Even if it cannot reproduce all the features of a real transport, it reproduces quite well the general behaviour of the lepton fractions and the dynamics of the core collapse, giving a position of formation of the shock wave in general agreement with the literature, despite differences which can come from the microphysics inputs or transport properties.
We have also implemented a Newtonian version of the code, changing the expressions for the source terms as described in Section 7.5 and re-deriving (and implementing) the expressions for the eigenvectors in the HRSC scheme.

We focused on the collapse phase, but we reserve a deeper post-bounce investigation for the near future.

I will go on working on this code. The first step would be the inclusion of tabulated version of different EoS, among others the modified LS EoS described in Appendix F. I also would like to test the impact in the GR framework of the temperature dependent symmetry energy discussed in Chapters 5 and 6: at first, for comparison, we could use

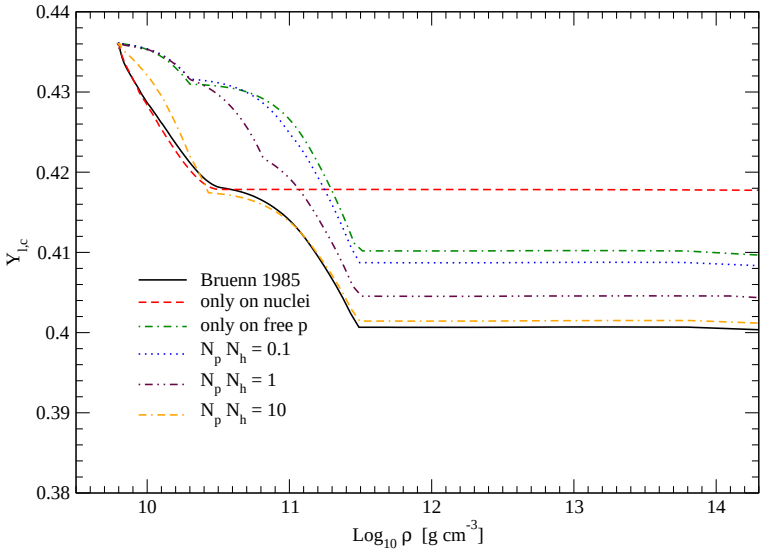

Figure 7.16: Central lepton fractions as a function of central density, for different strengths of electron capture rates.

Model	$\rho_{c,bounce}$ $[10^{14}$ g cm$^{-3}]$	$M_{b,encl,bounce}$ $[M_\odot]$	$Y_{e,c,bounce}$	$Y_{l,c,bounce}$
GR (no capture)	5.98	0.73	0.397*	0.397
Newtonian (no capture)	4.15	0.94	0.397*	0.397
GR ("std" trapping)	5.05	0.70	0.332	0.401
Newtonian ("std" trapping)	3.87	0.82	0.326	0.400

Table 7.3: Central density, enclosed mass, electron and lepton fraction at bounce, for the GR and Newtonian simulations, with or without deleptonization. The "*" indicates that an initial 10% decrease of Y_e has been made to accelerate the collapse.

the BBAL EoS, then we would like to include such a temperature dependence in a recent finite-temperature EoS such as the LS one. Then, a more accurate treatment of the electron capture (e.g. implementing the new electron capture rates on nuclei calculated by Paar and collaborators [263]), and microscopic calculations of neutrino mean free paths in dense matter (e.g. the one calculated by Margueron *et al.*[224]) are foreseen. A long term plan of this work would account for the implementation of neutrino transport.

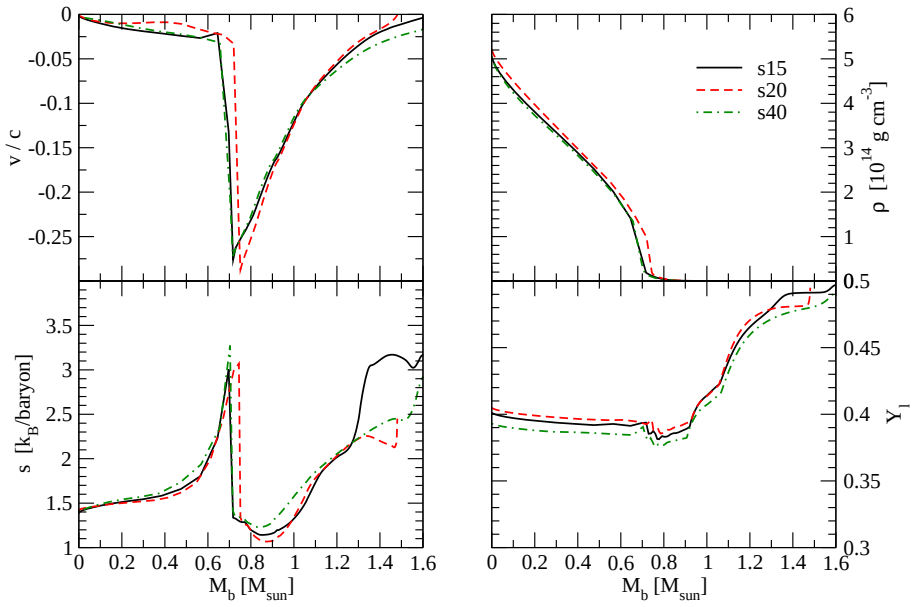

Figure 7.17: Velocity (upper left panel), density (upper right panel), entropy (lower left panel) and lepton fraction (lower right panel) as a function of the enclosed baryon mass at bounce for s15 (solid black lines), s20 (dashed red lines), and s40 (dashed-dotted green lines) progenitor models.

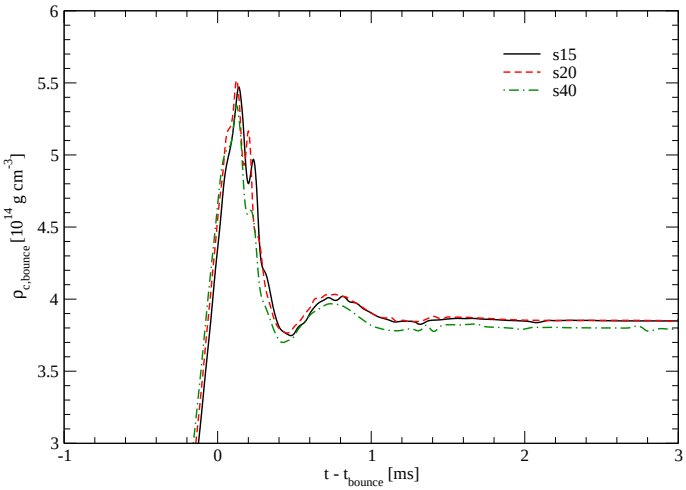

Figure 7.18: Central density as a function of the post bounce time for the s15 (solid black line), s20 (dashed red line) and s40 (dashed-dotted green line) models.

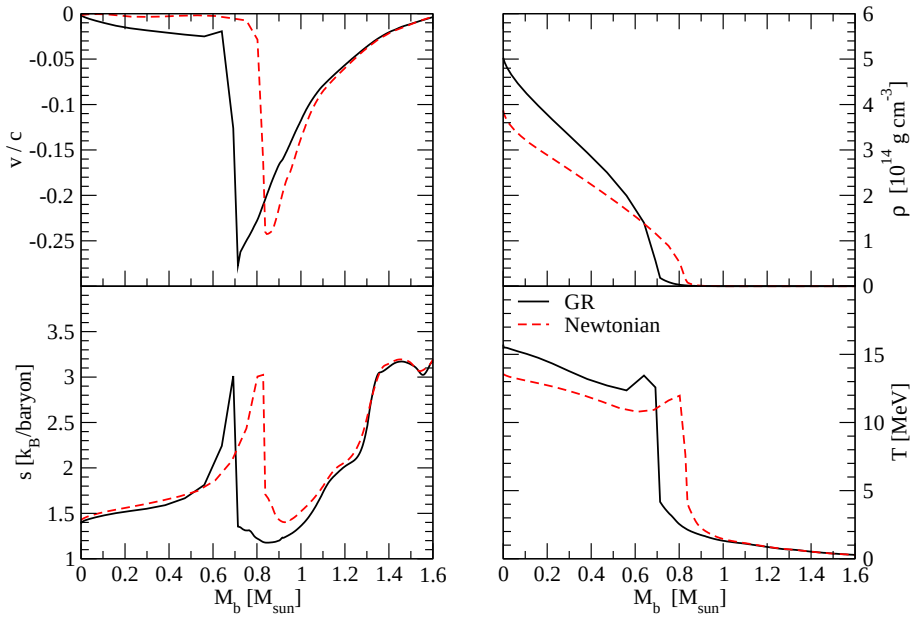

Figure 7.19: Velocity (upper left panel), density (upper right panel), entropy (lower left panel) and temperature (lower right panel) as a function of the enclosed mass at bounce for s15 progenitor model, without neutrino contribution.

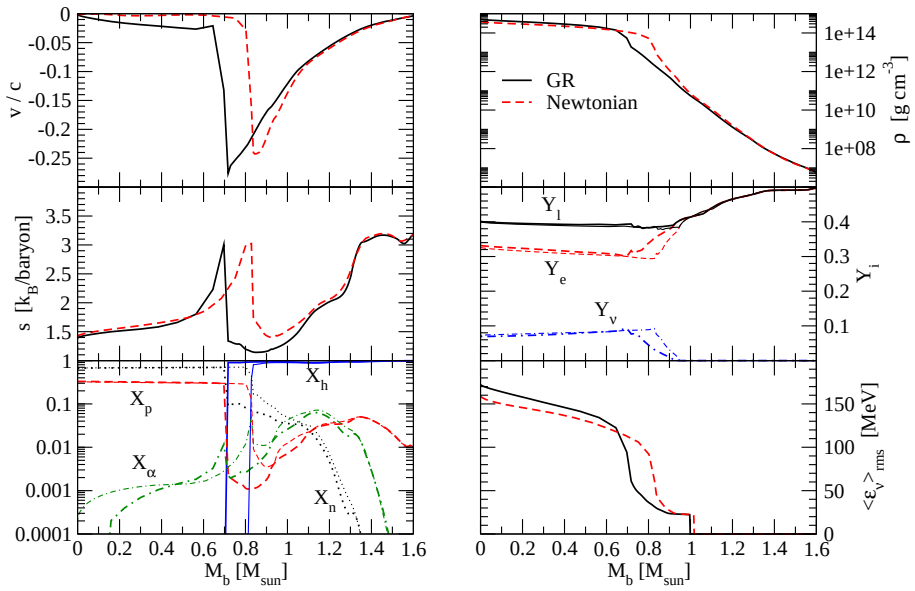

Figure 7.20: Velocity (upper left panel), density (upper right panel), entropy (middle left panel), lepton fractions (middle right panel), mass fractions (lower left panel), rms neutrino energy (lower right panel) as a function of the radial coordinate at bounce for s15 progenitor model, with "standard" neutrino trapping. Except for the leptons and mass fractions, where thick lines correspond to the GR run while the thin lines correspond to the Newtonian run, solid black lines correspond to the GR run and dashed red lines to the Newtonian run.

General conclusions and Outlooks

The aim of this thesis has been to investigate the impact of some microphysical inputs in the type II core collapse supernova scenario. Working in a collaboration among the Institut de Physique Nucléaire d'Orsay, the University of Milan, the CEA/DAM, and the Observatoire de Paris-Meudon has allowed to avail ourselves of the expertise in the different fields (nuclear physics, hydrodynamics, astrophysics) in order to have a larger and more complete overview on the subject.

From the nuclear physics point of view, we have worked to include in an Energy Density Functional framework the effect of a surface peaked effective mass, which comes from the microscopic particle-vibration coupling. This has been possible adding a term to the Skyrme functional which is able to reproduce the enhancement of the effective mass at the nuclear surface, increasing the level density around the Fermi surface as expected from experimental observations. It has been shown, in Chapter 3, the impact of this new term on the mean field properties in ^{40}Ca and ^{208}Pb nuclei, and on the pairing properties at zero and finite temperature in the nucleus ^{120}Sn.
We have also started new calculations to evaluate the temperature dependence of the nucleon effective mass in the microscopic RPA framework, whose preliminary results are shown in Appendix D.

Concerning the astrophysical models, we started from the study of the core collapse by means of a one zone code, which has proven efficient to reproduce the deleptonization phase during the collapse. The results obtained in this framework and described in Chapter 5, namely a systematic reduction of the deleptonization and a gain in the shock wave dissociation energy when a temperature dependent nuclear symmetry energy is implemented, have encouraged to perform more detailed simulations. Therefore, we have worked on a Newtonian one-dimensional code with neutrino transport, described in Chapter 6, in order to discuss this particular issue. The outcomes of the simulations confirmed the previous results, i.e. a systematic reduction of the deleptonization. Moreover, it has been possible to estimate the impact of the temperature dependent nuclear symmetry energy on the position of the formation of the shock wave, which is shifted outwards of a non-negligible amount. We have also worked on the Newtonian code to implement a routine version of the Lattimer and Swesty equation of state.

Furthermore, we have run simulations with a General Relativistic code, depicted in Chapter 7. This code is not as advanced as the Newtonian code with respect to the treatment of neutrinos: indeed, no transport is included. However, the evolution equation for neutrinos is already implemented in a multi-group fashion. We have analysed the impact of the equation of state and the electron capture on the collapse phase. A Newtonian version of the code has then been implemented, obtaining results in global agreement with the literature.

Finally, we have also worked to extend the Lattimer and Swesty equation of state at lower densities and corrected a known problem with the α particles binding energy. We have generated tables as described in Appendix F.

In the future, we plan to continue the study on the temperature dependence of the nucleon effective mass, which we would like to include in a finite temperature equation of state such as the Lattimer and Swesty one.

We also foresee to go on working on the supernova models. We want to test, in the Newtonian and GR framework, the impact of different equations of state, and of the new electron capture rates calculated by Paar and collaborators. As longer time plan, we want also to include microscopic neutrino mean free paths to treat more realistically the neutrino interactions in dense matter, and the neutrino transport in the GR code.

Appendix A

Units, Constants, Notations

Table A.1 and Table A.2 list the fundamental constants used in the text, taken from Refs. [247, 3].

A.1 Constants

Constant	Symbol	Units	Value	Uncertainty
Atomic mass unit	m_u	kg	1.660538782 $\times 10^{-27}$	0.000000083 $\times 10^{-27}$
Avogadro number	N_A	mol^{-1}	6.02214179 $\times 10^{23}$	0.00000030 $\times 10^{23}$
Boltzmann constant	k_B	erg K^{-1}	1.380650524 $\times 10^{-16}$	0.00000018 $\times 10^{-16}$
Elementary charge	e	C	1.602176487 $\times 10^{-19}$	0.000000040 $\times 10^{-19}$
Fermi coupling constant	G_F	GeV^{-2}	1.16637 $\times 10^{-5}$	0.00001 $\times 10^{-3}$
Fine-structure constant	α	dimensionless	7.2973525376 $\times 10^{-3}$	0.0000000050 $\times 10^{-3}$
Newtonian constant of gravitation	G	$\text{m}^3\ \text{kg}^{-1}\ \text{s}^{-2}$	6.67428 $\times 10^{-11}$	0.00067 $\times 10^{-11}$
Planck constant	h	J s	6.62606896 $\times 10^{-34}$	0.00000033 $\times 10^{-34}$
Planck constant over 2π	$\hbar$	J s	1.054571628 $\times 10^{-34}$	0.000000053 $\times 10^{-34}$
Speed of light	c	cm s^{-1}	2.99792458 $\times 10^{10}$	-
Stefan-Boltzmann constant	σ	$\text{W m}^{-2}\ \text{K}^{-4}$	5.670400 $\times 10^{-8}$	0.000040 $\times 10^{-8}$
Alpha particle mass	m_α	kg	6.64465620 $\times 10^{-27}$	0.000000033 $\times 10^{-27}$
Electron mass in m_u	m_e	m_u	5.4857990943 $\times 10^{-4}$	0.000000023 $\times 10^{-4}$
Muon mass in m_u	m_μ	m_u	0.1134289256	0.0000000029
Neutron mass	m_n	kg	1.674927211 $\times 10^{-27}$	0.000000084 $\times 10^{-27}$
Proton mass	m_p	kg	1.672621637 $\times 10^{-27}$	0.000000083 $\times 10^{-27}$

Table A.1: Fundamental physical constants (from [247]).

A.2 Unit conversion

When dealing with "nuclear" quantities (such as in the EoS), the natural units are the nuclear units (MeV and fm for energy and length), while in astrophysical context

Constant	Symbol	Units	Value
Solar Mass	$M_\odot$	g	1.9884 $\times 10^{33}$
Solar Radius	$R_\odot$	cm	6.9551 $\times 10^{10}$
Solar Luminosity	$L_\odot$	erg s^{-1}	3.8427 $\times 10^{33}$
Year (solar)	yr	s	3.1558 $\times 10^{7}$
Light year	ly	cm	9.461 $\times 10^{17}$
Parsec	pc	cm	3.086 $\times 10^{18}$
Astronomical Unit	AU	cm	1.496 $\times 10^{13}$

Table A.2: Astronomical constants (from [3]).

Dimension / Quantity	cgs	$c = G = 1$	$c = G = M_\odot$ = 1
Speed of light	2.99792458 $\times 10^{10}$ cm s^{-1}	1.0	1.0
Solar mass	1.9891 $\times 10^{33}$ g	1.4765 $\times 10^{5}$ cm	1.0
Time	1 s	3.33564095 $\times 10^{-11}$ cm	2.0295 $\times 10^{5}$
Length	1 cm	1 cm	6.7696 $\times 10^{-6}$
Mass	1 g	7.4261 $\times 10^{-29}$ cm	5.0274 $\times 10^{-34}$
Density	1 g cm^{-3}	7.4261 $\times 10^{-29}$ cm^{-2}	1.6207 $\times 10^{-18}$
Energy	1 erg = 1 g cm^2 s^{-2}	8.2627 $\times 10^{-50}$ cm	5.5936 $\times 10^{-55}$
Specific internal energy	1 erg g^{-1}	1.11265005605 $\times 10^{-21}$	1.11265005605 $\times 10^{-21}$
Pressure	1 dyn cm^{-2} = 1 erg cm^{-3}	6.67424 $\times 10^{-8}$	1.8030 $\times 10^{-39}$

Table A.3: Unit conversions between the cgs, geometric and $c = G = M_\odot$ units, based on fundamental constants listed in Table A.1.

the natural units are the cgs units. Moreover, codes written in GR usually adopt the geometric units $c = G = 1$, while other codes (such as the Newtonian code) work with $c = G = M_\odot = 1$ units. For this reason, one should pay attention to unit conversions in comparing quantities and outputs of different codes, or, for example, while implementing the routines which relate EoS variables to the hydrodynamical ones.
To that extent in Tables A.3, A.4 and A.5 some relevant unit conversions, based on the fundamental constants in Tables A.1 and A.2, are listed.

Dimension / Quantity	cgs	nuclear
Speed of light	2.99792458 $\times 10^{10}$ cm s^{-1}	$\hbar c = 197.3271502$ MeV fm
Length	1 cm	1 fm = 10^{-13} cm
Mass	1 g	1 MeV c^{-2} = 1.7826 $\times 10^{-27}$ g
Density	1 g cm^{-3}	1 fm^{-3} = 6.02214179 $\times 10^{-16}$ g cm^{-3}
Energy	1 erg	1 MeV = 1.602176487 $\times 10^{-6}$ erg
Pressure	1 erg cm^{-3}	1 MeV fm^{-3} = 1.602176487 $\times 10^{33}$ erg cm^{-3}
Atomic mass unit	1.660538783 $\times 10^{-24}$ g	931.494028 MeV/c^2
Electron mass	9.10938215 $\times 10^{-27}$ g	0.510998910 MeV/c^2
Neutron mass	1.674927211 $\times 10^{-24}$ g	939.56536 MeV/c^2
Proton mass	1.672621638 $\times 10^{-24}$ g	938.272013 MeV/c^2

Table A.4: Unit conversions between the cgs and nuclear units, based on fundamental constants listed in Table A.1.

Units	erg	eV	s^{-1}	cm	K
erg	1	1.60217722 $\times 10^{-12}$	1.66260755 $\times 10^{-27}$	1.9864475 $\times 10^{-16}$	1.380658 $\times 10^{-16}$
eV	6.2415064 $\times 10^{11}$	1	4.1356692 $\times 10^{-15}$	1.23984244 $\times 10^{-4}$	8.617385 $\times 10^{-5}$
s^{-1}	1.50918897 $\times 10^{26}$	2.41798836 $\times 10^{14}$	1	2.99792458 $\times 10^{10}$	2.083674 $\times 10^{10}$
cm^{-1}	5.0341125 $\times 10^{15}$	8.0655410 $\times 10^{3}$	3.335640952 $\times 10^{-11}$	1	6.950387 $\times 10^{-1}$
K	7.242924 $\times 10^{15}$	1.160445 $\times 10^{4}$	4.799216 $\times 10^{-11}$	1.438769	1

Table A.5: Energy conversion factors. Units of energy are related as: 1 J = 10^7 erg; 1 erg = $1/e$ eV = $1/h$ s^{-1} = $1/hc$ cm^{-1} = $1/k_B$ K (from [86]).

A.3 Notations

- Vectors.
  Vector quantities are written in **bold** (e.g. $\mathbf{r}$ for the radial vector position). Vectors in curvilinear coordinates can be described by *contravariant* or *covariant* components. Contravariant components are denoted with superscripts; covariant components with subscripts.

- Scalars.
  Scalar quantities are written in the current *math* font (e.g. r stands for the modulus of vector $\mathbf{r}$).

- Operators.
  Operators are designated by the *hat* (e.g. $\hat{\sigma}$ stands for the spin operator).

- Einstein summation convention.
  We use also the Einstein summation convention, by which repeated indices imply a sum over the appropriate range (i.e., usually, Roman indices go from 1 to 3, while

Greek indices go from 0 to 3.); e.g.:

$$a^i b_i \equiv a^1 b_1 + a^2 b_2 + a^3 b_3 \ . \tag{A.1}$$

- Derivatives.
The notation $\mathrm{D}/\mathrm{D}t$ indicates the Lagrangian time derivative, while $\partial/\partial t$ stands for the partial time derivative. In the literature one can also find the notations:

$$\begin{aligned} ,t &= \partial_t = \frac{\partial}{\partial t} \\ ,i &= \partial_i = \frac{\partial}{\partial x^i} \end{aligned}$$

and for the covariant derivative: $_{;i} \equiv \nabla_i$ (see e.g. [141]).
Since we work in spherical symmetry and RGPS coordinate, often the Greek indices indicate the coordinates (t, r, θ, ϕ), and Latin indices indicate (r, θ, ϕ). Using the superscript "t" instead of the superscript index 0 for the time coordinate helps not to be misunderstood when, in most cases, the superscript "0" refers to the quantities calculated in the comoving frame.

Appendix B

Skyrme effective interaction

The Skyrme force is a phenomenological interaction which describes the NN force in dense medium. It contains a certain number of parameters which have to be fitted to reproduce experimental data around saturation density.
The standard form of the Skyrme interaction [302] is given by Eq. (2.9).

The total energy of the system is then given by the mean value of the total Hamiltonian [282, 77, 24]:

$$H = \int \mathcal{H}(\mathbf{r}) \mathrm{d}\mathbf{r} \ , \tag{B.1}$$

where:

$$\mathcal{H} = \mathcal{K} + \mathcal{H}_0 + \mathcal{H}_3 + \mathcal{H}_{eff} + \mathcal{H}_{fin} + \mathcal{H}_{so} + \mathcal{H}_{sg} + \mathcal{H}_{Coul} \ , \tag{B.2}$$

where the kinetic term reads:

$$\mathcal{K} = \frac{\hbar^2}{2m} \tau \ , \tag{B.3}$$

$\mathcal{H}_0$ is the zero-range term, $\mathcal{H}_3$ is the density-dependent term, $\mathcal{H}_{eff}$ accounts for an effective mass term, $\mathcal{H}_{fin}$ is a finite range term, $\mathcal{H}_{so}$ is the spin-orbit term, $\mathcal{H}_{sg}$ represents the spin-gradient coupling and $\mathcal{H}_{Coul}$ is the Coulomb term. All the terms are given for example in Refs. [76, 77, 239], but for sake of completeness I recall them here. From now on, I will neglect the tensor spin-gradient coupling term $\mathcal{H}_{sg}$. Note also that, in writing the expressions for the functional, the effective mass and the mean field terms, I omit the

r-dependence in the densities for simplicity, i.e. $\rho = \rho(\mathbf{r})$, $\tau = \tau(\mathbf{r})$, $\mathbf{J} = \mathbf{J}(\mathbf{r})$.

$$
\begin{aligned}
\mathcal{H}_0 &= \frac{1}{4}t_0\left[(2+x_0)\rho^2 - (2x_0+1)(\rho_n^2+\rho_p^2)\right] \\
\mathcal{H}_3 &= \frac{1}{24}t_3\rho^\alpha\left[(2+x_3)\rho^2 - (2x_3+1)(\rho_n^2+\rho_p^2)\right] \\
\mathcal{H}_{eff} &= \frac{1}{8}\left[t_1(2+x_1)+t_2(2+x_2)\right]\tau\rho \\
&\quad +\frac{1}{8}\left[t_2(2x_2+1)-t_1(2x_1+1)\right](\tau_n\rho_n+\tau_p\rho_p) \\
\mathcal{H}_{fin} &= \frac{1}{32}\left[3t_1(2+x_1)-t_2(2+x_2)\right](\nabla\rho)^2 \\
&\quad -\frac{1}{32}\left[3t_1(2x_2+1)+t_2(2x_2+1)\right]\left[(\nabla\rho_n)^2+(\nabla\rho_p)^2\right] \\
\mathcal{H}_{so} &= \frac{1}{2}W_0\left[\mathbf{J}\cdot\nabla\rho+\mathbf{J}_n\cdot\nabla\rho_n+\mathbf{J}_p\cdot\nabla\rho_p\right] \\
\mathcal{H}_{sg} &= -\frac{1}{16}(t_1x_1+t_2x_2)\mathbf{J}^2+\frac{1}{16}(t_1-t_2)\left[\mathbf{J}_n^2+\mathbf{J}_p^2\right] \ , \qquad \text{(B.4)}
\end{aligned}
$$

with the total baryon, kinetic and spin densities given by Eq. (2.14)-(2.16). Note that in this case ρ is the density in nuclear units (cf. Appendix A).

Of course the notations for the standard Skyrme functional in Chabanat *et al.* [77], which are exactly the same as in Meyer [239], are equivalent to the ones in Bender *et al.* [24], which are used in Chapter 2, 3 and in Ref. [112], if one defines the coupling

constants $C_0^{\cdot}$ in Bender *et al.* [24] as (cf. Appendix A in Ref. [24]):

$$
\begin{aligned}
C_0^{\rho} &= \frac{3}{8}t_0 + \frac{3}{48}t_3\rho_0^{\alpha} \\
C_1^{\rho} &= -\frac{1}{8}t_0(1+2x_0) + \frac{1}{48}t_3(1+2x_3)\rho_0^{\alpha} \\
C_0^{\tau} &= \frac{3}{16}t_1 + \frac{1}{16}t_2(5+4x_2) \\
C_1^{\tau} &= -\frac{1}{16}t_1(1+2x_1) + \frac{1}{16}t_2(1+2x_2) \\
C_0^{J} &= \frac{1}{16}t_1(1-2x_1) - \frac{1}{16}t_2(1+2x_2) \\
C_1^{J} &= \frac{1}{16}t_1 - \frac{1}{16}t_2 \\
C_0^{\nabla^2\rho} &= -\frac{9}{64}t_1 + \frac{1}{64}t_2(5+4x_2) \\
C_1^{\nabla^2\rho} &= \frac{3}{64}t_1(1+2x_1) + \frac{1}{64}t_2(1+2x_2) \\
C_0^{\nabla J} &= -\frac{3}{4}W_0 \\
C_1^{\nabla J} &= -\frac{1}{4}W_0 \\
C_0^{s} &= -\frac{1}{8}t_0(1-2x_0) - \frac{3}{48}t_3(1-2x_3)\rho_0^{\alpha} \\
C_1^{s} &= -\frac{1}{8}t_0 - \frac{1}{48}t_3\rho_0^{\alpha} \\
C_0^{\nabla^2 s} &= \frac{3}{64}t_1(1-2x_1) + \frac{1}{64}t_2(1+2x_2) \\
C_1^{\nabla^2 s} &= \frac{3}{64}t_1 + \frac{1}{64}t_2 \\
C_0^{\nabla s} &= 0 \\
C_1^{\nabla s} &= 0 \\
C_0^{j} &= -C_0^{\tau} \\
C_1^{j} &= -C_1^{\tau} \\
C_0^{sT} &= -C_0^{J} \\
C_1^{sT} &= -C_1^{J} \\
C_0^{\nabla j} &= C_0^{\nabla J} \\
C_1^{\nabla j} &= C_1^{\nabla J} \,,
\end{aligned}
$$

and, if one takes into account only the time-even component, the terms C_T^{sT}, C_T^{s}, $C_0^{\nabla^2 s}$, $C_T^{\nabla s}$, C_T^{j} and $C_T^{\nabla j}$ are neglected in the model.

Finally, for completeness, we report here the expressions for the effective mass and the mean field derived from Skyrme interaction (cf. Eqs. (3.20), (3.21)), as also implemented in our code solving the Schrödinger equation in the HF approximation (the $\mathbf{r}$ dependence

in writing the expressions is omitted for simplicity) [302, 282, 76, 77, 24]:

$$\begin{aligned}
\frac{\hbar^2}{2m_q^*(\mathbf{r})} \equiv \frac{\delta H^{Sky}}{\delta \tau_q} &= \frac{\hbar^2}{2m} + \frac{1}{8}[t_1(2+x_1) + t_2(2+x_2)]\,\rho \\
&\quad -\frac{1}{8}[t_1(1+2x_1) - t_2(1+2x_2)]\,\rho_q \qquad \text{(B.5)} \\
U_q^{Sky}(\mathbf{r}) \equiv \frac{\delta H^{Sky}}{\delta \rho_q} &= \frac{1}{2}t_0\,[(2+x_0)\rho - (1+2x_0)\rho_q] \\
&\quad +\frac{1}{24}t_3\left\{(2+x_3)(2+\alpha)\rho^{\alpha+1}\right. \\
&\quad \left.-(2x_3+1)[2\rho^\alpha\rho_q + \alpha\rho^{\alpha-1}(\rho_n^2+\rho_p^2)]\right\} \\
&\quad +\frac{1}{8}\,[t_1(2+x_1) + t_2(2+x_2)]\,\tau \\
&\quad +\frac{1}{8}\,[t_2(1+2x_2) - t_1(1+2x_1)]\,\tau_q \\
&\quad +\frac{1}{16}\,[t_2(2+x_2) - 3t_1(2+x_1)]\,\nabla^2\rho \\
&\quad +\frac{1}{16}\,[3t_1(1+2x_1) + t_2(1+2x_2)]\,\nabla^2\rho_q \\
&\quad -\frac{1}{2}W_0\,[\nabla\cdot\mathbf{J} + \nabla\cdot\mathbf{J}_q]\ , \qquad \text{(B.6)}
\end{aligned}$$

and, in Eq. (2.31):

$$\mathbf{W}_q(\mathbf{r}) = \frac{1}{2}W_0\,(\nabla\rho + \nabla\rho_q) + \frac{1}{8}(t_1 - t_2)\mathbf{J}_q - \frac{1}{8}(t_1x_1 - t_2x_2)\mathbf{J}\ . \qquad \text{(B.7)}$$

Using the notation in Bender *et al.* [24], for the time even component:

$$\frac{\hbar^2}{2m_T^*(\mathbf{r})} = \frac{\hbar^2}{2m} + C_T^\tau\rho_T\ , \qquad \text{(B.8)}$$

$$\begin{aligned}
U_T^{Sky}(\mathbf{r}) &= 2C_T^\rho\rho_T + C_T^\tau\tau_T + 2C_T^{\nabla^2\rho}\nabla^2\rho_T + C_T^{\nabla J}\nabla\cdot\mathbf{J} \\
&\quad +\sum_T \frac{\partial C_T^\rho}{\partial\rho_0}\rho_T^2\ , \qquad \text{(B.9)}
\end{aligned}$$

where $T = 0$ ($T = 1$) stands for the isoscalar (isovector) component, related to the neutron and proton components as:

$$\begin{aligned}
C_n &= \frac{C_0 + C_1}{2} \\
C_p &= \frac{C_0 - C_1}{2}\ . \qquad \text{(B.10)}
\end{aligned}$$

The additional terms (3.19) we have introduced are given in Chapter 3. The correction to the effective mass (B.5) is given in Eq. (3.20) and that to the mean field (B.6) in Eq. (3.22). The parameter $C_0^{\rho^2(\nabla\rho)^2}$ is fixed to be $C_0^{\rho^2(\nabla\rho)^2} = 12\ C_0^{\tau(\nabla\rho)^2}$ fm. Therefore, the additional terms are controlled by a single new parameter $C_0^{\tau(\nabla\rho)^2}$.

B.1 Parameters of the Skyrme forces used in the text

In Table B.1, the parameters of the Skyrme forces used or quoted in the thesis are listed, together with the properties of the infinite nuclear matter for these effective forces. A more extensive list is given e.g. in Refs. [76, 77, 239].

Force	SIII [23]	SkM* [21]	SkX [51]	SLy4 [76, 77]	LNS [71]	BSk14 [140]
t_0 [MeV fm^3]	-1128.75	-2645.00	-1438.00	-2488.91	-2484.97	-1822.67
t_1 [MeV fm^5]	395.00	410.00	244.00	486.82	266.735	377.47
t_2 [MeV fm^5]	-95.00	-135.00	-133.00	-546.39	-337.135	-2.41056
t_3 [MeV fm$^{3+3\alpha}$]	14000.00	15595.00	12116.30	13177.00	14558.2	11406.3
x_0	0.45	0.09	0.288	0.834	0.06277	0.302096
x_1	0.00	0.00	0.611	-0.3444	0.65845	-0.823575
x_2	0.00	0.00	0.145	-0.10	-9.5382	61.9411
x_3	1.00	0.00	-0.056	1.354	-0.3413	0.47346
α	1.00	1/6	1/2	1/6	1/6	0.3
W_0 [MeV fm^5]	120.00	130.00	145.70	123.00	96.00	135.565
ρ_0 [fm^{-3}]	0.145	0.160	0.156	0.159	0.1746	0.1586
a_v [MeV]	-15.851	-15.786	-16.07	-15.987	-15.33	-15.853
K_∞ [Mev]	355.40	216.80	271.3	230.01	210.99	239.30
$(m^*/m)_s$	0.76	0.79	0.99	0.67	0.826	0.80
a_{sym} [MeV]	28.16	30.03	31.09	32.00	33.43	30.0
L [MeV]	9.84	44.51	33.04	46.06	61.43	43.89
K_{sym} [MeV]	-392.24	-147.62	-250.64	-120.30	-127.35	-152.02

Table B.1: Parameters and properties of the infinite nuclear matter (saturation density, binding energy at saturation, incompressibility, isoscalar effective mass, symmetry coefficient $a_{sym} = s$, L and K_{sym}) for the Skyrme forces used in this thesis.

Appendix C

Temperature dependence of the level density parameter

The nuclear level density and the level density parameter have been the object of many investigations, since the pioneering work by Bethe in 1936 [32], where the level density $\rho(E^*)$ was estimated in an IPM picture (see Eq. (2.50)). Since then, more refined models have been employed, including different phenomenological corrections, in order to reproduce the data.

In this Appendix an analysis where we relate the calculation of the temperature dependent nucleon effective mass used in the astrophysical model and the level density parameter which can be extracted from nuclear physics experiments is carried out. As explained in Section 2.3, it is not easy to relate these two quantities, and neither it is straightforward to identify the level density parameter extracted from experiments (either a_{ST}, or a_{SE}, or a_{ET}) to the one which is calculated (see Eqs. (2.55)). Our aim is to propose a model which allows to reproduce both the data for intermediate mass and heavy nuclei. In fact, even if there already exists in the literature a phenomenological parameterization of the effective mass which contains the temperature dependence and seems to reproduce quite well the data (see Shlomo and Natowitz [300, 301]), we want to present a model which comes from more microscopic calculations and compare it with the works in Refs. [300, 301].

C.1 Parameterization of $m_\omega(T)$

Since there are not many investigations on the temperature dependent nucleon effective mass in finite nuclei based on a microscopic framework, we rely our analysis on the work by Donati *et al.* [106], who performed calculations in ^{98}Mo, ^{64}Zn and ^{64}Ni, and by Bortignon and Dasso [47] who studied the T-dependence of the m_ω in ^{208}Pb. To get a parameterization of the m_ω which unifies the two sets of results, we first observe that the T-dependence of m^* seems to be better reproduced by an exponential profile for intermediate mass nuclei [106] and by a Gaussian profile for heavy nuclei [47]. As a consequence, we decide, for the following analysis, to parameterize the quantity $\Delta m_\omega(T)/\Delta m_\omega(0)$, where $\Delta m_\omega := m_\omega(T)/m - 1$, by the general expression:

$$\frac{\Delta m_\omega(T)}{\Delta m_\omega(0)} = f(A,T) = [1 + \delta(A)T]\ e^{-T/T_0(A)}\ , \tag{C.1}$$

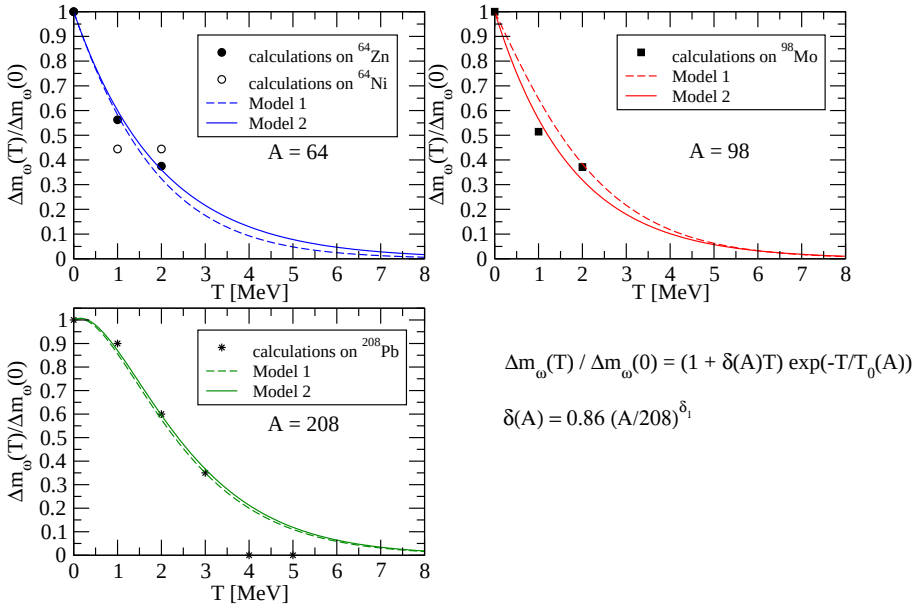

Figure C.1: Ratio $\Delta m_\omega(T)/\Delta m_\omega(0)$ as a function of temperature. The points represent the calculations from Donati *et al.* [106] (for $A = 64$ and $A = 98$) and from Bortignon and Dasso [47] (for $A = 208$), while the solid lines correspond to the fits obtained according to Eq. (C.1).

where the A-dependence in $\delta(A)$ and $T_0(A)$ have to be determined by a fit. In choosing the coefficient $\delta(A)$, we have required that: *(i)* $\delta(A)T \ll 1$ for intermediate mass nuclei in order to recover the A-independent expression obtained by Donati *et al.* [106]; *(ii)* $\delta(A = 208)T$ shall not be negligible and is adjusted to reproduce the results in Bortignon and Dasso [47] for $A = 208$. We have obtained for $\delta(A)$ the following best fit (i.e. the one which minimizes the chi-squared):

$$\delta(A) = 0.86 \left(\frac{A}{208}\right)^{\delta_1} , \tag{C.2}$$

where δ_1 is a constant. We fix then $T_0(A) \propto A^{-1/3}$, in analogy with the works by Shlomo and Natowitz [300, 301], who have calculated the temperature dependence of the level density parameter in the Thomas-Fermi approach taking into account, among other effects, the T-dependence of the effective mass. In Ref. [301] a parameterization of the ω-mass as a gradient of the nuclear profile has been adopted (cf. Eq. (8) in Ref. [301]):

$$\frac{m_\omega(r)}{m} = 1 - \beta \frac{\mathrm{d}n(r)}{\mathrm{d}r} , \tag{C.3}$$

where $n(r)$ is the nuclear matter density profile normalized to the nuclear saturation density, and $\beta = 0.4\ A^{1/3} e^{-(T/\gamma)^2}$, with: $\gamma = 21 A^{-1/3}$.

In Fig. C.1 we display the ratio $\Delta m_\omega(T)/\Delta m_\omega(0)$ as a function of temperature for the three different mass numbers $A = 64, 98, 208$. The points represent the calculations from Donati *et al.* [106] (for $A = 64$ and $A = 98$) and from Bortignon and Dasso [47] (for $A = 208$). Notice that for the case $A = 64$, we have shown the calculated points for ^{64}Zn (filled circles) and ^{64}Ni (empty circles). As expected, for $A = 64$ and $A = 98$, the fast

drop of the points with respect to the temperature indicates that an exponential function is well suited to reproduce the points while for $A = 208$ the reduction of the quantity $\Delta m_\omega(T)/\Delta m_\omega(0)$ is smoother with respect to the temperature, indicating an important effect of the term $\delta(A)$ in Eq. (C.1). We have however found two sets of parameters which equally well reproduce the points in Fig. C.1, and which are:

- Model 1:

$$\begin{aligned} \delta_1 &= 1 \\ T_0 &= 1.29\ \mathrm{MeV}\ , \end{aligned} \tag{C.4}$$

- Model 2

$$\begin{aligned} \delta_1 &= 5 \\ T_0(A) &= 7.8\ A^{-1/3}\ \mathrm{MeV}\ . \end{aligned} \tag{C.5}$$

The main difference between the sets of parameters (C.4) and (C.5) is that the typical temperature T_0 is independent of A in Model 1 (Eq. (C.4)) and dependent on A according to the work by Shlomo and Natowitz [300, 301] in Model 2 (Eq. (C.5)). The fitting procedure to get the models 1 and 2 is illustrated in Fig. C.2, where the dependence on A of δ and T_0 is shown. The points correspond to the different fits obtained to reproduce the calculations by Donati *et al.*[106] and Bortignon and Dasso [47]. A first fit of $\Delta m_\omega(T)/\Delta m_\omega(0)$ assuming a T-dependence of the form $(1 + x_1 T)e^{-T/x_2}$ has been done for each A (A = 64, 98, 208). The corresponding x_1 is shown by the star dots in Fig. C.2a) as a function of A. Noticing that the A-dependence of $\delta(A)$ is important for heavy nuclei, we have decided to adopt the parameterization Eq. (C.2), where a new free parameter, δ_1, appears. The function (C.2) for different values of δ_1 is plotted with lines in the panel a). Fixing x_1 according to the expression in Eq. (C.2), we have then fixed the parameter x_2, for different A and δ_1. The star dots (with the error bars coming from the fit procedure) in panels b), c), d), e), f) correspond to the values of x_2 obtained with a fit, which we compare with the A-dependent expression $T_0(A) = 7.8A^{-1/3}$. Notice that in panel b) the fitted values lie on an almost straight line at $T = 1.29$ MeV. We observe that the best fit aimed at parameterizing the calculations by Donati *et al.*[106] and Bortignon and Dasso [47] is well reproduced by Model 1 (panel b)) and Model 2 (panel f)).

Then, to have a complete parameterization of $m_\omega(T)$, only the absolute value $m_\omega(T = 0)$ has to be determined. We suppose $m_\omega(0)$ either constant or A-dependent:

$$m_\omega(0) = 1.66 \quad \text{(A)} \tag{C.6a}$$

$$m_\omega(0) = 1 + 0.15\ A^{1/3} \quad \text{(B)}\ , \tag{C.6b}$$

where 1.66 is just the mean value of the different values of $m_\omega(0)$ obtained in Ref. [106], the $A^{1/3}$ dependence is chosen again in analogy with the parameterization in Ref. [301] (cf. Eqs. (8) and (14) in Ref. [301]), and the coefficient 0.15 which appears in Eq. (C.6b) results from the best fit to reproduce the calculations in [106].

Summarizing, a generalization of the parameterization of the temperature dependent effective mass derived by Donati *et al.*[106] is proposed. This new parameterization reproduces equally well the calculations in Ref. [106] for intermediate mass nuclei and those

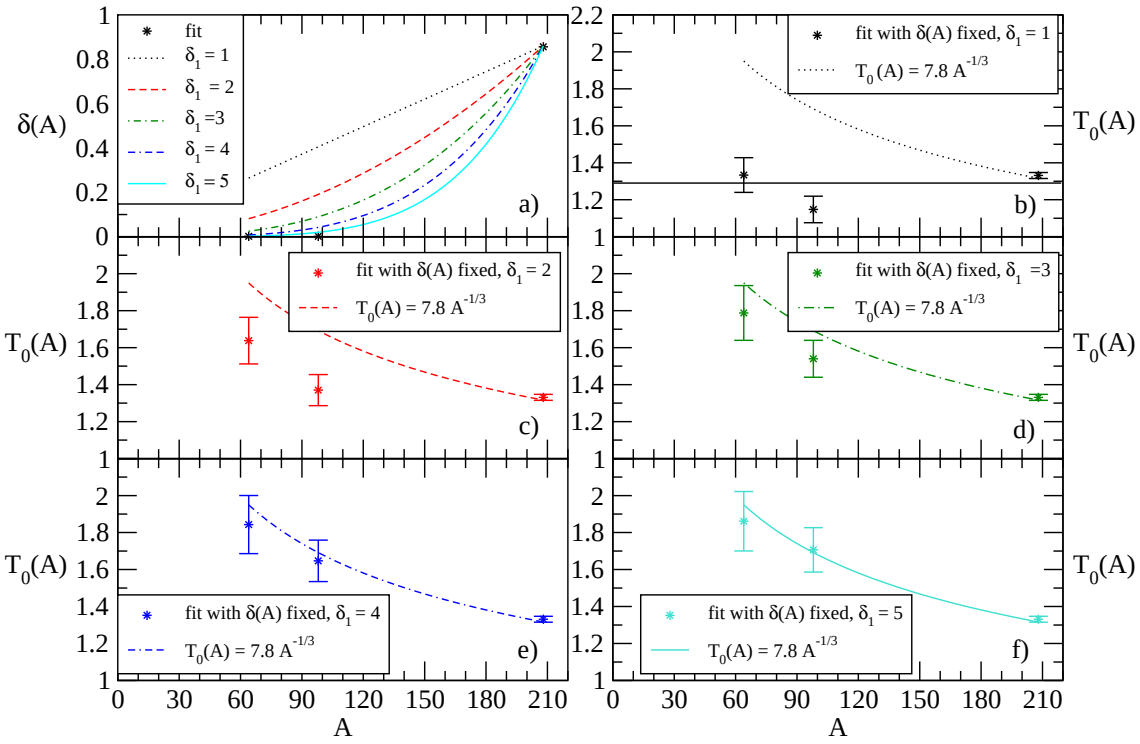

Figure C.2: Fit of $\delta(A)$ and $T_0(A)$ to reproduce the calculations by Donati *et al.* [106] and by Bortignon and Dasso [47]. See text for details. The straight line in panel b) is located at $T = 1.29$ MeV.

of Bortignon and Dasso [47] for heavy nuclei. In a general form, this parameterization reads:

$$m_\omega(T) = 1 \; + \; \xi(A) \; f(A,T) \; , \tag{C.7}$$

with:

$$\xi(A) := m_\omega(0) - 1 = \begin{cases} 0.66 & \text{(A)} \\ 0.15 \; A^{1/3} & \text{(B)} \; , \end{cases} \tag{C.8}$$

The expressions for $f(A,T)$ and $\delta(A)$ are given in Eqs. (C.1) and (C.2), and the two sets of parameters are given in expressions (C.4) and (C.5).

C.2 Comparison to experimental level density

In the following we proceed, as proposed by Lestone [195], to relate the parameterization of the effective mass to the level density parameter a. In Ref. [195], Lestone has compared the parameter a/A obtained in the local density approximation with the one derived in the Thomas-Fermi approach by Shlomo and Natowitz, which is claimed to be in reasonable agreement with experimental data and which is directly linked to a T-dependent m^* [300, 301]. He studied the case of $A = 60$ (closer to the kind of nuclei studied by Donati *et al.*) and $A = 210$ (closer to the case of ^{208}Pb).

It shall be noticed that in the work of Shlomo and Natowitz [300, 301] the effective mass depends on the nuclear density profile $n(r)$. Therefore, they have introduced a density averaged effective mass which is proportional to the effective mass calculated by Donati *et al.*[106] and Bortignon and Dasso [47]. To be compared with the work by Shlomo and Natowitz [300, 301], there is a factor $\langle \left| \frac{\mathrm{d}n(r)}{\mathrm{d}r} \right| \rangle \approx 0.2$ between the temperature dependent coefficients $\beta(T)$ in Ref. [301] and $\xi(A) \cdot f(A,T)$. Notice also that in our case the k-mass is constant. We have:

$$\beta(T) = \frac{m_\omega(0) - 1}{0.2}(1 + \delta(T))e^{-T/T_0} \; . \tag{C.9}$$

Lestone [195] has pointed out that one should be careful in the definition of a (a_{ST}, a_{SE}, a_{ET} in Eqs. (2.55)). In fact, if one writes the definition of the nuclear temperature Eq. (2.53), considering the dependence of the density of states on the excitation energy as [44, 195] (Eq. (1) in Ref. [195]):

$$\rho(E^*) \propto \frac{e^{2\sqrt{aE^*}}}{(E^*)^2} \tag{C.10}$$

one gets [195]:

$$T^{-1} = \frac{1}{\rho(E^*)}\frac{\mathrm{d}\rho}{\mathrm{d}E^*} = \sqrt{\frac{a}{E^*}} + \sqrt{\frac{E^*}{a}}\frac{\mathrm{d}a}{\mathrm{d}E^*} - \frac{2}{E^*} \simeq \sqrt{\frac{a}{E^*}} + \sqrt{\frac{E^*}{a}}\frac{\mathrm{d}a}{\mathrm{d}E^*} \; , \tag{C.11}$$

where, since $E^* \propto T^2$, the term $2/E^*$ can be neglected. Thus, if a is independent of E^*, then $\mathrm{d}a/\mathrm{d}E^* = 0$ in Eq. (C.11), and the relation $a(T) = E^*/T^2$ is verified. On the other hand, if a is E^*-dependent, one can define an "effective" level density parameter a_{ET} which reads [195]:

$$a_{ET} = a + 2E^*\frac{\mathrm{d}a}{\mathrm{d}E^*} + \frac{(E^*)^2}{a}\left(\frac{\mathrm{d}a}{\mathrm{d}E^*}\right)^2 \approx a + 2E^*\frac{\mathrm{d}a}{\mathrm{d}E^*} \; , \tag{C.12}$$

at second order in T. The derivative of a with respect to the excitation energy is given by:

$$\frac{\mathrm{d}a}{\mathrm{d}E^*} = \frac{\partial a}{\partial T}\frac{\partial T}{\partial E^*} = \frac{1}{2aT}\frac{\partial a}{\partial T} \; . \tag{C.13}$$

At this point one can still relate the effective a_{ET} to the temperature and the excitation energy:

$$\frac{a_{ET}(T)}{A} = \frac{E^*}{T^2}\frac{1}{A} \; , \tag{C.14}$$

and the inverse of the level density parameter, K_{ET}, reads:

$$\frac{1}{K_{ET}(T)} = \frac{1}{K} + 2\frac{E^*}{A}\frac{\mathrm{d}a}{\mathrm{d}E^*} \; , \tag{C.15}$$

with: $K = \frac{A}{a}$ and $K_{ET} = \frac{A}{a_{ET}}$. This quantity can be directly compared with the results in Shlomo and Natowitz's paper. In the case of Shlomo and Natowitz, a is calculated from

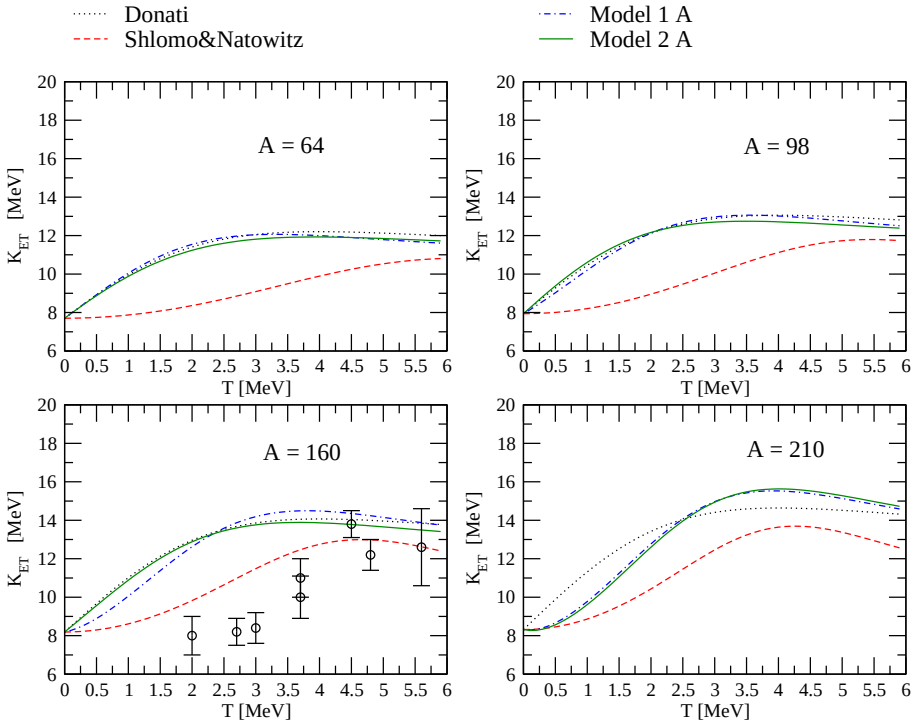

Figure C.3: Inverse of the level density parameter, K_{ET}, as a function of temperature, extracted from different parameterizations of $m_\omega(T)$, for the case A = 64, 98, 160, 210. The dot black lines correspond to the original parameterization by Donati *et al.* [106], the dashed red lines are the results of Shlomo and Natowitz [301], the dotted-dashed blue and solid green lines correspond to Model 1 A and Model 2 A.

a T-dependent m^* and so it contains an implicit dependence on E^*; this can be also seen from Fig. (1) in Ref. [300], where the plot of $(a/A)^{-1}$ versus T^2 is not a straight line.
In Figs. C.3 and C.4 the parameter K_{ET} as a function of temperature, extracted from different parameterizations of $m_\omega(T)$ for the mass numbers A = 64, 98, 160, 210 is displayed (the values of A = 160, 210 are chosen for comparison with Ref. [195]). We compare the original parameterization of Donati *et al.*[106], where $m_\omega(0) = 1.7$, $T_0 =$ 2 MeV (labelled as "Donati"), the parameterization of Shlomo and Natowitz [301] where $\beta = 0.4A^{1/3}$, $T_0 = 21A^{-1/3}$ (labelled as "Shlomo&Natowitz"), with the two sets of parameters we propose (labelled as "Model 1 X" and "Model 2 X", where X=A and X=B stand, respectively, for the parameterization (C.6a) and (C.6b)). The points in the lower left panels in Figs. C.3 and C.4 correspond to experimental data from [84, 145, 136] (cf. Fig. 2 in Ref. [300]). The trend followed by the points seems to favour a Gaussian-like shape for m^* for large A. As expected, for A = 64 and 98, the results from the original paper by Donati *et al.*and the more general parameterization are in very good agreement. Discrepancies are present for heavier mass numbers (A = 160, 208). In all cases, there is however a noticeable difference with the results obtained by Shlomo and Natowitz. This might be due to the different parameterization of the m^* where a Gaussian is taken in Shlomo and Natowitz instead of an exponential function in our case.

We represent in Figs. C.5 and C.6 the diagram T versus E^*. Despite the discrepancies

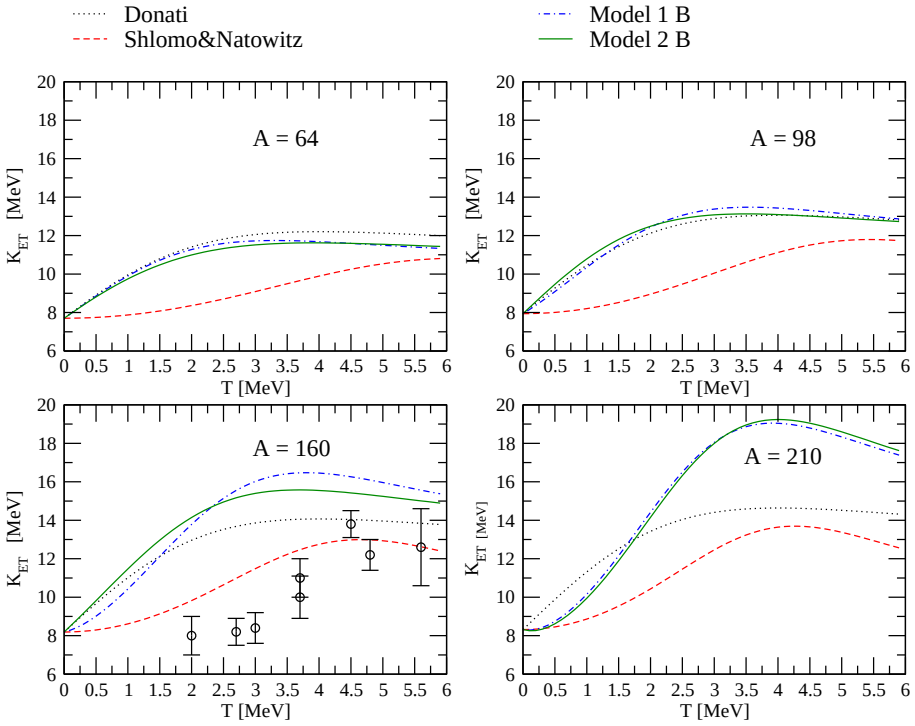

Figure C.4: Same as Fig. C.3, but with Model 1 B and Model 2 B.

previously remarked and shown in Figs. C.3 and C.4, we surprisingly do not find for the plot T versus E^* a big difference between the different parameterizations.

C.3 Conclusions

In this Appendix we have aimed at relating the calculations of the temperature dependent nucleon effective mass and the level density parameter which can be extracted from nuclear physics experiments. We have proposed a generalization of the parameterization of the temperature dependent effective mass by Donati *et al.*[106], which reproduces equally well the calculations in Ref. [106] for intermediate mass nuclei and those of Bortignon and Dasso [47] for heavy nuclei. The differences between the models we have explored is small compared to the experimental resolution. However, the data seem to favour a Gaussian-like profile, as in the work by Shlomo and Natowitz [300], (see Figs. C.3 and C.4).

It would be interesting to have experimental data for intermediate-mass nuclei in order to check the temperature dependence of the level density parameter and of the nucleon effective mass.

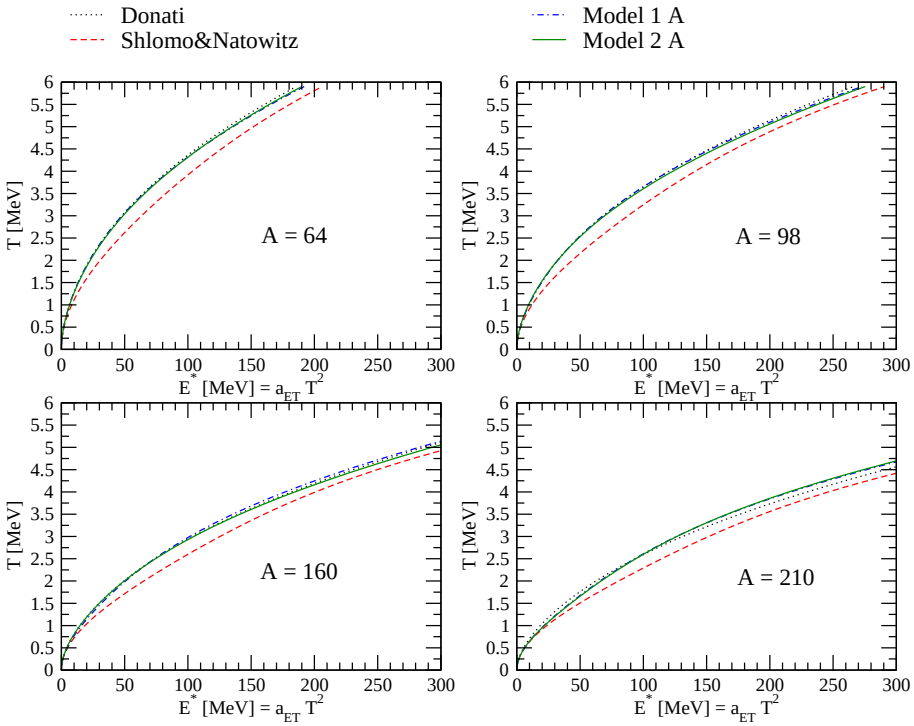

Figure C.5: Temperature versus excitation energy profile. The legend is the same as in Fig. C.3.

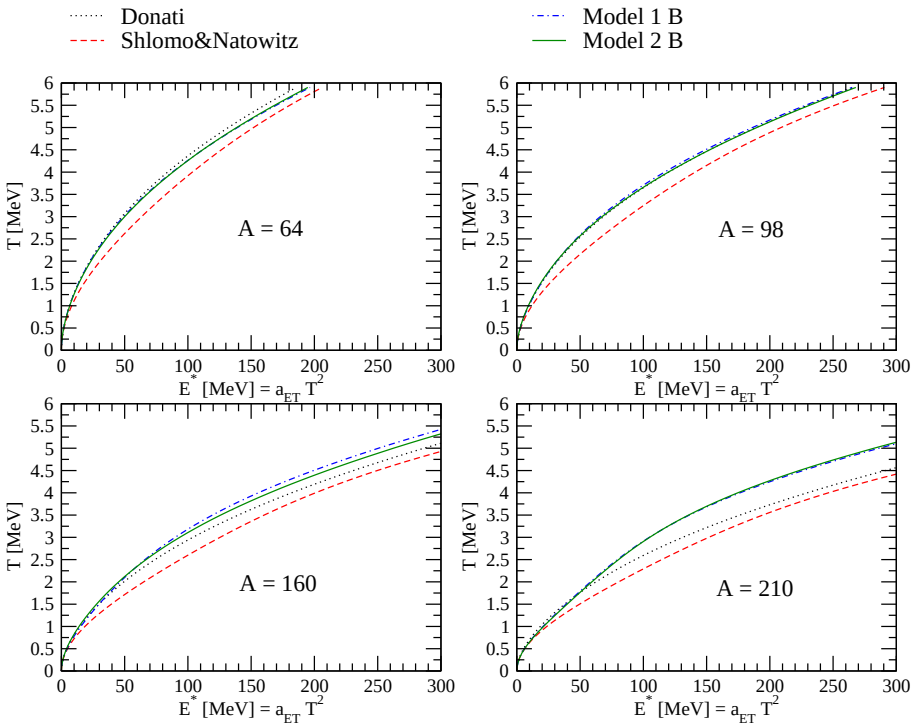

Figure C.6: Same as Fig. C.5. The legend is the same as in Fig. C.4.

Appendix D

Self-energy in the RPA approximation

The work discussed in this Appendix is not yet completed. Therefore we present essentially the framework and some preliminary results. The aim of this work is to extend the calculations on the temperature dependent nucleon effective mass made by Donati *et al.* [106] in order to obtain both a radial and an energy dependence of the effective mass. In fact, any information on the radial profile of the effective mass was absent in Ref. [106]; the self-energy was only energy dependent and only an average value weighted over the wave functions for each single particle state of the so-called ω-mass was calculated.

The Green function method is a very general approach in the many-body theory to describe mean field and beyond. The mean field potential in which a particle moves can be identified with the mass operator or proper self-energy[1], Σ. In the Green's function approach, the motion of a single nucleon is represented by the single particle propagator $\mathcal{G}(\mathbf{r}_1, t_1, \mathbf{r}_2, t_2)$ which obeys the Dyson equation (see e.g. [115, 214] for details). If the Hamiltonian is time independent, $\mathcal{G}$ depends only on the difference $t = t_1 - t_2$, i.e.: $\mathcal{G}(\mathbf{r}_1, t_1, \mathbf{r}_2, t_2) \equiv \mathcal{G}(\mathbf{r}_1, \mathbf{r}_2, t)$. Operating the Fourier transform over the time coordinate ($t \rightarrow \omega$), one gets the Lehmann (or spectral) representation of the Green's function:

$$\mathcal{G}(\mathbf{r}_1, \mathbf{r}_2, \omega) = \sum_p \frac{\varphi_p^*(\mathbf{r}_1)\varphi_p(\mathbf{r}_2)}{\omega - \epsilon_p + i\eta} + \sum_h \frac{\varphi_h(\mathbf{r}_1)\varphi_h^*(\mathbf{r}_2)}{\omega - \epsilon_h - i\eta} \ , \tag{D.1}$$

where the sums run over the particle (p) and hole (h) states. The terms in the denominator $\pm i\eta$ come from the integration on the complex ω-plane; indeed the particle (hole) Green's function has poles ϵ_p (ϵ_h) above (below) the chemical potential (i.e. the Fermi energy at zero temperature), which is located on the real axis.
In Eq. (D.1), φ_p (φ_h) are the wave functions of unoccupied (occupied) states:

$$\varphi_p(\mathbf{r}) = \langle \Phi_p^{A+1} | \hat{a}^\dagger(\mathbf{r}) | \Phi_0^A \rangle \tag{D.2}$$

$$\varphi_h(\mathbf{r}) = \langle \Phi_h^{A-1} | \hat{a}(\mathbf{r}) | \Phi_0^A \rangle \ , \tag{D.3}$$

being $\hat{a}^\dagger$ ($\hat{a}$) the creator (annihilator) operator, $|\Phi_0^A\rangle$ the ground state eigenstate of the Hamiltonian of the A-particle system, $|\Phi_p^{A+1}\rangle$ ($|\Phi_h^{A-1}\rangle$) the eigenstate of the Hamiltonian

[1] We have actually referred to the self-energy (or mean field) labelling it as U; however, in the literature usually U does not contain the energy dependence; this justifies the change in the notation.

of the $A+1$ ($A-1$)-particle system with energy E_p^{A+1} (E_h^{A-1}), and:

$$\begin{aligned} \epsilon_p &= E_p^{A+1} - E_0^A \\ \epsilon_h &= E_0^A - E_h^{A-1} \end{aligned} \tag{D.4}$$

are the single particle energies. Taking into account the Lehman representation of the Green function, the Dyson equation,

$$\left(\omega + \frac{\hbar\nabla^2}{2m}\right)\mathcal{G}(\mathbf{r}_1,\mathbf{r}_2,\omega) - \int \mathcal{M}(\mathbf{r}_1,\mathbf{r}',\omega)\mathcal{G}(\mathbf{r}',\mathbf{r}_2,\omega)\mathrm{d}\mathbf{r}' = \delta(\mathbf{r}_1-\mathbf{r}_2)\ , \tag{D.5}$$

where $\mathcal{M}$ is called proper self-energy or mass-operator, can be written in terms of the sp wave functions $\Phi(\mathbf{r})$ (see [115] for details):

$$-\frac{\hbar\nabla^2\Phi(\mathbf{r}_1)}{2m} + \int \mathcal{M}(\mathbf{r}_1,\mathbf{r}',\omega)\Phi(\mathbf{r}') = \epsilon\ \Phi(\mathbf{r})\ . \tag{D.6}$$

This is the general form of a single particle wave equation in which the quantity $\mathcal{M}$ plays the role of the potential in which the particle moves. Although it looks very similar to the one particle equation of mean field approach like Hartree-Fock, it does not constitute a mean field formulation, since the self-energy takes all dynamic many-body processes into account. Consequently, the functions Φ and energies ϵ must not be understood as single-particle quantities. The self-energy can be derived using the dynamical equations for Green's functions (see [331, 332] for details) making the following assumptions:

a. three-body Green functions can be replaced by suitable combinations of one- and two-body Green functions;

b. particle-particle propagators are treated in the ladder (first order) approximation, and particle hole propagators in the bubble (RPA) approximation;

c. one-body Green functions can be described by HF propagators.

D.1 Approximation for the mass operator $\mathcal{M}$

The final expression for the mass operator is given by two terms, the one-body Hartree-Fock potential and a term that describes the coupling between the sp motion to the p-h and p-p vibrations of the core [26, 27]:

$$\mathcal{M}(\mathbf{r},\mathbf{r}',\omega) = \Sigma_{HF}(\mathbf{r},\mathbf{r}') + \Sigma(\mathbf{r},\mathbf{r}';\omega), \tag{D.7}$$

where the self-energy is the sum of three terms:

$$\Sigma(\mathbf{r},\mathbf{r}';\omega) = \Sigma_{pp}(\mathbf{r},\mathbf{r}';E) + \Sigma_{RPA}(\mathbf{r},\mathbf{r}';E) - V_{d.c.}(\mathbf{r},\mathbf{r}';E)\ . \tag{D.8}$$

The first contribution, Σ_{pp}, represents the dynamical effect due to the coupling to p-p excitations, Σ_{RPA} describes the correction to the mean field due to the coupling to p-h excitations and the third term is necessary to remove the double counting in Σ_{RPA}.
In this work we have decided to take into account only p-h coupling and neglect the

Figure D.1: a) Polarization and b) Correlation processes contributing to the RPA self-energy term.

correction terms because they give a small contributions to the self-energy [26, 27, 324]. We plan to study in details all terms and their influence on the dynamical part of the mean potential in a future work where we foresee to treat everything in a self-consistent way.

The Random Phase Approximation (RPA) term of the self-energy is composed of two terms: the polarization and correlations contributions (see Fig. D.1). The polarization graph generally tends to shift the energies of the unoccupied (occupied) states down (up) whereas the correlation graph has the opposite effect.

The contributions of these two graphs to the mean potential is calculated using the following expression:

$$\Sigma_{RPA}(\mathbf{r},\mathbf{r}';E) = \int V(\mathbf{r},\mathbf{r}_1)\mathcal{G}(\mathbf{r},\mathbf{r}';E-E')\mathcal{G}_{RPA}(\mathbf{r}_1,\mathbf{r}_2;E')V(\mathbf{r}',\mathbf{r}_2)\frac{dE'}{2\pi i}d^3\mathbf{r}_1 d^3\mathbf{r}_2 \,, \tag{D.9}$$

where V is the particle-hole residual interaction, $\mathcal{G}$ is the single particle propagator Eq. (D.1), and the dependence on $E-E'$ comes from energy conservation reasons at vertices. The quantity $\mathcal{G}_{\mathcal{RPA}}$ is the RPA particle-hole Green function defined as:

$$\mathcal{G}_{RPA}(\mathbf{r}_1,\mathbf{r}_2,\omega) = \sum_N \delta\rho_N(\mathbf{r}_1)\delta\rho_N^*(\mathbf{r}_2)\left[\frac{1}{E_N-\omega-i\eta}+\frac{1}{E_N+\omega-i\eta}\right] \,, \tag{D.10}$$

where:

$$\delta\rho_N(\mathbf{r}) \equiv < \Psi_N|\hat{\Psi}^\dagger(\mathbf{r})\hat{\Psi}(\mathbf{r})|\Psi_0 > \,, \tag{D.11}$$

E_N is the excitation energy corresponding to the excited state $|\Psi_N\rangle$ calculated in RPA, $|\Psi_0>$ is the correlated ground state and $\hat{\Psi}^\dagger(\mathbf{r})$ ($\hat{\Psi}(\mathbf{r})$) creates (annihilates) a nucleon at point $\mathbf{r}$ and can be written as a suitable combination of the $\hat{a}^\dagger$ $\hat{a}$ operators [115]. The quantity $\delta\rho_N(\mathbf{r})$ is then called transition density, which we define from the ground state to the excited state.

In the work of Bernard and Van Giai [26, 27], the HF potential was determined using the Skyrme interaction and the RPA states were coupled to the single particle states by the antisymmetrized p-h interaction which is defined as the second derivative of the HF total energy with respect to the densities. In the case of the Skyrme force this definition leads to a coupling interaction which is zero range and it has the simple form:

$$V(\mathbf{r}_1,\mathbf{r}_2) = \tilde{v}(r_1)\delta(\mathbf{r}_1-\mathbf{r}_2) \tag{D.12}$$

with

$$\tilde{v}(r) = \begin{cases} \frac{3}{4}t_0 + \frac{3}{8}t_3\rho(r) & T = 0 \\ -\frac{1}{4}t_0\,(1 + 2x_0) - \frac{1}{8}t_3\rho(r) & T = 1\,. \end{cases} \tag{D.13}$$

The case $T = 0$ ($T = 1$) corresponds to the coupling to an isoscalar (isovector) mode. The parameters t_i and x_0 were taken as those of the force SIII and $\rho(r)$ is the total density profile of the ground state.
Using this p-h interaction in Eq. (D.9), it is possible to get a simplified expression for the self-energy due to the presence of the delta functions in the V-terms which cancel the volume integrals leaving only the energy summation. The final expression is thus:

$$\Sigma_{Sky}(\mathbf{r}, \mathbf{r}'; E) = \tilde{v}(r_1)\tilde{v}(r_2) \int \mathcal{G}(\mathbf{r}, \mathbf{r}_1; E - E')\mathcal{G}_{RPA}(\mathbf{r}_1, \mathbf{r}_2; E')\frac{dE'}{2\pi i}. \tag{D.14}$$

Following the procedure in [26], it is necessary to calculate the (l, j)-component of the self-energy given by:

$$\Sigma^{lj}_{Sky}(r, r'; E) = \frac{\tilde{v}(r)\tilde{v}(r')}{2j+1} \sum_{L,N} \delta\rho_{LN}(r)\delta\rho_{LN}(r') \left[F^{LN}_p(r, r', E) + F^{LN}_h(r, r', E)\right] \tag{D.15}$$

where N runs over the RPA solutions and L over the multipolarity, and:

$$F^{LN}_{p/h}(r, r', E) = \sum_{p/h} \frac{R_{p/h}(r)R_{p/h}(r')| < \frac{1}{2}lj||Y_L||\frac{1}{2}l_{p/h}j_{p/h} > |^2}{E - \epsilon_{p/h} \mp E_N \pm i\eta}\,. \tag{D.16}$$

In the spherical symmetric case, the vector dependence can be dropped down factorizing into a radial and angular part (plus the spin part). The term $R(r)$ is the radial part of the single wave function defined as:

$$\Phi(\mathbf{r}) = R(r)\; i^l\; \mathcal{Y}_{ljm} = R(r)\; i^l \sum_{m_1 m_2} < lm_1, \frac{1}{2}m_2|jm > Y_{lm_1}\chi_{m_2} \tag{D.17}$$

and $< \frac{1}{2}lj||Y_L||\frac{1}{2}l_pj_p >$ is the reduced matrix element of the spherical harmonics:

$$< \frac{1}{2}lj||Y_L||\frac{1}{2}l_pj_p >= \delta\,\sqrt{\frac{(2j_p+1)(2L+1)}{4\pi}} < j_p\frac{1}{2}, L0|j\frac{1}{2} > \;. \tag{D.18}$$

The phase i^l is introduced to have the standard definition of time reversal state [44], while $\delta = \frac{1}{2}\left[1 + (-1)^{l+L+l_p}\right]$ takes into account that the reduced matrix elements of the spherical harmonics can become zero if $l + L + l_p$ is an odd number (because of the selection rules contained in the properties of the Clebsch Gordan coefficients). The presence of the factor $2j + 1$ in the formula Eq. (D.15) compared to the one of Eq. (9) in [26] comes from a different definition of the reduced matrix element of the spherical harmonics [323].
In the work of Bernard-Van Giai the RPA states were calculated by a self consistent RPA calculation in coordinate representation following the method proposed in Ref. [30], while the transition densities were deduced by a curve fitting of the quantity $\sqrt{ImG_{RPA}(r, r, E_N)}$

using a parameterization very close to the so-called Tassie model [311].
The transition density can also be calculated without any approximation using the information about the excited states coming from the solutions of the RPA matrix equation. Indeed, the transition density can be defined as

$$\delta\rho_{LN}(r) = \sum_{ph} \frac{R_p(r)R_h(r)}{\sqrt{2L+1}} \left[X_{ph}(LN) + Y_{ph}(LN)\right] < \frac{1}{2} l_p j_p || Y_L || \frac{1}{2} l_h j_h >, \quad \text{(D.19)}$$

where $X_{ph}(LN)$ ($Y_{ph}(LN)$) are the forward- (backward-) going amplitude (see next Section).

It is possible to avoid all complications coming from the definition of the p-h residual interaction using a separable p-h interaction; in this case the RPA matrix equation reduces to only one equation [287]. However, an additional problem emerges: the expression of the self-energy found in Eq. (D.14) is not any more valid because this interaction does not contain delta function and it is necessary to compute the volume integrals. Expanding all the quantities in Eq. (D.9) in spherical harmonics using the general expression:

$$f(\mathbf{r}_1, \mathbf{r}_2) = \sum_L f_L(r_1, r_2) \sum_M Y^*_{LM}(\hat{r}_1) Y_{LM}(\hat{r}_2) \quad \text{(D.20)}$$

and considering, for the radial part of the residual interaction, the following form:

$$V_L(r, r') = -k_L f_L(r) f_L(r') \,, \quad \text{(D.21)}$$

it is possible to obtain the correction of the self-energy due to the p-h interaction:

$$\begin{aligned} \Sigma^{lj}_{sep}(r, r'; E) &= k_L^2 f(r) f(r') \int \frac{dE'}{2\pi i} \mathcal{G}_L(r, r; E - E') \times \\ &\int dr_1 r_1^2 \int dr_2 r_2^2 f(r_1) f(r_2) \mathcal{G}^L_{RPA}(r_1, r_2; E') \,. \end{aligned} \quad \text{(D.22)}$$

Using the spectral representation of $\mathcal{G}_{RPA}$ in terms of the transition density, and following the same procedure used to obtain the Eq. (D.14), it is possible to write

$$\Sigma^{lj}_{sep}(r, r'; E) = \frac{k_L^2 f(r) f(r')}{2j+1} \sum_{L,N} \left(\frac{\beta_{LN}}{\sqrt{2L+1}} \right) \left[F_p^{LN}(r, r'; E) + F_h^{LN}(r, r', E) \right] \,, \quad \text{(D.23)}$$

where the term $\frac{\beta_{LN}}{\sqrt{2L+1}}$ has been introduced:

$$\frac{\beta_{LN}}{\sqrt{2L+1}} = \int dr\, r^2 f(r) \delta\rho_{LN}(r) \,. \quad \text{(D.24)}$$

Taking into account the definition of the transition density, the square of Eq. (D.24) is the probability that the system goes from the ground state $|\Psi_0>$ to the excited state $|\Psi_N>$ due to the application of an external field $f(r)$. To evaluate the RPA self-energy in the separable case, i.e. in a phenomenological framework, it is possible to take the following shape for the form factor [44]:

$$f(r) = R_0 \frac{dU(r)}{dr} \,, \quad \text{(D.25)}$$

where R_0 is the nuclear radius while $U(r)$ is the mean field potential. In this way, one obtain the same expression of the collective model of Bohr and Mottelson for the particle-vibration Hamiltonian [44]:

$$H_{PVC} = -\sum_{L} \sqrt{2L+1}\, k_L R_0 \frac{dU(r)}{dr} \sum_{MN} \beta_{LN} Y^*_{LM} \,. \tag{D.26}$$

The quantity β_{LN} can be deduced from the measured $B(EL; 0 \rightarrow L)$ while the coupling constant k_L can be determined using the self-consistency condition as explained in [44]. An alternative approach consists in determining k_L starting from experimental energies of the low-lying collective states, in such a way that the calculated β_{LN} is of the same order of magnitude of the experimental corresponding quantity.

The above discussion holds if the system is at equilibrium, at zero temperature. The extension of the previous expressions to finite temperature is straightforward if one uses the Matsubara formalism [115, 214] so that the only quantity which changes is $F_{p/h}$, where the temperature appears explicitly. Indeed, it is possible to show that $F_{p/h}$ can be substituted by the expression F_T defined as:

$$\begin{aligned} F^{LN}_T(r,r';E) &= \sum_a R_a(r) R_a(r') \left| \langle \frac{1}{2} lj || Y_L || \frac{1}{2} l_a j_a \rangle \right|^2 \left[\frac{1 + n_B(E_N) - n_F(\varepsilon_a)}{E - \varepsilon_a - E_N + i\eta} + \right. \\ &+ \left. \frac{n_B(E_N) + n_F(\varepsilon_a)}{E - \varepsilon_a + E_N - i\eta} \right] \,, \end{aligned} \tag{D.27}$$

where $n_B(E_N)$ and $n_F(E_N)$ are the boson and fermion occupation factors. In Eq. (D.27), one does not anymore distinguish between unoccupied (p) or occupied (h) states because of the Fermi factor n_F. The Bose occupation factor, n_B, is related to the collective state E_N; at zero temperature this quantity becomes zero. Actually, also β_{LN} changes with temperature in the self-energy expression, but it is an implicit dependence, as we will see in the next Section.

For practical purposes, it is convenient to define a local potential $\Sigma^L_{RPA}(R,E)$ equivalent to the non-local one $\Sigma_{RPA}(\mathbf{r},\mathbf{r}';E)$. In Refs. [332, 26, 324] it was shown that this non-local potential can be parameterized in a simple way using a Gaussian form; in this way, the local equivalent potential can be written in the form:

$$\Sigma^L_{RPA}(R,E) \equiv \int \Sigma_{RPA}(\mathbf{r},\mathbf{r}',E) d^3s = (\beta\sqrt{\pi})^3 \sum_{lj} \frac{2j+1}{4\pi} \Sigma^{lj}_{RPA}(R,R;E), \tag{D.28}$$

where $\mathbf{s} = \mathbf{r} - \mathbf{r}'$ while $\mathbf{R} = \frac{1}{2}(\mathbf{r} + \mathbf{r}')$. The factor β is the non-locality range of the order of 1 fm. Our main aim is to analyse this local equivalent potential as a function of energy, radial coordinate, and temperature.

D.2 RPA Equations in p-h configuration space

The most important results one can obtain in the RPA framework are presented especially in connection with the energy of the collective states and the β_{LN} parameters, that is the quantity needed to calculate Σ_{RPA} (details are explained in Ref. [287]). The random phase approximation (RPA) has provided a convenient and useful method to describe

excited states of many-fermion systems. There are different ways to formulate the RPA, in this Section we present the RPA in the framework of the particle-hole configuration space because it is suitable either for separable particle-hole interactions or for density dependent ones as Skyrme.
The starting point is the equation of motion method which is based on the knowledge of the Hamiltonian of the system H and the phonon operator $\hat{O}^\dagger_L$:

$$[\hat{H}, \hat{O}^\dagger_L]|0>=(E_L - E_0)\hat{O}^\dagger_L|0>=\omega_L\hat{O}^\dagger_L|0>, \tag{D.29}$$

where $\hat{O}_L$ is the ground state defined by $\hat{O}_L|0>=0$, while E_L is the energy of the excited state $|L>=\hat{O}^\dagger_L|0>$ characterized by the momentum L. The phonon operator can be written as a function of the p-h creation (annihilation) operators $\hat{a}^\dagger_m$ ($\hat{a}_i$) introducing two quantities, X and Y, called forward-going and backward-going RPA amplitude:

$$\hat{O}^\dagger_L = \sum_{mi}\left[X^L_{mi}\hat{a}^\dagger_m\hat{a}_i - Y^L_{mi}\hat{a}_i\hat{a}^\dagger_m\right] \ . \tag{D.30}$$

The meaning of this definition is the following: an excited state $|L>$ can be reached either directly from the boson vacuum acting with the operator $\hat{O}^\dagger_L$, or starting with the HF vacuum $|HF>$ and exciting a coherent superposition of p-h configurations with amplitude X_{mi}, or destroying correlated p-h configurations already present in the ground state with amplitude Y_{mi}. Using the equation of motion defined at the beginning of this Section, it is possible to obtain the RPA matrix equation (see e.g. [282]):

$$\begin{cases} \sum_{nj}\left[A_{mi,nj}X^L_{mi} + B_{mi,nj}Y^L_{mi}\right] = \omega_L X^L_{mi} \\ \sum_{nj}\left[B^*_{mi,nj}X^L_{mi} + A^*_{mi,nj}Y^L_{mi}\right] = -\omega_L Y^L_{mi} \end{cases} \tag{D.31}$$

where

$$A_{mi,nj} = <HF|[\hat{a}^\dagger_i\hat{a}_m, [\hat{H}, \hat{a}^\dagger_n\hat{a}_j]]|HF> \tag{D.32}$$

$$B_{mi,nj} = <HF|[\hat{a}^\dagger_i\hat{a}_m, [\hat{H}, \hat{a}^\dagger_j\hat{a}_n]]|HF> \ . \tag{D.33}$$

The indices m, n indicate particle states, while the indices i, j indicate hole states. In case of Skyrme interaction, the two matrices take the form:

$$\begin{cases} A_{mi,nj} = (\epsilon_m - \epsilon_i)\delta_{mn}\delta_{ij} + \frac{\delta E}{\delta\rho_{im}\delta\rho_{nj}} \\ B_{mi,nj} = \frac{\delta E}{\delta\rho_{im}\delta\rho_{jn}}, \end{cases} \tag{D.34}$$

where $E[\rho]$ is the HF energy, which is a functional of the sp density ρ, and ϵ_m are the sp energies.
The general properties of RPA solutions can be found using the so-called schematic separable interaction that appears in the collective model of Bohr-Mottelson. Indeed, the Hamiltonian of the system can be written as the sum of two terms: $H = H_0 + H_{res}$ in which H_0 is the mean field term and H_{res} the residual interaction (see Eq. (2.2)) which describes correlations beyond mean field. In the case of separable interaction, H_{res} assumes the form:

$$H_{res} = -\frac{k_L}{2}\sum_{ij}\hat{Q}^L_i\cdot\hat{Q}^L_j \ , \tag{D.35}$$

so that the RPA matrix equation (D.31) reduces to a simple equation:

$$\sum_{mi} \frac{2|\hat{Q}^L_{mi}|^2\,\epsilon_{mi}}{\epsilon^2_{mi}-\omega^2} = \frac{1}{k_L}\,, \tag{D.36}$$

where $\epsilon_{mi} = \epsilon_m - \epsilon_i$ is the energy of the 1p-1h configuration. The solutions of this equation are the RPA energies used in Eq. (D.9), i.e. E_N. The X and Y amplitudes are then defined as:

$$\begin{cases} X^{LN}_{mi} = \frac{\Lambda_{LN} Q^L_{mi}}{\epsilon_{mi}-E_N} \\ Y^{LN}_{mi} = \frac{\Lambda_{LN} Q^{L*}_{mi}}{\epsilon_{mi}+E_N}\,, \end{cases} \tag{D.37}$$

where Λ_{LN} is a constant coming from the normalization condition:

$$\sum_{mi} \left[|X^{LN}_{mi}|^2 - |Y^{LN}_{mi}|^2\right] = 1\,. \tag{D.38}$$

This constant is related to the transition probability of exciting a collective state [44]; indeed the following relation holds:

$$\frac{\beta_{LN}}{\sqrt{2L+1}} = \sqrt{2L+1}\Lambda_{LN}\,. \tag{D.39}$$

It is now possible to show that the RPA equation in the case of separable interaction at finite temperature becomes:

$$\sum_{mi} \frac{2|\hat{Q}^L_{mi}|^2\,\epsilon_{mi}}{\epsilon^2_{mi}-\omega^2}\;\left[n_F(\varepsilon_i) - n_F(\varepsilon_m)\right] = \frac{1}{k_L}\,, \tag{D.40}$$

while the normalization condition becomes:

$$\sum_{mi} \left[|X^{LN}_{mi}|^2 - |Y^{LN}_{mi}|^2\right]\;\left[n_F(\epsilon_i) - n_F(\epsilon_m)\right] = 1\,. \tag{D.41}$$

It is clear from these expressions that both Λ_{LN} and β_{LN} depend on temperature.

D.3 Application to ^{208}Pb: preliminary results

We show the preliminary results on the self-energy and effective mass obtained in the case of the spherical nucleus ^{208}Pb [105]. We have chosen this nucleus since collective excitations are expected to give a strong effect. Moreover, we wanted to compare our results with the ones published in the literature in Refs. [26, 324, 47]. We construct the sp energies and wave functions using a phenomenological Woods-Saxon potential, while we leave the analysis in the case of a Skyrme potential for further studies. We use a separable interaction for the RPA. This leads to an inconsistency in the calculation; we have decided to leave the self-consistent calculations for future investigations.

	neutron	proton
$V_{0,q}$ [MeV]	-45.0	-59.80
a_q [fm]	0.55	0.67
$a_{so,q}$ [fm]	0.45	0.59

Table D.1: Parameters of the Woods-Saxon potential (D.42) used in the calculations for neutrons and protons.

D.3.1 Woods-Saxon mean field potential

We have constructed the sp energies and wave functions using a Woods-Saxon potential [44]:

$$U(r) = \frac{V_{0,q}}{1 + e^{(r-R_0)/a_q}} + U_{so}(a_{so,q}) + U_{Coul} \ , \tag{D.42}$$

where $q = n, p$. The parameters of this potential have been chosen in such a way to have sp energies comparable with the ones of [26, 47], at least around the Fermi energy, and to get reasonable value of $B(EL; 0 \to L)$ compared to the experimental ones. The coupling constant used to solve the RPA equation is [44]:

$$k_L = -\int dr R_0 \frac{dU(r)}{dr} R_0 \frac{d\rho(r)}{dr} \ , \tag{D.43}$$

where in the derivative of U we take into account only the central part without spin-orbit and Coulomb contribution. We decide to employ this definition of the coupling constant instead of using a value fixed at zero temperature, since, in this way, Eq. (D.43) depends on the density of the system which changes if the temperature changes. The mean field parameters used in the calculations are given in Table D.1.

The local equivalent potential $\Sigma^L_{RPA}(R, E)$ has been calculated for neutrons and protons but, since the results are similar, we display only those for protons. The parameter η in Eq. (D.10) is set equal to 1 MeV.

In Fig. D.2 the behaviour of the real part of the local potential is shown as function of the radial coordinate, for three different values of energies. As one can see, Σ^L_{RPA} has a strong surface-peaked shape with small values in the nuclear interior in the whole range of energies considered. This shape is due to enhancement of the form factor $f(r)$ close to the surface.

The consequence of the behaviour around the Fermi surface of the dynamical term of the mean field potential is shown in Fig. D.3, where one can see that the general shape of the total potential well (Woods-Saxon plus the real part of the local potential) is not modified compared to the mean field Woods-Saxon, except for the slope around the Fermi surface. This means that the additional dynamical term produces a modification in the surface geometry of the total potential.

We now analyse the behaviour of the local potential and the effective mass as a function of the energy. The real and imaginary part of the local potential Σ^L_{RPA} as a function of energy at $R = 7.35$ fm, the nuclear radius, is shown in Fig. D.4. One can see that the potential is deeper above the Fermi energy than below because there are more available

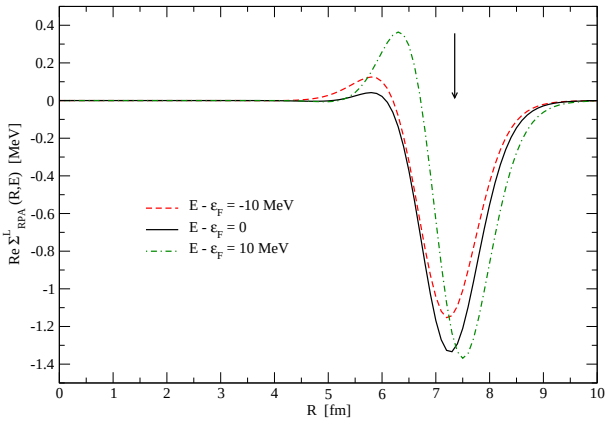

Figure D.2: Real part of the local potential $\Sigma^L_{RPA}(R,E)$ for protons as a function of the radial coordinate, for three different energies: $E = \epsilon_F$ (solid black line), $E = \epsilon_F \pm 10$ MeV (dashed-dotted green and dashed red lines). The arrow at $R = 7.35$ fm indicates the position of the surface.

intermediate states among the unoccupied levels than among the occupied ones so that the symmetry with respect the Fermi energy present in a infinite medium is broken. The plots can be compared to Fig. 1 of Ref. [324]. Despite differences which might come from the different sp energies (we use Woods-Saxon while the authors use Skyrme SIII) and different residual interaction (separable in our case, Skyrme in Ref. [324]), the energy dependence of Σ^L_{RPA} confirms the results of [26, 324]. We also point out that the quasi-particle approximation is valid *only* around the Fermi energy (where the imaginary part of the equivalent potential is, with a good approximation, energy independent).

We now can define a local effective ω-mass using the local potential through the relation:

$$\frac{m_\omega}{m}(R,E) = 1 - \mathrm{Re}\left(\frac{\partial \Sigma^L_{RPA}(R,E)}{\partial E}\right) . \tag{D.44}$$

In Fig. D.5 the energy dependence of the ω-mass at $R = 7.35$ fm and at zero temperature is plotted. At the nuclear surface, the ω-mass m_ω/m has a narrow enhancement peak. This indicates that near the Fermi energy the dynamical correction mainly arises from the coupling of the single particle to low-lying surface vibrations of the core. This result is in agreement with the one obtained in the so-called dispersion relation approach [217, 215, 218, 219], where the starting point is the empirical value of the imaginary part of the optical potential from which one can calculate, using the dispersion relation, the real part of it. The quantity m_ω/m deviates from unity in the nuclear surface region as a consequence of the narrow localization of Σ^L_{RPA} and it assumes a value greater than one due to the decreasing behaviour of $\mathrm{Re}\ \Sigma^L_{RPA}$ around the Fermi energy (see Fig. D.4 and Eq. (D.44)). Outside this interval, the effective mass can become less than one due to the wiggles present in the shape of Σ^L_{RPA} which are, probably, related to the coupling to more complicated states. We notice that also at $E - \epsilon_F \approx 10$ MeV the effective mass becomes greater than one, but in this energy range the approximation done to obtain $\Sigma^L_{RPA}(R,E)$ (Eq. (D.28)) is maybe questionable (see Fig. D.4).

We now want to explore the behaviour of this local effective mass as a function temperature, which was the main point we want to analyse. In Fig. D.6 the energy dependence

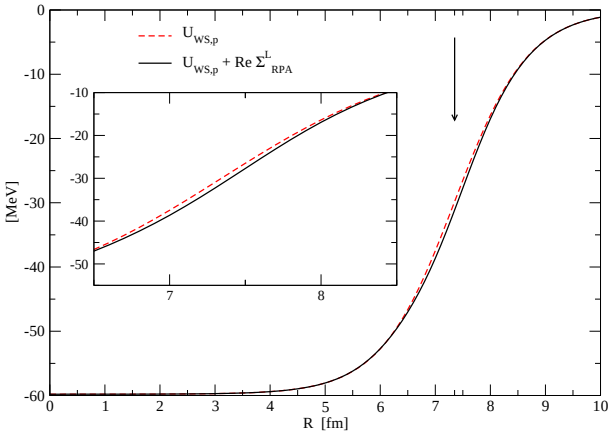

Figure D.3: Woods-Saxon potential (dashed red line) and total potential well (solid black line), i.e. Woods-Saxon plus the real part of the local potential $\Sigma^L_{RPA}(R, E)$, as a function of the radial coordinate at Fermi energy. The arrow at $R = 7.35$ fm indicates the position of the surface. The inset shows a zoom of the curves close to the surface.

of the proton effective mass at $R = 7.35$ fm for different temperatures is displayed. The effect of temperature on the effective mass is clear: as the temperature increases the effective mass around the Fermi energy decreases reaching the limit value of 1. However, one can also notice that there are wiggles around the Fermi surface when temperature goes from $T = 0$ MeV to finite temperature. This trend can be understood if one investigates the fraction of energy weighted sum rule (EWSR) followed by the low-lying collective states as a function of temperature. The importance of this quantity is related to the fact that it gives informations on the collectivity of this vibrational mode and, as a consequence, on the strength of the coupling to the sp states. At very low energy, states which were not present at $T = 0$ might appear with a quite big strength. This would produce the wiggles shown in Fig. D.6 in the effective mass profiles around the Fermi energy. At finite temperature, the Fermi surface becomes smooth leaving the possibility to have p-p or h-h configurations not allowed at zero temperature due to the occupation factors of the sp states (see Eq. (D.40)). The increased number of sp configurations from which one calculates the collective modes and the fact that some of these new configurations can have an energy less than the lowest one at zero temperature might explain the kinks in the effective mass. In order to understand these discrepancies, one should explore the behaviour of the EWSR for all the multipolarities.

D.4 Conclusions and Outlooks

The aim of this preliminary work has been to investigate in the RPA framework at finite temperature the effect of the temperature on the local energy-dependent potential which takes into account p-h correlations beyond the mean field picture. We then wanted to derive the energy-dependent ω-mass and analyse how it changes with temperature. At this level, we have used a Woods-Saxon potential to calculate the sp energies and wave functions and then computed the RPA at finite temperature; this leads to an inconsistency

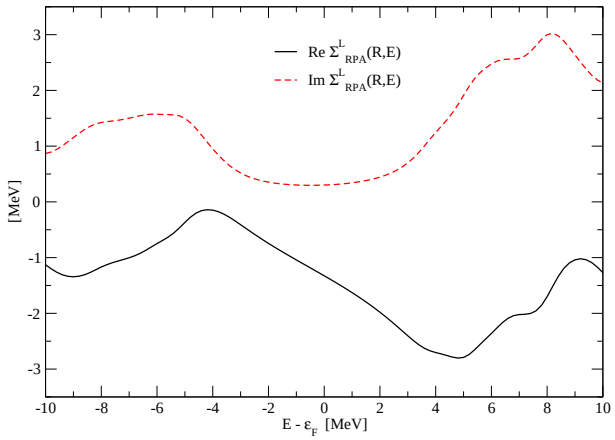

Figure D.4: The real (solid black line) and imaginary (dashed red line) part of the local potential $\Sigma^{L}_{RPA}(R,E)$ for protons, as a function of energy at $R = 7.35$ fm.

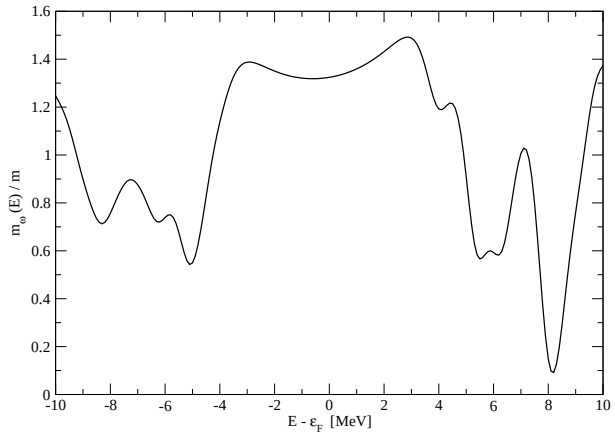

Figure D.5: Energy dependence of the local effective ω-mass for protons at the nuclear surface ($R = 7.35$ fm), at $T = 0$.

in the calculation. However, the general trend of the results (energy and radial dependence of the local potential as well as the energy dependence of the ω-mass) are in global agreement with the literature (see e.g. [216]).

This is an encouraging starting point to pursue this work. First of all we want to construct the RPA starting from the Skyrme sp energies and wave functions instead of using the Woods-Saxon potential. Then we plan to perform in a consistent way both the HF calculations and the RPA employing the Skyrme interaction, and compare the results with the ones present in the literature (e.g. [26, 324]). Another reason to prefer a self-consistent approach relies on the fact that the results obtained for the temperature dependence of the ω-mass change (quantitatively but not qualitatively) with the parameters of the phenomenological Woods-Saxon potential. Finally, we want to extend the study to other nuclei than ^{208}Pb in order to perform a systematic analysis.

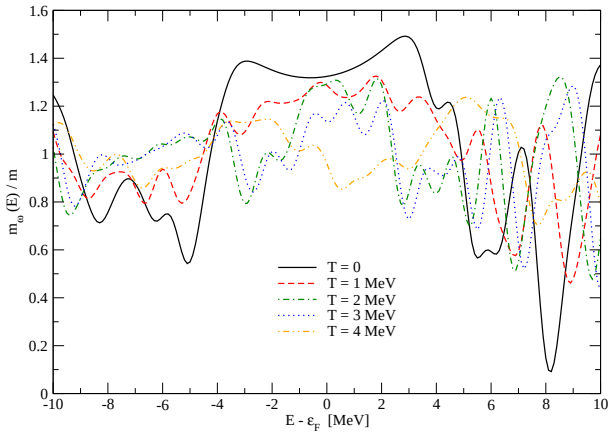

Figure D.6: Energy dependence of the local effective ω-mass for protons at the nuclear surface ($R = 7.35$ fm). Solid black line corresponds to the $T = 0$ case, while dashed red line, dashed-dotted green line, dotted blue line and dashed-dotted-dotted orange line correspond respectively to $T =$1, 2, 3, 4 MeV.

Appendix E

npe gas Equation of State

In this Appendix I will describe an EoS for a gas formed by neutrons, protons, electrons (*npe*) at finite temperature.
For more details and applications of the original routines of the EoS, which have been improved, we refer to [223].

E.1 Basics of the *npe* EoS

The matter is treated as a uniform gas composed of free electrons, neutrons and protons; there are no clusters (i.e. no nuclei) in the model. A version of the EoS includes neutrinos, which are considered as massless ultra-relativistic particles; where no neutrinos are included, their chemical potential μ_ν is set to zero. The electrons are considered as degenerate relativistic fermions. The nucleons are modelled as interacting non-relativistic particles; the interaction can be chosen among different Skyrme or Gogny forces.
The system conserves both the charge neutrality and the total baryon number; the EoS can be calculated both in β equilibrium or out of β equilibrium.

In the following, we will restrict the analysis to the results obtained with Skyrme forces, without assuming β equilibrium, since we want to construct a table as a function of the three "standard" independent variables: the baryon density, the temperature, and the electron fraction.

E.1.1 Thermodynamics

The independent variables for the EoS are the baryon density, the temperature, and the electron fraction: (n_b, T, Y_e). For each set of variables, we calculate the other thermodynamical quantities, like the pressure, the energy, the entropy. In the version of the EoS in which β equilibrium is assumed, the only independent variables needed are the baryon density and the temperature (n_b, T).
Once the baryon density, the electron fraction and the temperature are fixed, the neutron and proton densities are straightforwardly derived by the charge and baryon number conservation equations. Then, we can calculate the other quantities which characterize the system. We recall in the following the main definitions and equations used.

- **Chemical potentials**

The chemical potential for each species is calculated, via a Newton-Raphson method (i.e. a root finder, see Eq. (F.1)), by finding the root of the equation: $n_i = n_i(\mu_i)$, where n_i is the (known) density of the species i and $n_i(\mu_i)$ is the density derived from the searched chemical potential μ_i. The density is defined as:

$$n = \frac{g}{h^3} \int f \mathrm{d}\mathbf{p} \,, \tag{E.1}$$

where $g = 2$ is the spin degeneracy, $\mathbf{p}$ is the momentum and f is the distribution function. Assuming a Fermi-Dirac distribution function, defining $\mathbf{p} = \hbar\mathbf{k}$, and in spherical symmetry, one gets for $n_i(\mu_i)$:

$$f_i(k) = \frac{1}{1 + e^{\frac{\epsilon_i - \mu_i}{k_B T}}} \,. \tag{E.2}$$

$$n_i(\mu_i) = \frac{1}{\pi^2} \int f_i(k) k^2 \mathrm{d}k \,. \tag{E.3}$$

The energy per particle is:

$$\epsilon = \begin{cases} \frac{\hbar^2 k^2}{2m^*} & \text{nucleons} \\ \sqrt{(m_e c^2)^2 + (\hbar k c)^2} & \text{electrons} \,. \end{cases} \tag{E.4}$$

At low temperature, a technical problem is encountered in calculating the integral in Eq. (E.3), because of the Fermi function. Thus, we consider explicitly the low-temperature case which can be derived analytically (see e.g. [188, 295] for reference):

$$\mu_i(T \ll T_F) = \epsilon_{F,i} \left[1 - \frac{1}{12} \left(\frac{\pi k_B T}{\epsilon_{F,i}} \right)^2 + \frac{7}{960} \left(\frac{\pi k_B T}{\epsilon_{F,i}} \right)^4 \right] \,, \tag{E.5}$$

where T_F is the temperature associated to $\epsilon_{F,i}$, the Fermi energy for the species i:

$$\epsilon_{F,i} = \begin{cases} \frac{\hbar^2 k_{F,i}^2}{2m_i^*} & \text{nucleons} \\ \sqrt{(m_e c^2)^2 + (\hbar k_{F,i} c)^2} & \text{electrons} \,, \end{cases} \tag{E.6}$$

and: $k_{F,i} = (3\pi n_i)^{1/3}$.
To the nucleon chemical potential, we have added the mean field contribution.

- **Energy**
  For nucleons, the internal energy is given by the kinetic plus the mean field contribution. According to the notation in [77] ($q = n$,p stands for neutrons and protons), the energy density (i.e. energy per volume) is given by[1]:

$$\begin{aligned} \varepsilon_q \;=\; & \frac{\hbar^2}{2m_q^*} \tau_q(T) \\ & + \frac{1}{4} t_0 \left[(2 + x_0)(n_n + n_p)^2 - (2x_0 + 1)(n_n^2 + n_p^2) \right] \\ & + \frac{1}{24} t_3 (n_n + n_p)^\sigma \left[(2 + x_3)(n_n + n_p)^2 - (2x_3 + 1)(n_n^2 + n_p^2) \right] \end{aligned} \tag{E.7}$$

[1] A quantity Q expressed per volume is related to the same quantity per baryon by: $\frac{Q}{V} = n_b \, Q_{perbaryon}$.

where the Skyrme parameters are given in Appendix B and the kinetic energy density τ_q reads:

$$\tau_q = \frac{1}{\pi^2} \int k^4 \, f_q(k) \, \mathrm{d}k \, . \tag{E.8}$$

At low temperature we calculate τ_q by means of its analytical expression [188]:

$$\tau_q(T \ll T_F) = \frac{3}{5} \, k_F^2 \, n_q \left[1 + \frac{5}{12} \left(\frac{\pi k_B T}{\epsilon_F} \right)^2 \right] \, . \tag{E.9}$$

For electrons, we have only the kinetic contribution:

$$\varepsilon_e = \frac{1}{\pi^2} \int \epsilon_e \, f_e(k) \, \mathrm{d}k \, , \tag{E.10}$$

which, at low temperatures, reads [188]:

$$\begin{aligned} \varepsilon_e(T \ll T_F) \;=\; & n_e m_e c^2 \\ & + \frac{m_e c^2}{24\pi^2} \left(\frac{m_e c^2}{\hbar c} \right)^3 \Big\{ 3x_e(2x_e^2+1)\sqrt{1+x_e^2} - 8x_e^3 \\ & - 3 \sinh^{-1} x_e \\ & + \frac{4\beta_e^2}{x_e} \left[(1+3x_e^2)\sqrt{1+x_e^2} - 1 - 2x_e^2 \right] \Big\} \, , \end{aligned} \tag{E.11}$$

where we have introduced:

$$x_i \;:=\; \frac{\hbar k_F c}{m_i c^2} \tag{E.12a}$$

$$\beta_i \;:=\; \frac{\pi k_B T}{m_i c^2} \, . \tag{E.12b}$$

- **Entropy**
  The entropy per baryon (in units of the Boltzmann constant) is given for both nucleons and electrons by:

$$s_i = -\frac{1}{n_b} \frac{1}{\pi^2} \int \left[f_i(k) \log f_i(k) + (1 - f_i(k)) \log(1 - f_i(k)) \right] \, k^2 \mathrm{d}k \, . \tag{E.13}$$

  At $T = 0$, $s = 0$. At low temperature, both for nucleons and electrons, the entropy reads [188]:

$$s_i(T \ll T_F) = \frac{1}{n_b} \frac{1}{3\pi^2} \left(\frac{m_i c^2}{\hbar c} \right)^3 \pi \beta_i \sqrt{1+x_i^2} \left[x_i + \frac{7}{15} \frac{\beta_i^2}{x_i^3} (x^2 - 0.5) \right] \, . \tag{E.14}$$

- **Pressure**
  The pressure for nucleons is calculated by means of the thermodynamical relation:

$$P_q = \sum_q \tilde{\mu}_q n_q - f \, n_b \, , \tag{E.15}$$

where $\tilde{\mu}_q$ contains also the mean field contribution and f is the free energy per baryon, which is calculated from the usual relation:

$$f = \epsilon - T\, s\ , \tag{E.16}$$

and: s is the entropy per baryon in units of k_B. Notice that Eq. (E.15) holds even at low temperature.
For the electrons, the pressure contains only the kinetic contribution; thus, it is given by:

$$P_e = \frac{1}{3\pi^2}\ \int (\hbar c)^2 \frac{k^4}{\epsilon_e} f_e(k)\ \mathrm{d}k\ . \tag{E.17}$$

At low temperature [188]:

$$\begin{aligned} P_e(T \ll T_F) \ &= \ \frac{m_e c^2}{24\pi^2}\ \left(\frac{m_e c^2}{\hbar c}\right)^3\ \Big[x_e(2x_e^2-3)\sqrt{1+x_e^2} \\ &\quad +3\sinh^{-1} x_e + 4\beta_e^2 x_e \sqrt{1+x_e^2}\Big]\ , \end{aligned} \tag{E.18}$$

where x and β have been previously defined in Eqs. (E.12).

E.2 Results

We present now the results of the EoS for the *npe* gas. As an example, for the Skyrme interaction, we have chosen the LNS Skyrme force derived in Ref. [71]. A comparison with the results obtained employing the SLy4 force will be also discussed.

In order to check the EoS, we compare our results with the ones obtained by the Catania group in Refs. [12, 71].
In Fig. E.1 we show the effective masses, the internal energy and free energy per baryon and the pressure of the gas. In the upper left panel, the neutron and proton effective masses are plotted as a function of the asymmetry, at $T = 0$ and at saturation density. This Figure can be compared to Fig. 3 of Ref. [71]. We of course obtain the same results since we use the same Skyrme parameterization. We notice, as commented in Section III of Ref. [71], the opposite trend of the neutron and proton effective mass deduced with the SLy4 force [76, 77] with respect to the LNS force [71]. As discussed in Refs. [320, 197], the correct splitting is the one reproduced by the LNS parameterization. In particular, in Ref. [320], theoretical considerations are given to justify that $m_n^* > m_p^*$, as also resulting from DBHF calculations. Moreover, in Ref. [196], it is also shown that the behaviour $m_n^* < m_p^*$ leads to a symmetry potential inconsistent with the energy dependence of the Lane potential (fitted phenomenologically) which is constrained by NN scattering data.
In the upper right panel, we display the baryon internal energy per baryon, ϵ_b, as a function of the baryon density, for different values of $\beta := (N-Z)/A$ (to facilitate the comparison, we kept the same notation as in the mentioned papers). This plot can be directly compared to Fig. 4 of Ref. [71], where the energy per particle is obtained within the microscopic BHF approach. Again, as expected, we obtain the same results.
In the lower panels, we display the baryon free energy per baryon and the baryon pressure

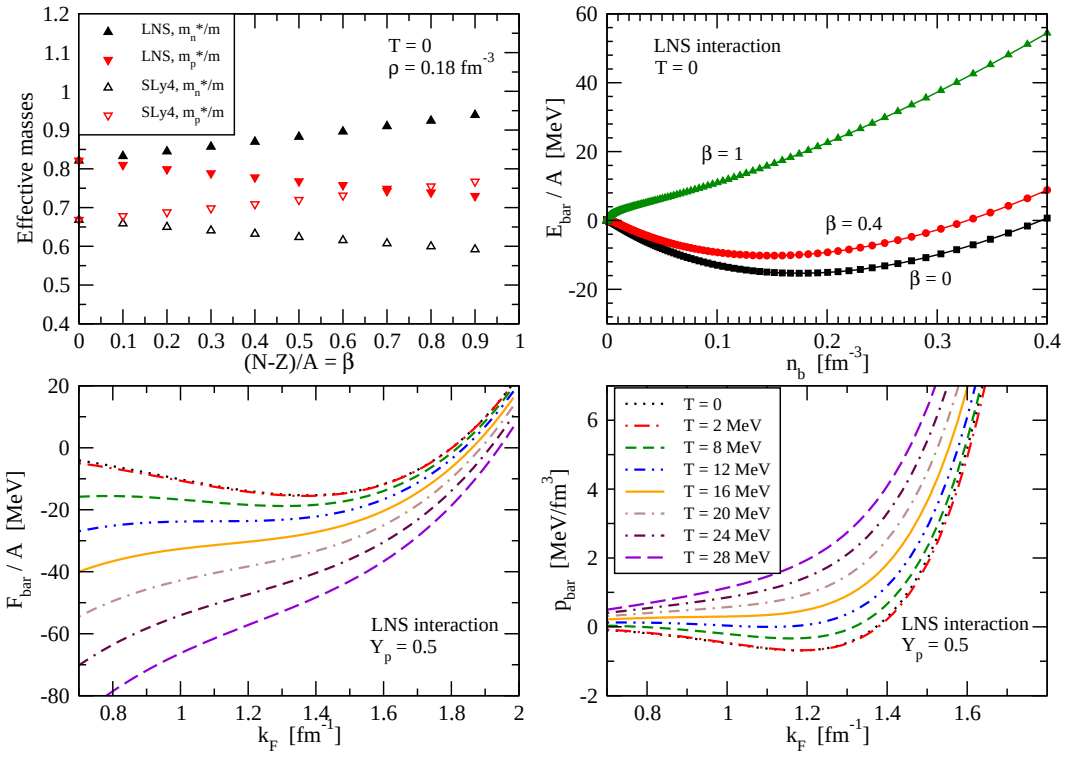

Figure E.1: In the upper left panel: neutron and proton effective masses as a function of $\beta := (N-Z)/A$ calculated with the LNS and SLy4 Skyrme forces; in the upper right panel: baryon internal energy per baryon as a function of baryon density calculated with the LNS Skyrme force for different β. In the lower panels, baryon free energy per baryon and baryon pressure as a function of k_F, calculated with the LNS Skyrme force for different temperatures.

as a function of the Fermi momentum k_F for different temperatures. We compare these plots to Fig. 1 of Ref. [12], where the results are obtained in a microscopic framework. We cannot reproduce exactly the same curves since the approach is different, and the Bonn potential is employed in Ref. [12] instead of the phenomenological Skyrme force. However, the results agree quite well. We notice that, for $T = 0$, the pressure is negative up to nuclear saturation density (which corresponds to $k_F \approx 1.4$ fm^{-1}), where the pressure is equal to zero, meaning that the energy has a minimum (indeed, the pressure is the derivative of the energy per particle). As a consequence, nucleons in symmetric matter cannot exist at zero temperature for densities lower that the saturation density, unless at very low density. The region where the derivative of the pressure with respect to the density is negative corresponds to the region of negative compressibility, i.e. to the hydrodynamically unstable regime. We notice also the typical behaviour associated to the existence of a critical temperature for the liquid-gas phase transition, characterized by the first monotonic isotherm. The critical temperature, T_c, is the inflexion point, which in this case occurs at $T \approx 16$ MeV, in agreement with the literature (see, e.g., [12, 188]).

We now want to analyse the dependence of the pressure on the temperature and the asymmetry.

In Fig. E.2 the pressure of the system is shown as a function of the baryon density, up to nuclear saturation density, at zero temperature. In the upper panels, we display, at zero

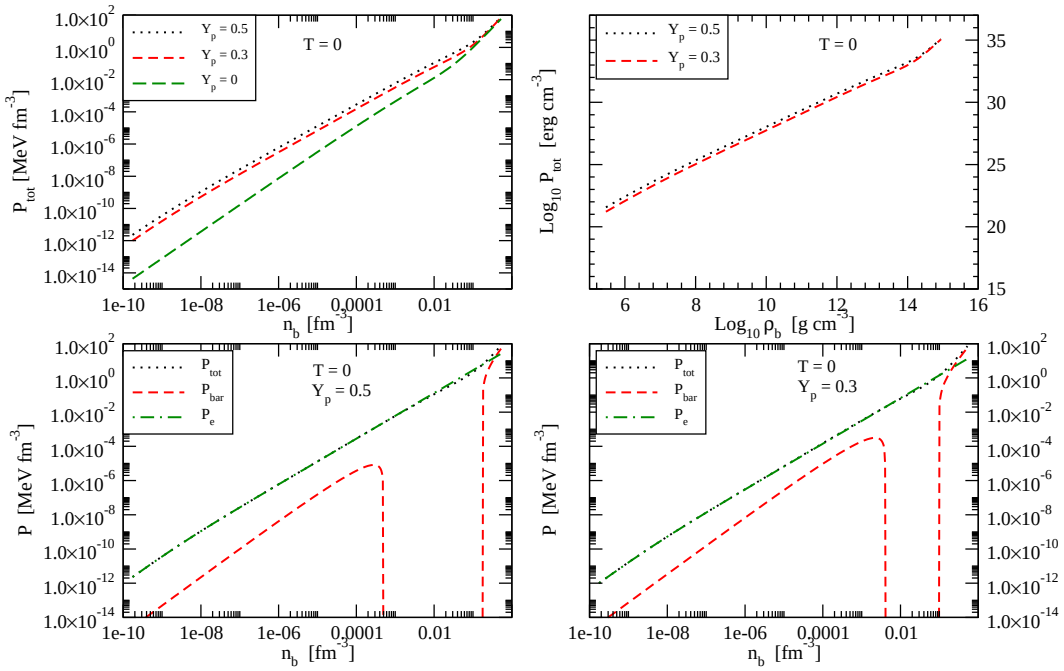

Figure E.2: In the upper panels: total pressure as a function of baryon density, at $T = 0$ and for different $Y_p = Y_e$. In the lower panels, the different contributions to the total pressure are displayed as a function of baryon number density, at $T = 0$ and for different $Y_p = Y_e$. The results are obtained with the LNS Skyrme force.

temperature, the effect of the asymmetry of the matter ($Y_p \equiv Y_e$ as a consequence of the charge conservation) on the total pressure. In the upper left panel, one can see that going from a pure neutron matter ($Y_p = 0$) to symmetric matter ($Y_p = 0.5$), the pressure increases of about two orders of magnitude at low density; this is due to the fact that, in this region, the main contribution to the pressure comes from the electrons. This is clearly shown in the lower panels, where the baryon and electron contributions to the pressure are plotted together with the total pressure: only at high density, $n_b \gtrsim 0.01$ fm$^{-1} \approx 10^{13}$ g cm^{-3}, the baryon component becomes important. The sharp decrease and subsequent increase of the baryon component in the lower panels is due to the fact that, in that region, P_{bar} is negative and therefore does not appear on a logarithmic scale. The increasing importance of the baryon contribution to the pressure at rather high densities was already pointed out by Harrison and Wheeler [150] who have shown that above 4×10^{12} g cm^{-3}more pressure was provided by free neutrons than by electrons.
In the upper right panel, we display the total pressure of the system in cgs units, in order to compare directly our results with the ones obtained with a cold *npe* gas EoS (see e.g. Fig. 2.2 of the Shapiro and Teukolski textbook [295]); the differences between the two plots are to be attributed to the fact that, in our case, interaction between nucleons is considered, while the *npe* gas EoS displayed in Fig. 2.2 of Ref. [295] is that of an ideal gas (i.e. no interactions are included). Despite some differences in the curves, the two results are in good agreement.

Finally, in Fig. E.3 we show the effect of the temperature on the pressure for the symmetric nuclear matter ($Y_e = Y_p = 0.5$). In the upper left panel, we plot the total pressure

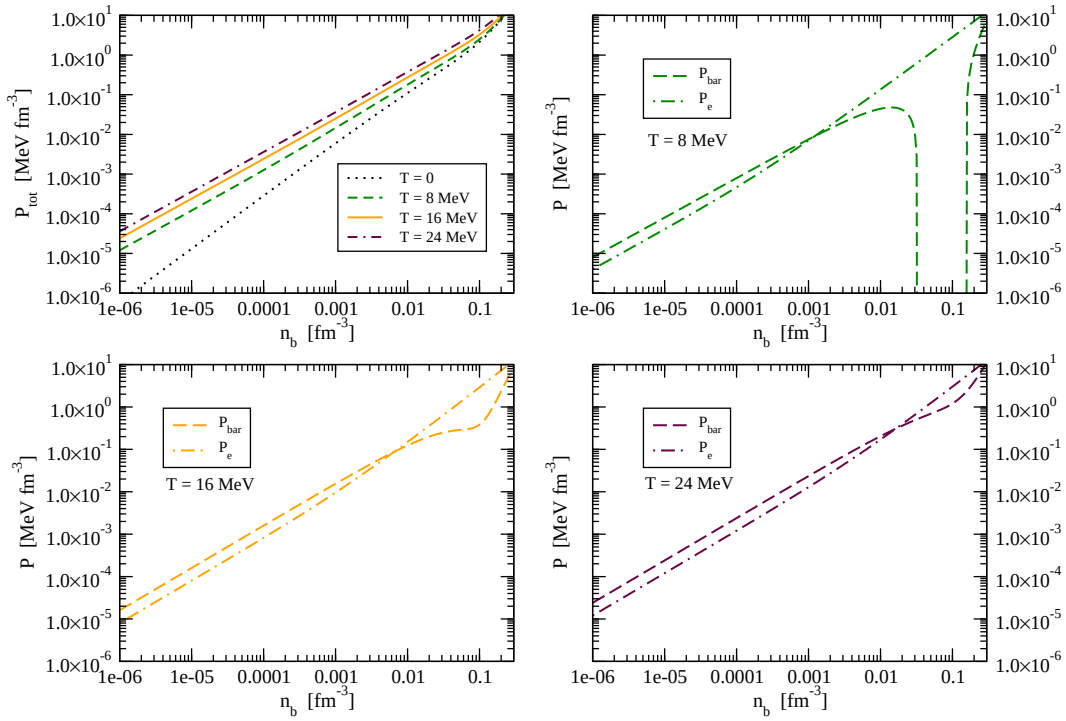

Figure E.3: In the upper left panels, the total pressure as a function of baryon density is shown for different temperatures $T = 0$, 8, 16, 24 MeV for the symmetric matter ($Y_p = Y_e = 0.5$). In the upper right and lower panels, the different contributions to the total pressure are displayed as a function of number baryon density, for the case of finite temperature: $T = 8$, 16, 24 MeV. The results are obtained with the LNS Skyrme force.

for different temperatures, from $T = 0$ to $T = 24$ MeV. We notice that, increasing the temperature, the total pressure of the system increases, especially at low density. In the upper right panel and in the lower panels, the baryon and electron contributions to the total pressure are shown. The effect of the temperature is to increase the baryon contribution, which is greater than the electron one at low density.

E.3 npe^* gas EoS

In Ref. [122] a comparison among the presupernova profiles computed with different EoS starting from density, temperature and asymmetry profiles of the s20 model (see Section 4.3) has been carried out. In particular, the profiles obtained with the LS EoS [192], a polytropic EoS and a npe gas EoS have been studied. During this analysis, it has been realized that, in the considered presupernova conditions, the baryon contribution in a npe gas is too high. The npe gas, in fact, does not contain any cluster, which are highly expected to be present in a presupernova profile; the overestimated effect of the baryon contribution is even stronger at finite temperature. This behaviour has already been shown in Fig. E.3. This gives very different results for the presupernova profiles with respect to the ones obtained with the LS EoS [192]. Starting from the consideration that, at low density, the electron contribution should dominate, a modified npe gas EoS has been proposed. In

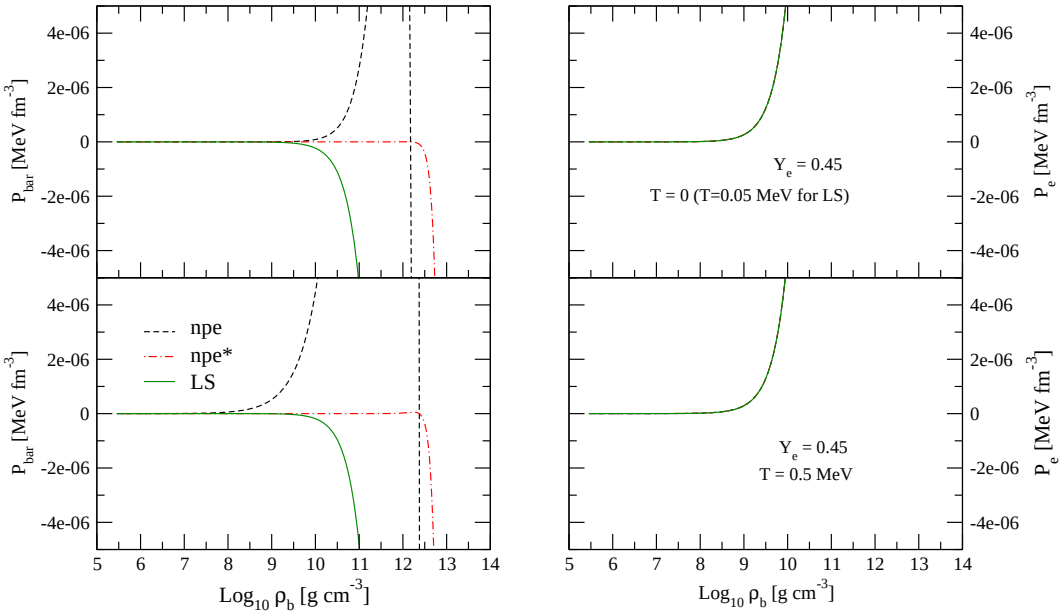

Figure E.4: Baryon (left panels) and electron (right panels) contributions as a function of density (in g cm^{-3}) obtained with the LS (green solid lines), npe gas (dashed black lines) and npe^* gas (dashed-dotted red lines) EoS. In the upper panels, $Y_e = 0.45$ and $T = 0$ ($T = 0.05$ MeV for the LS EoS); in the lower panels, $Y_e = 0.45$ and $T = 0.5$ MeV. The results are obtained with the LNS Skyrme force.

the npe^* EoS, the baryon contribution (both the pressure and the energy density) has been smoothed out at low density with the *ad hoc* exponential function $1 - \exp[-\rho_b/(\eta\rho_0)]^2$, where ρ_0 is the saturation density and η gives the scale at which the baryon component starts to play a role. In Fig. 4.3, it can be seen that the pressure profile computed with the npe^* EoS ($\eta = 0.2$) is closer to the one obtained by the LS EoS, unlike a standard npe gas EoS. In Fig. E.4, the baryon (left panels) and electron (right panels) contributions as a function of density (in g cm^{-3}) are plotted, for $Y_e = 0.45$, $T = 0$ (upper panels) and $T = 0.5$ MeV (lower panels), in the case of the LS ($K = 220$ MeV), npe gas, and npe^* gas EoS. Notice that the minimum temperature which allows the LS EoS to work is $T = 0.05$ MeV. A very good agreement for the electron contribution to the pressure is observed. Instead, for the baryon contribution, we notice an opposite behaviour of the pressure curve for the LS and the npe gas EoS in the density range starting from $\rho \approx 10^9$ g cm^{-3}(at $T = 0$) and $\rho \approx 10^{7.5}$ g cm^{-3}(at $T = 0.5$), showing that the discrepancies between the LS and the npe EoS are larger increasing the temperature. Despite remarkable differences between the LS and npe^* gas EoS, we recover at least the same decreasing trend of the pressure with respect to the density (at fixed temperature and asymmetry); the parameter η could be tuned to achieve a better agreement with the LS EoS behaviour.

Appendix F

Lattimer-Swesty Equation of State tables

In this Section it will be explained how a tabulated version of the EoS by Lattimer and Swesty [192] has been generated.
The original routines and user guide [305] for the EoS are provided by the authors at the website:
http://www.astro.sunysb.edu/dswesty/lseos.html .

F.1 Basics of the LS EoS

The matter is modelled as a mixture of nuclei, free neutrons and protons, α particles, leptons and photons. Electrons and positrons are treated as non-interacting relativistic gas in pair equilibrium, neglecting electron-screening effects; photons are modelled as an ideal ultra-relativistic gas. The inclusion of neutrinos, muons or other more exotic particles is neglected. Equilibrium with respect to strong and electromagnetic interactions is supposed, while no β equilibrium is assumed, as expected at the onset of core-collapse supernova. The EoS derived by LS follows the works by Lattimer *et al.* [190], with some simplifications in the free energy function (e.g. neutron skin is neglected and a simpler momentum-dependent NN interaction is employed instead of a standard Skyrme parameterization), and by Lattimer and Ravenhall [191]. Nuclei are treated in the "mean nucleus" approximation; however this approximation does not affect very much the thermodynamical properties of the system with respect to considering an entire distribution of nuclei [67]. The nuclei, well below saturation density, are supposed to arrange themselves in a BCC lattice which maximizes the separation of ions; in the Wigner-Seitz approximation, each ion in the neutral-charged cell is surrounded by a gas of free neutrons and protons, α and electrons. Interactions between the outside gas and nuclei are taken into account through particles excluded volume. Nucleons are treated as non-relativistic particles; α as hard spheres of volume $v_\alpha = 24\ \mathrm{fm}^3$ forming an ideal Boltzmann gas. As density increases, nuclei undergo geometrical shape deformations, until they dissolve in favour of homogeneous nuclear matter above saturation density. Phase transition to non-spherical nuclei ("*pasta-phase*") is done by modifying the Coulomb and surface energies of nuclei: a shape function which recovers the correct limit of having nuclei at low density and bubbles at high density and which reproduces the more sophisticated calculations by

Ravenhall *et al.* [276] in the in-between region is introduced to model the transition (see Section 2.8 of Ref. [192]). Phase transition to bulk nuclear matter phase is treated by the inclusion of a Maxwell construction between the two phases.
The configuration of matter and the balance between the different phases is given by the most thermodynamically favourable state, i.e. the one which minimizes the Helmholtz free energy of the system. The minimization procedure for the baryonic component requires the solution of a system of 5 equilibrium equations done by means of a Newton-Raphson method[1]. The lepton and photon contributions are decoupled from the baryon one and added separately.

F.2 LS tables

Our aim is to generate a table of the EoS for densities, temperatures, electron-over-baryon ratio significant for a CCSN simulation. To that extent, we have chosen as boundaries of our tables the following ranges (n_b stands for baryonic density):

$$\begin{aligned} 2 \times 10^{-10}\,\mathrm{fm}^{-3} < \quad & n_b \quad < 1\,\mathrm{fm}^{-3} \\ 100\,\mathrm{keV} < \quad & T \quad < 50\,\mathrm{MeV} \\ 0.04 < \quad & Y_e \quad < 0.5\,. \end{aligned} \tag{F.2}$$

In principle, a different set of independent variables could be employed, e.g.: (n_b, ϵ, Y_e) or: (n_b, s, Y_e); in hydrodynamical codes, for example, the energy is usually used as independent variable (here, ϵ is the energy per baryon). However, temperature is the natural variable for computing the EoS, since the free energy F has to be minimized; thus, writing the EoS with different variables would imply another level of iteration in the EoS code. Therefore one has to look up in the tables in two different steps: first recovering the correct temperature starting from the energy via a root-finding routine, then performing an interpolation to obtain the desired quantities (pressure, entropy, etc.) in terms of (n_b, T, Y_e).

It has been observed [189, 64] that the original LS EoS underestimate the fraction of alpha particles, because of an error in the definition of the α binding energy B_α. This small error has been corrected in the routine, i.e. B_α has to be measured with respect to the neutron mass, as well as the other energies calculated in the routines. We have then replaced the definition of the constant "BALPHA" in the include file "eos_m4c.inc" by: BALPHA = 28.3 + 2 DELTAM, being DELTAM = -1.2935 MeV, the proton-neutron mass difference.

[1]The Newton-Raphson method is a technique to find the solution of an equation (or a system of equations), i.e. it is a root finder. As an example, in one-dimensional case, starting from a first guess x_0 to the exact solution, the new approximated solution of $F(x) = 0$, is obtained as:

$$x_1 = x_0 - \frac{F(x_0)}{F'(x_0)}\,, \tag{F.1}$$

where $F'(x)$ indicates the first derivative with respect to the independent variable x, and so on until convergence is reached.

Moreover, in order to use for the nuclear part of the EoS the LS routines over the full density range, we have extended the code to be able to calculate a solution even at low densities ($\rho_b < 10^8$ g cm^{-3}). To that extent, in the subroutine "EOSLOG" in the "lseos_v2.7.f" file, we have added an if-condition when densities are lower than the minimum value for the Maxwell construction boundary (LNLOW), setting in this case the "I_BD" and "I_BNDY" indices to 1. This allows the EoS routine to find a regime (either with or without nuclei) where to search for the solution.
Nevertheless, at very low density, the LS approach to the nuclear EoS is not very reliable. However, the dominant contribution to the pressure in this region comes from the lepton part, so this should not be a too bad approximation. In a more realistic calculation one should take into account a distribution of nuclei, such as in the recent statistical EoS derived by Hempel and Schaffner-Bielich [157]. Recently, O'Connor and Ott [258] have generated an EoS table in which they employ, for densities $\rho_b > 10^8$ g cm^{-3}, the LS EoS, and, for lower densities, the Timmes EoS [314], under the assumption that the matter is composed by an ideal gas of electrons, photons, neutrons, protons, alpha particles and heavy nuclei with the average A and Z given by the LS at the transition. We have compared our tables [259] to the one made publicly available by O'Connor and Ott at the website: http://stellarcollapse.org. However, even if there is an agreement in the range where the LS routine is employed, it is difficult to make an exact comparison since the nuclear parameters they employ are slightly different from the ones we used.

We are currently working to extend our EoS table both at low and at high density, including an EoS matched with the LS one. We think that in the low density regime, it would not be a so bad approximation considering the matter as an ideal gas of alpha particles, nucleons, leptons, and nuclei whose abundances could be calculated by the Saha equation for thermodynamical equilibrium. At high density, the inclusion of hyperons and pions is foreseen [259, 260].

In constructing the EoS table we have paid attention to the calculation of the speed of sound. Since the LS EoS is derived in the non-relativistic framework, it might happen to have supraluminal points (i.e. points for which the speed of sound becomes greater then the speed of light). This is of course not physical, so for those points we have recalculated the EoS or replace the value of c_s with the one obtained in the case of a Fermi gas (in units of the speed of light) (see e.g. [76]):

$$c_s^2 = \frac{(\hbar c)^2}{3(m_e\, c^2)^2}\, (3\pi\, n_b\, Y_e)^{2/3}\ . \tag{F.3}$$

In generating the tables, we have used the nuclear parameters of the original code, namely:

$$\begin{aligned} n_s &= 0.155\ \mathrm{fm}^{-3} \\ S_v &= 29.3\ \mathrm{MeV} \\ B &= 16.0\ \mathrm{MeV} \\ S_s &= 45.8\ \mathrm{MeV} \\ \sigma_s &= 1.15\ \mathrm{MeV\ fm}^{-3}\ , \end{aligned} \tag{F.4}$$

where n_s is the saturation density of symmetric nuclear matter, S_v is the symmetry energy coefficient of bulk nuclear matter, B is the binding energy of saturated symmetric

nuclear matter, S_s is the surface symmetry energy coefficient and σ_s is the surface tension of symmetric nuclear matter. We have generated tables for the three possible values of the incompressibility modulus: $K = 180$, 220, 375 MeV. Three sets of boundaries and Maxwell construction tables are given together with the routines (files maxxxx.atb and bdxxx.atb, where 'xxx' stands for the value of K: 180, 220, 375). These tables are constructed by the authors in order to easily determine which regime of the EoS has to be employed (with or without nuclei, or perform a Maxwell construction in the coexistence phase). See Section 4.2 in Ref. [192] for further details.
We refer to the original paper [192] for the details on the matter of choice of the parameters employed. Finally, the routines are made under the assumption that the nucleon effective mass is equal to the bare mass: $m^* = m$.

The tables are thought to make them publicly available.
Our EoS table are currently tested in the CoCoNuT[2]code and we hope they will be also successfully included and used in other astrophysical simulations.

To show the improvements made by these corrections to the LS routine, we display the abundances, the entropy and pressure as a function of density, for $K = 180$ MeV, $Y_e = 0.3$ and for different values of temperatures ($T = 1$, 2, 3 MeV) in Fig. F.1. We observe, as expected, that in the original LS routine the abundance of α particles is underestimated; as a consequence, nuclei and free nucleons abundance is higher at given density. The pressure of the system (upper-left panel) is not very much affected by the corrections to the LS routine, since in this density range it is the contribution from leptons which dominates. This plot can be directly compared with Fig. 4 of Ref. [64], where the authors plot the results obtained by the original LS EoS and by their 4-species (neutrons, protons, α and ^{54}Mn as representative heavy nucleus) EoS derived assuming NSE[3]. The results obtained by our tables and by the NSE EoS introduced in the Ref. [64] are shown to be in agreement. Differences have to be noticed, especially for $T = 1$ MeV; this could be explained by the fact that in their 4-species EoS, the authors assume ^{54}Mn to be the representative heavy nucleus, while in LS EoS the mean nucleus varies as a function of density in order to satisfy the energy minimization condition. This affects the relative abundances and the macroscopic properties of the system.
In Fig. F.2 we display, in the left panel, the temperature versus density diagram, for different values of Y_e, and, in the right panel, the mass fractions versus density diagram for different values of temperature and fixing $Y_e = 0.2$. In all plots, we fixed $K = 220$ MeV. This plot can be compared to Fig. 1 in Shen *et al.* [298], showing a good agreement even at low density. However, the results shown in Ref. [298] are obtained in a different framework and for a higher value of the incompressibility, so differences have to be expected. Moreover, the Shen EoS can calculate such boundaries even at high asymmetry

[2]CoCoNuT stands for "Core-Collapse with 'Nu' (= new) Technology". It is a 3D GR hydrodynamical code, whose main aim is to study several astrophysical scenarios where GR can play an important role, such as collapse of rotating cores and isolated neutron stars. This code was mainly developed by H. Dimmelmeier (MPI, Germany), J. Novak (LUTH Meudon, France) and P. Cerdá-Durán (University of Valencia, Spain). One can refer to the CoCoNuT website http://www.mpa-garching.mpg.de/hydro/COCONUT/intro.php for more details and a list of publications.

[3]The authors claim that their simple NSE EoS gives results in excellent agreement in entropy, pressure, and helium mass fraction with respect to a sophisticated NSE solver which takes into account 32 different species of heavy nuclei, for physical conditions encountered in post-shock layers.

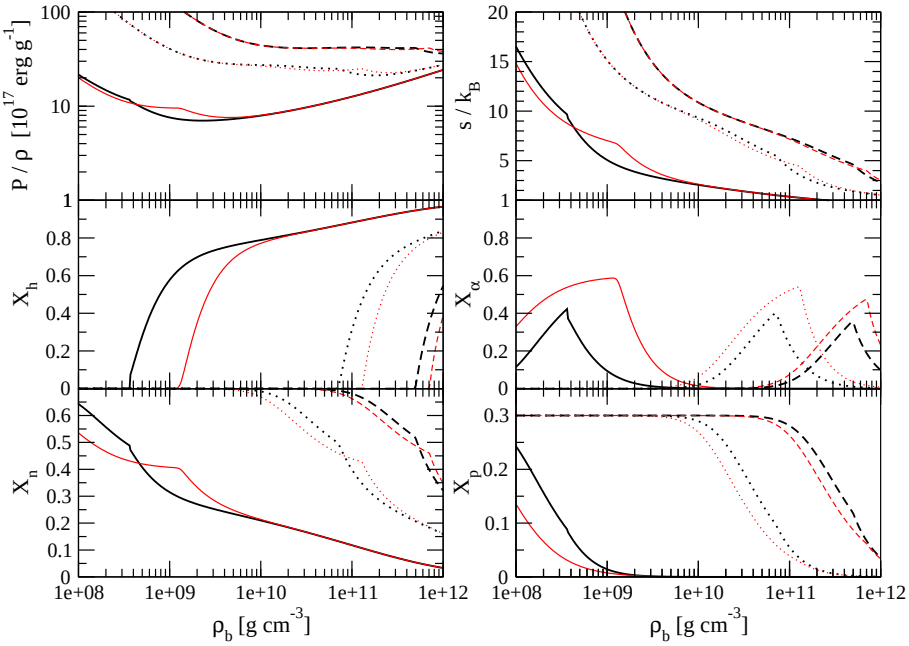

Figure F.1: Pressure, entropy and abundances (nuclei, α particles, free neutrons and protons) as a function of density, for $K = 180$ MeV, $Y_e = 0.3$ and $T = 1$ MeV (solid lines), 2 MeV (dotted lines) and 3 MeV (dashed lines). Thick black lines correspond to the results of the original LS routine, while thin red lines correspond to the values obtained with the modified routine. The main differences come from the correction to the binding energy of α particles.

($Y_e = 0.01$), while in the LS case, the minimum possible value for the electron fraction as input is $Y_e = 0.03$ (here, the case $Y_e = 0.05$ is displayed). The small oscillations appearing in the boundaries (left panels) can be attributed to the searching routine which, at each density, looks for the temperature to satisfy the transition condition: $X_h < 10^{-6}$ for the transition between the nuclear / bulk (with alpha particles) regime, $X_\alpha < 10^{-4}$ for the transition between the bulk (with alpha particles) and the bulk (without alpha) region.

F.3 Thermodynamical derivatives

The LS EoS computes analytically the thermodynamical derivatives with respect to (n_b, T, Y_e). Nevertheless, as already mentioned, often in hydrodynamical codes the energy is the independent variable instead of the temperature; thus derivatives at constant energy (or even at constant entropy) are required.
Indeed, by definition, the speed of sound is given (in units of the speed of light) by (see Appendix B in Ref. [76]):

$$c_s^2 = \left.\frac{\partial P}{\partial e}\right|_s , \tag{F.5}$$

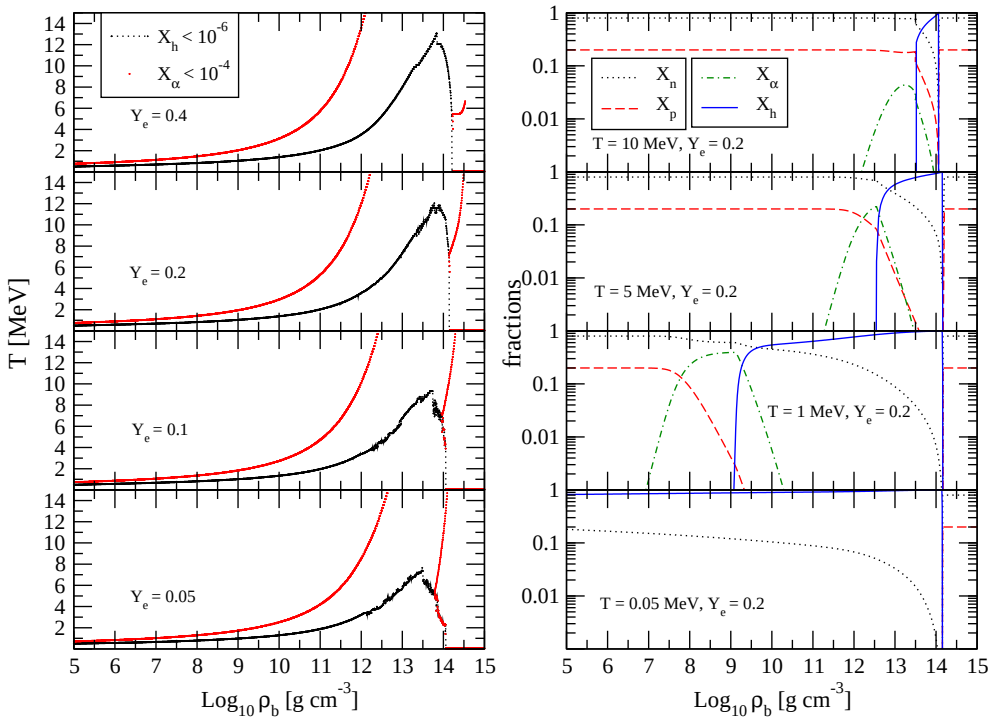

Figure F.2: On the left panels, boundary conditions (temperature versus baryon density, in g cm^{-3}) for different $Y_e = 0.05$, 0.1, 0.2 and 0.4. On the right panels, mass fractions (free neutrons X_n, free protons X_p, alpha particles X_α, and nuclei X_h) as a function of baryon density in g cm^{-3}for different temperatures $T = 0.05$, 1, 5, 10 MeV, and fixed $Y_e = 0.2$.

where $e = n_b(mc^2 + \epsilon)$. Introducing the relativistic enthalpy $h = 1 + \epsilon + \frac{p}{n_b}$, and:

$$\chi = \left.\frac{\partial P}{\partial n_b}\right|_{\epsilon} \tag{F.6}$$

$$\kappa = \left.\frac{\partial P}{\partial \epsilon}\right|_{n_b} , \tag{F.7}$$

the relativistic speed of sound (in units of the speed of light) can be expressed as [285, 118]:

$$h\, c_s^2 = \chi + \frac{P}{n_b^2}\,\kappa\,. \tag{F.8}$$

Moreover, the adiabatic index is defined as:

$$\Gamma = \left.\frac{\partial \ln P}{\partial \ln n_b}\right|_s = \frac{n_b}{P}\left.\frac{\partial P}{\partial n_b}\right|_s . \tag{F.9}$$

In order to obtain these additional derivatives, one can write the following differentials:

a. $P = P(n_b, T, Y_e)$

$$\mathrm{d}P = \left.\frac{\partial P}{\partial n_b}\right|_{T,Y_e} \mathrm{d}n_b + \left.\frac{\partial P}{\partial T}\right|_{n_b,Y_e} \mathrm{d}T + \left.\frac{\partial P}{\partial Y_e}\right|_{n_b,T} \mathrm{d}Y_e \tag{F.10}$$

b. $\epsilon = \epsilon(n_b, T, Y_e)$

$$\mathrm{d}\epsilon = \left.\frac{\partial\epsilon}{\partial n_b}\right|_{T,Y_e} \mathrm{d}n_b + \left.\frac{\partial\epsilon}{\partial T}\right|_{n_b,Y_e} \mathrm{d}T + \left.\frac{\partial\epsilon}{\partial Y_e}\right|_{n_b,T} \mathrm{d}Y_e \tag{F.11}$$

c. $s = s(n_b, T, Y_e)$

$$\mathrm{d}s = \left.\frac{\partial s}{\partial n_b}\right|_{T,Y_e} \mathrm{d}n_b + \left.\frac{\partial s}{\partial T}\right|_{n_b,Y_e} \mathrm{d}T + \left.\frac{\partial s}{\partial Y_e}\right|_{n_b,T} \mathrm{d}Y_e \,. \tag{F.12}$$

From these relations, and noticing that:

$$Y_e := \frac{n_e}{n_b} \Longrightarrow \left.\frac{\partial Y_e}{\partial n_b}\right|_T = -\frac{Y_e}{n_b} \,, \tag{F.13}$$

one can obtain derivatives at constant energy (i.e. imposing $\mathrm{d}\epsilon = 0$) or at constant entropy (i.e. imposing $\mathrm{d}s = 0$):

$$\left.\frac{\partial P}{\partial \epsilon}\right|_{n_b,Y_e} = \left.\frac{\partial P}{\partial T}\right|_{n_b,Y_e} \left(\left.\frac{\partial \epsilon}{\partial T}\right|_{n_b,Y_e}\right)^{-1} \tag{F.14}$$

$$\begin{aligned}
\left.\frac{\partial P}{\partial n_b}\right|_{\epsilon} &= \left.\frac{\partial P}{\partial n_b}\right|_{T,Y_e} + \left.\frac{\partial P}{\partial T}\right|_{n_b,Y_e} \left.\frac{\partial T}{\partial n_b}\right|_{\epsilon,Y_e} + \left.\frac{\partial P}{\partial Y_e}\right|_{n_b,T} \left.\frac{\partial Y_e}{\partial n_b}\right|_{T} \\
&= \left.\frac{\partial P}{\partial n_b}\right|_{T,Y_e} + \left.\frac{\partial P}{\partial T}\right|_{n_b,Y_e} \left(\left.\frac{\partial \epsilon}{\partial T}\right|_{n_b,Y_e}\right)^{-1} \left[-\left.\frac{\partial \epsilon}{\partial n_b}\right|_{T,Y_e} + \frac{Y_e}{n_b} \left.\frac{\partial \epsilon}{\partial Y_e}\right|_{n_b,T}\right] \\
&\quad -\frac{Y_e}{n_b} \left.\frac{\partial P}{\partial Y_e}\right|_{n_b,T}
\end{aligned} \tag{F.15}$$

$$\begin{aligned}
\left.\frac{\partial P}{\partial n_b}\right|_{s} &= \left.\frac{\partial P}{\partial n_b}\right|_{T,Y_e} + \left.\frac{\partial P}{\partial T}\right|_{n_b,Y_e} \left.\frac{\partial T}{\partial n_b}\right|_{s,Y_e} + \left.\frac{\partial P}{\partial Y_e}\right|_{n_b,T} \left.\frac{\partial Y_e}{\partial n_b}\right|_{T} \\
&= \left.\frac{\partial P}{\partial n_b}\right|_{T,Y_e} + \left.\frac{\partial P}{\partial T}\right|_{n_b,Y_e} \left(\left.\frac{\partial s}{\partial T}\right|_{n_b,Y_e}\right)^{-1} \left[-\left.\frac{\partial s}{\partial n_b}\right|_{T,Y_e} + \frac{Y_e}{n_b} \left.\frac{\partial s}{\partial Y_e}\right|_{n_b,T}\right] \\
&\quad -\frac{Y_e}{n_b} \left.\frac{\partial P}{\partial Y_e}\right|_{n_b,T} \,.
\end{aligned} \tag{F.16}$$

F.4 Issues on the LS EoS

During our study on the LS EoS and routine in order to extend it at lower densities, a certain number of instabilities have been noticed, especially in the phase transition region. In particular, difficulties in the convergence of the EoS have been observed [259]. Convergence problems mean both that no solution is found (especially at low temperature and electron fraction [189]), and that the solution found might be discontinuous with respect to adjacent points in density, or temperature, and/or electron fraction (see Fig. F.3).

We think that the latter might be due to the starting point values in the minimization routine. As an example, I show in Fig. F.3 the neutron (X_n), proton (X_p), α (X_α) and nuclei (X_h) mass fraction as a function of baryon density, for the chosen conditions: $Y_e = 0.2$, $T = 10$ MeV and for $K = 220$ MeV. In order to investigate the stability of the routine, after correcting the alpha-particles binding energy, we have run the routine scanning over a very small step in density. Instabilities which result in sudden variations of the mass fractions are observed. Two kinds of problems appear: *(i)* rapid changes of the regime, e.g. around $10^{13.5}$ g cm^{-3}, the "band" in the X_h profile is nothing but a consecutive transition between a phase without nuclei ($X_h = 0$) to a phase with nuclei ($X_h \neq 0$); *(ii)* the discontinuities in the profiles which seem to come from a convergence towards a "bad" point. The first kind of pathology might be due to the fact that a phase coexistence (and not a phase mixing) is considered to model the phase transition. The second one might come from "wrong" starting points which enter as a first guess in the minimization routine.
Especially in SN hydrodynamical codes, if the routine version of the EoS is employed and these points are encountered, they could generate discontinuities and subsequent instabilities in the code. In Fig. F.4 the mass fractions as a function of baryon density, for the chosen conditions: $Y_e = 0.2$, and for $K = 220$ MeV, are shown for different temperatures $T = 1, 2, 5, 8, 10, 12$ MeV; the instabilities are likely to appear especially around the critical temperature after which nuclei are expected to disappear (see lower right panel, where no more nuclei are present). This might be a consequence of the employed technique to determine in which regime the solution of the energy minimization procedure has to be looked for, i.e. the boundary and Maxwell construction conditions are charged before the first EoS call; close to boundaries, the determination of the right regime could be a delicate point.

The construction of a table partially overcomes these problems, since, when looking up the table, an interpolation is done and "critical" points in-between the grid points are usually avoided.

A different approach to treat the phase transition region is a statistical model, where a partition function can be written for the mixed phase. The equilibrium is established by the equivalence of the chemical potentials, but the total pressure is given by the sum of the pressures of the two systems. One might end up in a smooth transition, in contrast with the abrupt change of regime one observes in the LS EoS [143, 272]. This could be clearly a great advantage in simulations, where discontinuities of any kind usually generate numerical instabilities.

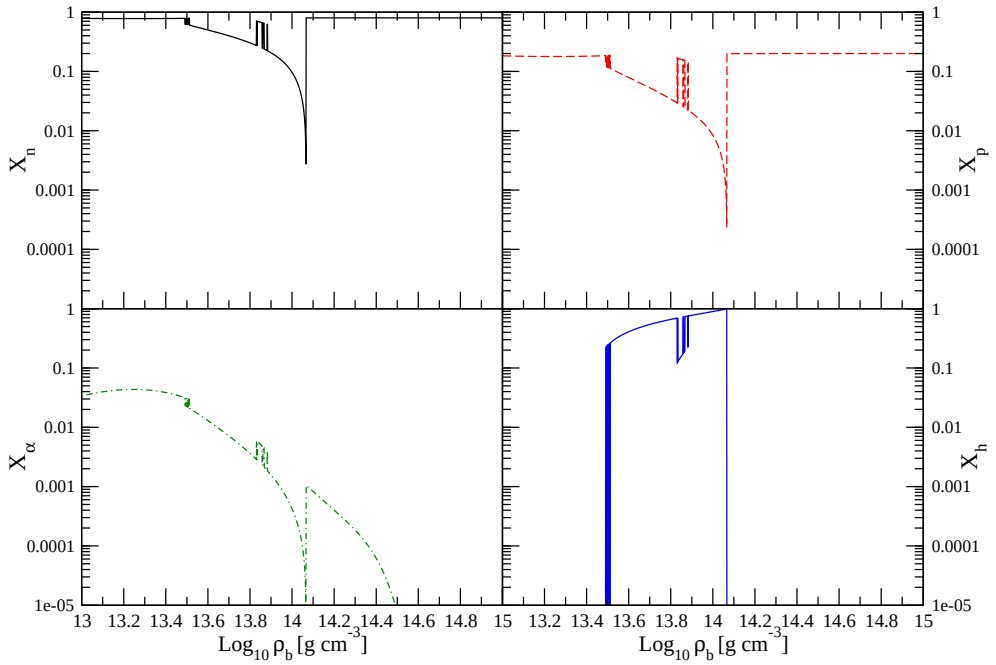

Figure F.3: Neutron (X_n), proton (X_p), α (X_α) and nuclei (X_h) mass fractions as a function of density, at $Y_e = 0.2$, $T = 10$ MeV and for $K = 220$ MeV.

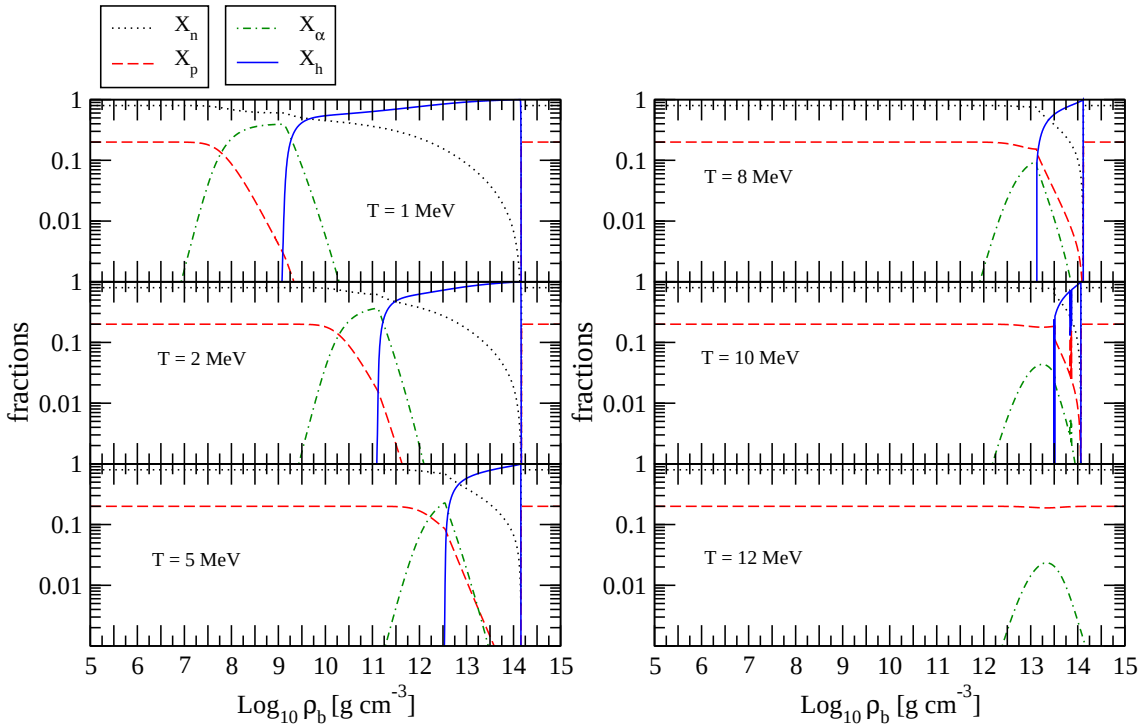

Figure F.4: Mass fractions (neutrons X_n, dotted black lines, protons X_p, dashed red lines, α X_α, dotted-dashed green lines, and nuclei X_h, solid blue lines) as a function of baryon density, for the chosen conditions: $Y_e = 0.2$, and for $K = 220$ MeV, for different temperatures $T = 1, 2, 5, 8, 10, 12$ MeV.

Appendix G

Neutrino processes

As already mentioned in the Introduction, the neutrino processes are very important in the SN event. In our simulations, we take into account only electron neutrinos, since mu and tau neutrino flavours play a central role only in advanced phase of SN mechanism, after the PNS formation, in heating and cooling processes, and not during core-collapse phase. Expressions for most of the rates are given e.g. in Tubbs and Schramm [318], and in Bruenn [56]. I refer to the detailed paper by Bruenn [56], where the "standard theory" by Weinberg and Salam was used to derive the rates, for a complete treatment of the processes listed below, since the expressions given therein are well suited for multi-group calculation and since they are the ones implemented in our simulations. I also refer to the papers by Bruenn [59, 56] and Refs. therein for an extensive treatment of the Multi-Group Flux-Limited Diffusion (MGFLD) scheme, which is adopted in the Newtonian code. In this Appendix I recall the main equations for the MGFLD approximation and neutrino processes, in order to mention explicitly the terms which are implemented in the codes[1]described in Chapters 6 and 7 and make some comments on the difficulties we have encountered in the inclusion of these terms.

Let us denote $r(p_i + p_j \rightarrow p'_k + p'_l)$ the reaction rate for the process: $i + j \rightarrow k + l$, being $p_.$ the initial momentum for the particles i and k, and $p'_.$ the final momentum for the particles k and l; p_i stands for the 4-momentum $p_i = (E_i, \mathbf{p}_i)$; for neutrinos we define its 4-momentum as $q = (w, \mathbf{q})$.

G.1 MGFLDA

The MGFLD Approximation is used to treat neutrino transport in the Newtonian code developed by P. Blottiau and Ph. Mellor. For sake of completeness, I report here the main expressions, valid in spherical symmetry, Newtonian dynamics and in the comoving frame. Details can be found in [59, 56].

One starts from the Boltzmann transport equation (BTE):

$$D[f] = \mathcal{C}[f] \ , \tag{G.1}$$

[1]An extensive treatment of the radiation hydrodynamics is given e.g. in Mihalas and Mihalas textbook [244] and of the other neutrino processes that should be considered in a supernova simulation is given e.g. in Bruenn [56] and Mezzacappa and Bruenn [240, 242].

where $D[\cdot]$ is the Liouville operator which contains the partial derivatives of the distribution function $f = f(t, r, \mu, \omega)$ along the trajectories of particles propagation (being r the distance of the considered fluid element from the center of the star in Lagrangian coordinates, μ the cosine angle between the propagation direction of the neutrino and the outward radial direction, ω the neutrino energy), which is defined in such a way that the mean number of neutrino at time t, at position r (within a volume $\mathrm{d}V$ and a solid angle $\mathrm{d}\Omega$) and with energy between ω and $\omega + \mathrm{d}\omega$ is given by: $f\mathrm{d}V\mathrm{d}\Omega\omega^2\mathrm{d}\omega/(2\pi\hbar c)^3$. In spherical symmetry, neglecting relativistic effects, this term reads:

$$D[f] = \frac{1}{c}\frac{\partial f}{\partial t} + \frac{\mu}{r^2}\frac{\partial (r^2 f)}{\partial r} + \frac{1}{r}\frac{\partial [(1-\mu^2) f]}{\partial \mu} \; . \tag{G.2}$$

Terms of the order of v/c are given by [56]:

$$\begin{aligned} -\frac{f}{c}\frac{\partial \log \rho}{\partial t} \quad - \quad & \frac{1}{c}\left[\left(\frac{\partial \log \rho}{\partial t} + 3\frac{v}{r}\right)\mu^2 - \frac{v}{r}\right]\left[1 - \frac{1}{\omega^3}\frac{\partial(\omega^4 f)}{\partial \omega}\right] \\ & + \frac{\partial}{\partial \mu}\left\{\left[\frac{1}{c}\left(\frac{\partial \log \rho}{\partial t} + 3\frac{v}{r}\right)\mu(1-\mu^2)\right] f\right\} \; . \end{aligned} \tag{G.3}$$

The right-hand side of Eq. (G.1), $\mathcal{C}[f]$, is the collision integral, which contains all of the informations about the changes in f due to reactions (absorption, emission), and collisions. In principle the collision integral should then take into account all the possible mechanisms of interaction of neutrinos (of all types) with matter, such as, in the specific case, electron capture (on free protons and nuclei, labelled as "AE"), scattering (labelled "S", which includes elastic scattering on nuclei and nucleons, labelled "IS", and inelastic scattering off electrons, labelled "NES"), pair production (labelled "TP"):

$$\mathcal{C}[f] = B_{AE}[f] + B_S[f] + B_{TP}[f] \; , \tag{G.4}$$

where the B_i terms (omitting the r- and t-label dependence in the distribution function, and keeping only the ω- and μ-label dependence) are given, in cm^{-1}, by:

$$B_{AE}[f] = j(\omega)\,[1 - f(\omega, \mu)] - \frac{1}{\lambda^a(\omega)}\, f(\omega, \mu) \tag{G.5}$$

$$\begin{aligned} B_S[f] \quad = \quad & \frac{1}{c(2\pi\hbar c)^3}[1 - f(\omega,\mu)] \int_0^\infty \omega'^2 \mathrm{d}\omega' \int_{-1}^1 \mathrm{d}\mu' f(\omega', \mu') \int_0^{2\pi} \mathrm{d}\phi R^{in}(\omega, \omega', \cos\theta) \\ - \quad & \frac{1}{c(2\pi\hbar c)^3} f(\omega,\mu) \int_0^\infty \omega'^2 \mathrm{d}\omega' \int_{-1}^1 \mathrm{d}\mu' [1 - f(\omega', \mu')] \int_0^{2\pi} \mathrm{d}\phi R^{out}(\omega, \omega', \cos\theta) \end{aligned} \tag{G.6}$$

$$\begin{aligned} B_{TP}[f] \quad = \quad & \frac{1}{c(2\pi\hbar c)^3}[1 - f(\omega,\mu)] \int_0^\infty \omega'^2 \mathrm{d}\omega' \int_{-1}^1 \mathrm{d}\mu' \int_0^{2\pi} \mathrm{d}\phi R^{in}_{TP}(\omega, \omega', \cos\theta)[1 - \bar{f}(\omega', \mu')] \\ - \quad & \frac{1}{c(2\pi\hbar c)^3} f(\omega,\mu) \int_0^\infty \omega'^2 \mathrm{d}\omega' \int_{-1}^1 \mathrm{d}\mu' \int_0^{2\pi} \mathrm{d}\phi R^{out}_{TP}(\omega, \omega', \cos\theta) \bar{f}(\omega', \mu') \; , \end{aligned} \tag{G.7}$$

where (see next Section) $j(\omega)$ is the neutrino emissivity, $\lambda^a(\omega)$ is the neutrino absorption mean free path, R^{in} (R^{out}) is related to the in(out)-coming scattering function (the integrals being proportional to the amount of particles which, from an initial configuration ω', μ' (ω, μ), goes into a final configuration ω, μ (ω', μ')), and R_{TP} is related to the pair

production function. θ and ϕ are the the angle and azimuthal angle of the incoming (or outcoming) neutrinos, which can be expressed in terms of μ as:

$$\cos\theta = \mu\mu' + [(1-\mu^2)(1-\mu'^2)]^{1/2}\cos(\phi-\phi') \; . \tag{G.8}$$

Similar notations are used for the pair production term, where $\bar{f}$ stands for the distribution function of the antiparticles.
In the scattering contribution $B_S[f]$ both an isoenergetic component (elastic scattering off nucleons and nuclei, labelled as "IS") and an inelastic component (scattering off electrons, labelled as "NES") are present. Both contributions produce an energy and angular redistribution of neutrinos; however, in the IS case, since nucleons and nuclei can be considered as non-relativistic particles and are much more massive than neutrinos and thus in collision processes can be assumed as a wall with respect to neutrinos, one can take $\omega' = \omega$, i.e. the IS changes the propagation direction of the neutrinos but not their energy. Therefore one has:

$$B_S[f] = B_{IS}[f] + B_{NES}[f] \tag{G.9}$$

$$B_{IS}[f] = \frac{1}{c(2\pi\hbar c)^3}\omega^2 \int_{-1}^{1} \mathrm{d}\mu' \int_0^{2\pi} \mathrm{d}\phi R'_{IS}(\omega,\omega,\cos\theta)[f(\omega,\mu') - f(\omega,\mu)] \tag{G.10}$$

$$\begin{aligned} B_{NES}[f] &= \frac{1}{c(2\pi\hbar c)^3}[1-f(\omega,\mu)] \int_0^{\infty} \omega'^2 \mathrm{d}\omega' \int_{-1}^{1} \mathrm{d}\mu' \int_0^{2\pi} \mathrm{d}\phi R^{in}_{NES}(\omega,\omega',\cos\theta) f(\omega',\mu') \\ &- \frac{1}{c(2\pi\hbar c)^3} f(\omega,\mu) \int_0^{\infty} \omega'^2 \mathrm{d}\omega' \int_{-1}^{1} \mathrm{d}\mu' \\ &\qquad \times \int_0^{2\pi} \mathrm{d}\phi R^{out}_{NES}(\omega,\omega',\cos\theta)[1-f(\omega',\mu')] \; , \end{aligned} \tag{G.11}$$

where: $R'_{IS}(\omega,\omega',\cos\theta)\delta(\omega-\omega') = R^{in/out}_{IS}(\omega,\omega',\cos\theta)$.
I will consider in the following only the processes implemented in the code, i.e. the electron capture (emission and absorption) and the scattering terms, while I will neglect the pair production contribution.

The MGFLDA is then obtained by expanding the neutrino distribution function in a Legendre series[2], and keeping only the first two terms:

$$f(t,r,\mu,\omega) = \psi^{(0)}(t,r,\omega) + \mu\psi^{(1)}(t,r,\omega) \; , \tag{G.15}$$

[2]The Legendre functions are solutions of the differential equation (see e.g. [1]):

$$\frac{\mathrm{d}}{\mathrm{d}x}\left[(1-x^2)\frac{\mathrm{d}}{\mathrm{d}x}P_n(x)\right] + n(n+1)P_n(x) = 0 \; , \tag{G.12}$$

where $P_n(x)$ are polynomials which can be expressed in a power series as:

$$P_n(x) = \frac{1}{2^n n!}\frac{\mathrm{d}^n}{\mathrm{d}x^n}\left[(x^2-1)^n\right] \; , \tag{G.13}$$

and satisfy the orthogonality relation:

$$\int_{-1}^{1} P_m(x)\, P_n(x)\mathrm{d}x = \frac{2}{2n+1}\delta_{mn} \; . \tag{G.14}$$

so that (I omit the t and r dependence):

$$\psi^{(0)}(\omega) = \frac{1}{2}\int_{-1}^{1} \mathrm{d}\mu f(\mu,\omega) \tag{G.16}$$

$$\psi^{(1)}(\omega) = \frac{3}{2}\int_{-1}^{1} \mathrm{d}\mu\mu f(\mu,\omega)\ , \tag{G.17}$$

with the assumption:

$$\frac{\partial\psi^{(1)}(\omega)}{\partial t} = 0\ . \tag{G.18}$$

The first term $\psi^{(0)}(\omega)$ is related to the energy density of neutrinos, while the second term $\psi^{(1)}(\omega)$ is related to the neutrino flux:

$$\epsilon(\omega) = \int_{-1}^{1} \mathrm{d}\mu f(\mu,\omega) = 2\,\psi^{(0)}(\omega) \tag{G.19}$$

$$F(\omega) = \int_{-1}^{1} \mathrm{d}\mu\mu f(\mu,\omega) = \frac{2}{3}\,\psi^{(1)}(\omega)\ . \tag{G.20}$$

Neglecting high order terms in the expansion Eq. (G.15) remains valid in f is not far from isotropy, which is the case when the mean free path is smaller with respect to the typical length scale of the problem [59]. In order to make the assumption Eq. (G.15) applicable also in regions where the mean free path become large, a flux limiter can be introduced in such a way to catch both neutrino-opaque and neutrino-transparent regime and prevent the velocity of neutrinos to become greater than speed of light. Bruenn *et al.* [59, 56] proposed the following prescription for the flux limiter:

$$\Lambda^{(t)}(\omega) = \frac{3\lambda^{(t)}(\omega)}{3+\lambda^{(t)}(\omega)\frac{|\nabla\psi^{(0)}(\omega)|}{\psi^{(0)}(\omega)}}\ , \tag{G.21}$$

where $\lambda^{(t)}(\omega)$ is related to the absorption/emission and scattering opacities. The above expression slightly differs from the one we adopted [48, 237] (cf. Eq. (6.18)).
In Refs. [59, 56], a diffusion-like equation for $\psi^{(0)}(\omega)$ has been derived by using the expression for f in Eq. (G.15), inserting it in the Boltzmann equation, integrating over μ (applying, respectively, $\frac{1}{2}\int_{-1}^{1}\mathrm{d}\mu$ and $\frac{3}{2}\int_{-1}^{1}\mu\mathrm{d}\mu$), neglecting $\mathcal{O}(v^2/c^2)$ terms (cf. Eq. (A27) in

The first-orders polynomials are:

$$P_0(x) = 1$$
$$P_1(x) = x$$
$$P_2(x) = \frac{1}{2}\left(3x^2-1\right).$$

Here, Legendre polynomials are used as coefficient in the expansion, identifying: $x \equiv \mu$, and only P_0 and P_1 have been retained.

[56], which I report here for completeness and where I have omitted t and r dependence):

$$\begin{aligned}\frac{1}{c}\frac{\partial}{\partial t}\psi^{(0)}(\omega) &- \frac{1}{3r^2}\frac{\mathrm{d}}{\mathrm{d}r}\left\{r^2\Lambda(t)(\omega)\left[\frac{\partial}{\partial r}\psi^{(0)}(\omega) - A^{(1)}(\omega)\psi^{(0)}(\omega) - C^{(1)}(\omega)\right]\right\} \\ &+ \frac{1}{3c}\frac{\partial \ln\rho}{\partial t}\left(\omega\frac{\partial}{\partial\omega}\psi^{(0)}(\omega)\right) = j(\omega) + C^{(0)}(\omega) + B^{(0)}(\omega)C^{(1)}(\omega)\Lambda(t)(\omega) \\ &+ \left(-j(\omega) - \frac{1}{\lambda^{(a)}(\omega)} + A^{(0)}(\omega) + B^{(0)}(\omega)A^{(1)}(\omega)\Lambda(t)(\omega)\right)\psi^{(0)} \\ &+ \left(-B^{(0)}(\omega)\Lambda(t)(\omega)\right)\frac{\partial}{\partial r}\psi^{(0)}\,, \end{aligned} \tag{G.22}$$

where the A, B, and C terms contain the "IS", "NES" and "TP" correspondent Legendre coefficients (see next Section).

G.2 Neutrino processes

G.2.1 Electron capture on free protons

The electron capture on free protons reads (in equilibrium):

$$e^- + p \rightleftarrows n + \nu_e\,. \tag{G.23}$$

The neutrino emissivity $j(\omega)$ (associated to the reaction "$\rightarrow$") and the absorptivity $1/\lambda^{(a)}(\omega)$ (associated to the reaction "$\leftarrow$") are related to the reaction rate as:

$$\begin{aligned} j(\omega) &= \int\frac{\mathrm{d}^3p_p}{(2\pi)^3}\int\frac{\mathrm{d}^3p_n}{(2\pi)^3}\int\frac{\mathrm{d}^3p_e}{(2\pi)^3}\,2f_p(E_p)\,[1-f_n(E_n)]\,2f_e(E_e) \\ &\qquad \times r(p_p + p_e \rightarrow p_n + q) \end{aligned} \tag{G.24}$$

$$\begin{aligned} \frac{1}{\lambda^{(a)}(\omega)} &= \int\frac{\mathrm{d}^3p_p}{(2\pi)^3}\int\frac{\mathrm{d}^3p_n}{(2\pi)^3}\int\frac{\mathrm{d}^3p_e}{(2\pi)^3}\,[1-f_p(E_p)]\,2f_n(E_n)\,[1-f_e(E_e)] \\ &\qquad \times r(p_n + q \rightarrow p_p + p_e)\,, \end{aligned} \tag{G.25}$$

where f_i are the Fermi-Dirac distributions of the particle i and the reaction rate of the inverse reaction is related to the reaction rate of the direct process, according to time-reversal symmetry properties, as:

$$(2s_i+1)(2s_j+1)\,r(p_i+p_j \rightarrow p'_k+p'_l) = (2s_k+1)(2s_l+1)\,r(p'_k+p'_l \rightarrow p_i+p_j)\,, \tag{G.26}$$

being s_i the spin of the particle i ($s=0$ for neutrinos).
With the following approximations: $|\mathbf{p}_n| \ll m_n c$ and $|\mathbf{p}_p| \ll m_p c$ (i.e. considering nucleons as non-relativistic particles), and ignoring the momentum transferred to the nucleon,

Bruenn gives the following expressions for $j(\omega)$ and $1/\lambda^{(a)}(\omega)$ (in cm^{-1})[3]:

$$j(\omega) = \frac{G_F^2}{(\hbar c)^4\pi}\,\eta_{pn}\,(g_V^2+3g_A^2)\,f_e(\omega+Q)\,(\omega+Q)^2 \times\left[1-\frac{(m_ec^2)^2}{(\omega+Q)^2}\right]^{1/2} \tag{G.27}$$

$$\frac{1}{\lambda^{(a)}(\omega)} = \frac{G_F^2}{(\hbar c)^4\pi}\,\eta_{np}\,(g_V^2+3g_A^2)\,[1-f_e(\omega+Q)]\,(\omega+Q)^2 \times\left[1-\frac{(m_ec^2)^2}{(\omega+Q)^2}\right]^{1/2}\,, \tag{G.28}$$

where G_F is the Fermi coupling constant $\frac{G_F^2}{(\hbar c)^4} = 5.18\times10^{-44}$ MeV^{-2} cm^2, $g_A = 1.23$ and $g_V = 1$ are the axial and vectorial coupling constants, $Q = 1.293$ MeV is the mass difference between neutron and proton, and

$$\eta_{np} = \int \frac{\mathrm{d}^3p_p}{(2\pi)^3}\,2f_n(E)\,[1-f_p(E)] \simeq \frac{n_b(X_p-X_n)}{e^{(\mu_p-\mu_n)/kT}-1}\,, \tag{G.29}$$

where it has been assumed $E = E_n = E_p = p^2/2m$ ($m = m_n = m_p$). η_{pn} is obtained by the replacement $n \leftrightarrow p$ in the above equation. η_{np} (η_{pn}) takes into account the nucleon final state blocking; the non degenerate limit of the term in Eq. (G.29) gives n_bX_n (n_bX_p), the number density of neutrons (protons).

Implementation

These processes are implemented in both the Newtonian and the Relativistic code. The implementation is done according to Bruenn paper [56], introducing directly the expressions written above. All the informations about the composition and the chemical potentials are given by the EoS. However, a special care must be taken in implementing the expression in Eq. (G.29). In fact, in Eq. (G.29), it has been assumed that $E = E_n = E_p = p^2/2m$, and $m = m_n = m_p$. In regions where $n_p > n_n$ and $\mu_n < \mu_p$, and where the fraction of free nucleons is small but not zero, the implementation of the last expression in Eq. (C14) in [56] can generate numerical problems and non-physical values of the blocking factors can result[4][259, 265]. Moreover, the assumption of equal neutron and proton mass is not necessarily made in all EoS calculations[5], so an inconsistency between the EoS and the capture rate calculations can arise.

In principle one must compute the full integral [265], but different approximations can be

[3]Starting from Eq. (C12) in Bruenn [56], one obtains the expression in Eq. (C13) in Bruenn [56] only applying the approximations written above after integrating over the angles, and performing the integration without taking into account $\delta(q+\mathbf{p}_n-\mathbf{p}_e-\mathbf{p}_p)$ factor resulting as a consequence of momentum conservation; otherwise, the last term in Eq. (C12) proportional to $p_e\cdot q$ gives an extra contribution which accounts for a quantitative difference of a few percent [259]. Moreover, the j and $1/\lambda$ should also contain a $|V_{ud}|^2$ factor (being $V_{ud} = 0.97425$) coming from the CKM matrix element [259].

[4]I also have verified that for some values of density and temperature encountered during the simulation, it can happen: $n_n < \eta_{np}$ and $n_p < \eta_{pn}$, which is in contrast with Fig. 34 in Bruenn [56].

[5]E.g., in the Shen EoS [297], an effective mass (which is different from the bare mass) in the uniform matter regime is calculated, and the recent tables based on the LS EoS work with arbitrary effective masses [189].

adopted. In a very first approximation, the non degenerate limit of the expression for η_{np} and η_{pn} can be taken, since the ratio $\frac{\eta_{np}}{n_b X_n}$ and $\frac{\eta_{pn}}{n_b X_p}$ is expected to be significantly different from 1 only at very high densities (Fig. 34 in Bruenn [56]), when the capture rates are no longer important, since β equilibrium for the matter is expected, and, as a consequence, a precise calculation of the blocking factor is no longer crucial.
Another choice is to compute the chemical potentials from the known neutron and proton densities (as given by the EoS), assuming nucleons as non-relativistic non-interacting particles (cf. e.g. Eq. (E.3)) [273].
Finally, it could be also shown that, substituting the expressions for $j(\omega)$ and $1/\lambda^{(a)}(\omega)$ in the capture rate Eq. (G.5) , with $1/\lambda^{(a)}(\omega) = \exp\{[\omega - (\mu_p - \mu_n + \mu_e)]\} j(\omega)$ (Eq. (C7) in [56]), and using the expression for η_{np} Eq. (G.29), β equilibrium is not satisfied [259].

- Newtonian code
  The electron capture on free nucleons is implemented *à la Bruenn* in the Newtonian code. Nucleons are assumed to be non-degenerate, i.e. the non-degenerate limit is taken for the blocking factors $\eta_{np(pn)}$; this is a good approximation for the case of the BBAL EoS, which assumes a Maxwell-Boltzmann distribution for free particles.

- Relativistic code
  This term is included in the Relativistic code, with the same formalism. Problems with the blocking factor term has been as a first step overcome by taking the non-degenerate limit for low densities ($\rho \lesssim 10^{10}$ g cm^{-3}).

G.2.2 Electron capture on nuclei

The electron capture on nuclei reads (in equilibrium):

$$e^- + (Z, A) \rightleftarrows (Z - 1, A) + \nu_e \, . \tag{G.30}$$

The main difference with respect to the previous case is that now one must in principle know the detailed structure of the transitions for nuclei far from the valley of β-stability encountered in CCSN (cf. also the Introduction, Chapter 1). The derivation by Bruenn follows the work by Fuller [126] and FFN [128], which consider that the electron capture on nuclei is dominated by the $1f_{7/2} \rightarrow 1f_{5/2}$ GT resonance and estimated the related matrix element for the transition as: $\frac{2}{7} N_p N_h$, being N_p is the number of protons in the $1f_{7/2}$ shell and N_h the number of neutron holes in the $1f_{5/2}$ shell. The estimate given for N_p and N_h is:

$$N_p(Z) = \begin{cases} 0 & Z \leq 20 \\ Z - 20 & 20 < Z \leq 28 \\ 8 & Z > 28 \end{cases} \, , \tag{G.31}$$

$$N_h(N) = \begin{cases} 6 & N \leq 34 \\ 40 - N & 34 < N \leq 40 \\ 0 & N > 40 \end{cases} \, . \tag{G.32}$$

The neutrino emissivity $j(\omega)$ (associated to the reaction "$\rightarrow$") and the absorptivity $1/\lambda^{(a)}(\omega)$ (associated to the reaction "$\leftarrow$") are thus given, in the approximations of non-relativistic

nucleons and ignoring the momentum transferred to the nucleon (in cm^{-1}), by [56]:

$$j(\omega) = \frac{G_F^2}{(\hbar c)^4\pi} n_b \frac{X_h}{A}\, g_A^2\, \frac{2}{7} N_p(Z) N_h(N)\, f_e(\omega + Q')\, (\omega + Q')^2 \times \left[1 - \frac{(m_e c^2)^2}{(\omega + Q')^2}\right]^{1/2} \tag{G.33}$$

$$\frac{1}{\lambda^{(a)}(\omega)} = \frac{G_F^2}{(\hbar c)^4\pi} n_b \frac{X_h}{A}\, e^{(\mu_n - \mu_p - Q')/k_B T}\, g_A^2\, \frac{2}{7} N_p(Z) N_h(N)\, [1 - f_e(\omega + Q')]\, (\omega + Q')^2 \times \left[1 - \frac{(m_e c^2)^2}{(\omega + Q')^2}\right]^{1/2} , \tag{G.34}$$

where $n_b X_h/A$ is the number density of the parent nucleus species, $n_b X_h \exp((\mu_n - \mu_p - Q')/k_B T)/A$ is the number density of excited $(Z-1, A)$ nuclei, and the Q-value for the reaction now is the difference in mass between the parent and the daughter nucleus in the excited state, which can be approximated as [126, 56]:

$$Q' = m^*_{Z-1,A} - m_{Z,A} = m_{Z-1,A} - m_{Z,A} + \Delta_N \approx \mu_n - \mu_p + \Delta_N \, . \tag{G.35}$$

In the Eq. (G.35), Δ_N is the energy of the neutron $1f_{5/2}$ state above the ground state and whose value has been estimated to be ~ 3 MeV [34, 128] [6], and A is the mean nucleus determined by the EoS. Actually, as pointed out e.g. in Ref. [232], one should take into account a detailed distribution of nuclei since it is not always true that the energetically favoured "mean nucleus" is also the one for which the capture is more probable. Moreover, Δ_N is assumed to be the same for all encountered nuclei. However, having tables with the mass differences and cross sections for all nuclei in the medium is not only hard but it would require additional computational time to the simulation.

Finally, final state blocking of nuclei can be ignored since nuclei are clearly non-degenerate.

Considering both the electron capture on free protons and nuclei, the B_{AE} contribution to the collision integral can be written as:

$$B_{AE} = j(\omega)[1 - f(\omega, \mu)] - \frac{1}{\lambda^{(a)}(\omega)} f(\omega, \mu) \, , \tag{G.36}$$

where $j(\omega)$ and $1/\lambda^{(a)}(\omega)$ account for the two processes (i.e. $j(\omega) = j_{ec-nucleons}(\omega) + j_{ec-nuclei}(\omega)$, and the same for $1/\lambda^{(a)}(\omega)$). When neutrino trapping holds, the forward and backward reaction equilibrate each other, so that the total contribution of B_{AE} should go to zero. In this case [240]:

$$j(\omega)[1 - f^{eq}(\omega, \mu)] - \frac{1}{\lambda^{(a)}(\omega)} f^{eq}(\omega, \mu) = 0 \, , \tag{G.37}$$

and therefore:

$$j(\omega) = \left(j(\omega) + \frac{1}{\lambda^{(a)}(\omega)}\right) f^{eq}(\omega, \mu) \, , \tag{G.38}$$

[6] In the fit performed by Langanke *et al.* [187] based on the Q-dependent expression for the capture rate (cf. Eq. (1.29) and Ref. [130]), the corresponding Δ_N was taken to be 2.5 MeV.

where f^{eq} stands for the neutrino distribution function at equilibrium, i.e. the one calculated at β equilibrium:

$$f^{eq} = \frac{1}{1 + e^{\frac{\epsilon_\nu - \mu_\nu^{eq}}{k_B T}}} \,, \tag{G.39}$$

where the neutrino chemical potential is: $\mu_\nu \equiv \mu_\nu^{eq} = \mu_p + \mu_e - \mu_n$. In the trapping regime we can thus write:

$$B_{AE} = \left(j(\omega) + \frac{1}{\lambda^{(a)}(\omega)} \right) \left(f^{eq}(\omega, \mu) - f(\omega, \mu) \right) , \tag{G.40}$$

where it is clear that f is driven towards the equilibrium by this source term.

Implementation

These processes are implemented in both the Newtonian and the Relativistic code. The implementation is done according to Bruenn paper [56], by means of the expressions written above. As in the previous case, the informations about the composition and the chemical potentials are given by the EoS. In order to make a parameter study varying the capture rates without employing a (not yet available to us) table with the capture rates computed over a nuclear network, the $N_p N_h$ factor has been changed "by hand", as in the paper by Hix *et al.* [166].
In the Relativistic code, the expression (G.40) was employed since the beginning of the simulation. In the "standard" trapping condition, the expression (G.40) is employed after a trapping density ρ_{tr}, while only the emission term $j(\omega)$ is taken into account for $\rho < \rho_{tr}$.

G.2.3 Neutrino-nucleon scattering

The neutrino-nucleon scattering proceeds according to the reaction (which is identical for all neutrino flavours, since it is mediated by the neutral current) [56]:

$$\nu_i + N \rightleftarrows \nu_i + N \,, \tag{G.41}$$

where N stands for the nucleon (neutron or proton). The scattering production and absorption kernel $R_{IS}^{in/out}$ are related to the scattering rate by [56]:

$$R_{IS}^{in} = \int \frac{\mathrm{d}^3 p_t}{(2\pi)^3} \int \frac{\mathrm{d}^3 p_{t'}}{(2\pi)^3} \left[1 - f_t(E_t)\right] 2 f_t(E_t') \, r(p_t' + q' \rightarrow p_t + q) \tag{G.42}$$

$$R_{IS}^{out} = \int \frac{\mathrm{d}^3 p_t}{(2\pi)^3} \int \frac{\mathrm{d}^3 p_{t'}}{(2\pi)^3} \, 2 f_t(E_t) \, \left[1 - f_t(E_t')\right] r(p_t + q \rightarrow p_t' + q') \,, \tag{G.43}$$

where, again, f_t is the distribution function, p_t and p_t' refer to the momentum of the target particles, q and q' refer to the momentum of the "in" and "out" beam neutrino. One can also relate the "in" and "out" scattering kernel by means of the Eq. (G.26) (detailed balance) as:

$$R_{IS}^{in}(\omega, \omega', \cos\theta) = e^{\frac{E_t - E_t'}{k_B T}} \, R_{IS}^{out}(\omega, \omega', \cos\theta) \,. \tag{G.44}$$

Assuming the nucleons as non-relativistic particles and neglecting nucleon recoil, the elastic scattering kernel of neutrinos off free nucleons is given by [56]:

$$R_{IS,N}(\omega,\theta) = \frac{2\pi G_F^2}{h}\eta_{NN}\left\{\left[(h_V^N)^2+3(h_A^N)^2\right]+\cos\theta\left[(h_V^N)^2-(h_A^N)^2\right]\right\}\delta(\omega-\omega')\,, \tag{G.45}$$

with η_{NN} the factor which takes into account the final nucleon state blocking:

$$\eta_{NN} = \int \frac{2\mathrm{d}^3 p_N}{(2\pi)^3} f_N(E_N)[1-f_N(E_N)] \rightarrow \left\{ \begin{array}{ll} n_b X_n & \text{nondegenerate N} \\ \frac{3}{2}k_B T\frac{n_b X_n}{\mu_N} & \text{degenerate N} \end{array}\right. \tag{G.46}$$

The nucleon form factors for neutral current h_V^N, h_A^N assume the following values:

$$\begin{aligned} h_V^p &= \frac{1}{2} - 2\sin^2\theta_W \\ h_A^p &= \frac{1}{2}g_A \\ h_V^n &= -\frac{1}{2} \\ h_A^n &= -\frac{1}{2}g_A\,, \end{aligned} \tag{G.47}$$

and $\sin^2\theta_W = 0.25$.

If one also expands the scattering kernel $R_{IS,N}(\omega,\theta)$:

$$R_{IS,N}(\omega,\omega,\theta) = \frac{1}{2}\Phi_{IS,N}^{(0)}(\omega) + \frac{3}{2}\Phi_{IS,N}^{(1)}(\omega)\cos\theta\,, \tag{G.48}$$

the Legendre coefficients $\Phi_{l,IS}$ are given by Bruenn, in MeV cm^3 s^{-1}:

$$\Phi_{IS,N}^{(0)}(\omega) = 4\pi\frac{G_F^2}{h}\eta_{NN}\left[(h_V^N)^2+3(h_A^N)^2\right] \tag{G.49}$$

$$\Phi_{IS,N}^{(1)}(\omega) = \frac{4}{3}\pi\frac{G_F^2}{h}\eta_{NN}\left[(h_V^N)^2-(h_A^N)^2\right]\,. \tag{G.50}$$

The A, B, and C terms appearing in the diffusion equation and related to the Φ coefficients are given in Bruenn's paper.

Implementation

This process has been implemented by Ph. Mellor in the Newtonian code.
In the Newtonian simulation, rather than implementing neutrino-nucleon scattering expanding the scattering kernel in Legendre coefficients, the following expression for the scattering (off neutrons and protons) mean free path (in cm) has been adopted [237, 41]:

$$\lambda_{IS,N} = 10^{20}\,\rho^{-1}\,\omega^{-2}\,\left[X_n+\frac{5}{6}X_p\right]^{-1}\,. \tag{G.51}$$

G.2.4 Coherent scattering on nuclei

The coherent scattering on nuclei proceeds through the reaction (valid for all neutrino types):

$$\nu_i + (A, Z) \rightleftarrows \nu_i + (A, Z) \; . \tag{G.52}$$

Among all the processes involved, coherent scattering off nuclei is the most important source of opacity for neutrinos in the outer layers of the protoneutron star and during stellar core collapse. Moreover, since the spectrum of the neutrinos is mainly determined by the position of the neutrinosphere which is located in the region where the coherent scattering is dominant, accurate calculations of the cross sections could affect significantly the predicted neutrino signal. Assuming the scattering being isoenergetic, and the nuclei as non-degenerate particles with a Gaussian nuclear wave function ($b = \frac{1}{6} < r^2 >$ [318]), the scattering kernel is related to the reaction rate as in the previous Section, and is given by [56]:

$$\begin{aligned} R_{IS,A} &= 2\pi \frac{G_F^2}{h} n_b \frac{X_h}{A} A^2 \left(C_{V0} + \frac{1}{2} \frac{N-Z}{A} C_{V1} \right)^2 \\ &\quad \times (1 - \cos\theta) e^{-4b\omega^2(1-\cos\theta)} \delta(\omega - \omega') \; , \end{aligned} \tag{G.53}$$

where the subscript "0" ("1") in the constants $C_{V0/1}$ stands for the isoscalar (isovector) component:

$$C_{V0} = \frac{1}{2}(h_V^p + h_V^n) \tag{G.54}$$

$$C_{V1} = (h_V^p - h_V^n) \; . \tag{G.55}$$

Again, one can expand $R_{IS,A}(\omega, \theta)$ in Legendre series (as in Eq. (G.48)), where [56]:

$$\Phi_{IS,A}^{(0)}(\omega) = 2\pi \frac{G_F^2}{h} n_b \, \frac{X_h}{A} A^2 \left(C_{V0} + \frac{1}{2} \frac{N-Z}{A} C_{V1} \right)^2 \, \frac{2y - 1 + e^{-2y}}{y^2} \tag{G.56}$$

$$\begin{aligned} \Phi_{IS,A}^{(1)}(\omega) &= 2\pi \frac{G_F^2}{h} n_b \, \frac{X_h}{A} A^2 \left(C_{V0} + \frac{1}{2} \frac{N-Z}{A} C_{V1} \right)^2 \\ &\quad \times \frac{2 - 3y + 2y^2 - (2+y)e^{-2y}}{y^3} \; , \end{aligned} \tag{G.57}$$

where $y = 4b\omega^2$.

Implementation

This process has been implemented by Ph. Mellor in the Newtonian code.
As in the previous case, instead of implementing the scattering using the Legendre expansion of the scatting kernel, the following expression for the neutrino mean free path has been used [91, 237, 41]:

$$\lambda_{IS,A} = 10^{20} \rho^{-1} \, \omega^{-2} \, \left[\frac{N^2}{6} \frac{X_h}{A} \right]^{-1} \; . \tag{G.58}$$

Summing the contributions to the opacities given by the scattering processes on nucleons, nuclei, α particles [318]:

$$\lambda_{IS} = 10^{20}\ \rho^{-1}\ \omega^{-2}\ \left[\frac{N^2}{6}\frac{X_h}{A} + X_n + \frac{5}{6}X_p + \frac{X_\alpha}{6}\right]^{-1} . \tag{G.59}$$

G.2.5 Neutrino-electron scattering

The neutrino-electron scattering (NES) is given, for all neutrino flavours, by [56]:

$$\nu_i + e^- \rightleftarrows \nu_i + e^- . \tag{G.60}$$

The scattering production and absorption kernel $R_{NES}^{in/out}$ are related to the scattering rate in the same way as in the IS case. Their expressions have been derived in [56]:

$$R_{NES}^{in} = \int \frac{\mathrm{d}^3 p_t}{(2\pi)^3} \int \frac{\mathrm{d}^3 p_{t'}}{(2\pi)^3} \left[1 - f_t(E_t)\right] 2 f_t(E_t')\ r(p_t' + q' \rightarrow p_t + q) \tag{G.61}$$

$$R_{NES}^{out} = \int \frac{\mathrm{d}^3 p_t}{(2\pi)^3} \int \frac{\mathrm{d}^3 p_{t'}}{(2\pi)^3} 2 f_t(E_t)\ \left[1 - f_t(E_t')\right] r(p_t + q \rightarrow p_t' + q') , \tag{G.62}$$

where f_t is the distribution function, p_t and p_t' refer to the momentum of the target particles (electrons), q and q' refer to the momentum of the "in" and "out" beam neutrino. One can once more relate the "in" and "out" scattering kernel by mean of the Eq. (G.26) as:

$$R_{NES}^{in}(\omega, \omega', \cos\theta) = e^{\frac{E_t - E_t'}{k_B T}}\ R_{NES}^{out}(\omega, \omega', \cos\theta) . \tag{G.63}$$

Expanding into the first two terms of Legendre series:

$$R_{NES}^{in/out}(\omega, \omega', \cos\theta) = \frac{1}{2}\Phi_{NES}^{(0),in/out}(\omega, \omega') + \frac{3}{2}\Phi_{NES}^{(1),in/out}(\omega, \omega')\cos\theta , \tag{G.64}$$

where ($l = 0, 1$):

$$\begin{aligned}\Phi_{NES}^{l,in} &= \frac{c(\hbar c)^2 G_F^2}{\pi \omega^2 \omega'^2} \int_0^\infty \mathrm{d}E_e f_e(E_e)[1 - f_e(E_e + \omega - \omega')] e^{-\frac{\omega - \omega'}{k_b T}} \\ &\quad \times \left[(C_V + C_A)^2 H^{l,I}(E_e, \omega, \omega') + (C_V - C_A)^2 H^{l,II}(E_e, \omega, \omega')\right] ,\end{aligned} \tag{G.65}$$

where $H^{l,I/II}(E_e, \omega, \omega')$ are given in Appendix A of Yueh and Buchler [353]. Integrals are calculated with the Laguerre method.
In addition to the coupling of neutrino distribution function in different spatial zones by the diffusion equation, NES couples also neutrino distribution probabilities in different energy bins.

Implementation

The implementation of the NES in the Newtonian code, according to Bruenn and Yueh and Buchler expressions [353, 56], is underway.

Acknowledgements

There are a lot of people I would like to thank in this moment, and I apologize if someone's name is not appearing on this list.

First of all I would like to thank my advisors and collaborators which have closely followed my work during these three years: Prof. Pierre Pizzochero, not only for having taught me physics, but also for the way he does it, for his always pertinent suggestions, his global vision on the subject and his support; Dr. Jérôme Margueron, for having taught me nuclear physics, for his availability, suggestions and for having carefully reading the thesis; Dr. Patrick Blottiau, for having made me use his hydrodynamical Newtonian code, for having helped me in hydro problems and going through the thesis, for his support and kindness; Dr. Elias Khan, for having introduced me to IPN, and the fruitful discussions on electron capture. I'm deeply gratefully in debt to Dr. Paola Donati, for her help in nuclear calculations, in particular in the RPA calculations, for her always kind availability, and support, especially at the end of the thesis.

I would like to acknowledge Dr. Jérôme Novak and Prof. José Pons for their kind help on the Relativistic code and for having provided me the GR code.

I thank Dr. Micaela Oertel, for the fruitful discussions and collaboration on the equation of state and in comparing our results.

Thanks to Dr. Philip Mellor for explanations about neutrino physics and the help in the hydrodynamical Newtonian code; Prof. Nguyen Van Giai for interesting discussions, Dr. Nicu Sandulescu for checking our HF+BCS results.

Thanks to Dr. Isaac Vidaña Haro for the BHF calculations on the k-mass (y por las lecciónes de Español!).

I acknowledge Prof. J. M. Ibáñez for his pertinent suggestions on the GR code, and how to check instabilities.

Fruitful discussions with Dr. Nicolas Chamel, Dr. Stéphane Goriely and Dr. Michael Pearson on EDF have been very much appreciated.

I would like to thank Prof. Marcello Baldo and Prof. Francesca Gulminelli, for being referees of the thesis and for their pertinent remarks and corrections.

I express my gratitude to the Groupe de Physique Théorique de l'IPNO, to Dr. Marcella Grasso for having helped me with French-Italian translations, and for all the fruitful and friendly discussions.

Thanks also to the colleagues at CEA/DAM, for having welcomed me et pour les "pauses gâteau"!

Thanks to Morgane Fortin for the work we have done together on the Presupernova models, for her French lessons, her guide-tour in Mont St. Michel, her sympathy and nice time spent together at IPN, during Copenhagen school and Valencia meeting.

Thanks to Bruno Peres for the comparisons on the neutrino leakage scheme.

A big big thank to Daniel Peña Arteaga, for the help in compilation problems, and for his support and encouragement especially in a couple of critical moments.

Thanks to the colleagues in the CompStar network, for the nice discussions, schools, workshops, dinners, ... In particular I would like to thank Roberto Anglani, Debarati Chatterjee, Filippo Galeazzi, Fabrizio Grill, Matthias Hempel, Roger Kaeppeli, Albino Perego, Irina Sagert, Simon Scheidegger, Vittorio Somà for their friendship.

Merci beaucoup à mes collègues de bureau, Jean-Paul Ebran, Sébastien Galais, Jérôme Gava, pour les conversations très sympas, et pour m'avoir enseigné vraiment beaucoup sur la langue française!

Thanks to Mr. and Mrs. Hawken, for having welcomed me in their house and for their help whenever needed.

Grazie a tutte le persone che dall'Italia mi hanno sempre aiutato, sostenuto e fatto sentire la loro vicinanza con ogni mezzo. Grazie a Benedetta Baiocchi, Andrea Barbieri, Valerio Bartoloni, Riccardo Consonni, Giuliana Dattero, Miriam Gilardi, Greta Gruppi, Roberto Lo Russo, Laura Maraviglia, Sara Rech, Franca Stilo, Michele Teamira, Irene Tessaro, Claudia Tintori (RDG), Angela Vozzolo.
Grazie a Stefano Galbiati, per il supporto e per aver creduto in me, da lungo tempo!
Grazie a Luca Ricevuti, per l'amicizia.

Last but not least, I thank with love my parents, Marinella and Armando, for their help, patience, and strong support, in any one of my decisions.

This thesis has been supported by the exchange fellowship program of the Université Franco-Italienne and Université Paris Sud, and partially by CompStar, a Research Networking Programme of the European Science Foundation.

Anthea F. Fantina, Orsay - 31st October 2010

Bibliography

[1] M. Abramowitz, and I. A. Stegun, *Handbook of Mathematical Functions with Formulas, Graphs, and Mathematical Tables*, Dover Publications Inc., New York, USA (1965)

[2] B. K. Agrawal, and A. Ansari, Phys. Lett. **B 421**, 13 (1998)

[3] C. Amsler *et al.*(Particle Data Group), Phys. Lett. **B 667**, 1 (2008)

[4] P. W. Anderson, and N. Itoh, Nature **256**, 25 (1975)

[5] W. D. Arnett, Astrophys. J. **153**, 341 (1968)

[6] W. D. Arnett, Nature **219**, 1344 (1968)

[7] W. D. Arnett, Astrophys. J. **218**, 815 (1977)

[8] W. D. Arnett, "Gravitational collapse of evolved stars as a problem in physics", in *Sources of Gravitational Radiation*, Proceedings of the Workshop, Seattle, Wanshington, USA, July 1978, Cambridge and New York Cambridge University Press (1979)

[9] W. D. Arnett, *Supernovae and Nucleosynthesis*, Princeton University, Princeton, New Jersey, USA (1996)

[10] R. Arnowitt, S. Deser, C. W. Misner, *Gravitation: an introduction to current research*, L. Witten Ed., Wiley, New York, USA (1962)

[11] W. Baade, and F. Zwicky, Phys. Rev. **46**, 76 (1934)

[12] M. Baldo, L. S. Ferreira, and O. E. Nicotra, Phys. Rev. **C 69**, 034321 (2004)

[13] M. Baldo, U. Lombardo, S. S. Pankratov, and E. E. Saperstein, J. Phys. **G 37**, 064016 (2010)

[14] F. Banyuls, J. A. Font, J. M. Ibáñez, J. M. Martí, and J. A. Miralles, Astrophys. J. **476**, 221 (1997)

[15] J. Bardeen, L. N. Cooper, and J. R. Schrieffer, Phys. Rev. **108**, 1175 (1957)

[16] E. Baron, H. A. Bethe, G. E. Brown, J. Cooperstein, and S. Kahana, Phys. Rev. Lett. **59**, 736 (1987)

[17] E. Baron, and J. Cooperstein, Astrophys. J. **353**, 597 (1990)

[18] E. Baron, J. Cooperstein, and S. Kahana, Phys. Rev. Lett. **55**, 126 (1985)

[19] E. Baron, J. Cooperstein, and S. Kahana, Nucl. Phys. **A 440**, 744 (1985)

[20] M. Barranco, and J. Treiner, Nucl. Phys. **A 351**, 269 (1981)

[21] J. Bartel, P. Quentin, M. Brack, C. Guet, and H.-B. Hakansson, Nucl. Phys. **A 386**, 79 (1982)

[22] G. Baym, H. A. Bethe, and C. J. Pethick, Nucl. Phys. **A 175**, 225 (1971)

[23] M. Beiner, H. Flocard, N. Van Giai, and P. Quentin, Nucl. Phys. **A 238**, 29 (1975)

[24] M. Bender, P.-H. Heenen, and P.-G. Reinhard, Rev. Mod. Phys. **75**, 121 (2003)

[25] J.-F. Berger, M. Girod, and D. Gogny, Comp. Phys. Comm. **63**, 365 (1991)

[26] V. Bernard, and N. Van Giai, Nucl. Phys. **A 327**, 397 (1979)

[27] V. Bernard, and N. Van Giai, Nucl. Phys. **A 348**, 75 (1980)

[28] G. F. Bertsch, D. J. Dean, and N. Nazarewicz, SciDAD Review **6**, 42 (2007)

[29] G. F. Bertsch, and T. T. S. Kuo, Nucl. Phys. **A 112**, 204 (1968)

[30] G. F. Bertsch, and S. F. Tsai, Phys. Rep. **18**, 125 (1975)

[31] C. A. Bertulani, H. F. Lü, and H. Sagawa, Phys. Rev. **C 80**, 027303 (2009)

[32] H. A. Bethe, Phys. Rev. **50**, 332 (1936)

[33] H. A. Bethe, Rev. Mod. Phys. **62**, 801 (1990)

[34] H. A. Bethe, G. E. Brown, J. Applegate, and J. M. Lattimer, Nucl. Phys. **A 324**, 487 (1979)

[35] H. A. Bethe, G. E. Brown, J. Cooperstein, and J. R. Wilson, Nucl. Phys. **A 403**, 625 (1983)

[36] H. A. Bethe, and M. B. Johnson, Nucl. Phys. **A 230**, 1 (1974)

[37] H. A. Bethe, and P. M. Pizzochero, Astrophys. J. Lett. **350**, L33 (1990)

[38] H. A. Bethe, and J. R. Wilson, Astrophys. J. **295**, 14 (1985)

[39] S. I. Blinnikov, I. V. Panov, M. A. Rudzsky, and K. Sumiyoshi, arXiv:0904.3849 [astro-ph.HE]

[40] J. M. Blondin, A. Mezzacappa, and C. DeMarino, Astrophys. J. **584**, 971 (2003)

[41] P. Blottiau, *Modélisation des Supernovae de type II: hydrodynamique, instabilité gravitationnelle*, PhD thesis, Université Paris VII, Paris, France (1989)

[42] S. A. Bludman, I. Lichtenstadt, and G. Hayden, Astrophys. J. **261**, 661 (1982)

[43] N. N. Bogolyubov, Dokl. Akad. Nauk SSSR **119**, 244. (1959)

[44] A. Bohr, and B. R. Mottelson, *Nuclear Structure* Vols. I and II, Benjamin, New York, USA (1964)

[45] P. Bonche, and D. Vautherin, Nucl. Phys. **A 372**, 496 (1981)

[46] P. Bonche, and D. Vautherin, Astron. Astrophys. **112**, 268 (1982)

[47] P. F. Bortignon, and C. H. Dasso, Phys. Lett. **B 189**, 381 (1987)

[48] R. Bowers, and J. R. Wilson, Astrophys. J. Suppl. **50**, 115 (1982)

[49] R. Bowers, and J. R. Wilson, Astrophys. J. **263**, 366 (1982)

[50] R. A. Broglia, P. M. Pizzochero, P. Donati, and P. F. Bortignon, in *Proceedings of the International School of Heavy-Ion Physics: Probing the Nuclear Paradigm*, edited by R. A. Broglia, P. Kienle and P. F. Bortignon (World Scientific, Singapore, 1994), p.309

[51] B. A. Brown, Phys. Rev. **C 58**, 220 (1998)

[52] G. E. Brown, H. A. Bethe, and G. Baym, Nucl. Phys. **A 375**, 481 (1982)

[53] G. E. Brown, J. S. Dehesa, and J. Speth, Nucl. Phys. **A 330**, 290 (1979)

[54] G. E. Brown, J. A. Evans, and D. J. Thouless, Nucl. Phys. **45**, 164 (1963)

[55] G. E. Brown, J. H. Gunn, and P. Gould, Nucl. Phys. **46**, 598 (1963)

[56] S. W. Bruenn, Astrophys. J. Suppl. **58**, 771 (1985)

[57] S. W. Bruenn, Astrophys. J. Suppl. **62**, 331 (1986)

[58] S. W. Bruenn, Astrophys. Space Sci. **143**, 15 (1988)

[59] S. W. Bruenn, J. R. Buchler, and W. R. Yueh, Astrophys. Space Sci. **59**, 261 (1978)

[60] S. W. Bruenn, K. R. De Nisco, and A. Mezzacappa, Astrophys. J. **560**, 326 (2001)

[61] S. W. Bruenn, C. J. Dirk, A. Mezzacappa, J. C. Hayes, J. M. Blondin, W. R.. Hix, and O. E. B. Messer, J. Phys. Conf. Ser., **46**, 393 (2006)

[62] R. Buras, H.-Th. Janka, M. Rampp, and K. Kifonidis, Astron. Astrophys. **457**, 281 (2006)

[63] R. Buras, M. Rampp, H.-Th. Janka, and K. Kifonidis, Phys. Rev. Lett. **90**, 0241101 (2003)

[64] R. Buras, M. Rampp, H.-Th. Janka, and K. Kifonidis, Astron. Astrophys. **447**, 1049 (2006)

[65] E. M. Burbidge, G. R. Burbidge, W. A. Fowler, and F. Hoyle, Rev. Mod. Phys. **29**, 547 (1957)

[66] A. Burrows, J. Hayes, and B. A. Fryxell, Astrophys. J. **450**, 830 (1995)

[67] A. Burrows, and J. M. Lattimer, Astrophys. J. **307**, 178 (1986)

[68] A. Burrows, E. Livne, L. Dessart, C. D. Ott, and J. Murphy, Astrophys, J. **640**, 878 (2006)

[69] A. Burrows, S. Reddy, and T. A. Thompson, Nucl. Phys. **A 777**, 356 (2006)

[70] O. L. Caballero, C. J. Horowitz, and D. K. Berry, Phys. Rev. **C 74**, 065801 (2006)

[71] L. G. Cao, U. Lombardo, C. W. Shen, and N. Van Giai, Phys. Rev. **C 73**, 014313 (2006)

[72] E. Cappellaro, R. Evans, and M. Turatto, Astron. Astrophys. **351**, 459 (1999)

[73] V. Castellani, *Astrofisica stellare*, Zanichelli, Bologna, Italy (1985)

[74] J. I. Castor, Astrophys. J. **178**, 779 (1972)

[75] E. Caurier, K. Langanke, G. Martínez-Pinedo, and F. Nowacki, Nucl. Phys. **A 653**, 439 (1999)

[76] E. Chabanat, P. Bonche, P. Haensel, J. Meyer, and R. Schaeffer, Nucl. Phys. **A 627**, 710 (1997)

[77] E. Chabanat, P. Bonche, P. Haensel, J. Meyer, and R. Schaeffer, Nucl. Phys. **A 635**, 231 (1998)

[78] N. Chamel, and P. Haensel, Liv. Rev. Rel. **11**, 10 (2008)

[79] N. Chamel, J. Margueron, and E. Khan, Phys. Rev. **C 79**, 012801(R) (2009)

[80] S. Chandrasekhar, *An Introduction to the Study of Stellar Structure*, University of Chicago Press, Chicago, Illinois, USA (1939)

[81] R. J. Charity, L. G. Sobotka, J. F. Dempsey, M. Devlin, S. Komarov, and D. G. Sarantites, A. L. Caraley, and R. T. deSouza, W. Loveland, and D. Peterson, B. B. Back, C. N. Davids, and D. Seweryniak, Phys. Rev. **C 67**, 044611 (2003)

[82] A. Chieffi, M. Limongi, and O. Straniero, Astrophys. J. **502**, 737 (1998)

[83] A. Chodos, R. L. Jaffe, K. Johnson, C. B. Thorn, and V. F. Weisskopf, Phys. Rev. **D 9**, 3471 (1971)

[84] E. Chulick, M. N. Namboodiri and J. B. Natowitz, unpublished data

[85] D. D. Clayton, *Principles of Stellar Evolution and Nucleosynthesis*, University of Chicago Press, Chicago, Illinois, USA (1983)

[86] E. R. Cohen, and B. N. Taylor, Rev. Mod. Phys. **59**, 1121 (1987)

[87] P. Colella, and P. R. Woodward, J. Comp. Phys. **54**, 174 (1984)

[88] S. A. Colgate, and M. H. Johnson, Phys. Rev. Lett. **5**, 235 (1960)

[89] S. A. Colgate, and R. H. White, Astrophys. J. **143**, 626 (1966)

[90] J. Cooperstein, Nucl. Phys. **A 438**, 722 (1985)

[91] J. Cooperstein, Phys. Rep. **163**, 95 (1988)

[92] J. Cooperstein, and E. Baron, in *Supernovae*, edited by A. Petscheck, Springer, Berlin, Germany (1990)

[93] J. Cooperstein, and J. Wambach, Nucl. Phys. **A 420**, 591 (1984)

[94] P. Danielewicz, R. Lacey, and W. G. Lynch, Science **298**, 1592 (2002)

[95] P. J. Davis, and P. Rabinowitz, *Methods of Numerical Integration*, Academic Press, New York, USA (1975)

[96] J. N. De, S. Shlomo, and S. K. Samaddar, Phys. Rev. **C 57**, 1398 (1998)

[97] D. J. Dean, and M. Hjorth-Jensen, Rev. Mod. Phys. **75**, 607 (2003)

[98] D. J. Dean, S. E. Koonin, K. Langanke, and P. B. Radha, Phys. Lett. **B 356**, 429 (1995)

[99] D. J. Dean, K. Langanke, and J. M. Sampaio, Phys. Rev. **C 66**, 045802 (2002)

[100] P. G. de Gennes, and J. Prost, *The Physics of Liquid Crystal*, Oxford Science Publications, Oxford, UK (1993)

[101] H. Dimmelmeier, *General Relativistic Collapse of Rotating Stellar Cores in Axisymmetry*, PhD thesis, Technische Universität München Max-Planck-Institut für Astrophysik (2001)

[102] H. Dimmelmeier, P. Cerdá-Durán, A. Marek, and G. Faye, AIP Conference Proceedings, **861**, 600 (2006), arXiv:0603760 [astro-ph]

[103] H. Dimmelmeier, C. D. Ott, A. Marek, and H.-Th. Janka, Phys. Rev. **D 78**, 064056 (2008)

[104] J. Dobaczewski, W. Nazarewicz, T. R. Werner, J. F. Berger, C. R. Chinn, and J. Dechargé, Phys. Rev. **C 53**, 2809 (1996)

[105] P. Donati, private communications

[106] P. Donati, P. M. Pizzochero, P. F. Bortignon, and R. A. Broglia, Phys. Rev. Lett. **72**, 2835 (1994)

[107] B. Einfeldt, *On Godunov-type methods for gas dynamics*, SIAM J. Numer. Anal. **25**, 294 (1988)

[108] S. El-Kateb, K. P. Jackson, W. P. Alford, R. Abegg, R. E. Azuma, B. A. Brown, A. Celler, D. Frekers, O. Häusser, R. Helmer, R. S. Henderson, K. H. Hicks, R. Jeppesen, J. D. King, G. G. Shute, B. M. Spicer, A. Trudel, K. Raywood, M. Vetterli, and S. Yen, Phys. Rev. **C 49**, 3128 (1994)

[109] R. I. Epstein, and C. J. Pethick, Astrophys. J. **243**, 1003 (1981)

[110] A. F. Fantina, *Supernovae di tipo II: processi deboli e dinamica del collasso gravitazionale*, Tesi di Laurea Magistrale, Università degli Studi di Milano, Milano, Italy (2007)

[111] A. F. Fantina, P. Donati, and P. M. Pizzochero, Phys. Lett. **B 676**, 140 (2009)

[112] A. F. Fantina, J. Margueron, P. Donati, and P. M. Pizzochero, accepted for publication in J. Phys. **G** (2010)

[113] M. Farine, J. M. Pearson, and F. Tondeur, Nucl. Phys. **A 696**, 396 (2001)

[114] E. Fermi, *Termodinamica*, Boringhieri, Torino, Italy (1958)

[115] A. L. Fetter, and J. D. Walecka, *Quantum Theory of Many-Particle Systems*, McGraw-Hill, New York, USA (1971)

[116] T. Foglizzo, Astron. Astrophys. **392**, 353 (2002)

[117] T. Foglizzo, P. Galletti, L. Scheck, and H.-Th. Janka, Astrophys. J. **654**, 1006 (2007)

[118] J. A. Font, Liv. Rev. Relativ. **6**, 4 (2003)

[119] J. A. Font, *An Introduction to Relativistic Hydrodynamics: Theory, Numerics, and Astrophysical Applications*, talk at VII Mexican School on Gravitation and Mathematical Physics "Relativistic Astrophysics and Numerical Relativity", Playa del Carmen, Quintana Roo, Mexico (2006)

[120] J. A. Font, Liv. Rev. Relativ. **11**, 7 (2008)

[121] J. A. Font, J. M. Ibáñez, A. Marquina, and J. M. Martí, Astron. Astrophys. **282**, 304 (1994)

[122] M. Fortin, *Microphysics inputs for core-collapse supernovae*, Stage de Master 2 Astronomie, Astrophysique et Ingénierie Spatiale, spécialité Astrophysique, Observatoire de Paris, France (2009)

[123] B. Friedman, and V. R. Pandharipande, Nucl. Phys. **A 361**, 502 (1981)

[124] C. L. Fryer, W. Benz, M. Herant, and S. A. Colgate, Astrophys. J. **516**, 892 (1999)

[125] C. L. Fryer, and M. S. Warren, Astrophys. J. **601**, 391 (2004)

[126] G. M. Fuller, Astrophys. J. **252**, 741 (1982)

[127] G. M. Fuller, W. A. Fowler, and M. J. Newman, Astrophys. J. Suppl. **42**, 447 (1980)

[128] G. M. Fuller, W. A. Fowler, and M. J. Newman, Astrophys. J. **252**, 715 (1982)

[129] G. M. Fuller, W. A. Fowler, and M. J. Newman, Astrophys. J. Suppl. **48**, 279 (1982)

[130] G. M. Fuller, W. A. Fowler, and M. J. Newman, Astrophys. J. **293**, 1 (1985)

[131] E. Garrido, P. Sarriguren, E. Moya de Guerra, and P. Schuck, Phys. Rev. **C 60**, 064312 (1999)

[132] N. Giovanardi, P. F. Bortignon, R. A. Broglia, and W. Huang, Phys. Rev. Lett. **77**, 24 (1996)

[133] P. Glaister, J. Comp. Phys. **74**, 382 (1988)

[134] S. K. Godunov, Mat. Sb. **47**, 271 (1959). In Russian.

[135] P. Goldreich, and S. V. Weber, Astrophys. J. **238**, 991 (1980)

[136] M. Gonin, L. Cooke, K. Hagel, Y. Lou, J. B. Natowitz, R. P. Schmitt, S. Shlomo, B. Srivastava, W. Turmel, H. Utsunomiya, R. Wada, G. Nardelli, G. Nebbia, G. Viesti, R. Zanon, B. Fornal, G. Prete, K. Niita, S. Hannuschke, P. Gonthier, and B. Wilkins, Phys. Rev. **C 42**, 2125 (1990)

[137] A. L. Goodman, Nucl. Phys. **A 352**, 30 (1981)

[138] G. Gori, F. Ramponi, F. Barranco, P. F. Bortignon, R. A. Broglia, G. Colò, and E. Vigezzi, Phys. Rev. **C 72**, 011302(R) (2005)

[139] S. Goriely, Nucl. Phys. **A 605**, 28 (1996)

[140] S. Goriely, M. Samyn, and J. M. Pearson, Phys. Rev. **C 75**, 064312 (2007).

[141] E. Gourgoulhon, Ann. Phys. Fr. **18**, 1 (1993)

[142] E. Gourgoulhon, *3+1 Formalism and Bases of Numerical Relativity*, Lecture notes, arxiv:0703035 [gr-qc]

[143] F. Gulminelli, private communications

[144] M. Guttormsen, M. Hjorth-Jensen, E. Melby, J. Rekstad, A. Schiller, and S. Siem, Phys. Rev. **C 64**, 034319 (2001)

[145] K. Hagel, D. Fabris, P. Gonthier, H. Ho, Y. Lou, Z. Majka, G. Mouchaty, M. N. Namboodiri, J. B. Natowitz, G. Nebbia, R. P. Schmitt, G. Viesti, R. Wada, and B. Wilkins, Nucl. Phys. **A 486**, 429 (1988)

[146] I. Hamamoto, Phys. Rep. **10**, 63 (1974)

[147] I. Hamamoto, and P. Siemens, Nucl. Phys. **A 269**, 199 (1976)

[148] M. Hamuy, Astrophys. J. **582**, 905 (2003)

[149] M. N. Harakeh, and A. Van der Woude, Giant Resonances, Oxford Studies in Nuclear Physics **24**, Oxford University Press, New York, USA (2001)

[150] B. K. Harrison, K. S. Thorne, M. Wakano, and J. A. Wheeler, *Gravitation Theory and Gravitational Collapse*, University of Chicago Press, Chicago, Illinois, USA (1964)

[151] A. Harten, P. D. Lax, and B. van Leer, SIAM Rev. **25**, 35 (1983)

[152] R. W. Hasse, and P. Schuck, Phys. Lett. **B 179**, 313 (1986)

[153] K. Hebeler, T. Duguet, T. Lesinski, and A. Schwenk, Phys. Rev. **C 80**, 044321 (2009)

[154] A. Heger, K. Langanke, G. Martínez-Pinedo, and S. E. Woosley, Phys. Rev. Lett. **86**, 1678 (2001)

[155] A. Heger, N. Langer, and S. E. Woosley, Astrophys. J. **528**, 368 (2000)

[156] A. Heger, S. E. Woosley, and H. C. Spruit, Astrophys. J. **626**, 350 (2005)

[157] M. Hempel, and J. Schaffner-Bielich, Nucl. Phys. **A 837**, 210 (2010)

[158] M. Herant, W. Benz, and S. A. Colgate, Astrophys. J. **395**, 642 (1992)

[159] M. Herant, W. Benz, W. R. Hix, C. L. Fryes, and S. A. Colgate, Astrophys. J. **435**, 339 (1994)

[160] W. Hillebrandt, Astron. Astrophys. **110**, L3 (1982)

[161] W. Hillebrandt, Ann. NY Acad. Sci. **442**, 197 (1984)

[162] W. Hillebrandt, and E. Müller, Astron. Astrophys. **103**, 147 (1981)

[163] W. Hillebrandt, K. Nomoto, and R. G. Wolff, Astron. Astrophys. **133**, 175 (1984)

[164] R. Hirschi, G. Meynet, and A. Maeder, Astron. Astrophys. **425**, 649 (2004)

[165] W. R. Hix, O. E. B. Messer, A. Mezzacappa, M. Liebendörfer, J. Sampaio, K. Langanke, D. J. Dean, and G. Martínez-Pinedo, Phys. Rev. Lett. **91**, 201102 (2003)

[166] W. R. Hix, O. E. B. Messer, A. Mezzacappa, J. Sampaio, K. Langanke, G. Martínez-Pinedo, M. Liebendörfer and D. J. Dean, Nucl. Phys. **A 758**, 31c (2005)

[167] C. J. Horowitz, M. A. Pérez-García, D. K. Berry, and J. Piekarewicz, Phys. Rev. **C 72**, 035801 (2005)

[168] C. J. Horowitz, and B. D. Serot, Nucl. Phys. **A 464**, 613 (1987)

[169] J. M. Ibáñez, private communications

[170] C. Ishizuka, A. Ohnishi, K. Tsubakihara, K. Sumiyoshi, and S. Yamada, J. Phys. **G 35**, 085201 (2008)

[171] H.-Th. Janka, Astron. Astrophys. **256**, 452 (1992)

[172] H.-Th. Janka, R. Buras, F. S. Kitaura Joyanes, A. Marek, M. Rampp, and L. Scheck, Nucl. Phys. **A 758**, 19c (2005)

[173] H.-Th. Janka, K. Langanke, A. Marek, G. Martínez-Pinedo, and B. Müller, Phys. Rep. **442**, 38 (2007)

[174] J. P. Jeukenne, A. Lejeune, and C. Mahaux, Phys. Rep. **25**, 83 (1976)

[175] E. Khan, N. Sandalescu, and N. Van Giai, Phys. Rev. **C 71**, 042801(R) (2005)

[176] E. Khan, N. Van Giai, and N. Sandalescu, Nucl. Phys. **A 789**, 94 (2007)

[177] F. S. Kitaura, H.-Th. Janka, and W. Hillebrandt, Astron. Astrophys. **450**, 345 (2006)

[178] T. Klähn, D. Blaschke, S. Typel, E. N. E. van Dalen, A. Faessler, C. Fuchs, T. Gaitanos, H. Grigorian, A. Ho, E. E. Kolomeitsev, M. C. Miller, G. Röpke, J. Trümper, D. N. Voskresensky, F. Weber, and H. H. Wolter, Phys. Rev. **C 74**, 035802 (2006)

[179] K. Kotake, S. Yamada, and K. Sato, Astrophys. J. **595**, 304 (2003)

[180] D. Q. Lamb, J. M. Lattimer, C. J. Pethick, and D. G. Ravenhall, Phys. Rev. Lett. **41**, 1623 (1978)

[181] D. Q. Lamb, J. M. Lattimer, C. J. Pethick, and D. G. Ravenhall, Nucl. Phys. **A 360**, 459 (1981)

[182] K. Langanke, Acta Phys. Pol. **B 39**, 265 (2008)

[183] K. Langanke, E. Kolbe, and D. J. Dean, Phys. Rev. **C 63**, 032801(R) (2001)

[184] K. Langanke, and G. Martínez-Pinedo, Nucl. Phys. **A 673**, 481 (2000)

[185] K. Langanke, and G. Martínez-Pinedo, At. Data Nucl. Data Tables **79**, 1 (2001)

[186] K. Langanke, and G. Martínez-Pinedo, Rev. Mod. Phys. **75**, 819 (2003)

[187] K. Langanke, G. Martínez-Pinedo, J. M. Sampaio, D. J. Dean, W. R. Hix, O. E. B. Messer, A. Mezzacappa, M. Liebendörfer, H.-Th. Janka, and M. Rampp, Phys. Rev. Lett. **90**, 241102 (2003)

[188] J. M. Lattimer, *The nuclear EoS and Supernovae*, Lecture notes, State University at Stony Brook, Stony Brook, New York, USA

[189] J. M. Lattimer, *Nuclear Data Needs for the Equation of State in Core Collapse Supernovae*, talk in Basel, Switzerland, June 2006

[190] J. M. Lattimer, C. J. Pethick, D. G. Ravenhall, and D. Q. Lamb, Nucl. Phys. **A 432**, 646 (1985)

[191] J. M. Lattimer, and D. G. Ravenhall, Astrophys. J. **223**, 314 (1978)

[192] J. M. Lattimer, and F. D. Swesty, Nucl. Phys. **A 535**, 331 (1991)

[193] J. M. LeBlanc, and J. R. Wilson, Astrophys. J. **161**, 541 (1970)

[194] T. Lesinski, T. Duguet, K. Bennaceur, and J. Meyer, Eur. Phys. J. **A 40**, 121 (2009)

[195] J. P. Lestone, Phys. Rev. **C 52**, 1118 (1995)

[196] B.-A. Li, Phys. Rev. **C 69**, 064602 (2004)

[197] B.-A. Li, L.-W. Chen, and C. M. Ko, Phys. Rep. **464**, 113 (2008)

[198] T. Li, U. Garg, Y. Liu, R. Marks, B. K. Nayak, and P. V. Madhusudhana Rao, M. Fujiwara, H. Hashimoto, K. Nakanishi, S. Okumura, and M. Yosoi, M. Ichikawa, M. Itoh, R. Matsuo, and T. Terazono, M. Uchida, Y. Iwao, T. Kawabata, T. Murakami, H. Sakaguchi, S. Terashima, Y. Yasuda, and J. Zenihiro, H. Akimune, K. Kawase, and M. N. Harakeh, Phys. Rev. **C 81**, 034309 (2010)

[199] M. Liebendörfer, Astrophys. J. **633**, 1042 (2005)

[200] M. Liebendörfer, O. E. B. Messer, A. Mezzacappa, S. W. Bruenn, C. Y. Cardall, and F.-K. Thielemann, Astrophys. J. Suppl. **150**, 263 (2004)

[201] M. Liebendörfer, A. Mezzacappa, O. E. B. Messer, G. Martínez-Pinedo, W. R. Hix, and F.-K. Thielemann, Nucl. Phys. **A 719**, 144c (2003)

[202] M. Liebendoerfer, A. Mezzacappa, G.-K. Thielemann, O. E. B. Messer, W. R. Hix, and S. W. Bruenn, Phys. Rev. **D 63**, 103004 (2001)

[203] M. Liebendörfer, M. Rampp, H.-Th. Janka, and A. Mezzacappa, Astrophys. J. **620**, 840 (2005)

[204] M. Liebendörfer, S. Rosswog, and F. K. Thielemann, Astrophys. J. Suppl. **141**, 229 (2002)

[205] M. Liebendörfer, S. C. Whitehouse, and T. Fischer, Astrophys. J. **698**, 1174 (2009)

[206] M. Limongi, *Presupernova evolution and explosion of massive stars*, seminar given in Observatoire de Meudon, France, September 2009

[207] M. Limongi, and A. Chieffi, Astrophys. J. **592**, 404 (2003)

[208] M. Limongi, and A. Chieffi, Astrophys. J. **647**, 483 (2006)

[209] E. Livne, A. Burrows, R. Walder, I. Lichtenstadt, and T. A. Thompson, Astrophys. J. **609**, 277 (2004)

[210] U. Lombardo, "Superfluidity in Nuclear Matter", in Int. Rev. Nucl. Phys. **8**, *Nuclear Methods and Nuclear Equation of State*, edited by M. Baldo, World Scientific, Singapore (1999)

[211] W.-H. Long, N. Van Giai, and J. Meng, Phys. Lett. **B 640**, 150 (2006)

[212] Z. Y. Ma, and J. Wambach, Nucl. Phys. **A 402**, 275 (1983)

[213] R. Machleidt, K. Holinde, and Ch. Elster, Phys. Rep. **149**, 1 (1987)

[214] G. D. Mahan, *Many-Particle Physics*, Plenum Press, New York, USA, Second Edition (1990)

[215] C. Mahaux, in *The Many-Body Problem, Jastrow Correlations versus Brueckner Theory*, Eds R. Guardiola and J. Ros, Springer-Verlag, Berlin, Germany (1981)

[216] C. Mahaux, P. F. Bortignon, R. A. Broglia, and C. H. Dasso, Phys. Rep. **120**, 1 (1985)

[217] C. Mahaux, and H. Ngô, Phys. Lett. **B 100**, 285 (1981)

[218] C. Mahaux, and H. Ngô, Nucl. Phys. **A 378**, 205 (1982)

[219] C. Mahaux, and H. Ngô, Phys. Lett. **B 126**, 1 (1983)

[220] C. Mahaux, and R. Sartor, Phys. Rep. **211**, 53 (1992).

[221] A. Marek, and H.-Th. Janka, Astrophys. J. **694**, 664 (2009)

[222] A. Marek, H.-Th. Janka, R. Buras, M. Liebendörfer, and M. Rampp, Astron. Astrophys. **443**, 201 (2005)

[223] J. Margueron, *Effets du milieu sur la propagation des neutrinos dans la matière nucléaire*, PhD Thesis, Université Paris Sud XI, Orsay, France (2001)

[224] J. Margueron, J. Navarro, and P. Blottiau, Phys. Rev. **C 70**, 028801 (2004)

[225] J. Margueron, H. Sagawa, and K. Hagino, Phys. Rev. **C 76**, 064316 (2007)

[226] J. Margueron, H. Sagawa, and K. Hagino, Phys. Rev. **C 77**, 054309 (2008)

[227] J. Margueron, N. Van Giai, and J. Navarro, Phys. Rev. **C 72**, 034311 (2005)

[228] J. M. Martí, J. M. Ibáñez, and J. A. Miralles, Astron. Astrophys. **235**, 535 (1990)

[229] J. M. Martí, J. M. Ibáñez, and J. A. Miralles, Phys. Rev. **D 43**, 3794 (1991)

[230] J. M. Martí, and E. Müller, Liv. Rev. Rel. **7**, 1 (2003)

[231] G. Martínez-Pinedo, K. Langanke, and D. J. Dean, Astrophys. J. Suppl. **126**, 493 (2000)

[232] G. Martínez-Pinedo, M. Liebendörfer, and D. Frekers, Nucl. Phys. **A 777**, 395 (2006)

[233] M. M. May, and R. H. White, Phys. Rev. **141**, 1232 (1966)

[234] M. M. May, and R. H. White, Methods Comput. Phys. **7**, 219 (1967)

[235] R. Mayle, and J. R. Wilson, Astrophys. J. **334**, 909 (1988)

[236] Ph. Mellor, *Modélisation des Supernovae de type II: simulation du transport des neutrinos*, PhD thesis, Université Paris VII, Paris, France (1988)

[237] Ph. Mellor, J. P. Chièze, and J. L. Basdevant, Astron. Astrophys. **197**, 123 (1988)

[238] P. Mészáros, Rep. Prog. Phys. **69**, 2259 (2006)

[239] J. Meyer, Ann. Phys. Fr. **28**, N. 3, 1 (2003)

[240] A. Mezzacappa, and S. W. Bruenn, Astrophys. J. **405**, 637 (1993)

[241] A. Mezzacappa, and S. W. Bruenn, Astrophys. J. **405**, 669 (1993)

[242] A. Mezzacappa, and S. W. Bruenn, Astrophys. J. **410**, 740 (1993)

[243] A. Mezzacappa, M. Liebendörfer, O. E. B. Messer, W. R. Hix, F.-K. Thielemann, and S. W. Bruenn, Phys. Rev. Lett. **86**, 1935 (2001)

[244] D. Mihalas, and B. Weibel-Mihalas, *Foundations of Radiation Hydrodynamics*, Dover Publications Inc., Mineola, New York, USA (1999)

[245] R. Minkowski, Publ. Astron. Soc. Pac. **53**, 224 (1941)

[246] C. W. Misner, K. S. Thorne, and J. A. Wheeler, *Gravitation*, Freeman and Co. New York, USA (1973)

[247] P. J. Mohr, and B. N. Taylor, Rev. Mod. Phys., **77**, 1 (2005); http://physics.nist.gov/cuu/Constants/

[248] E. Müller, "Simulation of astrophysical fluid flow", in *Computational Methods for Astrophysical Fuid Flow*, O. Steiner and A. Gautschy Eds., p. 343-494, Springer-Verlag, Berlin, Germany (1998)

[249] E. Müller, and W. Hillebrandt, Astron. Astrophys. **80**, 147 (1979)

[250] E. Müller, and W. Hillebrandt, Astron. Astrophys. **103**, 358 (1981)

[251] E. Müller, H.-Th. Janka, and H. Dimmelmeier, Astrophys. J. Suppl. **189**, 104 (2010)

[252] W. D. Myers, and W. J. Swiatecki, Annu. Rev. Nucl. Part. Sci. **32**, 309 (1982)

[253] E. S. Myra, and S. A. Bludman, Astrophys. J. **340**, 384 (1989)

[254] H. Nakada, Phys. Rev. **C 68**, 014316 (2003)

[255] B. Nerlo-Pomorska, K. Pomorski, and J. Bartel, Phys. Rev. **C 74**, 034327 (2006)

[256] W. F. Noh, J. Comp. Phys. **72**, 78 (1987)

[257] K. Nomoto, and M.-A. Hashimoto, Phys. Rep. **163**, 13 (1988)

[258] E. O'Connor, and C. D. Ott, Class. Quantum Grav. **27**, 114103 (2010)

[259] M. Oertel, private communications

[260] M. Oertel, and A. F. Fantina, Proceedings SF2A Marseille, June 2010

[261] A. M. Oros, *Study of the coupling between collective and single-particle excitation modes in medium heavy spherical nuclei*, PhD thesis, University of Köln, Germany (1996)

[262] C. D. Ott, *Stellar Iron Core Collapse in* $\{3+1\}$ *General Relativity and The Gravitational Wave Signature of Core-Collapse Supernovae*, PhD thesis, Albert-Einstein-Institut Max-Planck-Institut für Gravitationsphysik and Mathematisch-Naturwissenschaftliche Fakultät Universität Potsdam (2006)

[263] N. Paar, G. Colò, E. Khan, and D. Vretenar, Phys. Rev. **C 80**, 055801 (2009)

[264] D. Page, M. Prakash, J. M. Lattimer, and A. W. Steiner, Phys. Rev. Lett. **85**, 2048 (2000)

[265] B. Peres, *Transport des neutrinos dans les supernovae gravitationnelles*, Stage de Master 2 Recherche Astronomie et Astrophysique, Observatoire de Paris, France (2010)

[266] A. C. Phillips, *The Physics of Stars*, John Wiley & Sons, Chichester, UK (1994)

[267] J. Piekarewicz, J. Phys. **G 37**, 064038 (2010)

[268] D. Pines, and M. A. Alpar, Nature **316**, 27 (1985)

[269] J. A. Pons, J. A. Miralles, and J. M. Ibáñez, in *Some Topics on General Relativity and Gravitational Radiation*, p.293, edited by J. A. Miralles, J. A. Morales, D. Sáez, Proceedings of the "Spanish Relativity Meeting '96", Valencia, Spain (1996)

[270] M. Prakash, J. Wambach, and Z. Y. Ma, Phys. Lett. **B 128**, 141 (1983)

[271] W. H. Press, B. P. Flannery, S. A. Teukolsky, and W. T. Vetterling, *Numerical Recipes*, Cambridge University Press, UK (1986)

[272] A. R. Raduta, and F. Gulminelli, arXiv:1009.2226 [nucl-th]

[273] M. Rampp, *Radiation Hydrodynamics with Neutrinos: Stellar Core Collapse and the Explosion Mechanism of Type II Supernovae*, PhD Thesis, Technischen Universität München, Germany (2000)

[274] M. Rampp, and H.-Th. Janka, Astrophys. J. Lett. **539**, L33 (2000)

[275] M. Rampp, and H.-Th. Janka, Astron. Astrophys. **396**, 361 (2002)

[276] D. G. Ravenhall, C. J. Pethick, and J. R. Wilson, Phys. Rev. Lett. **50**, 2066 (1983)

[277] A. Ray, S. M. Chitre, and K. Kar, Astrophys. J. **285**, 766 (1984)

[278] R. V. Reid, Ann. Phys. **50**, 411 (1968)

[279] L. Rezzolla, *Numerical Methods for the Solution of Partial Differential Equations*, Doctoral Training Programme at ECT* Trento, Italy (2007); available at www.aei.mpg.de/~rezzolla

[280] R. D. Richtmyer, and K. W. Morton, *Difference Methods for Initial-Value Problems*, 2nd ed., Interscience Publisher, New York, USA (1967)

[281] P. Ring, and E. V. Litvinova, Phys. Atomic Nuclei **72**, N. 8, 1285 (2009); arXiv:0909.1276 [nucl-th]

[282] P. Ring, and P. Schuck, *The Nuclear Many-Body Problem*, Springer-Verlag, New York, USA (1980)

[283] A. Rios Huguet, *Thermodynamical Properties of Nuclear Matter from a Self-Consistent Green's Function Approach*, University of Barcelona, Spain (2007)

[284] P. L. Roe, J. Comp. Phys. **43**, 357 (1981)

[285] J. V. Romero, J. M. Ibáñez, J. M. Martí, and J. A. Miralles, Astrophys. J. **462**, 839 (1996)

[286] J. V. Romero, J. M. Ibañez, J. A. Miralles, and J. A. Pons, in *Some Topics on General Relativity and Gravitational Radiation*, p. 289, edited by J. A. Miralles, J. A. Morales, D. Sáez, Proceedings of the "Spanish Relativity Meeting '96", Valencia, Spain (1996)

[287] D. J. Rowe, *Nuclear Collective Motion*, Methuen and Co. Ltd, London, UK (1970)

[288] M. Ruffert, H-Th. Janka, and G. Shäfer, Astron. Astrophys. **311**, 532 (1996)

[289] I. Sagert, T. Fischer, M. Hempel, G. Pagliara, J. Schaffner-Bielich, A. Mezzacappa, F.-K. Thielemann, and M. Liebendörfer, Phys. Rev. Lett. **102**, 081101 (2009)

[290] E. E. Salpeter, Astrophys. J. **121**, 161 (1955)

[291] L. Scheck, K. Kifonidis, H.-Th. Janka, and E. Müller, Astron. Astrophys. **457**, 963 (2006)

[292] A. Schiller, A. Bjerve, M. Guttormsen, M. Hjorth-Jensen, F. Ingebretsen, E. Melby, S. Messelt, J. Rekstad, S. Siem, and S. W. Ødegard, Phys. Rev. **C 63**, 021306(R) (2001)

[293] B. D. Serot, and J. D. Walecka, Adv. Nucl. Phys. **16**, 1 (1986)

[294] B. D. Serot, and J. D. Walecka, Int. J. Mod. Phys. **E 6**, 515 (1997)

[295] S. L. Shapiro, and S. A. Teukolsky, *Black Holes, White Dwarfs, and Neutron Stars*, John Wiley & Sons, New York, USA (1983)

[296] G. Shen, C. J. Horowitz, and S. Teige, Phys. Rev. **C 82**, 015806 (2010)

[297] H. Shen, H. Toki, K. Oyamatsu, and K. Sumiyoshi, Nucl. Phys. **A 637**, 435 (1998)

[298] H. Shen, H. Toki, K. Oyamatsu, and K. Sumiyoshi, Nucl. Phys. **A 721**, 1048c (2003)

[299] H. Shen, H. Toki, K. Oyamatsu, and K. Sumiyoshi, "User Notes for the Relativistic EoS table", available at http://user.numazu-ct.ac.jp/~sumi/eos/

[300] S. Shlomo, and J. B. Natowitz, Phys. Lett. **B 252**, 187 (1990)

[301] S. Shlomo, and J. B. Natowitz, Phys. Rev. **C 44**, 2878 (1991)

[302] T. H. R. Skyrme, Phil. Mag. **1**, 1043 (1956)

[303] K. Sumiyoshi, S. Yamada, H. Suzuki, H. Shen, S. Chiba, and H. Toki, Astrophys. J. **629**, 922 (2005)

[304] E. Suraud, Astron. Astrophys. **143**, 108 (1985)

[305] F. D. Swesty, *User Notes for the Equation of State*, available at http://www.astro.sunysb.edu/dswesty/lseos.html

[306] F. D. Swesty, Astrophys. J. **445**, 811 (1995)

[307] F. D. Swesty, J. M. Lattimer, and E. S. Myra, Astrophys. J. **425**, 195 (1994)

[308] F. D. Swesty, and E. S. Myra, in *"Open Issues in Core Collapse Supernova Theory"*, p. 176, edited by A. Mezzacappa and G. M. Fuller, Published by World Scientific Publishing Co., Ltd., London, UK (2005)

[309] F. D. Swesty, and E. S. Myra, Astrophys. J. Suppl. **181**, 1 (2009)

[310] G. A. Tammann, W. Löffler and A. Schröder, Astrophys. J. Suppl. **92**, 487 (1994)

[311] L. J. Tassie, Aust. J. Phys. **9**, 407 (1956)

[312] B. ter Haar, and R. Malfliet, Phys. Rev. Lett. **56**, 1237 (1986)

[313] T. A. Thompson, A. Burrows, and P. A. Pinto, Astrophys. J. **592**, 434 (2003)

[314] F. X. Timmes, and D. Arnett, Astrophys. J. Suppl. **125**, 277 (1999)

[315] E. F. Toro, *Riemann solvers and numerical methods for fluid dynamics - a practical introduction*, Springer, Berlin, Germany (1997)

[316] W. M. Tscharnuter, and K.-H. A. Winkler, Comput. Phys. Commun. **18**, 171 (1979)

[317] D. L. Tubbs, Astrophys. J. Suppl. **37**, 287 (1978)

[318] D. L. Tubbs, and D. N. Schramm, Astrophys. J. **201**, 467 (1975)

[319] S. Typel, and H. H. Wolter, Nucl. Phys. **A 656**, 331 (1999)

[320] E. N. E. van Dalen, C. Fuchs, and A. Faessler, Phys. Rev. Lett. **95**, 022302 (2005)

[321] S. van den Bergh and G. A. Tammann, Ann. Rev. Astron. Astrophys. **29**, 363 (1991)

[322] N. Van Giai, *Étude du potentiel nucléon-noyau et des états analogues dans l'approximation de Hartree-Fock avec l'interaction de Skyrme*, PhD thesis, Univeristé Paris Sud XI, Orsay, France (1972)

[323] N. Van Giai, private communications

[324] N. Van Giai, and P. Van Thieu, Phys. Lett. **B 126**, 421 (1983)

[325] K. A. van Riper, Astrophys. J. **232**, 558 (1979)

[326] K. A. van Riper and J. M. Lattimer, Astrophys. J. **249**, 270 (1981)

[327] D. Vautherin, Phys. Rev. **C 7**, 296 (1973)

[328] D. Vautherin, and D. M. Brink, Phys. Rev. **C 5**, 626 (1972)

[329] I. Vidaña Haro, private communications

[330] I. Vidaña Haro, C. Providência, A. Polls, and A. Rios, Phys. Rev. **C 80**, 045806 (2009)

[331] N. Vinh Mau, *Theory of Nuclear Structure*, p. 931, IAEA, Vienna, Austria (1970)

[332] N. Vinh Mau, and A. Bouyssy, Nucl. Phys. **A 257**, 189 (1976)

[333] N. Vinh Mau, and D. Vautherin, Nucl. Phys. **A 445**, 245 (1985)

[334] D. Vretenar, T. Nikšić, and P. Ring, Phys. Rev. **C 65**, 024321 (2002)

[335] G. Watanabe, K. Sato, K. Yasuoka, and T. Ebisuzaki, Phys. Rev. **C 69**, 055805 (2004)

[336] T. A. Weaver, G. B. Zimmerman, and S. E. Woosley, Astrophys. J. **225**, 1021 (1978)

[337] R. D. Williams, and S. E. Koonin, Nucl. Phys. **A 435**, 844 (1985)

[338] J. R. Wilson, Astrophys. J. **163**, 209 (1971)

[339] J. R. Wilson, Astrophys. J. **173**, 431 (1972)

[340] J. R. Wilson, in *Numerical Astrophysics*, edited by J. M. Centrella, J. M. LeBlanc, and R. L. Bowers, Jones and Bartlett Publishers, Boston, USA, p. 422 (1985)

[341] J. R. Wilson, and G. J. Mathews, *Relativistic Numerical Hydrodymanics*, Cambridge University Press, Cambridge, UK (2003)

[342] J. R. Wilson, and R. Mayle, Phys. Rep. **163**, 63 (1988)

[343] J. R. Wilson, R. W. Mayle, S. E. Woosley, and T. Weaver, Ann. New York Acad. Sci. **470**, 267 (1986)

[344] S. E. Woosley, and J. S. Bloom, Ann. Rev. Astron. Astrophys. **44**, 507 (2006)

[345] S. E. Woosley, A. Heger and T. A. Weaver, Rev. Mod. Phys. **74**, 1015 (2002)

[346] S. E. Woosley, and H.-Th. Janka, Nature Physics **1**, 147 (2005)

[347] S. E. Woosley, and T. A. Weaver, *The Great Supernova of 1987*, Scientific American **261**, 32 (1989)

[348] S. E. Woosley, and T. A. Weaver, Astrophys. J. Suppl. **101**, 181 (1995)

[349] A. Yahil, Astrophys. J. **265**, 1047 (1983)

[350] S. Yamada, Astrophys. J. **475**, 720 (1997)

[351] K. Yoshida, Phys. Rev. **C 79**, 054303 (2009)

[352] S. Yoshida, and H. Sagawa, Phys. Rev. **C 77**, 054308 (2008)

[353] W. R. Yueh, and J. R. Buchler, Astrophys. J. **217**, 565 (1977)

[354] M. Zalewski, P. Olbratowski, and W. Satula, Int. J. Mod. Phys. **E 19**, 794 (2010)

[355] M. Zalewski, P. Olbratowski, and W. Satula, Phys. Rev. **C 81**, 044314 (2010)

[356] T. Zwerger, and E. Müller, Astron. Astrophys. **320**, 209 (1997)

[357] http://nn-online.org, a website mainteined by the Theoretical High Energy Physics Group of the Radboud University Nijmegen, The Netherlands

[358] http://gwdac.phys.gwu.edu, a website mainteined by the Center for Nuclear Studies, Departement of Physics, The George Washington University, Virginia Campus, USA

[359] http://www.mpa-garching.mpg.de/hydro/COCONUT/intro.php

[360] http://www.supernovae.net, february 2010